Spectral Super-Element Approach for Wave Propagation in Range Dependent Elastic Medium

by

Joo Thiam Goh

B.Eng. Electronics and Control Engineering, University of Birmingham (1987)

Submitted to the Department of Ocean Engineering
in Partial Fulfillment of the Requirements
for the Degree of

Doctor of Philosophy

at the

Massachusetts Institute of Technology
June 1996

Signature of Author _____

Department of Ocean Engineering
May 1, 1996

Certified by _____

Professor Henrik Schmidt
Professor of Ocean Engineering
Thesis Supervisor

Accepted by _____

Professor A. Douglas Carmichael
Chairman, Departmental Graduate Committee

Spectral Super-Element Approach for Wave Propagation in Range Dependent Elastic Medium

by

Joo Thiam Goh

Submitted to the Department of Ocean Engineering in Partial Fulfillment
of the Requirements for the Degree of Doctor of Philosophy
at the Massachusetts Institute of Technology

Abstract

This thesis develops coupled wavenumber integration approaches to solve the elastic wave equation in a range-dependent ocean environment. Spectral-based methods directly provide the spectral decomposition of the wave field in terms of modal components, which helps in the physical interpretation of the numerical results.

In Part I of the thesis, we performed extensive numerical experiments using the adiabatic transform technique developed by Lu and Felsen [1]. The experiments indicated that the adiabatic integral performs better than the classical adiabatic mode approach but suffers from serious limitations in handling the continuous spectrum. In addition, the *spectral mapping* operation needed to map the source spectrum involved time-consuming searches for complex roots. Furthermore, errors from the mapping process could erroneously contribute to mode coupling. Our studies also suggested that the standard adiabatic mode approach is invalid for *virtual* modes, a point not often appreciated.

In part II of the thesis, we proposed a new *spectral super-element* approach which uses a hybridization of finite elements, boundary integrals, and wavenumber integration to solve the wave equation in a range-dependent elastic ocean environment. The original acoustic for-

[1] I.T. Lu,L.B. Felsen,"Adiabatic transforms for spectral analysis and synthesis of weakly range-dependent shallow ocean Green's functions", *J. Acoust. Soc. Am.*, **81**, 897-911, 1987

mulation was developed by Seong [2]. In our approach, the range-dependent ocean is divided into range independent sectors or *super-elements*. Wavenumber integral representations can be derived for an influence matrix representing the relation between displacement and stress expansions on the vertical boundaries. The integration kernels are determined very efficiently by the Direct Global Matrix method in combination with a numerical quadrature scheme. The unknown expansion coefficients are then found by matching the boundary conditions of continuous displacements and stresses between the sectors, with the wave field following by evaluating the wavenumber integrals within each sector. The present implementation applies a single-scatter approximation at each vertical sector boundary, allowing for a marching solution. The back-scattered field can also be obtained via a 2-way marching scheme. By using SAFARI as the basic computational engine, many of the extensions found in SAFARI can be incorporated in a straightforward manner for each range-independent sector. *Extensive* benchmarking has demonstrated the accuracy and versatility of the proposed modeling approach.

Thesis supervisor : Prof. Henrik Schmidt
Professor of Ocean Engineering

[2] W. Seong, *Hybrid Galerkin boundary element - wavenumber integration method for acoustic propagation in laterally inhomogeneous media*, PhD thesis, MIT, Jan. 1991

Acknowledgements

It is my good fortune to have Prof. Henrik Schmidt as my thesis advisor. You were always helpful and your ability to combine rigorous theory with practical engineering 'hacks' never ceases to amaze me! My gratitude goes to you for your continuous guidance and enthusiasm in this work.

I would like to thank Dr. Leo Felsen and Dr. YuePing Guo for constructive discussions during the early part of this work. Prof. Rob Fricke and Dr. Guo were kind enough to agree to be on my committee. Special thanks to Prof. Paul Sclavounos and Dr. John Leonard who came to my rescue when Rob and YuePing decided to seek greener pastures elsewhere.

I would like to acknowledge helpful discussions with Dr. Peter Gerstoft of the SACLANT Undersea Research Center and Dr. Mike Collins of Naval Research Laboratory.

Thanks are also due to my fellow colleagues in 5-007 who were instrumental in helping to make my stay at MIT a lot more fun.

The continuous diligent efforts of the secretarial staff, Sabina, Isela, Taci, Patrick and many others, deserve my special thanks.

This thesis would not have been possible without the generous funding and study leave provided by the Government of Singapore.

To Pui Yi, my wife, I owe thanks for her unfailing support, encouragement and willingness to sacrifice. Thank you also for Anthony, who is probably too young to understand all this.

Dedicated to Pui Yi
and Anthony

Contents

Abstract 6

Acknowledgements 6

1 Introduction 18

1.1 Review of Current State-of-the-Art 19

1.2 About This Thesis 22

2 Adiabatic Transform Method 24

2.1 The Range-Dependent Spectral Integral 25

2.2 The Spectral Invariant 27

2.3 The Benchmark Problems 29

2.3.1 A : The "Ideal" Wedge 29

2.3.2 B : Penetrable Lossless Wedge 30

2.4 Numerical Results 31

2.4.1 A : "Ideal" Wedge 31

2.4.2 B : Penetrable Wedge 32

2.5 Summary 34

3 The Spectral Super-Element Approach 37

3.1 Introduction 37
3.2 Stratified Super-Elements 39
3.3 Field Expansion 41
3.4 Influence Functions 42
3.5 Element Connectivity 45
3.6 Numerical Implementation 46
3.6.1 Global Solution 46
3.6.2 Marching Algorithm 46
3.6.3 Reverberant Field 47
3.7 Numerical Examples 48
3.7.1 A : ASA Penetrable Wedge Benchmark 48
3.7.2 B : SACLANT Stair-Step Discontinuity 48
3.7.3 C : SACLANT Half-Cylindrical Ridge 49
3.7.4 D : Cylindrical Fluid Seamount 49
3.7.5 E : Coastal Wedge with a Faulted Basement Layer 54
3.7.6 F : Reverberation & Scattering Workshop Test 2a 54
3.7.7 G : Reverberation & Scattering Workshop Test 2b 57
3.7.8 H : Reverberation & Scattering Workshop Test 3a 57
3.7.9 I : Reverberation & Scattering Workshop Test 3b 57
3.8 Summary 60

4 Spectral Super-Element Approach for Elastic Media **62**

4.1 Introduction 62
4.2 Stratified Super-Elements 62
4.3 Field Expansion 64

4.4 Direct Panel Source Contribution 66
4.4.1 The Symmetric Problem 66
4.4.2 The Antisymmetric Problem 67
4.4.3 Series Representations 68
4.4.4 Horizontal Wavenumber Representations 69
4.5 Homogeneous Solution 70
4.6 Element Connectivity 71
4.7 Summary 72

5 The Elastic Benchmarks **73**

5.1 Benchmark Problems 74
5.1.1 A : Modified NORDA Case 3 74
5.1.2 B : Single Layer Benchmarks 76
5.1.3 C : Elastic Cylindrical Seamount 81
5.1.4 D : Low Contrast Embedded Elastic Step 84
5.1.5 E : High Contrast Embedded Elastic Step 84
5.1.6 F : Impedance Change at a Vertical Boundary 87
5.1.7 G,H : Corner Problems 91
5.1.8 I : Elastic ASA Wedge 95
5.1.9 J : Mode conversion - Point Source 95
5.1.10 K : Mode conversion - Vertical Point Force 97
5.1.11 L : Mode conversion - Horizontal Point Force 97
5.1.12 M : Step Periodic Roughness Patch 97
5.1.13 N : Elastic Half-Cylindrical Ridge 104
5.1.14 O : Elastic Ice Lead 108

5.1.15 P : Entrenched Elastic Layer 111
5.1.16 Q : Lloyd-mirror beam diffraction 111
5.2 Summary 114

6 Epilogue **118**

A Axisymmetric Environments **122**

B Point Source Representation for Panel Sources **123**

C Direct Solution for Panel Sources **126**

D Homogeneous Solution for Panel Sources **129**

E Direct Solution for Physical Sources **131**
E.1 Explosive Point Source 131
E.2 Vertical Point Force 132
E.3 Horizontal Point Force 134

F Homogeneous Solution for Physical Sources **136**

G Deriving s-domain Forms for Panel Sources **138**

H Numerical Evaluation of Influence Integrals **142**
H.1 Adaptive Integration 142
H.2 Integrating in Between Zeros of the Integrand 143
H.3 Automatic Gauss-Chebyshev Quadrature 143
H.4 Contour Integration 145

I Contour Integration for Panel Source Solutions **146**

J Mapping Expansion Coefficients **150**

J.1 Case I - Splitting a Layer 150

J.2 Case II - Combining 2 Layers 152

K Elastic Media - Chebyshev Polynomial Formulation **153**

K.1 Field Expansions 153

K.2 Expansion Eigenfunctions 153

K.3 Displacement Potentials 154

K.4 Panel Source Solution 158

K.5 Homogeneous Solution 161

K.6 Symmetries of the Influence Function Integrals 164

K.7 Physical Source Solution 168

K.8 Homogeneous Solution for Physical Sources 169

K.9 Derivation of $\mathcal{Z}_m(\eta a)$ 171

K.10 Derivation of $I_c(m, j)$ 175

Appendix **122**

Bibliography **176**

List of Figures

2-1 ASA Benchmark I : Ideal wedge. Solid curve : Spectral integral method, Dashed curve : SUPERSNAP. 32

2-2 Comparison of results from PE, SUPERSNAP (30 m only) and the spectral integral. (a) Receiver at 30m, (b) receiver at 150m. Solid : PE, Dashed : Spectral integral, Dotted : SUPERSNAP. 33

2-3 Propagation in a range-dependent Bucker waveguide. (a) Density contrast = 1.8. (b) Density contrast = 2.1. In both cases the sound speeds in the water column and the fluid halfspace differ only by 10 m/s. Solid : PE, Dashed : Spectral integral. 35

3-1 Super-element discretization of range-dependent ocean waveguides 39

3-2 Connecting two sectors together via the boundary conditions 45

3-3 Ex. A : Schematic for the ASA benchmark problem 49

3-4 Solutions for the ASA benchmark (Ex. A). (a) Receiver at 30m, (b) Receiver at 150m: Solid - FEPE; Dashed - Spectral super-element solution. 50

3-5 Backscattering from stair-step ridge (Ex. B). (a) Schematic of the problem, (b) Receiver at 50m, (c) Receiver at 170m: Solid - COUPLE; Dashed - Spectral super-element solution. 51

3-6 Backscattering from half-cylindrical ridge (Ex. C). (a) Environment, (b) Receiver at 50m, (c) Receiver at 170m: Solid - COUPLE; Dashed - Spectral super-element solution. 52

3-7 Cylindrical seamount (Ex. D). (a) Environment, (b) Receiver at 50m. Solid - COUPLE; Dashed - Spectral super-element solution. 53

3-8 Wedge overlying a basement fault (Ex. E). (a) Contoured field without the fault, (b) Contoured field with the fault present 55

3-9 R & S Workshop Test 2a (Ex. F) : (a) Test geometry, (b) Forward normal stress, (c) Backscattered normal stress. Solid : COUPLE, Dashed : VISA, Dotted : Spectral super-element. 56

3-10 R & S Workshop Test 2b (Ex. G) : (a) Test geometry, (b) Forward normal stress, (c) Backscattered normal stress. Solid : COUPLE, Dashed : VISA, Dotted : Spectral super-element. 58

3-11 R & S Workshop Test 3a (Ex. H) : (a) Test geometry, (b) Forward normal stress, (c) Backscattered normal stress. Solid : COUPLE, Dashed : VISA, Dotted : Spectral super-element. 59

3-12 R & S Workshop Test 3b (Ex. I) : (a) Test geometry, (b) Forward normal stress, (c) Backscattered normal stress. Solid : COUPLE, Dashed : VISA, Dotted : Spectral super-element. 61

5-1 Modified NORDA 3A test case (Ex. A). (a) Test configuration, (b) Receiver at 50 m, (c) Receiver at 110 m. Solid : SAFARI, Dashed : Spectral super-element. 75

5-2 Ex. B. Configuration for single layer benchmarks 76

5-3 Solutions to the single layer benchmarks. (a) Case B1, (b) Case B2, Solid : BEM, Dashed : VISA, Dotted: Spectral super-element. 78

5-4 Solutions to the single layer benchmarks. (a) Case B3, (b) B4, Solid : BEM, Dashed : VISA, Dotted: Spectral super-element. For (a), instead of the BEM, we use SAFARI as the reference solution 79

5-5 Backscatter solutions to the single layer benchmarks. (a) Case B1, (b) B2, (c) B4, Solid : BEM, Dashed : VISA, Dotted: Spectral super-element. 80

5-6 Ex. C : Schematic of the elastic cylindrical seamount 81

5-7 Elastic cylindrical seamount (Ex. C). Receiver at 80 m. (a) Forward scattered bulk stress, (b) Forward scattered shear stress. Solid - VISA; dashed - Spectral super-element. 82

5-8 Elastic cylindrical seamount (Ex. C). Receiver at 80 m. (a) Back scattered bulk stress, (b) Back scattered shear stress. Solid - VISA; dashed - Spectral super-element. 83

5-9 Ex. D : Embedded step discontinuity 84

5-10 Embedded elastic step (Ex. D). Total normal stress. (a) Receiver at 100 m. (b) Receiver at 300 m. Solid - BEM; Dashed - VISA; Dotted - Spectral super-element. 85

5-11 Embedded elastic step (Ex. D). Back scattered normal stress solution. (a) Receiver at 100 m. (b) Receiver at 300 m. Solid - BEM; Dashed - VISA; Dotted - Spectral super-element. 86

5-12 High contrast embedded elastic step (Ex. E). Total normal stress. (a) Receiver at 100 m. (b) Receiver at 300 m. Solid - BEM; Dashed - VISA; Dotted - Spectral super-element. 88

5-13 High contrast embedded elastic step (Ex. E). Back scattered normal stress solution. (a) Receiver at 100 m. (b) Receiver at 300 m. Solid - BEM; Dashed - VISA; Dotted - Spectral super-element. 89

5-14 Dynamic range test - The average field at range zero as a function of sound speed contrast (log scale). *: BEM; +: CORE; o: VISA. For reference, the dotted line shows a 6 dB increase per sound speed doubling but with arbitrary absolute location. 90

5-15 Ex. G : Schematic for Elastic-Air corner problem 92

5-16 Ex. H : Schematic for Fluid-Elastic corner problem 92

5-17 Elastic-Air corner (Ex. G) - VISA solution (a) Total dilatation (b) Total shear 93

5-18 Fluid-Elastic corner (Ex. H) - VISA solution (a) Total dilatation (b) Total shear 94

5-19 Ex. I : Environment for the ASA elastic wedge 95

5-20 ASA elastic wedge (Ex. I) (a) Receiver at 30 m, (b) Receiver at 150 m; Solid - FEPE, Dashed - Spectral super-element 96

5-21 Mode conversion with a point source (Ex. J) - Forward scattered field (a) Normal stress, (b) vertical particle velocity, (c) horizontal particle velocity; Solid : BEM, Dashed : VISA, Dotted : Spectral super-element 98

5-22 Mode conversion with a point source (Ex. J) - Backward scattered field (a) Normal stress, (b) vertical particle velocity, (c) horizontal particle velocity; Solid : BEM, Dashed : VISA, Dotted : Spectral super-element 99

5-23 Mode conversion with a vertical point force (Ex. K) - Forward scattered field (a) Normal stress, (b) vertical particle velocity, (c) horizontal particle velocity; Solid : BEM, Dashed : VISA, Dotted : Spectral super-element. 100

5-24 Mode conversion with a vertical point force (Ex. K) - Backward scattered field (a) Normal stress, (b) vertical particle velocity, (c) horizontal particle velocity; Solid : BEM, Dashed : VISA, Dotted : Spectral super-element. 101

5-25 Mode conversion with a horizontal point force (Ex. L) - Forward scattered field (a) Normal stress, (b) vertical particle velocity, (c) horizontal particle velocity; Solid : BEM, Dashed : VISA, Dotted : Spectral super-element. . . . 102

5-26 Mode conversion with a horizontal force (Ex. L) - Backward scattered field (a) Normal stress, (b) vertical particle velocity, (c) horizontal particle velocity; Solid : BEM, Dashed : VISA, Dotted : Spectral super-element. 103

5-27 Ex. M : Configuration for step periodic roughness patch 104

5-28 Step periodic roughness patch (Ex. M). Forward dilatation : (a) Receiver at 50 m. (b) Receiver at 150 m. Solid - SAFARI; Dashed - Spectral super-element. 105

5-29 Step periodic roughness patch (Ex. M). Forward dilatation : (a) SAFARI solution without the patch (b) Spectral super-element solution with the roughness patch 106

5-30 Backscattering from an elastic half-cylindrical ridge (Ex. N). (a) Environment (b) Receiver at 50m, (c) Receiver at 170m: Solid - BEM; Dashed - VISA, Dotted - Spectral super-element solution. 107

5-31 Ex. O : Configuration for the ice lead problem 108

5-32 Ice lead problem (Ex. O). Forward vertical velocity : (a) Receiver at 5 m (b) Receiver at 10 m. Solid : VISA, Dashed : Spectral super-element 109

5-33 Ice lead problem (Ex. O). Forward dilatation : (a) Receiver at 5 m (b) Receiver at 10 m. Solid : VISA, Dashed : Spectral super-element 110

5-34 Ex. P : Configuration for the entrenched elastic layer problem 111

5-35 Entrenched layer problem (Ex. P). Forward normal stress: (a) Receiver at 100 m (b) Receiver at 300 m. Solid : BEM, Dashed : VISA, Dotted : Spectral super-element 112

5-36 Entrenched layer problem (Ex. P). Backward normal stress: (a) Receiver at 100 m (b) Receiver at 300 m. Solid : BEM, Dashed : VISA, Dotted : Spectral super-element 113

5-37 Ex. O : Configuration for the Lloyd-mirror beam diffraction problem 114

5-38 Diffraction from a Lloyd-mirror beam (Ex. O). Total normal stress (Spectral super-element solution) 115

5-39 Diffraction from a Lloyd-mirror beam (Ex. Q). Forward normal stress (a) Receiver at 100 m (b) Receiver at 300 m. Solid : BEM, Dashed : VISA, Dotted : Spectral super-element 116

5-40 Diffraction from a Lloyd-mirror beam (Ex. Q). Backward normal stress (a) Receiver at 100 m (b) Receiver at 300 m. Solid : BEM, Dashed : VISA, Dotted : Spectral super-element 117

G-1 Contour deformation to derive horizontal wavenumber representation. 139

I-1 Integration contours in the complex s-plane: (a) $h_n^{(1)}$-contour; (b) $h_n^{(2)}$-contour; Reprinted from Krenk and Schmidt. 148

J-1 Splitting of single layer 151

J-2 Combination of 2 layers 152

List of Tables

5.1 Parameters for the series of 2-sector canonical test problems. Wave speeds are given in m/s, densities in g/cm^3, and attenuation in dB/λ. 77

5.2 Parameters for the corner problems. Wave speeds are given in m/s, densities in g/cm^3, and attenuation in dB/λ. 91

Chapter 1

Introduction

In recent years, there has been a shift from deep ocean acoustics to the socalled littoral or shallow water acoustics and with it, the recognition that *range-dependence* and the *elasticity* of the seabed plays an important role in the overall propagation, particularly in the low frequency regime. The shallow water environment is an extremely complicated waveguide bounded above by a rough sea surface and below by an inhomogeneous, multi-layered elastic sea bed. Further, the acoustic properties of the water column are dependent on temperature, pressure and salinity, giving rise to a significant spatial and temporal variation. The elastic sea bed added another degree of complication. The excitation and propagation behaviours of seismic interface modes, inhomogeneous waves, and both headwave and multiply reflected wave interference are all important phenomena and the energy carried by seismic waves is not negligible compared to the water-borne field. This insight has prompted substantial research efforts during the last decade to develop numerical modeling tools where the effects of shear waves are included.

In the next section, we review some of the current techniques employed to solve the range dependent wave equation. The interested reader is referred to Jensen *et. al.* [1] for a more theoretical development of the standard theory and to Etter [2] for a quick overview of the many computer models in use in the underwater acoustics community.

1.1 Review of Current State-of-the-Art

The last couple of decades has seen a significant effort in improving the numerical modeling capability for range-independent seismo-acoustic propagation and reverberation in the ocean environment [1].

The most general approaches are direct solutions of the wave equations using discrete methods such as the *finite difference methods* (FDM), and *finite element methods* (FEM). These methods rely on spatial and temporal discretizations which are small compared to the wavelengths in the problem, and since ocean acoustics problems are typically concerned with ranges of several hundreds or thousands of wavelengths, these discrete methods are in general prohibitive for computational reasons. As a result, the discrete methods are only important for modeling propagation and scattering in the near field.

Galerkin finite-element or *spectral methods* are used extensively in fluid dynamics [3] and to a limited degree in seismo-acoustic modeling [4]. These methods are in general well suited to wave propagation problems. The basis functions inherently possess some of the wave nature of the actual field, and the spectral methods therefore in general require less degrees of freedom than the discrete finite-element and -difference approaches. However, the computational savings are still insufficient for use of these methods for general long-range ocean waveguide problems.

Because of the computational limitations on the direct numerical solution of the wave equations, most modeling development and application in ocean seismo-acoustics has been centered around the classical modeling approaches, *ray tracing*, *parabolic equations*, *wavenumber integration*, and *normal modes* [1]. In addition to the computational issues, these methods are also usually preferred because of the fact that they provide frequency domain solutions. Due to the low cross-spectral coherence of long range ocean waveguide propagation frequency domain solutions are usually more relevant than the time domain solutions provided by most seismo-acoustic FEM and FDM algorithms.

Ray tracing remains a popular method due to its numerical efficiency, and the direct physical interpretation of the results. Further, it is well suited to handling range-dependence in two as well as three dimensions. However, ray theory provides a high-frequency approxima-

tion, and the associated limitations for seismo-acoustic modeling are well established. Also, ray tracing is not easily applied to propagation in elastic media because of the ray splitting associated with elastic conversion at interfaces.

The *parabolic equation* (PE) algorithm has undergone a dramatic development over the last couple of decades, and today is without doubt the most popular approach to acoustic modeling in range-dependent ocean waveguides [5]. Even though the numerical solution is often performed using discrete methods such as FDM or FEM, the range discretization does not have to be smaller than a fraction of the wavelength. Also, the transformation into a parabolic equation allows for numerical solution using a marching scheme, and the PE is therefore in general extremely efficient compared to direct numerical solution of the elliptical Helmholtz equation. Due to the inherent one-way propagation assumption, the PE is limited to weak range dependence, but using a single-scatter approximation it has recently been extended to model backscattering [6]. However, in trying to extend the PE theory to elastic media, two main problems arise. Firstly, the field is described by a vector (displacement) rather than a scalar. Secondly, two different wave speeds exist in a solid and in a heterogeneous media or at boundaries, we have continuous conversion from one wave type to another. Furthermore, elastic bottoms support a wide spectrum of propagation angles. Therefore, even though several PE models have been proposed for wave propagation in elastic media [7, 8, 9, 10, 11, 12, 13], only a few of these models were implemented. Notable implementations include those of Wetton and Brooke [11] and Collins [12, 13]. Thus, for the most part, the parabolic theories for elastic waves have not been adequately tested numerically, particularly in two-way formulations. Compared to the other classical approaches a major drawback of the PE as well as the discrete methods is the fact that the solutions are not as easily interpreted physically. Thus, the modal structure of the field can only be determined through post-processing [14].

A common problem for all the classical, approximate aproaches, is the fact that the accuracy of the solution is not automatically guaranteed due to a dependency on computational parameters. However, this problem has traditionally been overcome by using two different modeling approaches. In that regard, extensive use of the elastic PE is hampered by a lack of other applicable modeling approaches. There is therefore a continuing effort being de-

voted to the development of the other classical modeling approaches to treat propagation and reverberation problems in a range-dependent ocean environment.

The wavenumber integration and normal mode approaches are based on integral transforms and therefore inherently limited to range-independent propagation problems. However, approximate solutions to range-dependent environments can be devised for both of these solution techniques.

Here, the adiabatic mode theory is well established and used extensively. However, due to the fact that it assumes that the mode shapes only undergo simple geometric scaling, the adiabatic approximation is restricted to weak range-dependence. Coupled-mode [15] algorithms have been developed which can handle strongly range dependent problems. The coupled mode approach is currently the primary provider of benchmark solutions, but existing implementations are limited to handling fluid waveguides only.

The wavenumber integration approach is the established benchmark for range-independent propagation in fluid-elastic waveguides [16], and a significant effort has been devoted to the development of an approximate extension to range-dependent environments. Lu and Felsen [17] derived an adiabatic transformation of the wavenumber integrals for weakly range-dependent problems. However, due to approximations made using dominant asymptotics, the method works well only for cases where the wave field is largely dominated by *discrete modes* [18]. Gilbert and Evans developed a one-way wavenumber integration approach for range-dependent fluid environments [19]. In contrast to the adiabatic approximation this approach handles full mode coupling, but the one-way approximation makes it applicable only to problems with weak contrasts in the range direction.

Wavenumber integration has been applied succesfully to range dependence which is *limited in its horizontal extent*, such as a finite size inhomogeneity in the seabed. By combining wavenumber integration with a boundary integral formulation for the scattered field, accurate solutions are obtained very efficiently for fluid as well as elastic environments [20, 21, 22, 23].

Recently Schmidt [24] extended the SAFARI model to handle range-dependent environments. It employs the recursive use of wave-number integration in step-wise range-dependent environment to march the wavefields out in range. A single-scatter approximation to the backscattered field is obtained by a backward marching scheme. We will be using this par-

ticular code (**VI**rtual **S**ource **A**lgorithm) a great deal to generate our reference solutions.

1.2 About This Thesis

Broadly, this thesis endeavours to develop general spectral-based formulations to solve the elastic wave equation in range-dependent environments. In particular, we are interested in approaches that could treat both short and long range propagation as well as model reverberation from large scale oceanic features. Spectral-based approaches are preferred because of their physical appeal - they provide the spectral decomposition of the wave field in terms of modal components, head waves as well as seismic interface waves which greatly helps in the physical interpretation of the numerical results. We start our investigations by numerically implementing the adiabatic transform approach of Lu and Felsen [17]. In this work described in Chapter 2, we find that the approach works well only when the field is largely dominated by discrete modes [18]. For the class of problems that were examined, even though the adiabatic spectral integral seem to perform better than the classical adiabatic mode approach, it suffers from several other limitations, the most severe of which is its inability to handle the continuous spectrum properly as well as its non-trivial extension to elastic media.

We next examined the boundary-integral formulation in Woojae's thesis [25]. Despite being a fluid-only formulation, the method could conceivably be extended to mixed fluid-elastic stratifications. However, before we proceed to do that, several practical limitations in the method needs to be worked around. One of these is that the original fully-coupled *global* approach is not suitable for solving long-range problems due to its severe requirements on computational resources. We introduced a single-scatter formulation which permits a marching algorithm to be implemented, thus enabling the boundary-integral method to solve a much broader class of problems. We have also implemented a 2-way marching scheme providing a single-scatter approximation to the reverberation from large scale features, similar to the approach used in the two-way PE [6]. This is significant since a reverberation capability is very much desired in a general purpose propagation code. We also derived mapping matrices that permit us to map expansion coefficients across sectors with different layering structures.

Chapter 3 discusses these extensions as well as provides numerous test cases that serve to validate the approach and the code.

The next thrust is to extend the present fluid-only formulation to the mixed fluid-elastic case. The extensions that were highlighted above decouple the *global* problem into a *local* one, thereby reducing tremendously the computational resources required and permit a practical elastic code to be developed. The generalisation is presented in Chapter 4 and is one of the main contribution of this thesis. The extension of the original fluid formulation to include elasticity is new and non-trivial especially in its numerical implementation. We have also expanded our toolbox of available source types to include vertical and horizontal point forces. The vertical and horizontal point forces are not as restrictive as one might surmise. Their usefulness arise from the fact that the field due to a point force, F, of arbitrary direction can be obtained by the superposition of the fields due to a vertical point force, $F\sin\theta$, and a horizontal point force , $F\cos\theta$, where θ is the vertical angle between F and the horizontal [26].

One of the biggest challenge facing modelers is the issue of benchmarking and testing their formulations. In this regard, this thesis makes a significant contribution by putting together probably the most extensive set of benchmarks for seismo-acoustic propagation codes. Some of these benchmarks are new while others are taken or modified from those in the literature. Chapter 5 describes the benchmarks and should serve as a useful reference for model developers.

In addition to the present implementation using Legendre polynomials, I have also derived another formulation which uses Chebyshev polynomials instead. Though this is never implemented, the approach is unique and some of the techniques employed there are useful. I have therefore included its derivations in Appendix K.

Chapter 2

Adiabatic Transform Method

In horizontally stratified oceanic waveguides, the acoustic field can be represented rigorously in terms of multiply reflected plane waves. The natural approach involves Fourier decomposition with respect to the direction parallel to the boundaries. The numerical solution of the full wavefield problem can then be carried out very efficiently using, *e.g.*, the Direct Global Matrix (DGM) approach [16, 1]. However, when the layer boundaries are not parallel, Fourier decomposition can no longer be used because the propagation angle of the plane waves is changed between reflections. One of the main reasons for employing the wavenumber integration approach is its physical appeal - the inherent representation of the acoustic field in terms of plane waves greatly helps in the physical interpretation of the numerical results. To treat range-dependent problems, researchers have therefore developed hybrid schemes involving a combination of wavenumber integration and the boundary integral methods [20, 27, 21, 22, 25]. Recent developments in the analysis of weakly range-dependent guiding channels, using the spectral approach, have led to the development of a global spectral Green's function for range-dependent waveguides. Kamel and Felsen [28] generalized the method of characteristic Green's functions for a two-dimensional ocean waveguide to accomodate weak range dependence. Lu and Felsen [17] developed approximate adiabatic transforms that accomplish for weakly range-dependent oceanic waveguides what the rigorous transforms (Fourier or Hankel) do exactly for the range-independent case. Both approaches involve spectral scaling in accordance with an adiabatic spectral invariant that

continuously adapts the spectrum to the gradually changing conditions without coupling to other spectral components. In addition to ignoring coupling between modes, the spectral scaling guarantees generation of the guided *local adiabatic modes* when these are extracted from the resonances in the integrand. The resulting spectral integral is not of the Fourier type but contains, instead of the simple exponential, the phase factor $exp[i\int_0^x \beta(\tau)d\tau]$, with the horizontal wavenumber $\beta(\tau)$ determined by the spectral invariant. Recently, a similar approach based on the method of multiple scales has been suggested [29].

An important part of these theories is the *assumption* that the spectral invariant maps not only modal wavenumbers but any spectral value in the entire spectrum. We will here assess the validity of such spectral integral representations by applying them to the ASA benchmark problems in Ref. [30]. Section 2.1 contains a brief review of the spectral integral representation for range-dependent waveguides; only the pertinent equations are given and their detailed derivations may be found elsewhere [17]. In Sec. 2.2 we discuss the main properties of the spectral invariant. In Sec. 2.3, we provide a short description of the benchmark problems and the approximate spectral representation of the field. Our numerical results are presented in Sec. 2.4, followed by some concluding remarks.

2.1 The Range-Dependent Spectral Integral

The presentation of the adiabatic spectral theory given here follows closely that of Lu and Felsen [17]. We consider a general 2-dimensional range-dependent waveguide bounded by two boundaries S_1 and S_2. Here, we will assume S_1 to be a pressure release ocean surface, and S_2 to be the ocean bottom. Then, suppressing a harmonic time dependence $\exp(-i\omega t)$, the range-dependent wave equation is

$$\left[\rho(\mathbf{r})\nabla\left(\frac{1}{\rho(\mathbf{r})}\,\nabla\right)+\frac{\omega^2}{c^2(\mathbf{r})}\right]\widehat{G}(\mathbf{r},\mathbf{r}')=-\delta(\mathbf{r}-\mathbf{r}'), \tag{2.1}$$

subject to the boundary conditions

$$\widehat{G} \quad \text{and} \quad \frac{1}{\rho(\mathbf{r})}\frac{\partial\widehat{G}}{\partial\nu} \quad \text{continuous across } S_{1,2}. \tag{2.2}$$

Furthermore, a radiation condition is imposed at infinity. Here $c(\mathbf{r})$ is the variable sound velocity, $\rho(\mathbf{r})$ is the fluid density and ν is the outer normal on $S_{1,2}$, while $\mathbf{r}$ and $\mathbf{r}'$ are the

receiver and source coordinates, respectively. In addition to the global coordinate system (x, z), it is sometimes convenient to adopt a local curvilinear orthogonal (u, v) system which is constructed so that the waveguide boundaries $S_{1,2}$ correspond to $v_{1,2}$ being constants. Here, we choose to normalize the depth coordinate z with the local depth. Therefore $v = 0$ corresponds to the upper boundary S_1 and $v = 1$ coincides with the bottom S_2.

In Ref. [17], it was shown that under conditions of slow variability (compared to the local wavelength) in boundary shapes, sound-speed and density profiles with range u, the range-dependent wave equation Eq. (2.1) reduces to

$$\left[\frac{1}{h_u^2}\frac{\partial^2}{\partial u^2} + \frac{1}{h_v^2}\frac{\partial^2}{\partial v^2} + \frac{\omega^2}{c^2(u,v)}\right]\widehat{G}(u,v;u',v') \approx -\frac{1}{h_u h_v}\delta(u-u')\delta(v-v'), \tag{2.3}$$

where h_u and h_v are the metric coefficients associated with u and v respectively.

The main result of applying the adiabatic transform to Eq. (2.3) is to reduce the partial differential operator in the (u, v) space to that of a single ordinary differential operator in the v space with u acting only as a parameter. This reduction is only approximate, subject to previously assumed conditions of weak range dependence. The spectral integral representation for the range-dependent Green's function then becomes [17]

$$\begin{aligned}\widehat{G}(u,v;u',v') \;\sim\; & \frac{1}{2\pi}\int_{-\infty}^{\infty}\frac{g_<(v_<,\beta_<)\,g_>(v_>,\beta_>)}{-W\{g_<[v,\beta(u)],\,g_>[v,\beta(u)]\}} \\ & \times\; (h_v h_v')^{1/2}\exp\left(i\int_{u'}^{u}\beta(\bar{u})h_{\bar{u}}d\bar{u}\right)\times\left[d\beta(u)d\beta(u')\right]^{1/2}.\end{aligned} \tag{2.4}$$

Here, $v_<$ and $v_>$ denote the lesser or greater of the coordinates v and v', respectively, while $\beta_< = \beta(u), \beta_> = \beta(u'), u_< = u$, and $u_> = u'$ if $v_< = v, v_> = v'$, and *vice-versa*. The functions $g_<$ and $g_>$ are solutions, at ranges $u_<$ and $u_>$, respectively, of the one dimensional reduced wave equation in the v coordinate,

$$\left(\frac{d^2}{dv^2} + (h_v\chi)^2\right)G_v\left[v,v';\beta(u)\right] \approx -h_v\delta(v-v'), \tag{2.5}$$

where

$$\chi = \left(\frac{\omega^2}{c^2(u,v)} - \beta^2(u)\right)^{\frac{1}{2}}, \qquad \mathrm{Im}\,(\chi) \geq 0 \tag{2.6}$$

and where the solutions satisfy impedance boundary conditions

$$\alpha G_v + \gamma\frac{1}{h_v\rho}\frac{\partial G_v}{\partial v} = 0, \qquad v = v_{1,2}. \tag{2.7}$$

The Wronskian W of the two homogeneous solutions $g_<$ and $g_>$ is a constant, independent of v but parameterized by the longitudinal coordinate u. The spectral values $\beta(u, \beta_o)$ corresponding to the resonance condition $W = 0$ define the longitudinal propagation coefficients of the adiabatic modes. Thus, the Wronskian may be chosen as the adiabatic invariant, which provides the scaling that adapts the spectrum adiabatically to the specified longitudinal variations in the waveguide properties. It is implied that $\beta(\bar{u})$ in the spectral integral is expressed in terms of the integration variable [$\beta(u')$ or $\beta(u)$] through the spectral invariant.

2.2 The Spectral Invariant

Perhaps the most important element of the range-dependent spectral integral is the spectral invariant which tracks the horizontal wavenumbers as the waveguide's geometry changes. In the formulation of the spectral integral for the wedge problem, the invariant obtained is

$$I_v(\beta, u) = \Gamma_D \, e^{2ih_v\kappa_1}, \tag{2.8}$$

where κ_1 is the vertical wavenumber in the water column and Γ_D is the Rayleigh-Fresnel reflection coefficient at the bottom interface. The metric coefficient h_v appropriate for the wedge problem turns out to be the local depth of the water column. We have also chosen a rotated coordinate system, with the range coordinate u running along the bottom of the wedge; in this way, the impedance boundary condition involving $\rho^{-1}\partial\hat{G}/\partial v$ can be satisfied exactly.

In a normal mode interpretation, the invariant in Eq. (2.8) is equivalent to

$$2h_v\kappa_1 + \phi + \pi = 2n\pi, \tag{2.9}$$

where

$$\phi = i \log\left|\frac{m\kappa_1 - \kappa_2}{m\kappa_1 + \kappa_2}\right| \tag{2.10}$$

is the phase of the bottom reflection coefficient, κ_2 is the vertical wavenumber in the bottom halfspace and $m = \rho_2/\rho_1$ with ρ_1 and ρ_2 denoting the densities in the water and bottom respectively. Note that Eq. (2.9) simply states that the round trip phase accumulation between

the top and bottom boundaries should be equal to $2n\pi$ where n is the mode number. This is consistent with the notion that a mode is a result of a constructive interferencc of an upgoing and downgoing plane wave of equal amplitude and vertical wavenumber.

In *conventional* adiabatic mode theory, an adiabatic mode may propagate without coupling to other modes, thereby preserving its modal identity but yet continually adjusting its depth profile to that of the local environment and adjusting its amplitude to conform to energy conservation considerations. It is precisely this constrained behaviour of the adiabatic mode that is being represented in Eq. (2.9).

In Refs. [28, 17] it was assumed that the spectral invariant can be generalized to any spectral value β, such that the spectral variables at any two range points u' and u are related by

$$I_v(\beta', u') = I_v(\beta, u). \tag{2.11}$$

Incorporating the symmetry between $\beta(u')$ and $\beta(u)$ implied in Eq. (2.11) into the spectral integral representation resulted in the presence of the operational forms $[d\beta(u')\, d\beta(u)]^{1/2}$ in Eq. (2.4).

The generalization made in Eq. (2.11) means that the spectral invariant is capable of mapping not only the discrete *modal* wavenumbers but also the continuous spectrum as well. However, our numerical results will show that the mapping is correct only for the *discrete* spectrum. To see this, we note that the spectral mapping is analogous to counting the number of zero crossings (tracking of phase accumulation between the top and bottom interfaces) in the mode shapes. In the *continuous* or *leaky* part of the spectrum where the oscillatory nature of the mode shape penetrates the bottom, one must in theory track phase changes right through the bottom instead of just in the water column. For leaky modes that are growing exponentially in depth, there is an infinite number of zero crossings rendering the phase tracking impossible This is consistent with the fact that leaky modes radiate energy into the bottom halfspace. When a mode is cutoff, it is moving from the discrete to the continuous part of the spectrum. When this happens, the vertical wavenumber tends to remain relatively constant with the field radiating into the bottom halfspace at a certain angle - corresponding to the beamlike radiation pattern found in the numerical results of Jensen and Kuperman [31]. Under these circumstances it is therefore *incorrect* to continue employing the *same* spectral

invariant determined by the channel depth alone to determine the horizontal wavenumbers at other ranges. Consequently, another form of spectral mapping must be devised for the continuous spectrum. Below we illustrate this behaviour by presenting the spectral integral solutions for the two benchmark problems. The expressions for the depth-dependent Green's functions will be adopted from Ref. [17]. However, all results have been reproduced using SAFARI [16] for computing the depth-dependent Green's functions as well.

2.3 The Benchmark Problems

We consider two of the ASA benchmark problems presented in Ref. [30]. The environment consists of a homogeneous water column $c_1 = 1500\text{m/s}, \rho_1 = 1\text{g/cm}^3$ limited above by a pressure-release flat sea surface, and below by a sloping sea floor. The water depth at the source position is 200 m, decreasing to zero at a distance of 4 km from the source with a slope of approximately 2.86°. Field solutions are computed for a 25-Hz source placed at mid-depth (100 m) and for two receivers at 30- and 150-m depth, respectively. The points in range where the two receivers cross the water-bottom interface is 3.4 km for the shallow receiver and 1 km for the deep receiver. Two different bottom boundary conditions are treated. The first is the idealized wedge where we have a perfectly reflecting bottom and the second is a penetrable lossless bottom. For the latter case, the bottom is a homogeneous fluid half-space with a compressional speed of 1700 m/s and a density of 1.5 g/cm^3.

2.3.1 A : The "Ideal" Wedge

For the ideal wedge, the depth function is $h_v = (R_{max} - x) \tan\alpha$, where α is the wedge angle, R_{max} is the maximum range from the source to the receiver (4 km in this case) and x is the horizontal range from the line source to the receiver. Choosing the source coordinates (primed quantities) as reference, then for a receiver depth of 30 m and a source depth of 100 m , we have

$$u' = 0, \qquad v = 30/h_v, \qquad v' = 100/200 = 0.5\ . \tag{2.12}$$

The spectral invariant is given by $I_v = \exp(2ih_v\kappa_1)$, which implies that

$$\exp(2ih_{v'}\kappa_1') = \exp(2ih_v\kappa_1),$$

or

$$h_{v'}\kappa_1' = h_v\kappa_1. \tag{2.13}$$

The resulting depth-dependent Green's function is

$$G_v = -\frac{\sin(h_{v_<}\kappa_{1_<}v_<)\sin(h_{v_>}\kappa_{1_>}[\,1-v_>\,])}{(\kappa_{1_>}\kappa_{1_<})^{1/2}\sin(h_v\kappa)}, \tag{2.14}$$

where

$$\left.\begin{aligned} v_< &= v', \\ \kappa_{1_<} &= \kappa_1|_{\beta(u',\beta_o)}, \\ v_> &= v, \\ \kappa_{1_>} &= \kappa_1|_{\beta(u,\beta_o)}, \end{aligned}\right\} \quad \text{if } v > v',$$

$$\left.\begin{aligned} v_< &= v, \\ \kappa_{1_<} &= \kappa_1|_{\beta(u,\beta_o)}, \\ v_> &= v', \\ \kappa_{1_>} &= \kappa_1|_{\beta(u',\beta_o)}, \end{aligned}\right\} \quad \text{if } v < v',$$

and $\kappa_1(u,\beta_o) = [\omega^2/c_1^2 - \beta^2(u,\beta_o)]^{1/2}$ is the vertical wavenumber in the fluid. The complete spectral integral is then

$$\begin{aligned} \widehat{G}(u,v;u',v') \;\sim\; & \frac{1}{2\pi}\int_0^\infty -\frac{\sin(h_{v_<}\kappa_{1_<}v_<)\sin(h_{v_>}\kappa_{1_>}[\,1-v_>\,])}{(\kappa_{1_>}\kappa_{1_<})^{1/2}\sin(h_v\kappa)} \\ & \times \frac{h_{v'}}{h_v}\left(\frac{\beta'}{\beta}\right)^{1/2} \times \exp\left(i\int_{u'}^{u}\beta(\bar{u})\,d\bar{u}\right)d\beta'. \end{aligned} \tag{2.15}$$

2.3.2 B : Penetrable Lossless Wedge

The spectral integral for the penetrable wedge is given by

$$\widehat{G}(u,v;u',v') \sim \frac{1}{2\pi}\int_0^\infty G_v \exp\left(i\int_{u'}^{u}\beta(\bar{x})\,d\bar{x}\right)\left(\frac{\partial I/\partial\beta'}{\partial I/\partial\beta}\right)^{1/2}d\beta', \tag{2.16}$$

where the depth dependent Greens' function is now given by [17]

$$\begin{aligned} G_v \;\sim\; & \{-2i[(-\Gamma_D e^{2ih_v\kappa_1})^{-1/2} - (-\Gamma_D e^{2ih_v\kappa_1})^{1/2}]\}^{-1} \\ \times\; & [-i\exp(-ih_{v_<}\kappa_{1_<}v_<) + i\exp(ih_{v_<}\kappa_{1_<}v_<)]\ (\ \kappa_{1_<}\ \kappa_{1_>}\ )^{-1/2} \\ \times\; & \{(\Gamma_D)_>^{1/2}\exp[ih_{v_>}\kappa_{1_>}(1-v_>)] + (\Gamma_D)_>^{-1/2}\exp[-ih_{v_>}\kappa_{1_>}(1-v_>)]\}, \\ & 0 \le (v_<, v_>) \le 1 \end{aligned} \tag{2.17}$$

where

$$\left.\begin{aligned} v_< &= v', \\ \kappa_{1_<} &= \kappa_1|_{\beta(u',\beta_o)}, \\ v_> &= v, \\ \kappa_{1_>} &= \kappa_1|_{\beta(u,\beta_o)}, \\ (\Gamma_D)_> &= \Gamma_D|_{\beta(u,\beta_o)} \end{aligned}\right\} \quad \text{if } v > v',$$

$$\left.\begin{aligned} v_< &= v, \\ u_< &= u, \\ \kappa_{1_<} &= \kappa_1|_{\beta(u,\beta_o)}, \\ v_> &= v', \\ u_> &= u', \\ \kappa_{1_>} &= \kappa_1|_{\beta(u',\beta_o)}, \\ (\Gamma_D)_> &= \Gamma_D|_{\beta(u',\beta_o)} \end{aligned}\right\} \quad \text{if } v < v',$$

and $\kappa_2(u,\beta_o) = [\omega^2/{c_2}^2 - \beta^2(u,\beta_o)]^{1/2}$ is the vertical wavenumber in the bottom.

2.4 Numerical Results

2.4.1 A : "Ideal" Wedge

Fig. 2-1 compares the spectral integral solution with those generated using the conventional adiabatic mode theory (SUPERSNAP code [32]). The two solutions show good agreement - in fact, the spectral solution reproduce the details at the modal cut-off ranges more accurately than SUPERSNAP (see COUPLE solution in Ref. [30]). Therefore, in this idealized ocean

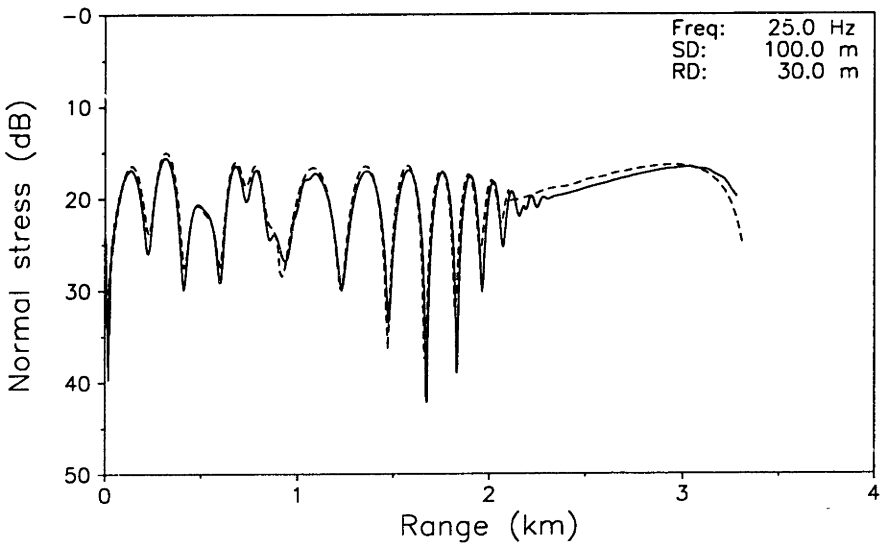

Figure 2-1: ASA Benchmark I : Ideal wedge. Solid curve : Spectral integral method, Dashed curve : SUPERSNAP.

waveguide where we do not have energy continually leaking away from the water column, the adiabatic transform solution performs excellently.

2.4.2 B : Penetrable Wedge

In the penetrable, lossless wedge, propagation in the water column is dominated by modes 1, 3 and 5 which cut off at 3362, 2086 and 810 m ranges respectively. To demonstrate the limitations of the *traditional* adiabatic mode theory, where the continuous spectrum is not computed, we have included the SUPERSNAP solution. We used the FEPE [33] solution as our reference since it is verified in Ref. [33] that the FEPE provides accurate solutions to the ASA benchmark problems.

Fig. 2-2 compares the parabolic equation (PE) reference solution with those obtained using the spectral and adiabatic mode solution. For the shallow receiver in the water column, the spectral solution agrees well with the PE up to about 3100 m when mode 1 is approaching its cut-off. Here it is clear that in addition to properly tracking the modal spectra across the

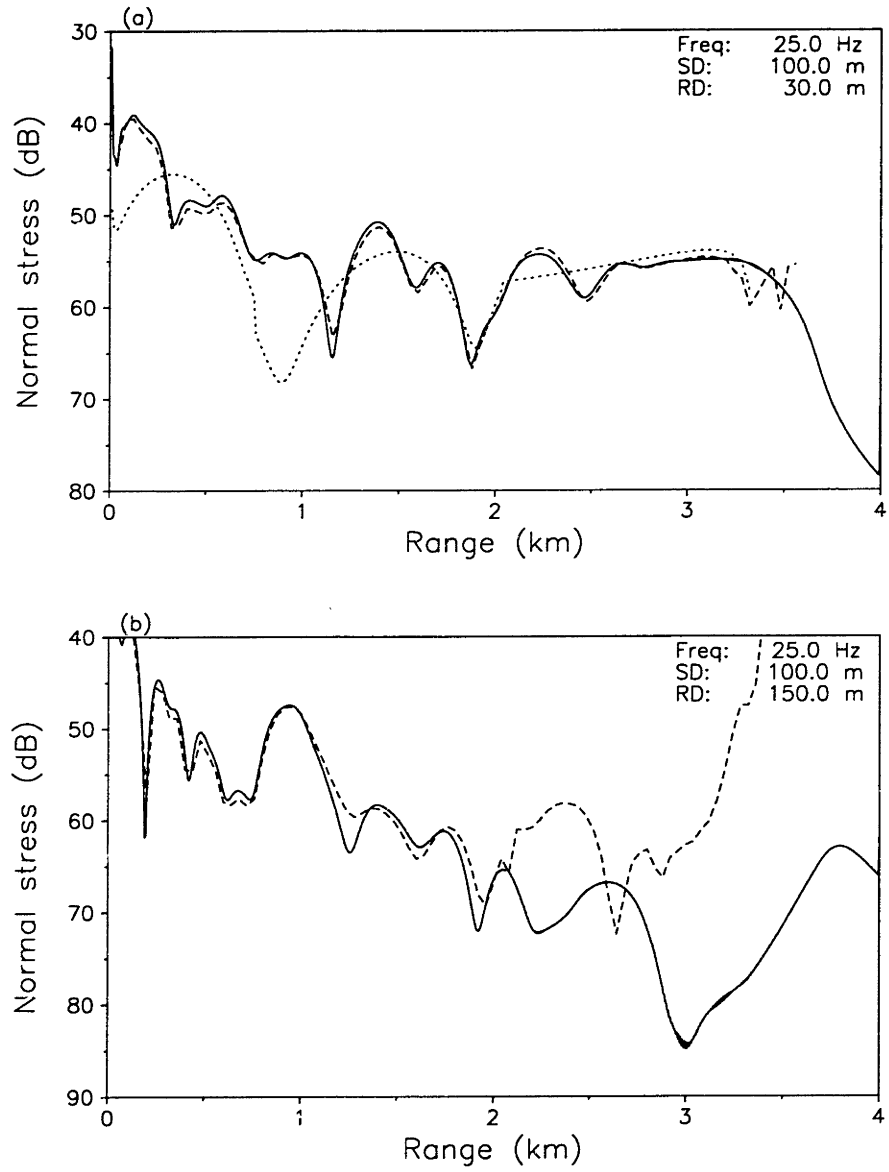

Figure 2-2: Comparison of results from PE, SUPERSNAP (30 m only) and the spectral integral. (a) Receiver at 30m, (b) receiver at 150m. Solid : PE, Dashed : Spectral integral, Dotted : SUPERSNAP.

entire range, the invariant reproduces the continuous spectrum *sufficiently well* to give the correct solution even at ranges near the source. On the other hand, the *conventional* adiabatic mode solution is poor because of the relative small number of modes and the associated significance of the continuous spectrum. Unfortunately, the nice agreement between the spectral representation and the PE in the water column does not extend to the solution for the bottom halfspace; the poor solution provided by the spectral integral in the sediment halfspace supports the hypothesis described above concerning the failure of the invariant to map the *entire* continuous spectrum.

We illustrate this further by running the same benchmark but instead consider a bottom similar to that of the Bucker waveguide [1]. The geometry of the waveguide remains the same except that now the environment is characterized by a strong density contrast at the bottom which yields a large number of *virtual* modes. Furthermore, the sound speed contrast ($c_1 = 1500$ m/s , $c_2 = 1510$ m/s) is small, yielding only a small number of normal modes with real propagation wavenumber. Now we have a situation where the continuous spectrum with its oscillatory nature in the bottom is obviously important. We used the higher-order PE code FEPE [33] to generate the reference solutions. To justify the use of FEPE for the Bucker waveguide, we have verified that in the equivalent range-independent Bucker waveguide, the FEPE solution agrees with that of SAFARI.

Fig. 2-3a shows the results for a density contrast (ρ_2/ρ_1) of 1.8 and Fig. 2-3b is for a contrast of 2.1. We see that the solution in the water column deteriorates rapidly for the higher density contrast case, again indicating the failure of the spectral invariant to properly map the bottom penetrating virtual modes for this problem.

2.5 Summary

Extensive numerical experiments have shown that the wavenumber integration formulation in Refs. [28, 17] work well on cases where the acoustic field is well described by propagating, discrete modes. This is consistent with the fact that the present invariant is constructed from *dominant asymptotics*, and is only valid for the *discrete modal wavenumbers.* Consequently, this is also the cause of the poor solution in unbounded halfspaces or in situations where the

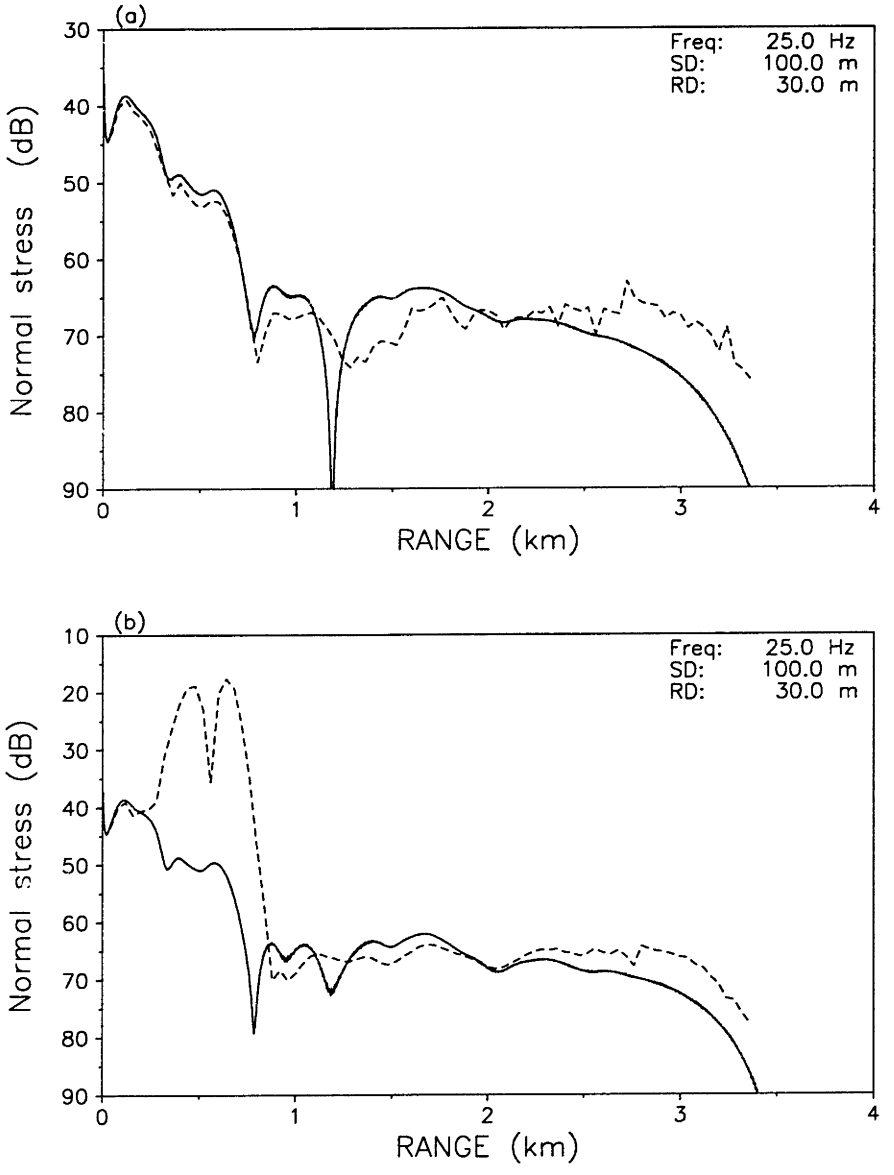

Figure 2-3: Propagation in a range-dependent Bucker waveguide. (a) Density contrast = 1.8. (b) Density contrast = 2.1. In both cases the sound speeds in the water column and the fluid halfspace differ only by 10 m/s. Solid : PE, Dashed : Spectral integral.

field is dominated by leaky modes, since the present invariant does not allow for the proper tracking of the wavenumbers past the cutoff region. In the discrete spectrum, where the field is evanescent in the halfspace, the spectral mapping coincides with the constrained adaptation of the conventional adiabatic mode. However, the virtual modes, and the continuous spectrum in general, with the dominant energy in the bottom, are not properly handled by the present spectral invariant. The physical explanation for this is the following: The coupling of a mode into a radiating field in the bottom, represented in the theory by the mapping of a discrete spectral component into a continuous component, is happening over a relatively short range interval. As shown by Jensen and Kuperman [31], the result of this cutoff process is a beam radiating into the bottom halfspace. Since this beam is not interacting with any boundaries, it propagates with *constant* vertical and horizontal wavenumber spectrum. The continued use, beyond the cutoff range, of the spectral mapping controlled by the channel alone will change the vertical wavenumber of the beam, and is therefore inconsistent with the physics. This restricts the applicability of the adiabatic spectral mapping to situations where the field is largely modal in nature, and the results produced for receivers in the bottom is in general incorrect. This suggests that a more refined asymptotic theory is needed which would help in establishing a more robust invariant that would permit tracking the wavenumbers past cutoff. Another problem with *spectral mapping* techniques of this kind is the need to search for complex roots. Since this search for the mapped spectral values at the new range step, any errors in the search process can erroneously contribute to mode coupling thereby corrupting the numerical results.

It is interesting to note that generalized transforms have been developed in the field of electromagnetics for inhomogeneous multilayered structures of varying thickness. These generalized transforms provide a suitable basis for the expansion of electromagnetic fields in structures with non-separable geometry [34, 35, 36, 37]. Since one should be able to make analogies between electromagnetic and acoustic wave propagation [38], it would be interesting to see if these generalized transforms can be applied to the field of underwater acoustics.

Chapter 3

The Spectral Super-Element Approach

3.1 Introduction

In the previous chapter we showed that the spectral invariant method is not suitable for implementation as a general purpose range-dependent code. In addition, its extension to the elastic case is not obvious and possibly non-trivial. We next turned to a spectral element method previously developed by Seong [25] where the formulation is described in the framework of a boundary integral method. In this chapter, we present the same fluid formulation in a different manner and using a different set of notations which make it easier to understand. In addition, we introduced important changes that extended the method to include handling of large scale problems. These changes include the implementation of the single-scatter approximation as well as a two-pass marching scheme that allows the reverberation field to be obtained as well.

In the present *spectral super-element* method, the range-dependent ocean is divided into a series of range-independent sectors separated by vertical boundaries. In spite of some similarity to the traditional *spectral element* approach, there is a fundamental difference in terms of the horizontal dependence of the solution. In the spectral element approach this dependence is included in the degrees of freedom, whereas it is given explicitly in terms of a

boundary integral in the present super-element approach. This is the key to the efficiency of the present approach to propagation in waveguides of long horizontal extent, prohibitive to traditional spectral element approaches.

The field in each sector or *super-element* is expressed as a superposition of that produced by any real source that might be present in the sector and the field produced by panel sources representing the discontinuities of the vertical boundaries. Since the super-element is horizontally stratified, the source field is given by a wavenumber integral, with the kernels determined very efficiently using the Direct Global Matrix (DGM) approach [39, 16]. The panel source contributions are expressed as a boundary integral which is changed to a discrete summation of influence functions by expanding the field along the vertical boundary in orthogonal polynomials. Using Legendre polynomials for the expansion, wavenumber integral representations for the influence functions are obtained. The kernels of these integrals are also evaluated very efficiently using DGM.

Since it does not rely on any wavelength-dependent discretization in the horizontal direction, the spectral super-element approach can be applied to short- as well as long-range propagation and reverberation problems. The wavenumber integration approach inherently decomposes the total solution into spectral components which is important for physical interpretations.

We describe two different solution algorithms. The first is the original *global* approach by Seong [25] yielding both the forward propagating field and the back-scattered components. The coefficients are obtained from simultaneously matching the boundary conditions along all vertical sector boundaries. For ocean environments with continuously changing bathymetry, the construction and inversion of this matrix in a global manner presents a severe computational load. This deficiency has motivated the search for a more efficient formulation of the hybrid scheme. By employing the *single-scatter* approximation, where the back-scattered component from the opposite vertical boundary is neglected, a computationally efficient forward-marching scheme can be derived. We have also implemented a 2-way marching scheme providing a single-scatter approximation to the reverberation from large scale features, similar to the approach used in the two-way PE [6].

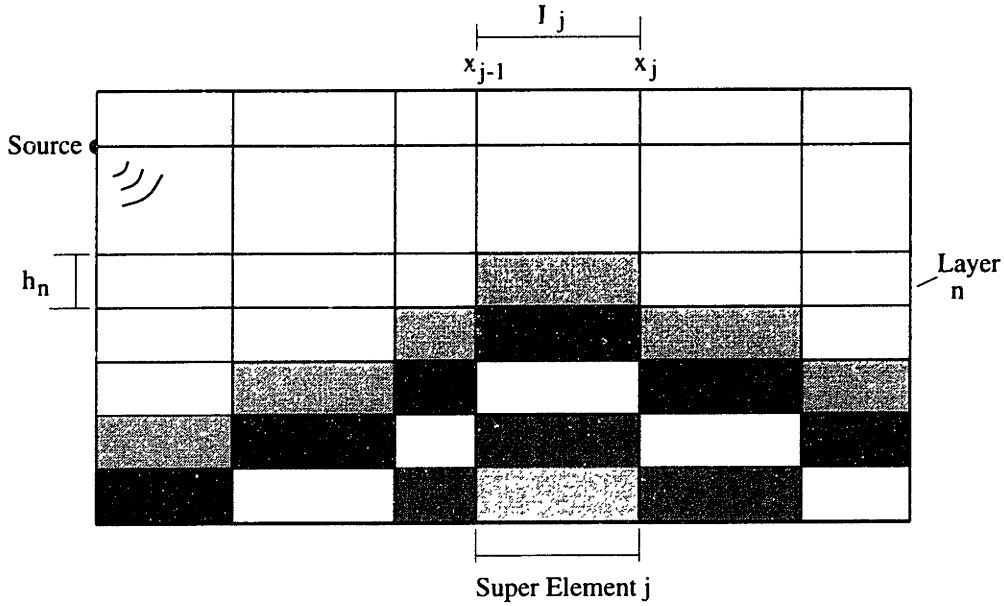

Figure 3-1: Super-element discretization of range-dependent ocean waveguides

3.2 Stratified Super-Elements

In the *spectral super-element* approach, the environment is first divided into a series of range-independent *sectors* or *super-elements*, separated by vertical boundaries or *cuts*, as illustrated in Fig 3-1. The different grey-scales within each super-element denote layers with different material properties. Within each sector, the ocean environment is horizontally stratified.

In deriving the spectral-element equations we will assume the acoustic field to be plane. Thus, in order to account for cylindrical spreading in axisymmetric scenarios, the spreading factor is applied explicitly to the resulting field. The validity of this approach is described in Appendix A and an example of a numerical calculation is shown in Fig. 3-7b.

Within each sector the acoustic pressure of time dependence $\exp i\omega t$ is given by

$$p(\mathbf{r}) = \rho\omega^2\phi(\mathbf{r}), \tag{3.1}$$

where ϕ is the displacement potential, satisfying the Helmholtz equation [1],

$$\left[\nabla^2 + k^2(\mathbf{r})\right]\phi(\mathbf{r}) = f(\mathbf{r})\ , \tag{3.2}$$

and $\mathbf{r}$ represents the spatial coordinates (x, z). The field in sector j is now expressed as a superposition of the field produced in the stratified element in the absence of the vertical boundaries, ϕ^*, the field arising from the left boundary ϕ^-, and the field arising from the right boundary, ϕ^+,

$$\phi(x,z) = \phi^*(x,z) + \phi^-(x,z) + \phi^+(x,z) \tag{3.3}$$

The contributions $\phi^\pm$ from the vertical boundaries are determined using an *indirect* boundary integral method [25], based on Green's theorem for the virtual element obtained by eliminating the other vertical boundary and letting the element continue to infinity,

$$\phi^\pm(\mathbf{r}) \;=\; \int_{S^\pm} \left[G(\mathbf{r},\mathbf{r}^\pm)\frac{\partial\phi^\pm(\mathbf{r}^\pm)}{\partial\mathbf{n}^\pm} \;-\phi^\pm(\mathbf{r}^\pm)\frac{\partial G(\mathbf{r},\mathbf{r}^\pm)}{\partial\mathbf{n}^\pm}\right] dS^\pm \,. \tag{3.4}$$

Here $S^\pm$ is the boundary of the semi-infinite elements. $G(\mathbf{r},\mathbf{r}^\pm)$ is an arbitrary Green's function satisfying the homogenous Helmholtz equation everywhere within the virtual element but not necessarily the boundary conditions. By choosing a Green's function which satisfies all boundary conditions at the horizontal interfaces, including the lower and upper boundaries of the super-element, then the contributions to the surface integral from the horizontal boundaries are eliminated. Note here, that the super-elements always have finite depth. Thus, in the presence of a lower halfspace, the lower boundary of the super-element is chosen deep enough into the halfspace to ensure that the field satisfies the radiation condition along the horizontal boundary, in which case the associated surface integral contribution vanishes. We would like to emphasize that this is different from the false bottom modal formulation of Evans [15] where the false bottom is introduced to achieve a complete mode set. In our approach, we only need to truncate the last layer at a depth where the dominant part of the field is downgoing.

If in addition we choose a Green's function which is symmetric in the horizontal coordinate x, $G(\mathbf{r},\mathbf{r}') = G(|x-x'|;z,z')$, then the term involving $\partial G/\partial\mathbf{n}^\pm$ in Eq. (3.4) will vanish, yielding

$$\phi^\pm(\mathbf{r}) = \int_{S^\pm} G(\mathbf{r},\mathbf{r}^\pm)\frac{\partial\phi^\pm(\mathbf{r}^\pm)}{\partial\mathbf{n}^\pm}dS^\pm \,, \tag{3.5}$$

3.3 Field Expansion

The boundary conditions to be satisfied between the super-elements, together with Eq. (3.5) now provides an integral equation for the field $\phi^{\pm}$ on the vertical boundaries of the super-element, the numerical solution of which requires some kind of discretization. For fluid super-elements, the boundary conditions are the continuity of pressure and the horizontal component u of displacement, i.e. at the vertical boundary j separating super-elements j and $j+1$,

$$\left\{ \begin{array}{c} u(x_j,z) \\ p(x_j,z) \end{array} \right\}^j = \left\{ \begin{array}{c} u(x_j,z) \\ p(x_j,z) \end{array} \right\}^{j+1} \tag{3.6}$$

A superscript is used to identify the super-element here and in the following. Since the field within each layer in the stratification is a smooth function of depth, we here choose a *Galerkin boundary element* approach [1]. In the Galerkin approach, the continuity of the field across the vertical boundaries is expressed in the *weak form*

$$\int_0^{h_n} u^j(x_j,z)[u^{j+1}(x_j,z) - u^j(x_j,z)]dz = 0\,, \tag{3.7}$$

where z is the local depth coordinate and similarly for the pressure. The field parameters displacement and pressure are now expressed as expansions in terms of a set of basis functions. By choosing an orthogonal set of expansion functions Eq. (3.7) requires the expansion coefficients in the two neighboring sectors to be identical. Here we choose an orthonormal set of Legendre polynomials, normalized within each layer n:

$$\left\{ \begin{array}{c} u_n(x,z) \\ p_n(x,z) \end{array} \right\}^j = \frac{2\pi}{h_n} \sum_{m=1}^{\infty} \left\{ \begin{array}{c} U_{nm}(x) \\ S_{nm}(x) \end{array} \right\}^j P_{m-1}(\bar{z}) \tag{3.8}$$

where m is the order of expansion, P_m is the Legendre function and h_n is the thickness of layer n. The argument to the Legendre polynomial is the normalized, local depth coordinate

$$\bar{z}_n = \frac{z - h_n/2}{h_n/2}. \tag{3.9}$$

With the normal derivative of the displacement potential in the kernel of Eq. (3.5) representing the horizontal displacements at the vertical boundaries, insertion of Eq. (3.8) yields the following expression for the total field in super-element j

$$\phi(x,z) \;=\; \sum_{l,k} F^j_{lk}(x - x_{j-1}, z) \left\{U^-_{lk}\right\}^j - F^j_{lk}(x_j - x, z) \left\{U^+_{lk}\right\}^j + \phi^*(x,z)\,. \tag{3.10}$$

Here, $\{U_{lk}^{-}\}^j$ and $\{U_{lk}^{+}\}^j$ represent the unknown *panel source strengths* at the left and right boundary, respectively, of super-element number j, and

$$F_{lk}^j(x,z) = \frac{2\pi}{h_l}\int_{-1}^{1} P_{k-1}(\bar{z}_l')\, G(x;z,\bar{z}_l')\, d\bar{z}_l' \,. \tag{3.11}$$

Expanding the field parameters in Legendre polynomials within each layer n as in Eq. (3.8) then yields the following expression for the field expansion coefficients in terms of the unknown panel source strengths, $\{U_{lk}^{\pm}\}^j$

$$\begin{Bmatrix} U_{nm}(x) \\ S_{nm}(x) \end{Bmatrix}^j = \begin{Bmatrix} U_{nm}^*(x) \\ S_{nm}^*(x) \end{Bmatrix}^j + \sum_{l,k}\left[\begin{Bmatrix} C_{nm,lk}(x-x_j) \\ D_{nm,lk}(x-x_j) \end{Bmatrix}^j \left\{U_{lk}^{-}\right\}^j - \begin{Bmatrix} -C_{nm,lk}(x_{j+1}-x) \\ D_{nm,lk}(x_{j+1}-x) \end{Bmatrix}^j \left\{U_{lk}^{+}\right\}^j\right], \tag{3.12}$$

and U_{nm}^* and S_{nm}^* are the expansion coefficients for the displacement and pressure produced by sources within the super-element. $C_{nm,lk}^j(x)$ and $D_{nm,lk}^j(x)$ are the expansion *influence functions* for displacement and pressure, respectively,

$$\begin{Bmatrix} C_{nm,lk}(x) \\ D_{nm,lk}(x) \end{Bmatrix}^j = \frac{2m-1}{2\pi}\int_{-1}^{1}\begin{Bmatrix} \partial/\partial x \\ \rho_n\omega^2 \end{Bmatrix} F_{lk}^j(x,z)\, P_{m-1}(\bar{z}_n)\, d\bar{z}_n. \tag{3.13}$$

3.4 Influence Functions

It is clear from Eqs. (3.11) and (3.13) that the influence functions formally are obtained by a double depth-integral of the symmetric Green's function. However, using the direct global matrix (DGM) approach [39] we can replace these depth integrals by a wavenumber integral representation.

Basically the influence functions represent the expansion coefficients of order m in layer n produced by a *panel source* of order k in layer l. Thus, the total field is given as a superposition of the field $\hat{\phi}^{\pm}$ produced by the panel source in the absence of boundaries, and homogeneous solutions $\bar{\phi}^{\pm}$ accounting for interface reflections and transmissions [1]

$$\phi^{\pm}(x,z) = \hat{\phi}^{\pm}(x,z) + \bar{\phi}^{\pm}(x,z) \tag{3.14}$$

To determine the spectral representation of the field produced by the panel sources we use a generalization of the approach used by Heelan [40] for the constant stress panel. Thus, consider the panel source of order k in layer l, representing the displacement distribution

$$\hat{u}_l(x_{j-1}, z) = \begin{cases} 0 & z < 0\,,\ z > h_l \\ \frac{2\pi}{h_l} P_{k-1}(\bar{z}_l) & 0 \le z \le h_l \end{cases} . \tag{3.15}$$

The displacement potential which satisfies the Helmholtz equation and the radiation condition can be written in terms of vertical wavenumber spectral representation as

$$\hat{\phi}_{lk}(x, z) = \int_{-\infty}^{\infty} \hat{A}_{lk}(\eta)\, e^{-x\gamma} e^{-i\eta(z - h_l/2)}\, d\eta \tag{3.16}$$

where η and $i\gamma = i\sqrt{\eta^2 - k_l^2}$ are the vertical and horizontal wavenumbers respectively and k_l is the acoustic wavenumber.

Differentiating Eq. (3.16) with respect to x to produce the horizontal displacement u, followed by the forward Fourier transform with respect to z gives

$$-\gamma \hat{A}_{lk}(\eta)\, e^{-x\gamma} e^{i\eta h_l/2} = \frac{1}{2\pi} \int_{-\infty}^{\infty} \hat{u}_l(x, z) e^{i\eta z}\, dz\ . \tag{3.17}$$

In this thesis, we employ the following definition for the Fourier transform pair,

$$\begin{aligned} f(z) &= \int_{-\infty}^{\infty} g(\eta) e^{-i\eta z}\, d\eta, \\ g(\eta) &= \frac{1}{2\pi} \int_{-\infty}^{\infty} f(z) e^{i\eta z}\, dz. \end{aligned} \tag{3.18}$$

Substituting the boundary condition at $x = 0$, Eq. (3.15), and using the identity [41],

$$\int_0^{h_l} P_{k-1}(\bar{z}) e^{i\eta z} dz = h_l e^{i\eta h_l/2} i^{k-1} j_{k-1}\left(h_l \eta/2\right)\ , \tag{3.19}$$

the wavenumber kernel becomes

$$\hat{A}_{lk}(\eta) = -\frac{1}{\gamma}\, i^{k-1} j_{k-1}\left(h_l \eta/2\right)\ . \tag{3.20}$$

Note that the integration over z in the transform has been performed analytically and is accounted for by the spherical Bessel function j_{k-1}. Substitution into Eq. (4.13) yields

$$\hat{\phi}_{lk}(x, z) = -\frac{1}{\gamma} i^{k-1} \int_{-\infty}^{\infty} e^{-x\gamma} e^{-i\eta(z - h_l/2)}\, j_{k-1}\left(h_l \eta/2\right)\, d\eta\ , \tag{3.21}$$

which is the required free-space Green's function for the panel source in Eq. (3.15).

The DGM approach for the multi-layered sector requires the integral representation for the free-space Green's function to be expressed in terms of the horizontal wavenumber. Using contour integration as devised by Heelan [40], the vertical wavenumber integral of Eq. (3.21) is converted into a horizontal wavenumber integral,

$$\hat{\phi}_{lk}(x,z) = -i^{k-1} \int_{-\infty}^{\infty} \frac{1}{\alpha_l}\, j_{k-1}\Big(-\frac{i\mathcal{S}h_l\alpha_l}{2}\Big) e^{-|z-h_l/2|\alpha_l}\, e^{-isx}\, ds, \tag{3.22}$$

where s is the horizontal wavenumber, $\alpha_l = \sqrt{s^2 - k_l^2}$, and $\mathcal{S} = \text{sign}(z - h_l/2)$.

The above representation is valid only for $z \leq 0$ and $z \geq h_l$, but still allows for the application of the global matrix method when satisfying the horizontal interface boundary conditions since it is at the interfaces $z = 0$ and $z = h_l$ of each layer that the fields are being matched.

We now simply use Eq. (3.22) as the source contribution in the SAFARI code [16] to determine the associated homogeneous solution in layer n

$$\bar{\phi}_{n,lk}(x,z) = \int_{-\infty}^{\infty} \left[A^{-}_{n,lk} e^{-\alpha_n z} + A^{+}_{n,lk} e^{\alpha_n z}\right] e^{-isx}\, ds\,. \tag{3.23}$$

The influence functions are then obtained by expanding the total field in layer n in Legendre functions. The expansion of the homogeneous solution $\bar{\phi}_{n,lk}$ is performed directly using the identity in Eq. (3.19) to yield the homogeneous contribution to the influence functions:

$$\begin{Bmatrix} \bar{C}_{nm,lk}(x) \\ \bar{D}_{nm,lk}(x) \end{Bmatrix}^{j} = -(2m-1)i^{m-1} \int_{-\infty}^{\infty} \begin{Bmatrix} is \\ \rho_n\omega^2 \end{Bmatrix} \Big[\, A^{-}_{n,lk}(s) + (-1)^{m-1} A^{+}_{n,lk}(s) \,\Big]\, e^{-h_n\alpha_n/2}\, e^{-isx}\, j_{m-1}\left(ih_n\alpha_n/2\right)\, ds\,. \tag{3.24}$$

The corresponding direct contributions from the panel sources within the same layer are obtained by expanding the vertical wavenumber integral in Eq. (3.21) in Legendre functions, again using the identity in Eq. (3.19),

$$\begin{Bmatrix} \hat{C}_{nm,lk}(x) \\ \hat{D}_{nm,lk}(x) \end{Bmatrix}^{j} = \frac{\delta_{nl}h_n}{2\pi}\zeta_m\, i^{m+k-2} \int_{-\infty}^{\infty} d\eta \begin{Bmatrix} 1 \\ \rho_n\omega^2/\gamma \end{Bmatrix} e^{-x\gamma}\, j_{m-1}\Big(\frac{h_n\eta}{2}\Big) j_{k-1}\Big(\frac{h_l\eta}{2}\Big), \tag{3.25}$$

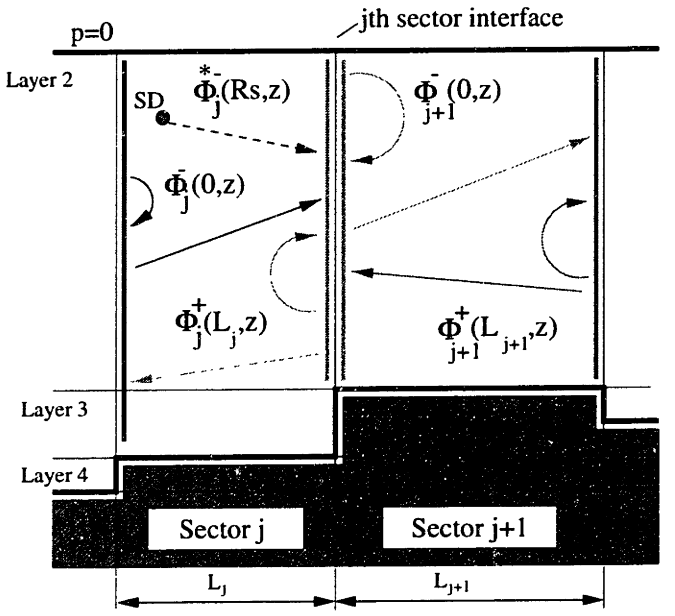

Figure 3-2: Connecting two sectors together via the boundary conditions

where δ_{nl} is the Kronecker delta and $\zeta_m = (2m-1)(-1)^{m-1}$. Each combination of indices l and k represents a single SAFARI run. However, the DGM can treat multiple right hand sides simultaneously. Hence, $A^{\pm}_{n,lk}$, and therefore all influence functions can be found using SAFARI for all combinations of the indices n, m, l, and k with just a single global matrix inversion. This makes the algorithm relatively efficient even for problems with a large number of layers and high orders of expansion.

3.5 Element Connectivity

Inserting the field expansions in Eq. (3.8) into the weak form of the boundary conditions in Eq. (3.7) leads to the *connectivity* equations between super-elements j and $j+1$,

$$\left\{ \begin{array}{c} U_{nm}(x_j) \\ S_{nm}(x_j) \end{array} \right\}^{j} = \left\{ \begin{array}{c} U_{nm}(x_j) \\ S_{nm}(x_j) \end{array} \right\}^{j+1}, \qquad \begin{array}{l} n = 1, \ldots N, \\ m = 1, \ldots M. \end{array}$$

Here N is the number of layers, and M is the number of expansion terms used within each layer. Fig. 3-2 shows a picture of the coupling between the sectors. Inserting Eq. (3.12) into

Eq. (4.36) then yields the following linear system of equations for the unknown *panel source strengths* for super-elements j and $j+1$,

$$\sum_{l,k}\left[\begin{Bmatrix} C_{nm,lk}(0) \\ D_{nm,lk}(0)\end{Bmatrix}^{j+1}\left\{U_{lk}^{-}\right\}^{j+1} - \begin{Bmatrix} -C_{nm,lk}(L_{j+1}) \\ D_{nm,lk}(L_{j+1})\end{Bmatrix}^{j+1}\left\{U_{lk}^{+}\right\}^{j+1} + \begin{Bmatrix} -C_{nm,lk}(0) \\ D_{nm,lk}(0)\end{Bmatrix}^{j}\left\{U_{lk}^{+}\right\}^{j} - \begin{Bmatrix} C_{nm,lk}(L_j) \\ D_{nm,lk}(L_j)\end{Bmatrix}^{j}\left\{U_{lk}^{-}\right\}^{j}\right] = \begin{Bmatrix} U_{nm}^{*}(x_j) \\ S_{nm}^{*}(x_j)\end{Bmatrix}^{j} - \begin{Bmatrix} U_{nm}^{*}(x_j) \\ S_{nm}^{*}(x_j)\end{Bmatrix}^{j+1} \tag{3.26}$$

Here, L_j is the horizontal length of the super-element. Solution of Eq. (3.26) yields the panel source strengths $\{U_{lk}^{\pm}\}^j$ in super-element j, and the resulting field is then given by Eq. (3.12), with the influence functions obtained through evaluation of the wavenumber integrals in Eqs. (3.24) and (3.25), using the FFP approach [1] and Gaussian quadrature, respectively.

3.6 Numerical Implementation

3.6.1 Global Solution

In the *global* approach, the influence matrix for all sectors are computed to determine the coefficients in Eq. (3.26) which is then solved directly for all sector boundaries. This approach accounts for multiple scattering between sector boundaries. In order to set up this *global* influence matrix, the environment must be discretized such that the depth of each layer is the same for all sectors. In an ocean environment where the bathymetry changes continuously, such as a coastal wedge, a straight forward stair-case discretization of the bathymetry will require an excessively large number of layers. Here lies the greatest deficiency of the *global* approach.

3.6.2 Marching Algorithm

A computationally efficient forward marching scheme can be derived by employing the single-scatter approximation, where the back-scattered component from the forward vertical bound-

ary is neglected. Thus, ignoring the term with $\{U_{lk}^{+}\}^{j+1}$ yields the following *marching* form of Eq. (3.26),

$$\sum_{l,k}\left[\begin{Bmatrix} C_{nm,lk}(0) \\ D_{nm,lk}(0) \end{Bmatrix}^{j+1}\left\{U_{lk}^{-}\right\}^{j+1} + \begin{Bmatrix} -C_{nm,lk}(0) \\ D_{nm,lk}(0) \end{Bmatrix}^{j}\left\{U_{lk}^{+}\right\}^{j}\right]$$
$$= \begin{Bmatrix} U_{nm}^{*}(x_j) \\ S_{nm}^{*}(x_j) \end{Bmatrix}^{j} - \begin{Bmatrix} U_{nm}^{*}(x_j) \\ S_{nm}^{*}(x_j) \end{Bmatrix}^{j+1} + \begin{Bmatrix} C_{nm,lk}(L_j) \\ D_{nm,lk}(L_j) \end{Bmatrix}^{j}\left\{U_{lk}^{-}\right\}^{j} \tag{3.27}$$

After solving Eq. (3.27) at super-element boundary j, the field everywhere in the next sector follows from Eq. (3.12) with the backward propagating field ignored. The marching algorithm therefore *decouples* the *global* problem into a *local* one. This decoupling reduces tremendously the amount of computational resources needed for the code but introduces a unique problem. When we propagate the field from one sector to the next, the layer structure at sector j may be different from that at sector $j+1$. This implies that the set of expansion coefficients at sector j cannot be used directly at the next range step but instead new sets of coefficients need to be derived. In Appendix J we discuss this in greater detail and derive mapping matrices that allow us to 'march' the expansion coefficients from one range step to the next, even when the layering structure has changed. Even though this is only an approximate solution due to the inherent truncation in the orders of expansion, our numerical experiments have shown that it does improve the solution.

3.6.3 Reverberant Field

In the *global* approach, the forward and back scattered fields are computed simultaneously. Using an approach similar to the two-way PE solution [6], we can recover an approximation to the reverberant field from the *marching* solution as well. We start the forward solution at the source range and propagate the outgoing field across the range-independent sectors. At each vertical boundary, the influence matrix and the panel source strengths in the back-scattered direction are saved for later use. Starting at the maximum range, a back-scattered field is marched backwards towards the source. During this backward pass, the source strengths saved from the forward pass are added in. This process thus recovers the backscattered field in all the sectors.

3.7 Numerical Examples

In the following we illustrate how the present approach provides accurate solutions to canonical propagation and reverberation benchmark problems. Unless otherwise stated, the water column is assumed to be homogeneous with a sound speed of 1500 m/s and density $\rho = 1.0\text{g/cm}^3$. As reference solutions, we use the FEPE [33] and COUPLE codes [15]. All our solutions are obtained using only four orders of expansion in the field parameters within each layer.

3.7.1 A : ASA Penetrable Wedge Benchmark

Example A is the socalled ASA benchmark problem involving a cylindrically symmetric sloping ocean bottom [30]. The environmental model is shown in Fig. 3-3. This problem is considered to illustrate the accuracy of the outgoing field obtained using the marching algorithm. The water depth decreases linearly from 200m at $r = 0$ to zero at $r = 4$km. A 25-Hz point source is placed at mid-depth. In the homogeneous sediment, $c = 1700$ m/s, $\rho = 1.5\text{g/cm}^3$, and $\alpha = 0.5$ dB/λ. The backscattered field is negligible for this problem [42]. The environment is discretized into 17 layers, each of about a wavelength in depth, and 113 range sectors. The solutions for this problem appear in Fig. 3-4. The solid line is the solution obtained with the FEPE and the agreement is very good for the shallow receiver and satisfactory for the deeper receiver and for most practical purposes the differences can be considered as insignificant.

3.7.2 B : SACLANT Stair-Step Discontinuity

Example B, taken from Jensen and Gerstoft [43], involves a stair step in the ocean bottom with the ocean bottom acoustic parameters of example A. The water depth is a constant 200m for $r < 1.5$ km and 150 m for $r > 1.5$ km. A 25-Hz line source is placed at depth $z = 100$m. The abrupt change in the environment causes a significant amount of energy to be reflected from the stair face and into the water column. We solved this problem using only 2 range sectors and 8 layers down to a depth of 350m. Fig. 3-5a shows the environmental model and our solutions to the stair-step problem appear in Fig. 3-5b and Fig. 3-5c. The super-element

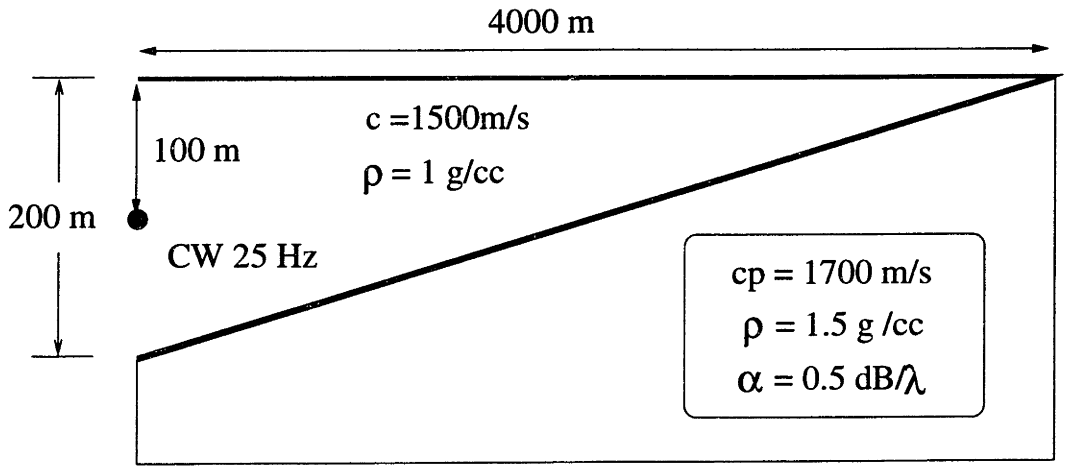

Figure 3-3: Ex. A : Schematic for the ASA benchmark problem

solution and the two-way coupled mode field are in excellent agreement. For this problem with only one vertical sector boundary, the global and marching schemes provide identical results.

3.7.3 C : SACLANT Half-Cylindrical Ridge

Example C, also from Jensen and Gerstoft [43], involves a half-cylindrical ridge in the ocean bottom with the ocean bottom acoustic parameters of Example B. A 25-Hz line source is placed at depth $z = 100$m. The ridge is positioned 1.5 km downrange and has a height of 50 m ($\sim$ 1 wavelength) above the sea floor. The environment is shown in Fig. 3-6a and in Fig. 3-6b and Fig. 3-6c, we present the super-element and the two-way coupled mode solutions. Despite the fact that the dominant lengthscale of the ridge is of the order of a wavelength and that we are using a single scatter formulation (with 10 range segments), the agreement between the two solutions is remarkable.

3.7.4 D : Cylindrical Fluid Seamount

Example D shown in Fig. 3-7a consider a seamount in a cylindrically symmetric ocean environment [19]. A 25 Hz source is located in the middle of the waveguide. The depth of the water column at the source range is 200 m. A 135 m high seamount has inner radius 5

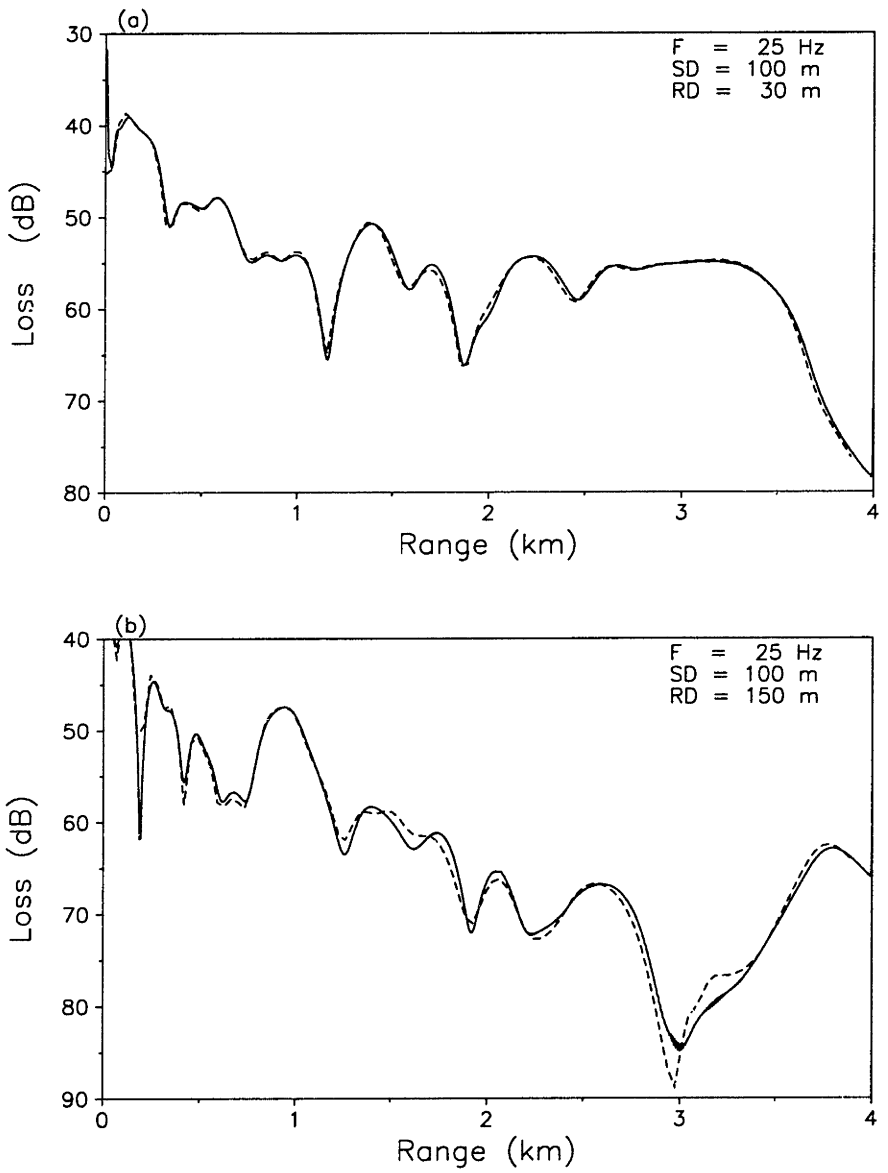

Figure 3-4: Solutions for the ASA benchmark (Ex. A). (a) Receiver at 30m, (b) Receiver at 150m: Solid - FEPE; Dashed - Spectral super-element solution.

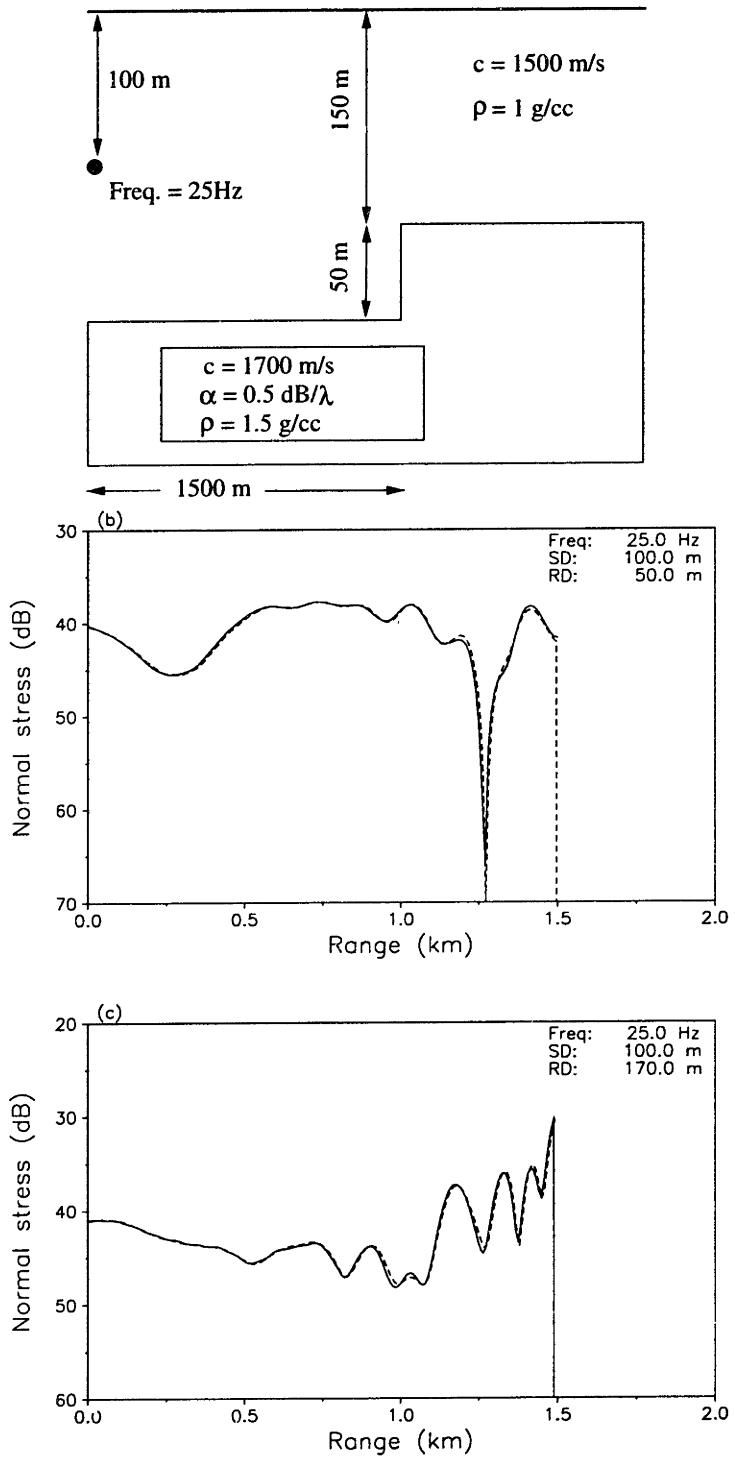

Figure 3-5: Backscattering from stair-step ridge (Ex. B). (a) Schematic of the problem, (b) Receiver at 50m, (c) Receiver at 170m: Solid - COUPLE; Dashed - Spectral super-element solution.

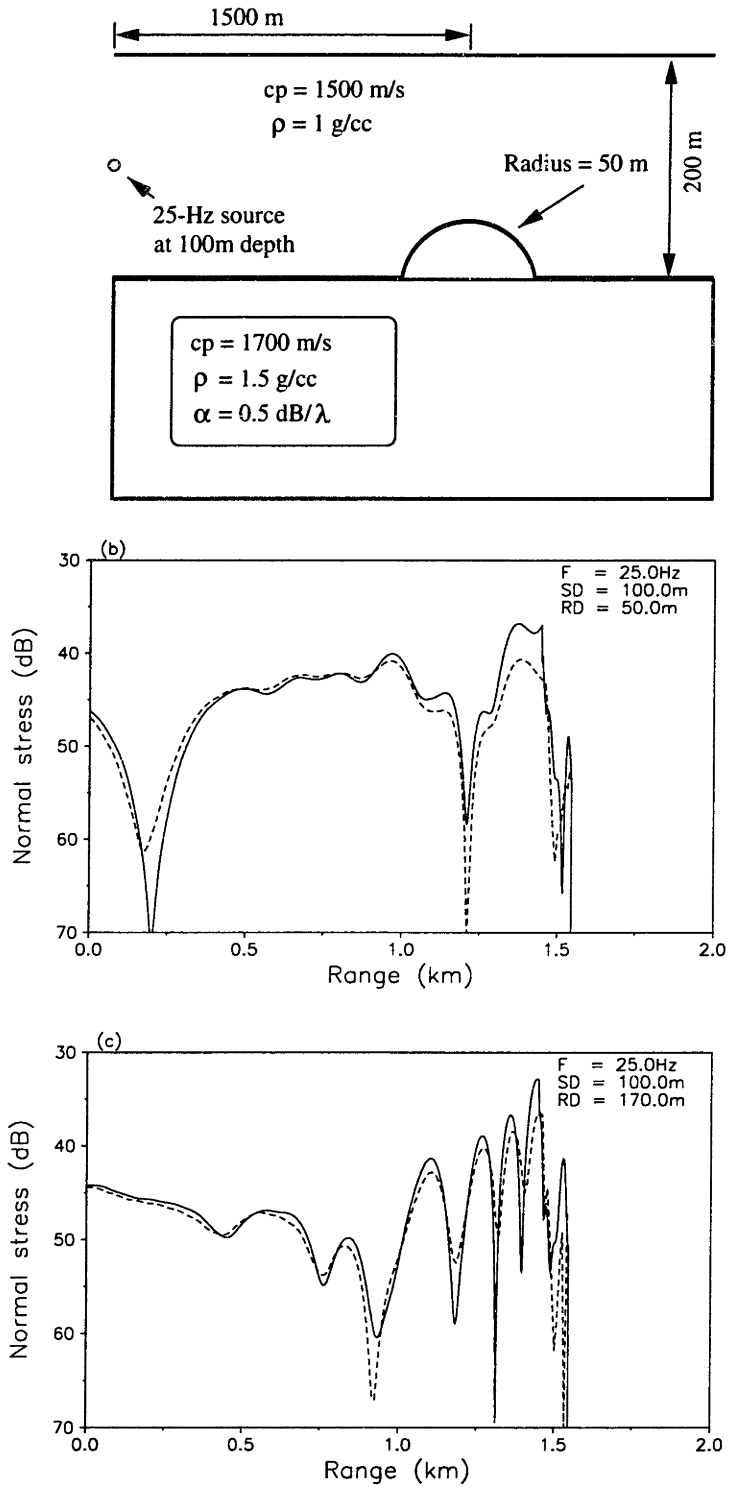

Figure 3-6: Backscattering from half-cylindrical ridge (Ex. C). (a) Environment, (b) Receiver at 50m, (c) Receiver at 170m: Solid - COUPLE; Dashed - Spectral super-element solution.

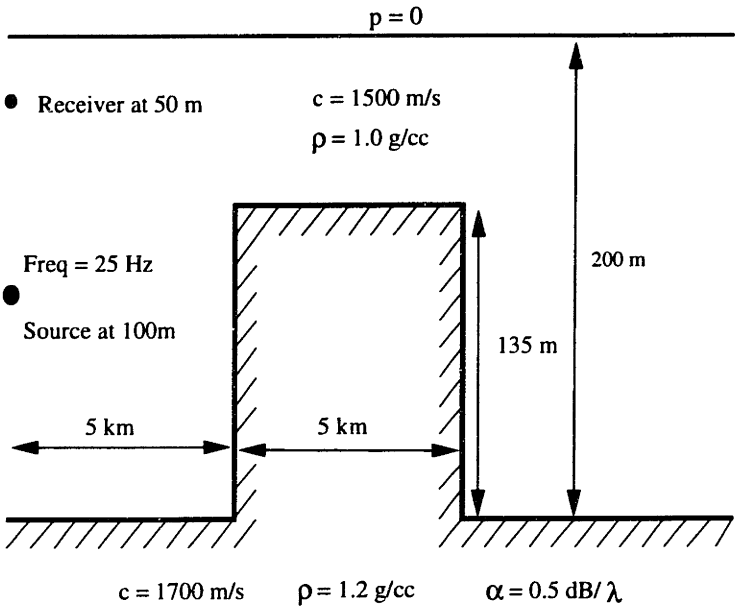

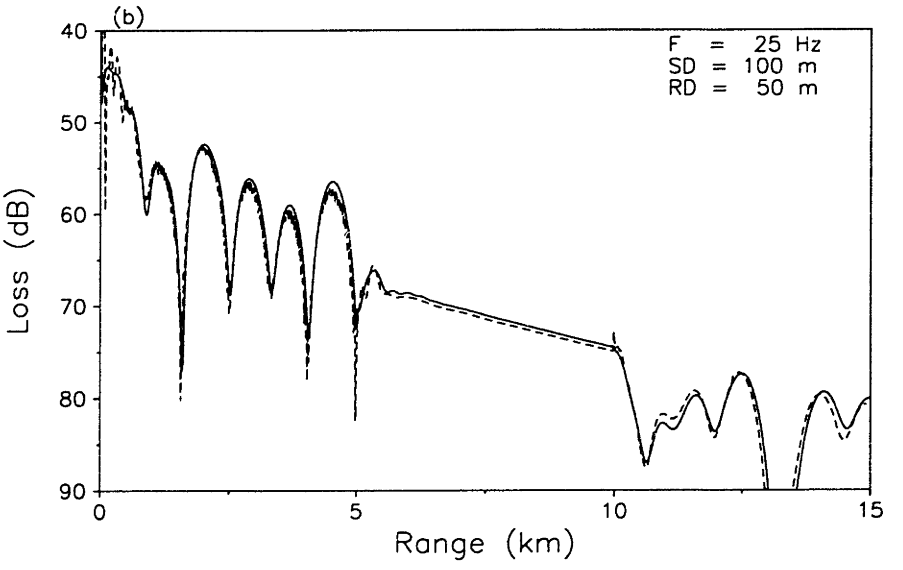

Figure 3-7: Cylindrical seamount (Ex. D). (a) Environment, (b) Receiver at 50m. Solid - COUPLE; Dashed - Spectral super-element solution.

km and outer radius 10 km. The bottom is a homogeneous half-space with a sound speed of 1700 m/s and density 1.5g/cm^3. The attenuation in the bottom is 0.5dB/λ. We solved this problem using only 3 range sectors and 8 layers down to a depth of 400m. Comparisons between COUPLE and our solutions are shown in Fig. 3-7b.

3.7.5 E : Coastal Wedge with a Faulted Basement Layer

Example E, taken from Collins and Evans [6], involves a 25-Hz line source in an ocean with a sloping sediment overlying a faulted basement layer. The ocean depth is 200 m for $r < 5$ km and decreases linearly from 200 m at $r = 5$ km to 60 m at $r = 10.173$ km. The source is placed at a depth of 112 m so that only the first and third modes are excited. The sound speed in the water column is 1704.5 m/s, $\rho = 1.15$g/cm^3, and $\beta = 0.5$ dB/λ in the sediment. Within the basement layer, which consists of $z > 400$ m for $r < 9$ km and of $z > 300$ m for $r > 9$ km, $c = 1850$ m/s, $\rho = 1.5$g/cm^3, and $\beta = 0.5$ dB/λ. Fig. 3-8a shows the contoured wavefield in the absence of the basement fault and Fig. 3-8b shows how the fault deflects the down going beam back towards the surface and excites a field in the water column consisting mainly of the third mode.

3.7.6 F : Reverberation & Scattering Workshop Test 2a

This example is taken from the 1994 Reverberation and Scattering Workshop [44].This test case is intended to test the accuracy of discretized codes when the scattering surface is discretely varying in height and range. A rectangular object of height 100 m and width 120 m is place at a range of 3 km from the *point* source. The water depth at the source is 150 m. The water sound speed is a constant 1500 m/s. The bottom is a half space with a sound speed of 1800 m/s, a density of 1.5 g/cm^3 and an attenuation of 0.5 dB/λ. The dimensions of the discontinuity (height and width) are defined by the center frequency of 30 Hz (i.e., 50 m and 60 m respectively). Fig. 3-9 shows the test geometry as well as the forward and backscattered normal stress for a receiver depth of 45 m. We note that there is excellent agreement among the three solutions.

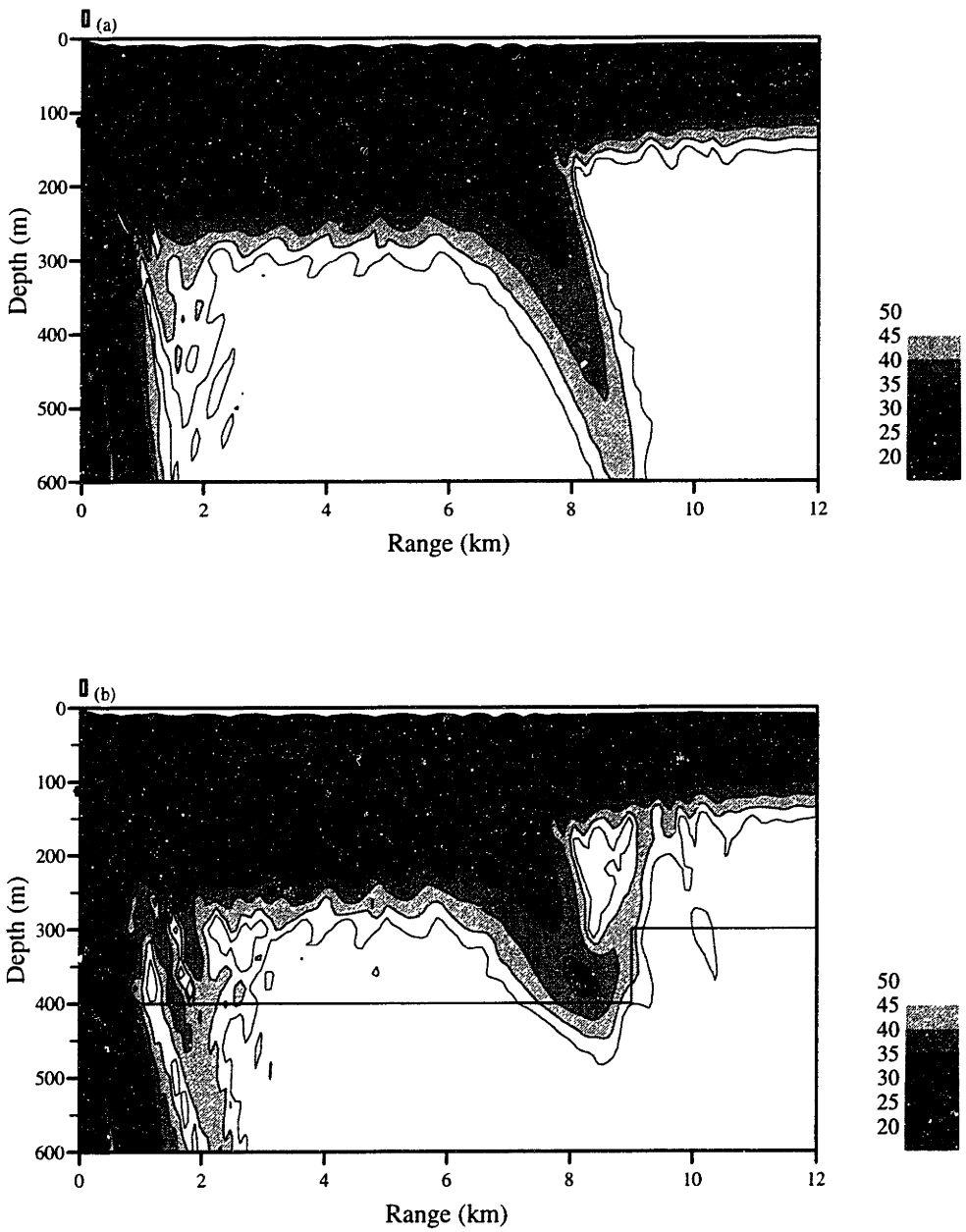

Figure 3-8: Wedge overlying a basement fault (Ex. E). (a) Contoured field without the fault, (b) Contoured field with the fault present

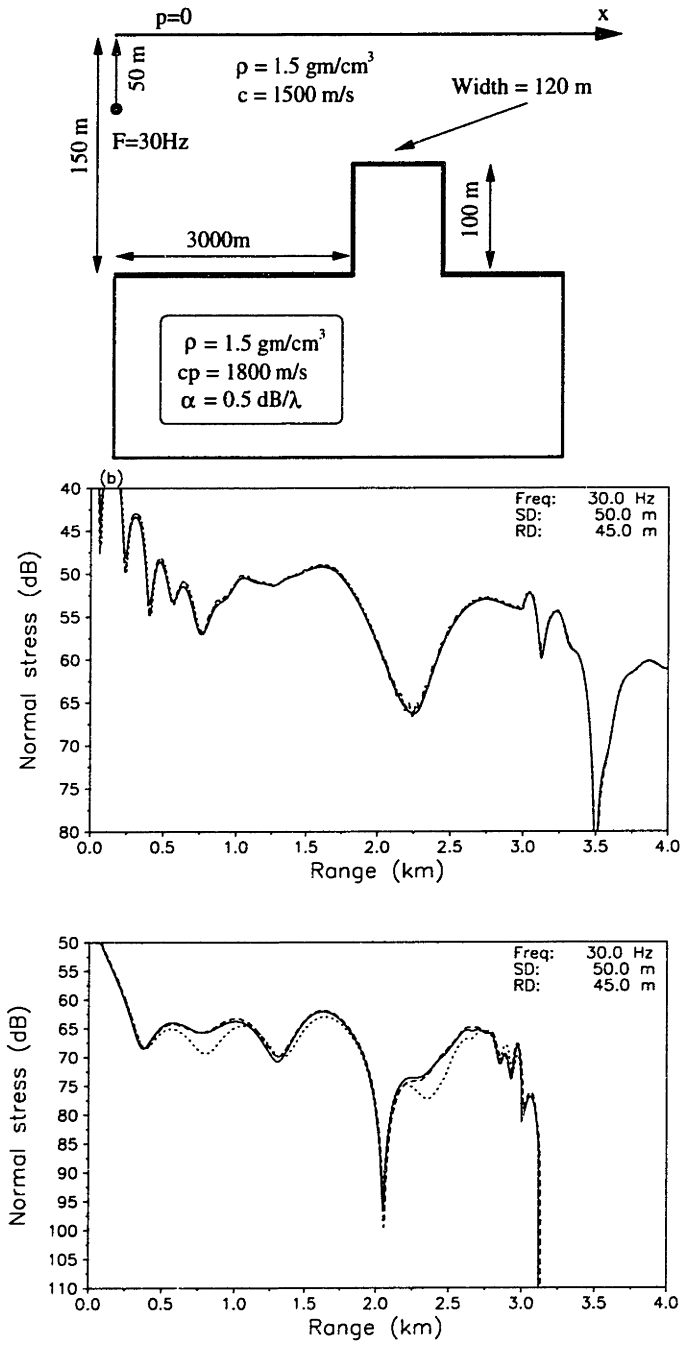

Figure 3-9: R & S Workshop Test 2a (Ex. F) : (a) Test geometry, (b) Forward normal stress, (c) Backscattered normal stress. Solid : COUPLE, Dashed : VISA, Dotted : Spectral super-element.

3.7.7 G : Reverberation & Scattering Workshop Test 2b

This example is similar to Example F except that the scatterer has a half-cylinder endcap. The CORE and VISA solutions were generated using 20 sectors to represent the endcap. Fig. 3-10 shows the test geometry as well as the forward and backscattered normal stress for a receiver depth of 45 m. We solve this problem using a point source configuration. The CORE and VISA solutions have good qualitative agreement with the COUPLE reference solution. The discrepancy is due to the breakdown of the single-scatter approximation as well as probably a poor representation of the endcap with 20 sectors. Increasing the number of sectors would most likely increase the errors arising from the single scatter approximation.

3.7.8 H : Reverberation & Scattering Workshop Test 3a

Example H is intended to test the ability of backscatter codes to accurately handle *multiple* scattering when the scattering surfaces are *discretely* varying in height and range. The schematic in Fig. 3-11(a) illustrates the configuration, which is very similar to Example F. In this case an additional scattering object has been added to the environments of Example F. The leading edge of a second rectangular scattering object is placed 100 m from the trailing edge of the first rectangular object. Each rectangular object has a height 100 m and a width 120 m. The first object is placed at a range of 3 km The water depth at the source is 150 m. The water sound speed is a constant 1500 m/s. The bottom is a half space with a sound speed of 1800 m/s, a density of 1.5 g/cm^3 and an attenuation of 0.5 dB/λ. We solve this problem with a *line* source. Fig. 3-11(b) and (c) shows the forward and backscattered normal stress at a receiver depth of 45 m for the various codes. Note that we have added a constant factor of 2.4857 dB ($10\log\sqrt{\pi}$) to the COUPLE reference solution to account for the difference in source normalizations.

3.7.9 I : Reverberation & Scattering Workshop Test 3b

This example is similar to Example H except that the scatterers have half-cylinder endcaps on them so that now the scattering surfaces are *continuously* varying in height and range. The CORE and VISA solutions were generated using 20 sectors to represent the endcap. Fig. 3-12

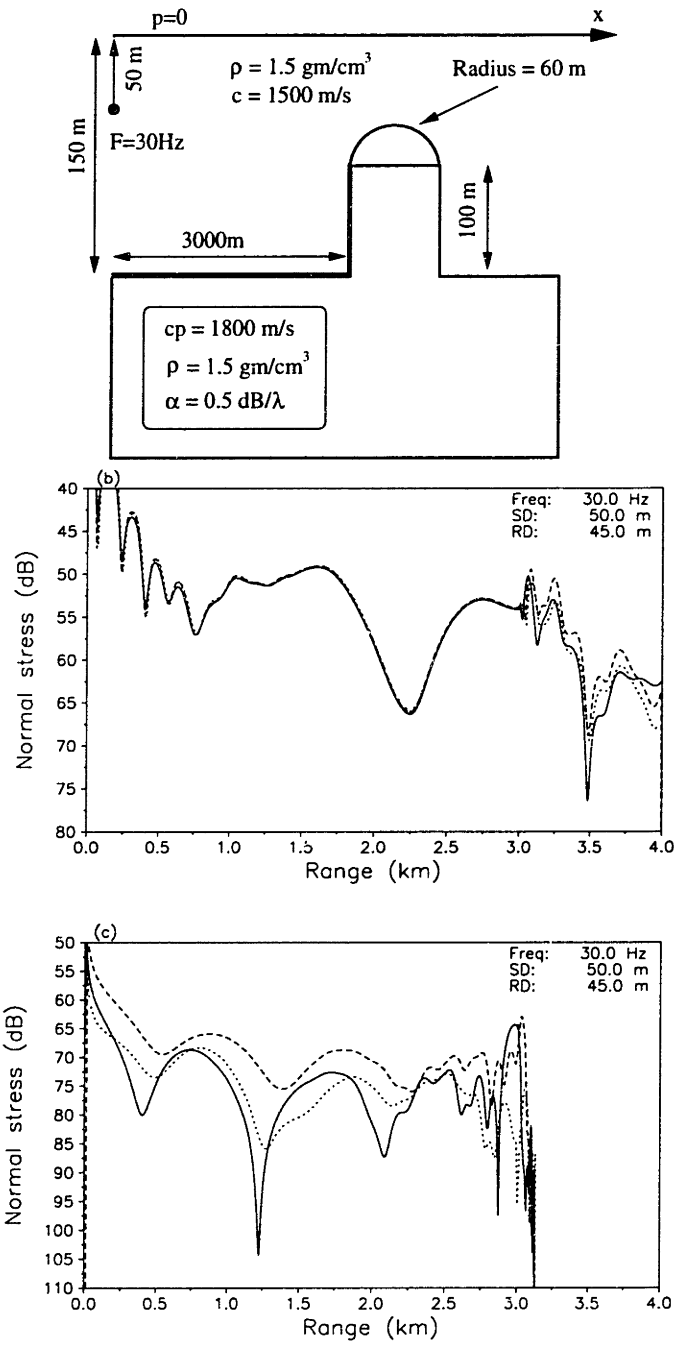

Figure 3-10: R & S Workshop Test 2b (Ex. G) : (a) Test geometry, (b) Forward normal stress, (c) Backscattered normal stress. Solid : COUPLE, Dashed : VISA, Dotted : Spectral super-element.

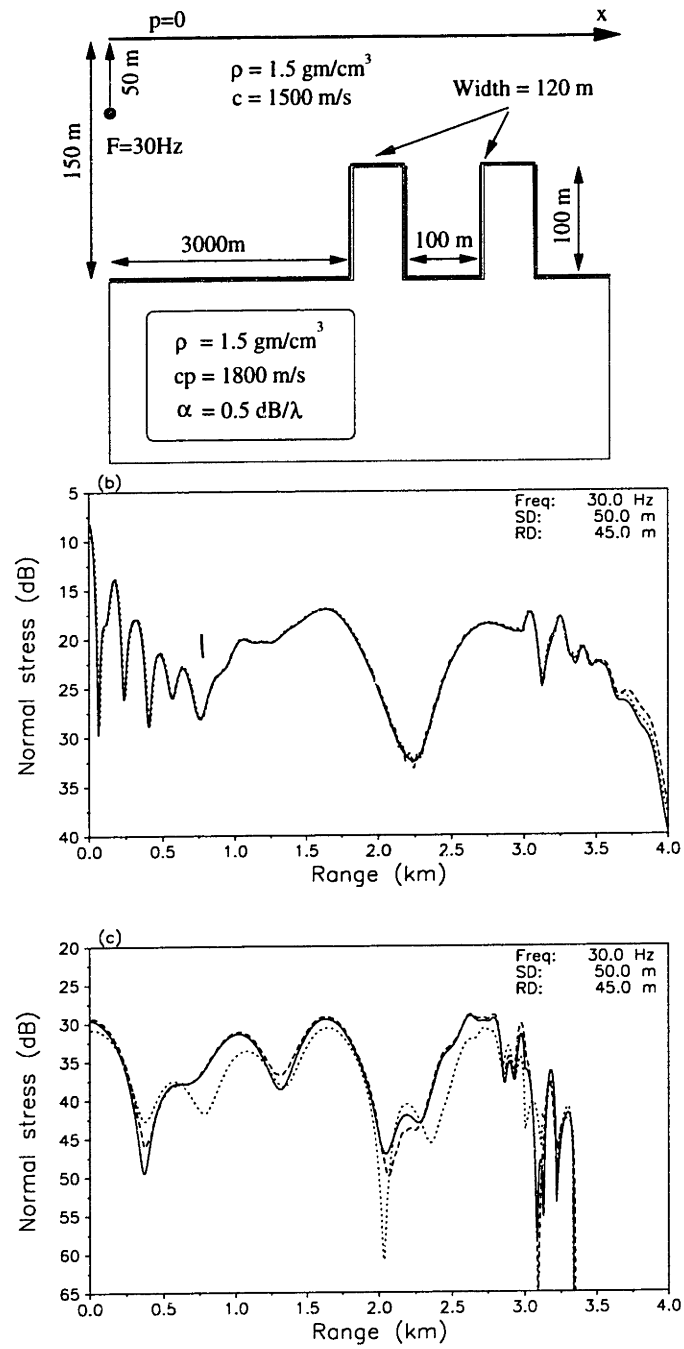

Figure 3-11: R & S Workshop Test 3a (Ex. H) : (a) Test geometry, (b) Forward normal stress, (c) Backscattered normal stress. Solid : COUPLE, Dashed : VISA, Dotted : Spectral super-element.

shows the test geometry as well as the forward and backscattered normal stress for a receiver depth of 45 m. We solve this problem using a *line* source configuration. The agreement with COUPLE is quite good though we see less favourable agreement in the backscatter due again to the inapplicability of the single-scatter approximation. As in Example H, the COUPLE solution was adjusted by 2.4857 dB.

3.8 Summary

In this chapter, we introduced the single-scatter approximation that decouples the *global* approach of Seong [25] into a *local* one that can be easily solved using a marching scheme. A 2-way marching algorithm then recovers the back-scattered field in an efficient manner. These modifications greatly reduce the computational requirements of the original fully-coupled formulation and paves the way for extending the method to mixed fluid-elastic stratifications. Several canonical propagation and reverberation problems are used to demonstrate the accuracy and versatility of the modified solution technique.

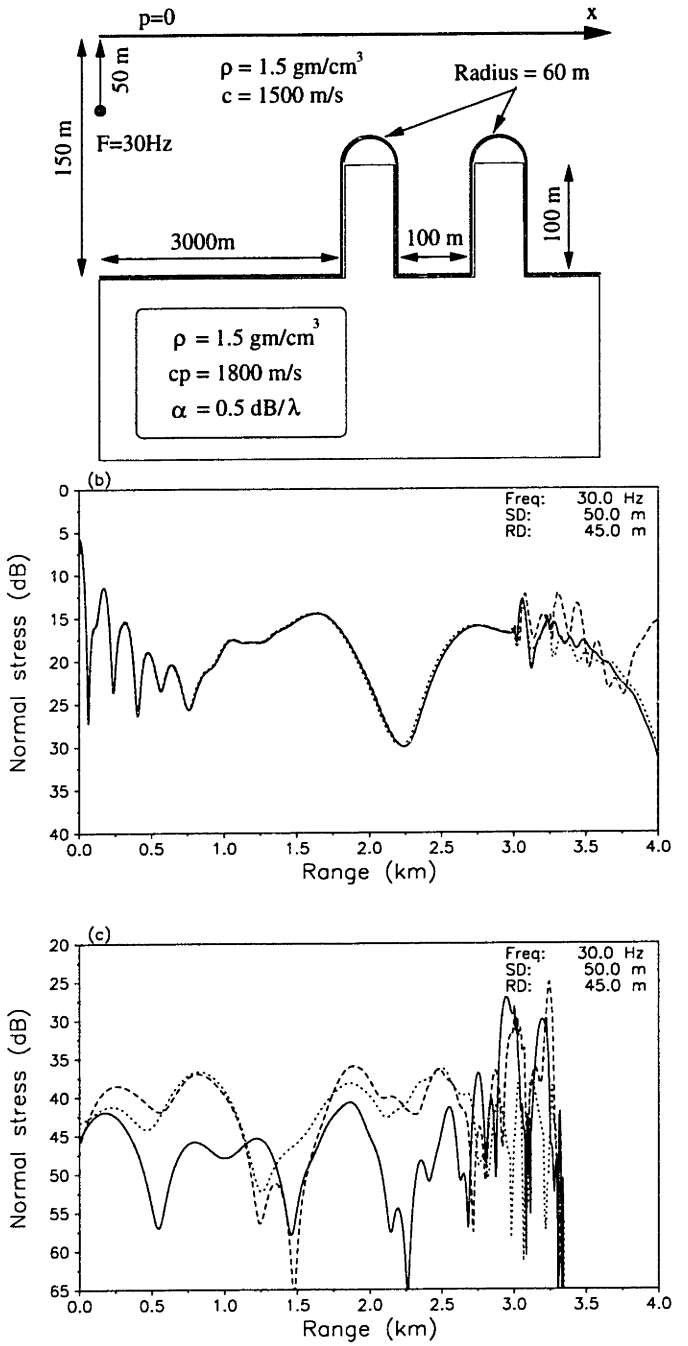

Figure 3-12: R & S Workshop Test 3b (Ex. I) : (a) Test geometry, (b) Forward normal stress, (c) Backscattered normal stress. Solid : COUPLE, Dashed : VISA, Dotted : Spectral super-element.

Chapter 4

Spectral Super-Element Approach for Elastic Media

4.1 Introduction

The modifications presented in the previous Chapter laid the groundwork for extending the method to include arbitrary fluid-elastic stratifications in a practical elastic code. Here, we present the theoretical development but we will depart from the previous notation and instead describes the approach in terms of symmetric and anti-symmetric source contributions.

4.2 Stratified Super-Elements

The equations of motion for a homogeneous isotropic elastic solid in plane strain are given by [45, 46]

$$(\lambda + 2\mu)\nabla\nabla \cdot \mathbf{u} - \mu\nabla \times \nabla \times \mathbf{u} + \rho\mathbf{f} = \rho\frac{\partial^2 \mathbf{u}}{\partial t^2} \quad , \tag{4.1}$$

where λ and μ are the Lamè constants, ρ is the density, $\mathbf{u} = (u, w)$ is the displacement vector and $\mathbf{f}$ is the body force per unit mass of material. We write the displacement vector in terms of two scalar potential fields, ϕ and ψ, i.e.,

$$\mathbf{u} = \nabla\phi + \nabla \times (0, \psi, 0), \tag{4.2}$$

where the first and second term represents the dilatational and rotational part of the solution respectively. These potentials are solutions of the scalar wave equations

$$\nabla^2\phi = \frac{1}{c_p^2}\frac{\partial^2\phi}{\partial t^2} \ , \qquad \nabla^2\psi = \frac{1}{c_s^2}\frac{\partial^2\psi}{\partial t^2} \ , \tag{4.3}$$

where c_p and c_s are the compressional and shear wave speeds respectively, and are given by

$$c_p^2 = \frac{\lambda + 2\mu}{\rho} \ , \ c_s^2 = \frac{\mu}{\rho} \ .$$

Assuming an $\exp(i\omega t)$ harmonic time dependence (suppressed henceforth), the potentials then also satisfy the following Helmholtz equations

$$\left(\nabla^2 + h^2\right)\phi = 0 \ , \qquad \left(\nabla^2 + \kappa^2\right)\psi = 0 \ ,$$

where $h = \omega/c_p$ and $\kappa = \omega/c_s$ denote the wavenumbers for the compressional and shear waves respectively.

The field in each sector is now expressed as a superposition of the field produced in the stratified element in the absence of the vertical boundaries, $\mathbf{u}^*$, the field arising from the left boundary $\mathbf{u}^-$, and the field arising from the right boundary, $\mathbf{u}^+$,

$$\mathbf{u}(x,z) = \mathbf{u}^*(x,z) + \mathbf{u}^-(x,z) + \mathbf{u}^+(x,z), \tag{4.4}$$

where $\mathbf{u}$ is taken to denote contributions from the potential ϕ and in the case of an elastic stratification, also includes contributions from ψ.

The wavefields are determined using an *indirect* boundary integral method [47], based on Green's theorem for the semi-infinite virtual element obtained by eliminating the other vertical boundary and letting the element continue to infinity,

$$\mathbf{u}_i^{\pm}(\mathbf{r}) = \int_{S^{\pm}} \left[G_{ji}(\mathbf{r};\mathbf{r}^{\pm})\, t_j(\mathbf{r};\mathbf{n}^{\pm}) - H_{ji}(\mathbf{r};\mathbf{r}^{\pm};\mathbf{n}^{\pm})\, u_j(\mathbf{r}) \right] dS^{\pm}. \tag{4.5}$$

Here $u_j(\mathbf{r})$ and $t_j(\mathbf{r};\mathbf{n}^{\pm})$ are the r_j components of the displacements and tractions on the boundary of the semi-infinite elements $S^{\pm}$. $G_{ji}(\mathbf{r},\mathbf{r}^{\pm})$ and $H_{ji}(\mathbf{r},\mathbf{r}^{\pm};\mathbf{n}^{\pm})$ are the jth components of the displacement and traction of the Green's functions at the point $\mathbf{r}$ on the surface $S^{\pm}$ with outgoing normal $\mathbf{n}^{\pm}$, due to a unit force applied in the ith direction at a point $\mathbf{r}^{\pm}$.

Note here, that the super-elements always have finite depth. Thus, in the presence of a lower halfspace, the lower boundary of the super-element is chosen deep enough into the halfspace to ensure that the field satisfies the radiation condition along the horizontal boundary, in which case the associated surface integral contribution vanishes.

To solve the integral equation in Eq. (4.5), we introduce both symmetric and antisymmetric panel sources at the boundary. A displacement formulation in combination with the Galerkin approach is then used to reduce the integral equation into a system of linear equations, the unknowns of which are the source strengths for the panel sources. Once these unknown source strengths are determined, the wavefield in each sector can be determined efficiently using Fast Field Program (FFP) techniques. As in the Direct Global Matrix (DGM) method, we express the field in each layer as a superposition of the field produced by the panel source within the layer in the absence of boundaries, referred to as the *direct* panel contribution $\hat{\mathbf{u}}$, and an unknown field $\bar{\mathbf{u}}$ which is necessary to satisfy the boundary conditions at the layer interfaces [1],

$$\mathbf{u} = \hat{\mathbf{u}} + \bar{\mathbf{u}}. \tag{4.6}$$

The latter field must satisfy the homogeneous equations of motion and is referred to as the *homogeneous* solution. In other words, they are the source-free waves that must be added to the direct panel contributions to satisfy the boundary conditions. The homogeneous field is governed by Eq. (4.1) with the body force term $\mathbf{f}$ equal to zero.

4.3 Field Expansion

The boundary conditions to be satisfied between the super-elements, together with Eq. (4.5) now provides an integral equation for the field $\mathbf{u}^{\pm}$ on the vertical boundaries of the super-element, the numerical solution of which requires some kind of discretization. For fluid super-elements, the boundary conditions are the continuity of pressure and particle displacement, i.e. at the vertical boundary j separating super-elements j and $j+1$,

$$\left\{ \begin{array}{c} u(x_j, z) \\ p(x_j, z) \end{array} \right\}^{j} = \left\{ \begin{array}{c} u(x_j, z) \\ p(x_j, z) \end{array} \right\}^{j+1}, \tag{4.7}$$

and for elastic super-elements, the boundary conditions are the continuity of stresses and displacements, i.e.,

$$\left\{ \begin{array}{c} u(x_j,z) \\ w(x_j,z) \\ \sigma_{xx}(x_j,z) \\ \sigma_{xz}(x_j,z) \end{array} \right\}^j = \left\{ \begin{array}{c} u(x_j,z) \\ w(x_j,z) \\ \sigma_{xx}(x_j,z) \\ \sigma_{xz}(x_j,z) \end{array} \right\}^{j+1} . \tag{4.8}$$

A superscript is used to identify the super-element here and in the following. Since the field within each layer in the stratification is a smooth function of depth, we here choose a *Galerkin boundary element* approach [1]. In the Galerkin approach, the continuity of the field across the vertical boundaries is expressed in the *weak form*

$$\int_0^{t_\ell} \mathbf{u}^j(x_j,z)[\mathbf{u}^{j+1}(x_j,z) - \mathbf{u}^j(x_j,z)]dz = 0 \,, \tag{4.9}$$

and similarly for the stresses. The displacements and stresses are now expressed as expansions in terms of a set of basis functions. By choosing an orthogonal set of expansion functions Eq. (4.9) requires the expansion coefficients in the two neighboring sectors to be identical. Here we choose an orthonormal set of Legendre polynomials, normalized within each layer ℓ:

$$\left\{ \begin{array}{c} u(x,z) \\ w(x,z) \\ \sigma_{xx}(x,z)/\mu \\ \sigma_{xz}(x,z)/\mu \end{array} \right\}^j = \frac{2\pi}{t_\ell} \sum_{m=1}^{\infty} \left\{ \begin{array}{c} \mathrm{U}_{\ell m}(x) \\ \mathrm{W}_{\ell m}(x) \\ \mathrm{T}_{\ell m}(x) \\ \mathrm{S}_{\ell m}(x) \end{array} \right\}^j P_{m-1}(\bar{z}) \tag{4.10}$$

where m is the order of expansion, P_m is the Legendre function and t_ℓ is the thickness of layer ℓ. The argument to the Legendre polynomial is the normalized, local depth coordinate

$$\bar{z} = \frac{z - t_\ell/2}{t_\ell/2}. \tag{4.11}$$

The expansion coefficients $\mathrm{U}_{\ell m}(x)$ through $\mathrm{S}_{\ell m}(x)$ are functions of $\mathrm{U}_{\ell m}(0)$ and $\mathrm{W}_{\ell m}(0)$, the unknown panel source strengths of the symmetric and antisymmetric source respectively. In effect, they are like the Green's functions for the panel sources. As outlined earlier, we decompose these Green's functions into two components: one corresponding to the direct field due to the panel source in the layer, the other corresponding to the reflections from the layer interfaces. We can then write the expansion coefficient $\mathrm{U}_{\ell m}(x)$ as

$$\mathrm{U}_{\ell m}(x) = \hat{\mathrm{U}}_{\ell m}(x) + \bar{\mathrm{U}}_{\ell m}(x), \tag{4.12}$$

where $\hat{\mathrm{U}}_{\ell m}(x)$ and $\bar{\mathrm{U}}_{\ell m}(x)$ denote the direct and homogeneous contributions respectively. The other coefficients can also be written in a similar manner. These expansion coefficients are used in the Galerkin scheme when solving the boundary integral equation. We first derive vertical wavenumber representations and subsequently these are transformed into wavenumber representations suitable for the DGM method. These latter forms are also useful for efficient computation of the resultant field.

4.4 Direct Panel Source Contribution

We start by defining the potentials for the panel sources. The compressional and shear displacement potentials which satisfy the Helmholtz equation and the radiation condition can be written in terms of vertical wavenumber spectral representation as

$$\begin{aligned} \phi_\ell(x,z) &= \int_{-\infty}^{\infty} A_\ell(\eta)\, e^{-x\gamma} e^{-i\eta(z-t_\ell/2)}\, d\eta, \\ \psi_\ell(x,z) &= \int_{-\infty}^{\infty} B_\ell(\eta)\, e^{-x\delta} e^{-i\eta(z-t_\ell/2)}\, d\eta, \end{aligned} \tag{4.13}$$

where η, $i\gamma = i\sqrt{\eta^2 - h^2}$ and $i\delta = i\sqrt{\eta^2 - \kappa^2}$ are the vertical and horizontal wavenumbers respectively. The quantities $A_\ell(\eta)$ and $B_\ell(\eta)$ are the source spectrums to be determined from boundary conditions at the vertical interface.

4.4.1 The Symmetric Problem

The symmetric problem is characterized by two conditions at the discontinuity ($x = 0$),

$$\begin{aligned} \sigma_{xz}(0,z)/\mu &= \frac{\partial u}{\partial z} + \frac{\partial w}{\partial x} \\ &= 0, \end{aligned} \tag{4.14}$$

$$\begin{aligned} u(0,z) &= \frac{\partial \phi}{\partial x} - \frac{\partial \psi}{\partial z}, \\ &= \begin{cases} \frac{2\pi}{t_\ell} \sum_{m=1}^{\infty} \mathrm{U}_{\ell m}(0) P_{m-1}(\tilde{z}), & 0 \le z \le t_\ell \\ 0. & \text{otherwise} \end{cases} \end{aligned} \tag{4.15}$$

Substitution of Eq. (4.13) into Eq. (4.15) yields a relationship between $\mathrm{U}_{\ell m}(0)$ and $A_\ell(\eta)$ and subsequently Eq. (4.15) becomes,

$$\begin{aligned} u(0,z) &= \int_{-\infty}^{\infty} \frac{\gamma\kappa^2}{\varphi}\, A_\ell^{(1)}(\eta)\, e^{i\eta t_\ell/2}\, e^{-i\eta z}\, d\eta, \\ &= \frac{2\pi}{t_\ell} \sum_{m=1}^{\infty} \mathrm{U}_{\ell m}(0) P_{m-1}(\bar{z}), \end{aligned} \tag{4.16}$$

where $\varphi = 2\eta^2 - \kappa^2$. We define the Fourier transform pair as

$$\begin{aligned} f(z) &= \int_{-\infty}^{\infty} g(\eta) e^{-i\eta z}\, d\eta, \\ g(\eta) &= \frac{1}{2\pi} \int_{-\infty}^{\infty} f(z) e^{i\eta z}\, dz, \end{aligned} \tag{4.17}$$

and taking the forward transform with respect to z of Eq. (4.16), we obtain,

$$\frac{\gamma\kappa^2}{\varphi}\, A_\ell^{(1)}(\eta)\, e^{i\eta t_\ell/2} = \frac{1}{t_\ell} \sum_{m=1}^{\infty} \mathrm{U}_{\ell m}(0) \int_0^{t_\ell} P_{m-1}(\bar{z}) e^{i\eta z}\, dz. \tag{4.18}$$

Making use of the relation [41],

$$\int_0^{t_\ell} P_{m-1}(\bar{z}) e^{i\eta z}\, dz = t_\ell\, e^{i\eta \frac{t_\ell}{2}}\, i^{m-1}\, j_{m-1}\left(\frac{t_\ell \eta}{2}\right), \tag{4.19}$$

where j_{m-1} is the spherical Bessel function, we obtain for the symmetric part of the source spectrum $A_\ell(\eta)$,

$$A_\ell^{(1)}(\eta) = \frac{\varphi}{\kappa^2\gamma} \sum_{m=1}^{\infty} \mathrm{U}_{\ell m}(0) i^{m-1} j_{m-1}\left(\frac{t_\ell \eta}{2}\right). \tag{4.20}$$

Substitution of the above into Eq. (4.14) yields,

$$B_\ell^{(1)}(\eta) = -\frac{2i\eta}{\kappa^2} \sum_{m=1}^{\infty} \mathrm{U}_{\ell m}(0) i^{m-1} j_{m-1}\left(\frac{t_\ell \eta}{2}\right). \tag{4.21}$$

4.4.2 The Antisymmetric Problem

The antisymmetric problem is similarly characterized by two conditions at the discontinuity,

$$\sigma_{xx}(0,z)/\mu = \left(\frac{\lambda + 2\mu}{\mu}\right) \frac{\partial u}{\partial x} + \frac{\lambda}{\mu} \frac{\partial w}{\partial z} = 0, \tag{4.22}$$

$$\begin{aligned} w(0,z) &= \frac{\partial \phi}{\partial z} + \frac{\partial \psi}{\partial x}, \\ &= \begin{cases} \frac{2\pi}{t_\ell} \sum_{m=1}^{\infty} \mathrm{W}_{\ell m}(0) P_{m-1}(\bar{z}), & 0 \le z \le t_\ell \\ 0. & \text{otherwise} \end{cases} \end{aligned} \tag{4.23}$$

After some algebra we obtain the antisymmetric part of the source spectrum as,

$$A_\ell^{(2)}(\eta) = \frac{2i\eta}{\kappa^2}\sum_{m=1}^{\infty} \mathrm{W}_{\ell m}(0) i^{m-1} j_{m-1}\left(\frac{t_\ell \eta}{2}\right), \tag{4.24}$$

$$B_\ell^{(2)}(\eta) = \frac{\varphi}{\kappa^2\delta}\sum_{m=1}^{\infty} \mathrm{W}_{\ell m}(0) i^{m-1} j_{m-1}\left(\frac{t_\ell \eta}{2}\right). \tag{4.25}$$

4.4.3 Series Representations

The unknown panel source strengths $\mathrm{U}_{\ell m}(0)$ and $\mathrm{W}_{\ell m}(0)$ are now determined through matching the relevant boundary conditions at the vertical cut. We do this by the Galerkin boundary element approach which simply requires that the expansion coefficients in the two neighbouring sectors be identical. These expansion coefficients can be straight-forwardly extracted from the potential representations above by using the orthogonality relation for the Legendre polynomials. In practice, we need to truncate the infinite series expansions at a sufficiently high order. Since the Legendre polynomials represent the vertical variation in the field, one can obtain the truncation limit from an estimate of the number of normal modes.

Let us consider the coefficient $\hat{\mathrm{U}}_{\ell k}(x)$,

$$u_\ell(x,z) = \frac{2\pi}{t_\ell}\sum_{k=1}^{\infty} \hat{\mathrm{U}}_{\ell k}(x)\, P_{k-1}(\bar{z}). \tag{4.26}$$

We first multiply both sides of Eq. (4.26) by $P_{m-1}(\bar{z})$. Integrating over the layer thickness and using the orthogonality properties of Legendre polynomials,

$$\int_0^{t_\ell} P_{m-1}(\bar{z})\, P_{k-1}(\bar{z})\, dz = \begin{cases} \frac{t_\ell}{2m-1} & m = k \\ 0 & m \neq k \end{cases} \tag{4.27}$$

together with the identity,

$$\int_0^{t_\ell} P_{m-1}(\bar{z})\, e^{-i\eta z}\, dz = t_\ell\, e^{-i\eta\frac{t_\ell}{2}} i^{m-1}\, (-1)^{m-1}\, j_{m-1}\left(\frac{t_\ell \eta}{2}\right), \tag{4.28}$$

and the expressions for the source spectrums derived previously, we obtain

$$\hat{\mathrm{U}}_{\ell m}(x) = C_m \sum_{k=1}^{\infty} i^{m+k-2} \int_{-\infty}^{\infty} d\eta \left\{ \left[-\frac{\varphi}{\kappa^2} e^{-x\gamma} + \frac{2\eta^2}{\kappa^2} e^{-x\delta} \right] \mathrm{U}_{\ell k}(0) \right.$$
$$\left. + \left[-\frac{2i\eta\gamma}{\kappa^2} e^{-x\gamma} + \frac{i\eta\varphi}{\kappa^2\delta} e^{-x\delta} \right] \mathrm{W}_{\ell k}(0) \right\} j_{m-1}\left(\frac{t_\ell \eta}{2}\right) j_{k-1}\left(\frac{t_\ell \eta}{2}\right), \tag{4.29}$$

where $C_m = (2m-1)\zeta_m t_\ell/(2\pi)$ and $\zeta_m = (-1)^{m-1}$. Expansion coefficients for the other field parameters can be obtained in a similar fashion and are summarized in Appendix C. When evaluating these integrals, we can exploit their symmetries in (m,k) to reduce the amount of computation. In addition, for $x = 0$, some of the integrals can be evaluated in closed-form. In Appendix H, we discuss some of the numerical issues involved in evaluating these integrals.

4.4.4 Horizontal Wavenumber Representations

The displacement potentials in the vertical wavenumber domain are

$$\begin{aligned}
\phi_\ell(x,z) &= \int_{-\infty}^{\infty} \left[\frac{\varphi}{\kappa^2\gamma}\,\Gamma(\eta) + \frac{2i\eta}{\kappa^2}\,\Theta(\eta) \right] e^{-x\gamma} e^{-i\eta(z-t_\ell/2)}\, d\eta, \\
\psi_\ell(x,z) &= \int_{-\infty}^{\infty} \left[-\frac{2i\eta}{\kappa^2}\,\Gamma(\eta) + \frac{\varphi}{\kappa^2\delta}\,\Theta(\eta) \right] e^{-x\delta} e^{-i\eta(z-t_\ell/2)}\, d\eta,
\end{aligned} \tag{4.30}$$

where

$$\begin{aligned}
\Gamma(\eta) &= \sum_{m=1}^{\infty} \mathrm{U}_{\ell m}(0)\, i^{m-1}\, j_{m-1}\!\left(\frac{t_\ell \eta}{2}\right), \\
\Theta(\eta) &= \sum_{m=1}^{\infty} \mathrm{W}_{\ell m}(0)\, i^{m-1}\, j_{m-1}\!\left(\frac{t_\ell \eta}{2}\right).
\end{aligned} \tag{4.31}$$

The DGM method for the multi-layered sector requires the integral representations for the free-space Green's function to be expressed in terms of the horizontal wavenumber, s. Using contour integration as devised by Heelan [40], the vertical wavenumber integrals of Eq. (4.30) are converted into horizontal wavenumber integrals. After some algebra, the potentials in the $s-$domain become

$$\begin{aligned}
\phi_\ell(x,z) &= \int_{-\infty}^{\infty} \left[-\frac{\vartheta}{s\kappa^2}\,\Gamma(-i\mathcal{S}\alpha) + \frac{2i\mathcal{S}\alpha}{\kappa^2}\,\Theta(-i\mathcal{S}\alpha) \right] e^{-|z-\frac{t_\ell}{2}|\alpha}\, \frac{s}{\alpha}\, e^{-ixs}\, ds, \\
\psi_\ell(x,z) &= \int_{-\infty}^{\infty} \left[-\frac{2i\mathcal{S}\beta}{\kappa^2}\,\Gamma(-i\mathcal{S}\beta) - \frac{\varpi}{s\kappa^2}\,\Theta(-i\mathcal{S}\beta) \right] e^{-|z-\frac{t_\ell}{2}|\beta}\, \frac{s}{\beta}\, e^{-ixs}\, ds,
\end{aligned} \tag{4.32}$$

where

$$\begin{aligned}
\mathcal{S} &= \mathrm{sign}(z - t_\ell/2), \\
i\alpha &= \sqrt{h^2 - s^2}, \\
i\beta &= \sqrt{\kappa^2 - s^2}, \\
\vartheta &= 2\alpha^2 + \kappa^2, \\
\varpi &= 2s^2 - \kappa^2,
\end{aligned}$$

and Γ and Θ are given by Eq. (4.31). The potentials given by Eq. (4.32) are valid only for $z \leq 0$ and $z \geq t_\ell$, but still allows for the application of the global matrix method when satisfying the horizontal interface boundary conditions since it is at the interfaces $z = 0$ and $z = t_\ell$ of each layer that the fields are being matched. However, it is desirable to have a horizontal wavenumber integral representation that is valid within the layer so that efficient FFP techniques can be employed for the resulting field computation. In Appendix B we derive a discretized equivalent point source horizontal wavenumber representation for these potentials that is valid for $0 \leq z \leq t_\ell$.

We now simply use Eq. (4.32) as the source contribution in the SAFARI code [16] to determine the associated homogeneous solution, the expansions of which are described in the next section.

4.5 Homogeneous Solution

The horizontal wavenumber integral representation for the homogeneous solution can be obtained by a direct extension of the equations presented in Schmidt and Jensen [48]. The complete homogeneous solution is given by the sum over all finite layers as well as over all orders of expansion. Using the orthogonality relation of Legendre polynomials, expansion coefficients can be extracted as

$$\bar{\mathbf{V}}_{\ell m}(x) = (2m-1)i^{m-1} \int_{-\infty}^{\infty} \sum_{n=2}^{N-1} \sum_{k=1}^{\infty} \bar{\mathbf{K}}_\ell \; \bar{\mathbf{E}}_\ell \; \bar{\mathbf{J}}_{\ell m} \times [\, \mathrm{U}_{nk}(0) \; \bar{\mathbf{A}}_{\ell,nk} \; + \; \mathrm{W}_{nk}(0) \; \bar{\mathbf{C}}_{\ell,nk} \,] \, e^{-ixs} \, ds, \tag{4.33}$$

where

$$\bar{\mathbf{V}}_{\ell m}(x) = \left[\begin{array}{cccc} \bar{\mathrm{U}}_{\ell m} & \bar{\mathrm{W}}_{\ell m} & \bar{\mathrm{T}}_{\ell m} & \bar{\mathrm{S}}_{\ell m} \end{array} \right]^T,$$

$$\bar{\mathbf{K}}_\ell = \left[\begin{array}{cccc} -is & -is & i\beta & -i\beta \\ -\alpha & \alpha & s & s \\ -\vartheta & -\vartheta & 2s\beta & -2s\beta \\ 2is\alpha & -2is\alpha & -i\varpi & -i\varpi \end{array} \right],$$

$$
\begin{aligned}
\bar{\mathbf{E}}_\ell &= \mathrm{diag}\left[e^{-\frac{t_\ell}{2}\alpha}, e^{-\frac{t_\ell}{2}\alpha}, e^{-\frac{t_\ell}{2}\beta}, e^{-\frac{t_\ell}{2}\beta}\right], \\
\bar{\mathbf{A}}_{\ell,nk} &= \left[\begin{array}{cccc} A^-_{\ell,nk} & A^+_{\ell,nk} & B^-_{\ell,nk} & B^+_{\ell,nk} \end{array}\right]^T, \\
\bar{\mathbf{C}}_{\ell,nk} &= \left[\begin{array}{cccc} C^-_{\ell,nk} & C^+_{\ell,nk} & D^-_{\ell,nk} & D^+_{\ell,nk} \end{array}\right]^T, \\
\bar{\mathbf{J}}_{\ell m} &= \mathrm{diag}\left[j_{m-1}\left(\frac{it_\ell\alpha}{2}\right), \zeta_m j_{m-1}\left(\frac{it_\ell\alpha}{2}\right), j_{m-1}\left(\frac{it_\ell\beta}{2}\right), \zeta_m j_{m-1}\left(\frac{it_\ell\beta}{2}\right)\right].
\end{aligned}
$$

Each combination of indices n and k represents a single SAFARI run. Here $A^{\mp}_{\ell,nk}$ and $B^{\mp}_{\ell,nk}$ are respectively the up/down going compressional and shear waves in layer ℓ due to the kth order *symmetric* source in layer n. The corresponding quantities from the *antisymmetric* source are $C^{\mp}_{\ell,nk}$ and $D^{\mp}_{\ell,nk}$. However, the DGM can treat multiple right-hand sides simultaneously and hence all the amplitudes of the up/down going waves can be found with just a single global matrix inversion. This makes the algorithm very efficient even for problems with a large number of layers and high orders of expansion. In addition, we can make use of the symmetries in the amplitudes of these up/down traveling waves to reduce the computation to only the positive spectrum. In particular, the free-waves of the symmetric panel source exhibit the following symmetry,

$$
\begin{aligned}
A^{\pm}_{\ell,nk}(-s) &= A^{\pm}_{\ell,nk}(s), \\
B^{\pm}_{\ell,nk}(-s) &= -B^{\pm}_{\ell,nk}(s).
\end{aligned} \tag{4.34}
$$

For the antisymmetric source we have,

$$
\begin{aligned}
C^{\pm}_{\ell,nk}(-s) &= -C^{\pm}_{\ell,nk}(s), \\
D^{\pm}_{\ell,nk}(-s) &= D^{\pm}_{\ell,nk}(s).
\end{aligned} \tag{4.35}
$$

Note that further simplifications can be easily derived from the above relations when $x = 0$.

4.6 Element Connectivity

Inserting the field expansions in Eq. (4.10) into the weak form of the boundary conditions in Eq. (4.9) leads to the *connectivity* equations between super-elements j and $j+1$. The number

of equations for each layer depends on the number of expansion terms used as well as the type of media in super-elements j and $j+1$. In general, the connectivity equations are

$$\left\{ \begin{array}{c} \mathrm{U}_{\ell m}(x_j) \\ \mathrm{W}_{\ell m}(x_j) \\ \mathrm{T}_{\ell m}(x_j) \\ \mathrm{S}_{\ell m}(x_j) \end{array} \right\}^{j} = \left\{ \begin{array}{c} \mathrm{U}_{\ell m}(x_j) \\ \mathrm{W}_{\ell m}(x_j) \\ \mathrm{T}_{\ell m}(x_j) \\ \mathrm{S}_{\ell m}(x_j) \end{array} \right\}^{j+1}, \quad \begin{array}{l} \ell = 1, \ldots N, \\ m = 1, \ldots M. \end{array} \tag{4.36}$$

Here N is the number of layers, and M is the number of expansion terms used within each layer. By systematically matching boundary conditions along the vertical cut, we obtain a linear system of equations for the unknown *panel source strengths* for super-elements j and $j+1$. Once the unknown source strengths are determined, the resulting field can then be determined efficiently with DGM using the horizontal wavenumber spectral representations. The reader is referred to Sec. 3.6.2 for a discussion on implementing an efficient marching algorithm from the system of connectivity equations.

4.7 Summary

We have proposed a new approach to model the range-dependent elastic ocean environment. The proposed method is not limited to weak range dependence and is capable of dealing with both short and long range propagation. Exact seismo-acoustic boundary conditions are satisfied at both the horizontal and vertical interfaces and the method should be able to handle large contrasts in the primary direction of propagation. In Chapter 5, we put the code through an exhaustive series of tests and benchmark problems. In the course of developing this model, we have also derived an alternative formulation based on Chebyshev polynomials. Even though this is never implemented, some of the derivations are quite interesting and the interested reader is referred to Appendix K for a complete description.

Chapter 5

The Elastic Benchmarks

The subject of quality assessment of numerical codes is an important one. The approach we choose to benchmark and validate our code can best be summed up by a comment made by Finn Jensen at the 112th Acoustical Society Meeting in Anaheim, CA, in 1986 and I quote,

> ... *While it is easy for anybody to produce "interesting" field solutions with a model, it is extremely difficult even for experts to generate numerical results that can be considered an accurate solution to a stated (propagation) problem. This difficulty derives from insufficient knowledge both of the approximations introduced to formulate a solvable set of equations, and of the accuracy and convergence problems associated with the numerical implementation itself. Excluding experimental data, there are in principle only two ways to gain confidence in the numerical result (even if reciprocity and energy conservation checks have been made): (1) Use a different model to confirm the validity of the original solution; or (2) Compare the numerical result with an accepted reference solution to a similar propagation problem. Currently, the* **intermodel comparison** *is the only route..."*

It is interesting to note that after almost a decade, the intermodel comparison method still remains as the only viable method to test and validate new formulations or modeling approaches. In this chapter, we developed a series of benchmarks aimed at testing the present formulation. These benchmarks are derived from several sources. Some are new and some

are modified examples taken from the existing literature. These benchmarks serve help to test and validate many aspects of our formulation and code, particularly its correctness and robustness. They are also useful as common yardsticks when making inter-model comparisons. Our solutions were obtained with a boundary element code by Gerstoft and Schmidt [22], the virtual source algorithm (VISA) by Schmidt [24], a finite element parabolic equation code by Collins [13] and the spectral super-element code [49]. Unless otherwise noted, the spectral super-element solutions are obtained using only four orders of expansion in the field parameters within each layer. In addition, in each of the examples, we take the water column to be lossless with a sound speed of 1500 m/s and a density of 1 g/cm^3.

5.1 Benchmark Problems

5.1.1 A : Modified NORDA Case 3

Example A is based on case 3A used in the NORDA Parabolic Equation Workshop [50]. This problem was first modified for use as a test case for elastic PE by Wetton and Brooke [11] and we run a slightly different version here. The waveguide, illustrated in Fig. 5-1(a), consists of a water layer with a thickness of 100 m, over a solid layer with a thickness of 100 m, a density of 1.2 g/cm^3, a compressional speed of 1590 m/s, and a shear speed of 500 m/s. The fluid is assumed to be lossless and the solid has a compressional attenuation of 0.2dB/λ and a shear attenuation of 0.5 dB/λ. A 25-Hz line source is placed at a distance of 5 km from an artificial transparent interface. The primary test here is to see how well energy is coupled through a transparent vertical interface and represents the extreme case of a low-contrast vertical step. Comparisons between SAFARI and our solutions for receiver depths of 50 and 110 m are shown in Fig. 5-1(b) and Fig. 5-1(c). For clarity we have shown the solution from 2 to 8 km and we see that the super-element solution agrees well with SAFARI. For ranges less than 5 km, the super-element formulation reduces to SAFARI exactly and we see perfect agreement in the solutions. For ranges beyond the artificial interface, the agreement is still quite good for both receivers, indicating proper coupling across the interface.

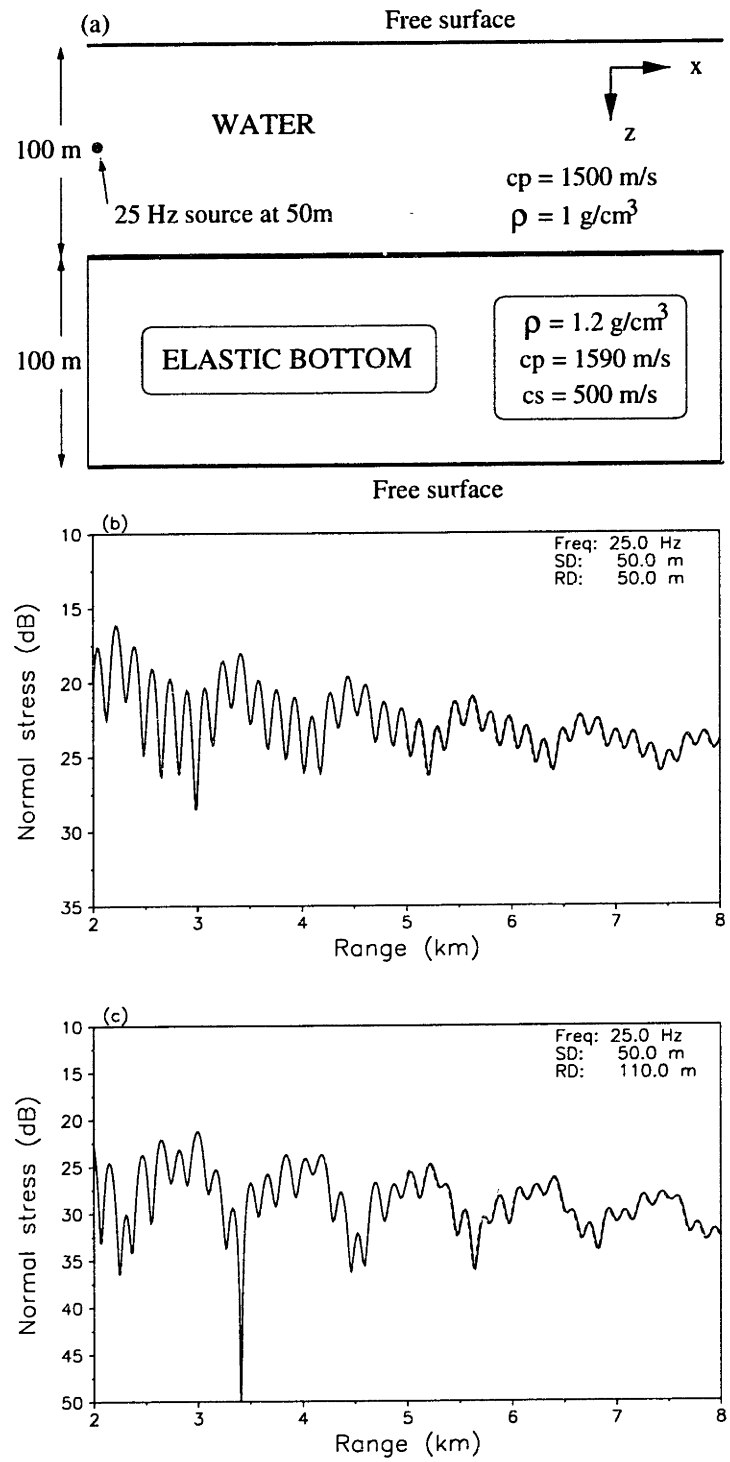

Figure 5-1: Modified NORDA 3A test case (Ex. A). (a) Test configuration, (b) Receiver at 50 m, (c) Receiver at 110 m. Solid : SAFARI, Dashed : Spectral super-element.

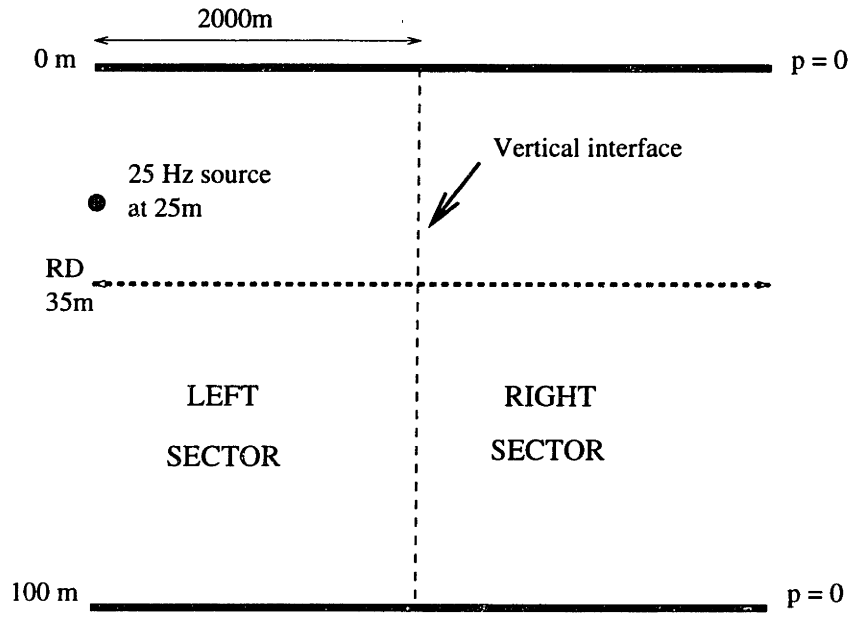

Figure 5-2: Ex. B. Configuration for single layer benchmarks

5.1.2 B : Single Layer Benchmarks

The next benchmark consists of a set of 2-sector problems shown in Fig. 5-2. The waveguide is bounded at the top and bottom by a pressure release boundary. A 25-Hz line source is placed at a depth of 25 m and at a distance of 2 km from the vertical discontinuity. By bounding the waveguide by pressure release boundaries, this benchmark requires the propagation code to properly conserve energy before one can arrive at the correct answer. In addition, by varying the material properties on both sides of the discontinuity, we can assess the sensitivity of a particular code to contrast in the primary direction of propagation. Table 5.1 shows the 4 different configurations that we have chosen.

The BEM code [22] is expected to produce good results for this set of benchmarks and is therefore taken as the reference solution. Solutions for the normal stress at a receiver depth of 35 m are shown in Fig. 5-3 and Fig. 5-4 and we generally have good agreement among the three solutions. We present the backscatter solutions in Fig. 5-5.

	Parameters	BENCHMARK			
		B1	B2	B3	B4
Left sector	ρ	1.0	1.5	1.5	1.5
	c_p	1500	1700	1700	1700
	c_s	0	700	700	700
	α_p	0.2	0.2	0.2	0.2
	α_s	0	0.5	0.5	0.5
Right sector	ρ	1.5	1.0	1.5	1.5
	c_p	1700	1500	1700	1800
	c_s	700	0	700	900
	α_p	0.2	0.2	0.2	0.2
	α_s	0.5	0.5	0.5	0.5

Table 5.1: Parameters for the series of 2-sector canonical test problems. Wave speeds are given in m/s, densities in g/cm^3, and attenuation in dB/λ.

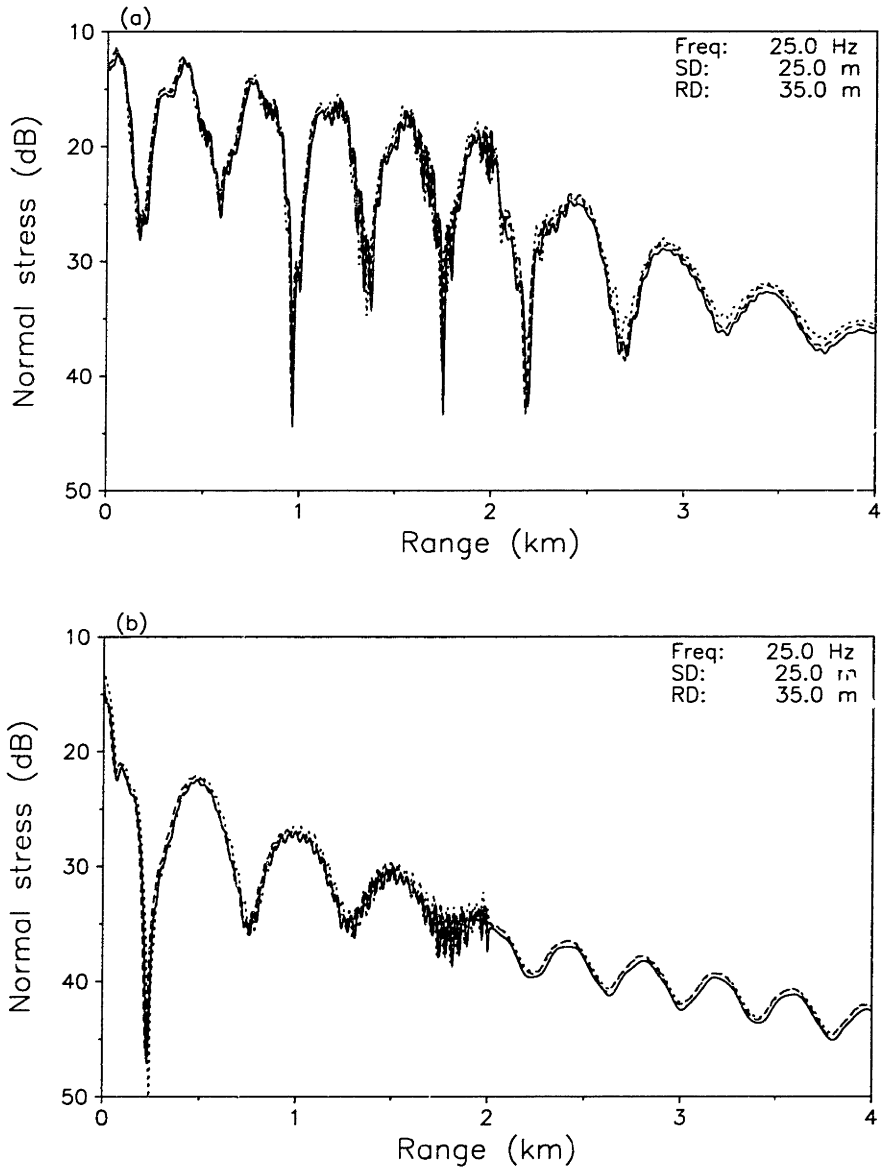

Figure 5-3: Solutions to the single layer benchmarks. (a) Case B1, (b) Case B2, Solid : BEM, Dashed : VISA, Dotted: Spectral super-element.

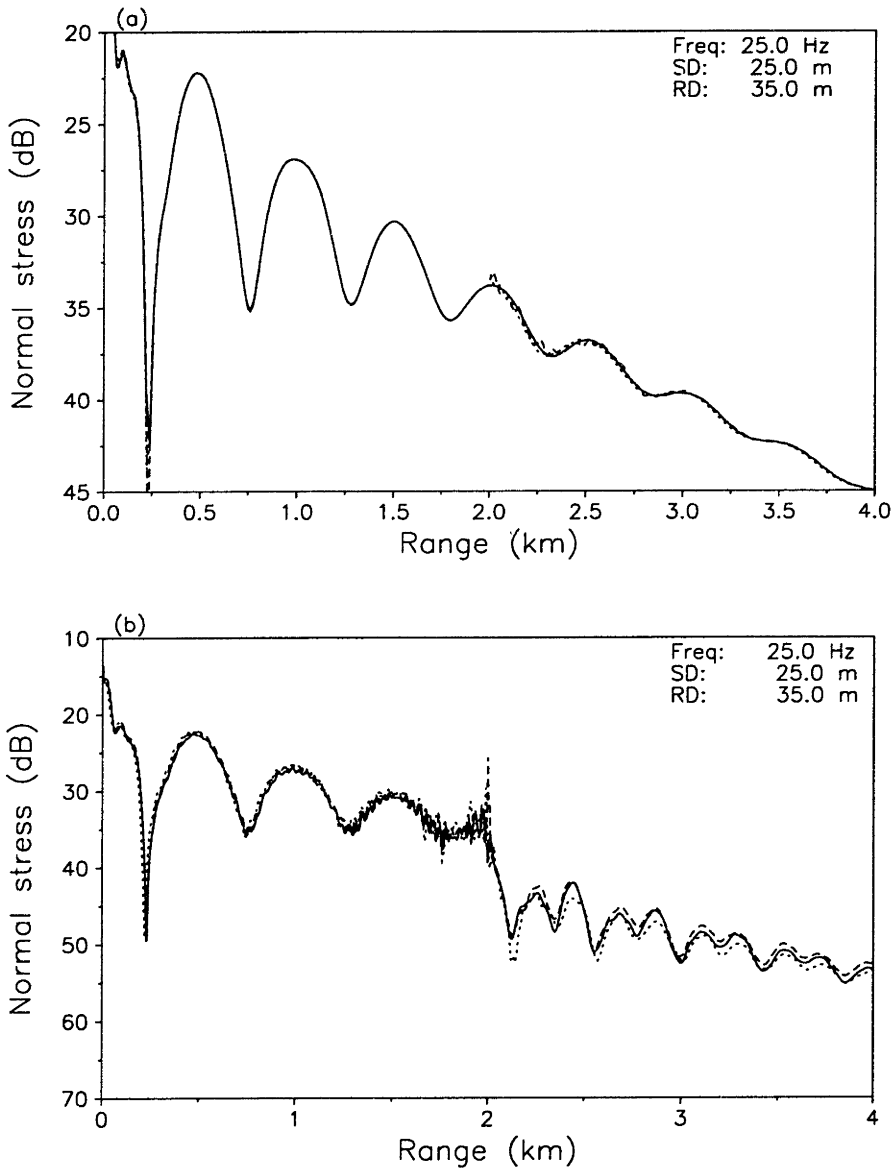

Figure 5-4: Solutions to the single layer benchmarks. (a) Case B3, (b) B4, Solid : BEM, Dashed : VISA, Dotted: Spectral super-element. For (a), instead of the BEM, we use SAFARI as the reference solution

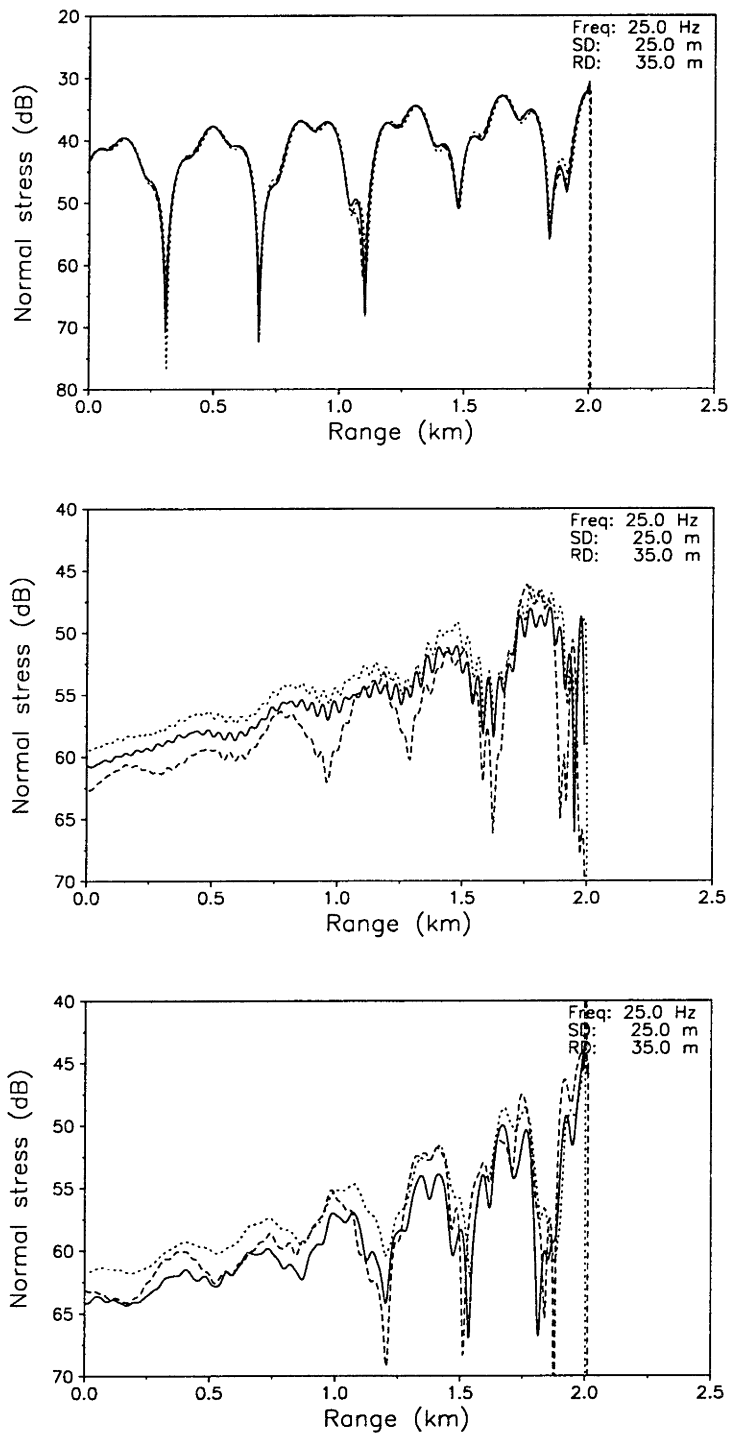

Figure 5-5: Backscatter solutions to the single layer benchmarks. (a) Case B1, (b) B2, (c) B4, Solid : BEM, Dashed : VISA, Dotted: Spectral super-element.

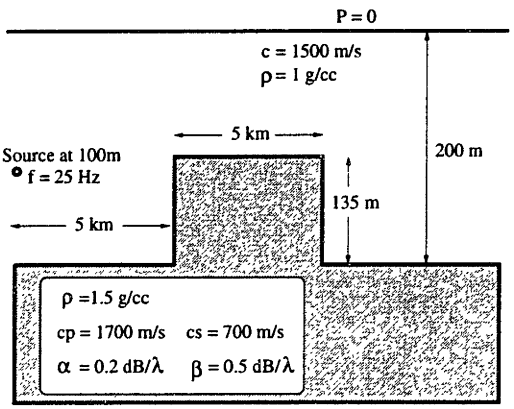

Figure 5-6: Ex. C : Schematic of the elastic cylindrical seamount

5.1.3 C : Elastic Cylindrical Seamount

Example C, shown in Fig. 5-6, consider an elastic seamount in a cylindrically symmetric ocean environment. The fluid version of this problem first appeared in Gilbert and Evans [19]. A 25-Hz source is located in the middle of the waveguide. The depth of the water column at the source range is 200 m. A 135 m high seamount has inner radius 5 km and outer radius 10 km. The bottom is a homogeneous half-space with a compressional sound speed of 1700 m/s and a shear speed of 700 m/s. The density is $1.5\,\mathrm{g/cm^3}$ and the compressional and shear attenuation in the bottom is 0.2 dB/λ and 0.5 dB/λ respectively. We solved this problem using only 3 range sectors and 8 layers down to a depth of 400 m. We show both forward and back-scattered dilatational and shear stress at a receiver depth of 80 m. Comparisons between the virtual source algorithm and the super-element method are shown in Fig. 5-7 and 5-8. In forward scatter, we have excellent agreement between the two solutions. There is also good agreement in the back-scatter solutions. The increase in back-scatter energy at the source range in Fig. 5-8(a) is due to the fact that for a point source in a cylindrically symmetric waveguide the back-scattered energy focuses at the source range. The high-frequency oscillations seen in the back-scatter VISA solution are due to numerical noise creeping into the extremely low field values computed.

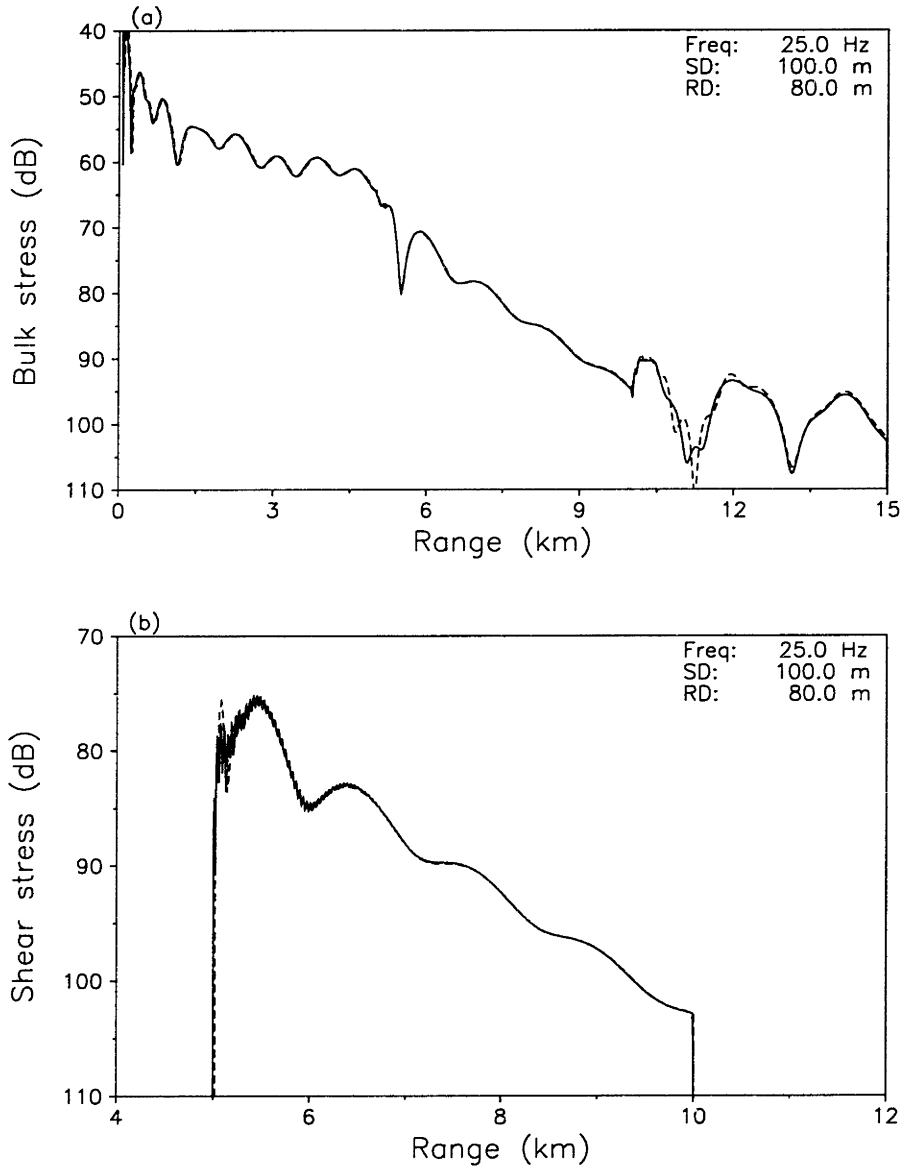

Figure 5-7: Elastic cylindrical seamount (Ex. C). Receiver at 80 m. (a) Forward scattered bulk stress, (b) Forward scattered shear stress. Solid - VISA; dashed - Spectral super-element.

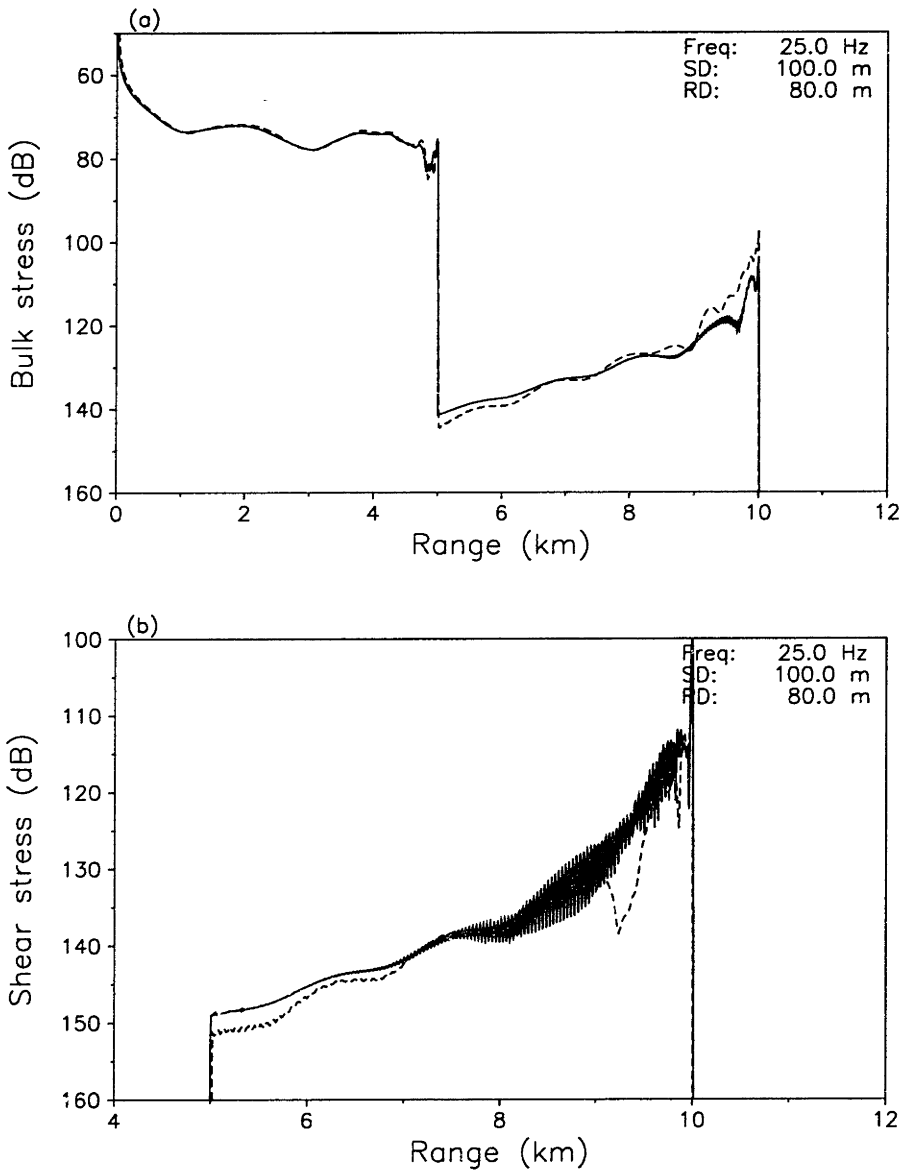

Figure 5-8: Elastic cylindrical seamount (Ex. C). Receiver at 80 m. (a) Back scattered bulk stress, (b) Back scattered shear stress. Solid - VISA; dashed - Spectral super-element.

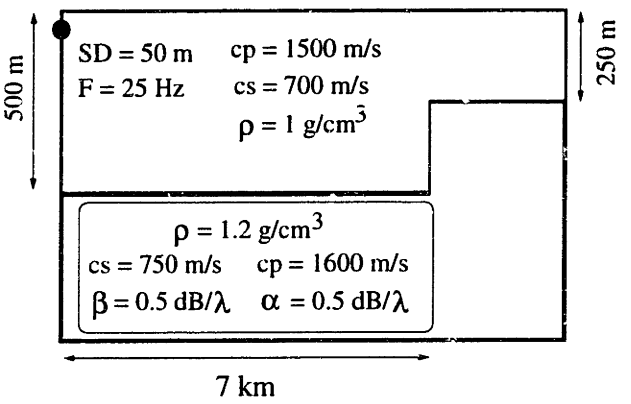

Figure 5-9: Ex. D : Embedded step discontinuity

5.1.4 D : Low Contrast Embedded Elastic Step

Example D, taken from Collins [12] and shown in Fig. 5-9 involves two solid layers and a step discontinuity in layer thickness. A 25-Hz source is placed at a depth of 50 m in the upper layer, which is 500 m thick for ranges less than 7 km and 250 m for ranges beyond 7 km. The compressional and shear speeds in the upper layer is 1500 m/s and 700 m/s respectively and the medium is assumed to be lossless. The lower layer is a half-space with compressional and shear speeds equal to 1600 m/s and 750 m/s respectively. The attenuations in the lower medium is 0.5 dB/λ for both wave types. The density in the upper and lower medium is $1\,g/cm^3$ and $1.2\,g/cm^3$ respectively. This particular problem has a very low contrast across the vertical interface and we present forward and back-scatter solutions at two receiver depths. In the forward direction, we have good agreement between the three solutions.

In the back-scatter, there is some disagreement, particularly near the scattering surface. We believed this is due to inaccuracies associated with the large dynamic range between the forward and back-scattered field.

5.1.5 E : High Contrast Embedded Elastic Step

Current PE-based formulations converges only for small differences across the vertical interfaces between the range-independent regions. Therefore, it is interesting to test the performance of a model under high contrast conditions and we have constructed Example E which

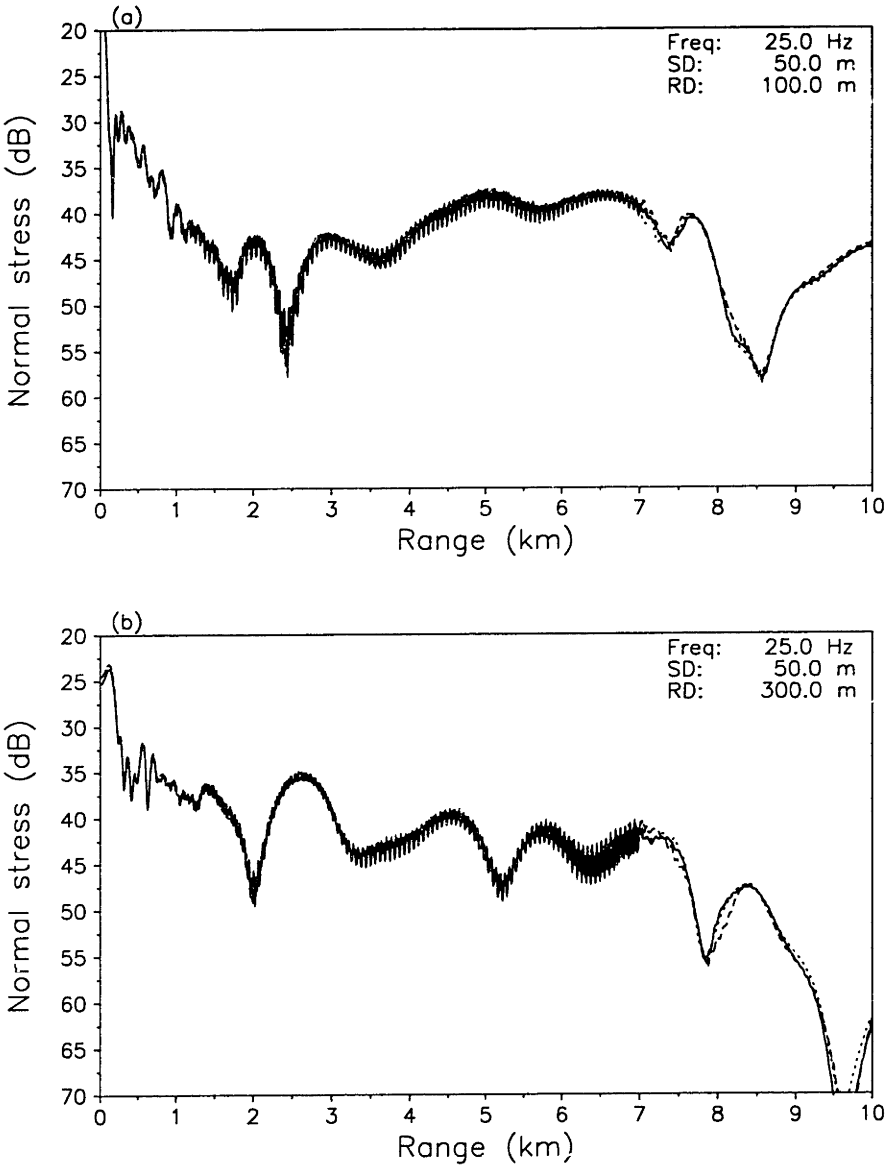

Figure 5-10: Embedded elastic step (Ex. D). Total normal stress. (a) Receiver at 100 m. (b) Receiver at 300 m. Solid - BEM; Dashed - VISA; Dotted - Spectral super-element.

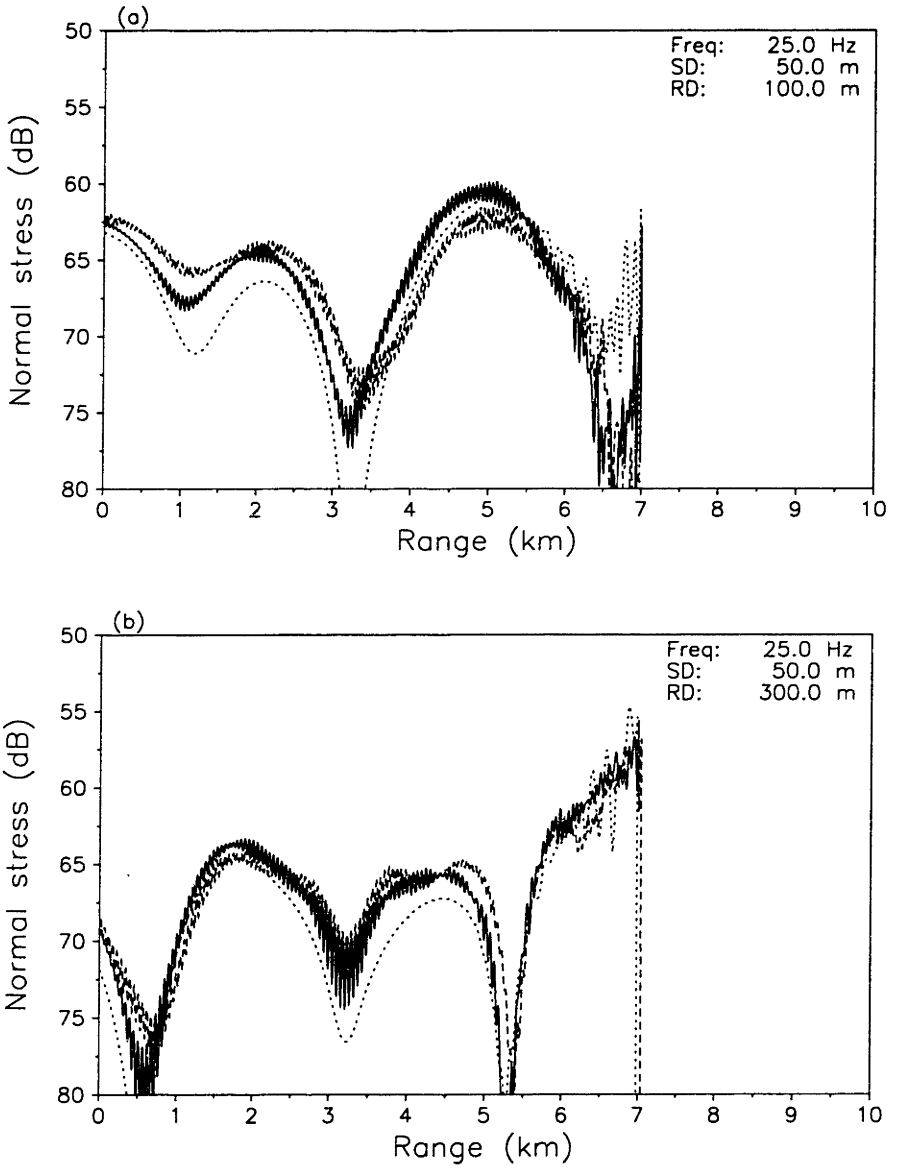

Figure 5-11: Embedded elastic step (Ex. D). Back scattered normal stress solution. (a) Receiver at 100 m. (b) Receiver at 300 m. Solid - BEM; Dashed - VISA; Dotted - Spectral super-element.

is essentially a high contrast version of Example D. The lower layer now has a compressional speed of 2000 m/s and a shear speed of 1200 m/s. It is hoped that the stronger back-scatter field might help eliminate differences due to the numerics. Again in Fig. 5-12 we see good agreement in the forward direction between the three different solutions. There is also good qualitative agreement in the back scatter.

5.1.6 F : Impedance Change at a Vertical Boundary

The issue of how well a particular formulation handles the dynamic range in a problem is an interesting one. An algorithm that performs well when there is a strong contrast in the vertical direction does not necessarily implies that it will work well at low contrasts. In Example F, we design a simple fluid test case to examine the behaviour of the code under changes of impedance across the vertical cut. We employ the 2-sector waveguide configuration of Example B and starting from a low-contrast problem, we systematically increase the sound speed in the right sector. Since all the other parameters in the problem remain the same, we should see the back-scattered field increasing in a way proportional to the impedance change at the vertical boundary. If a formulation is unable to handle large dynamic ranges in the field values, we will observe that the calculated field is insensitive to small changes in the sound speed. The left sector has a nominal sound speed of 1500 m/s and we systematically doubles the sound speed difference between the left and right sector from 0.625 m/s to 80 m/s. The increment is sufficiently small such that we can assume that the reflection coefficient is correspondingly doubled and hence we should expect to see a 6 dB increase in the backscattered field. Fig. 5-14 shows the depth-averaged backscattered field at the source range obtained using the various codes. From our tests, we observed that the integral methods (BEM and spectral element) which rigorously attempts to account for both the forward and back-scattered field simultaneously, regardless of their dynamic range, breaks down earlier than VISA, which determines the field solely as a reflection-transmission problem at the interface.

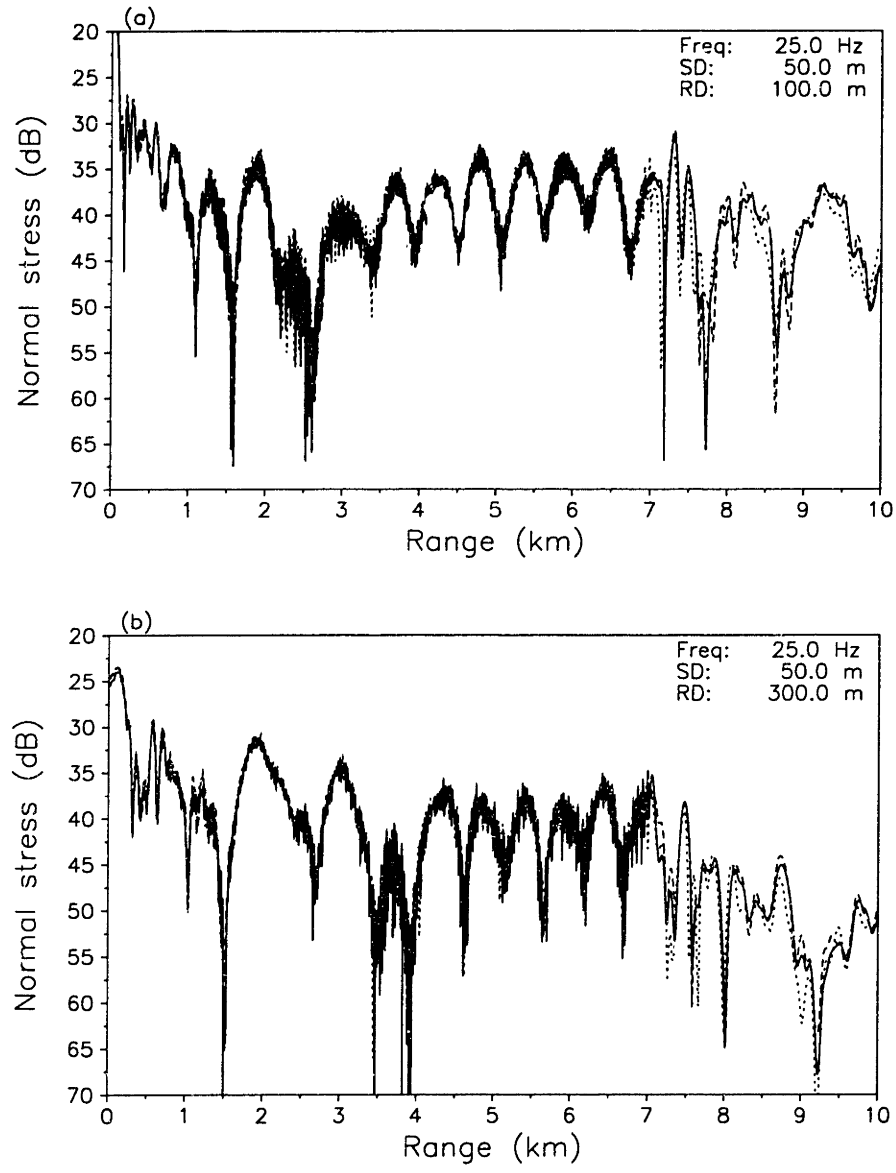

Figure 5-12: High contrast embedded elastic step (Ex. E). Total normal stress. (a) Receiver at 100 m. (b) Receiver at 300 m. Solid - BEM; Dashed - VISA; Dotted - Spectral super-element.

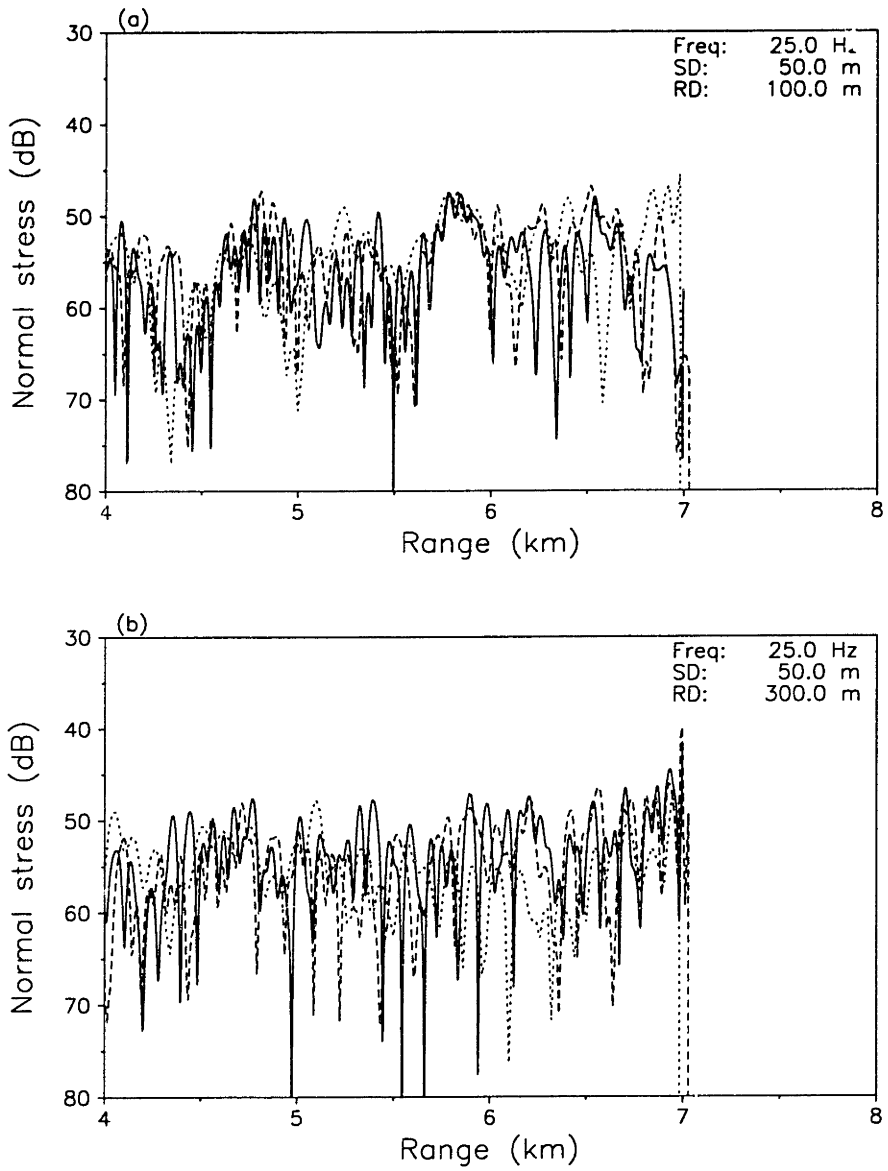

Figure 5-13: High contrast embedded elastic step (Ex. E). Back scattered normal stress solution. (a) Receiver at 100 m. (b) Receiver at 300 m. Solid - BEM; Dashed - VISA; Dotted - Spectral super-element.

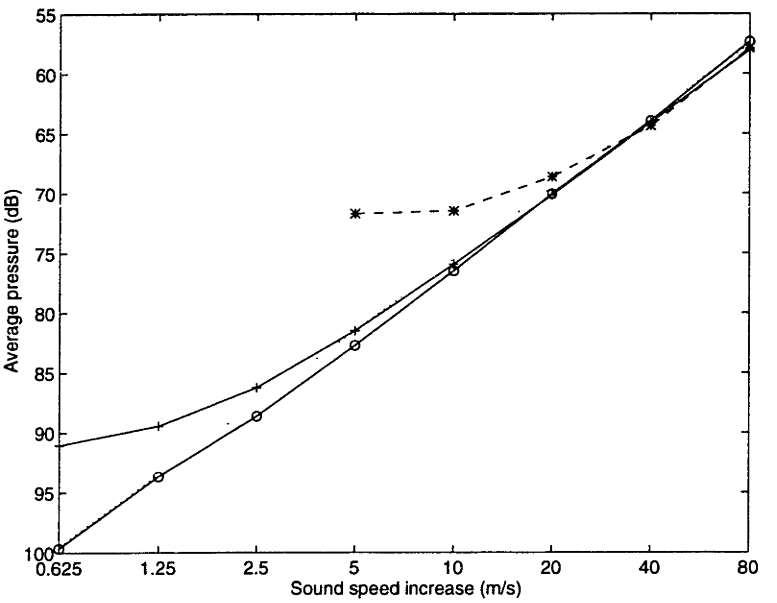

Figure 5-14: Dynamic range test - The average field at range zero as a function of sound speed contrast (log scale). *: BEM; +: CORE; o: VISA. For reference, the dotted line shows a 6 dB increase per sound speed doubling but with arbitrary absolute location.

	Parameters	BENCHMARK G	BENCHMARK H
Host Media	ρ	1.5	1.0
	c_p	1500	1500
	c_s	700	0
	α_p	0.1	0.1
	α_s	0.2	0.
Corner	ρ	0.001	1.5
	c_p	340	1700
	c_s	0	800
	α_p	0.1	0.1
	α_s	0.0	0.2

Table 5.2: Parameters for the corner problems. Wave speeds are given in m/s, densities in g/cm^3, and attenuation in dB/λ.

5.1.7 G,H : Corner Problems

Example G and H considers reflection and diffraction from a corner. We have a beam impinging onto a corner of a square at an angle of 45 degrees measured from the horizontal. The array is made up of 20 sources spaced at 30 m apart, extending from the surface down to a depth of 580 m. Again, we can construct a multitude of different combinations for the host media (containing the source) as well as the corner. Example G, shown in Fig. 5-15, considers the case of an elastic host media and an air corner. Example H, shown in Fig. 5-16, has a fluid host media with an elastic corner. The relevant parameters for the problem are listed in Table 5.2. We present only VISA generated solutions for the total bulk and shear stress. We see that the characteristic symmetric 'butterfly' field contours are very useful features when comparing solutions.

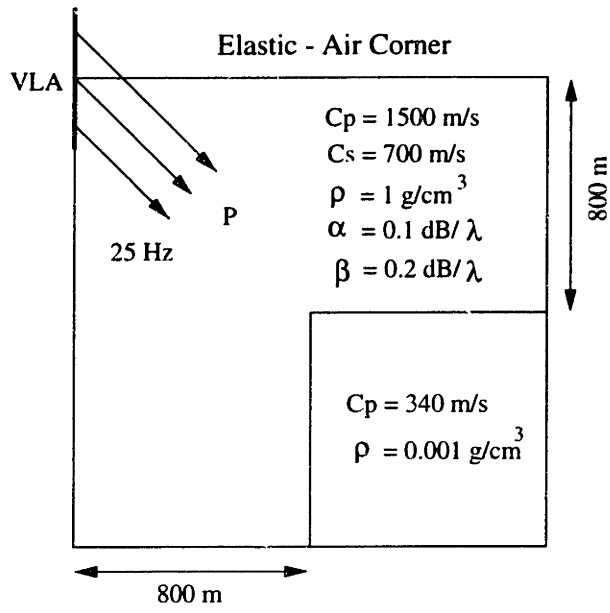

Figure 5-15: Ex. G : Schematic for Elastic-Air corner problem

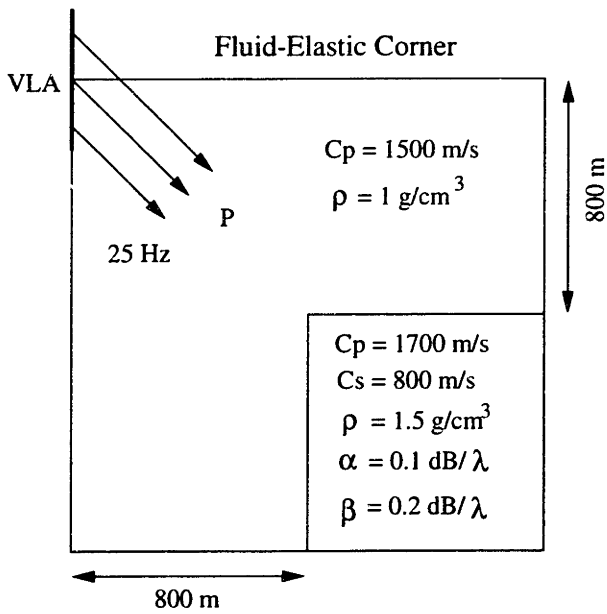

Figure 5-16: Ex. H : Schematic for Fluid-Elastic corner problem

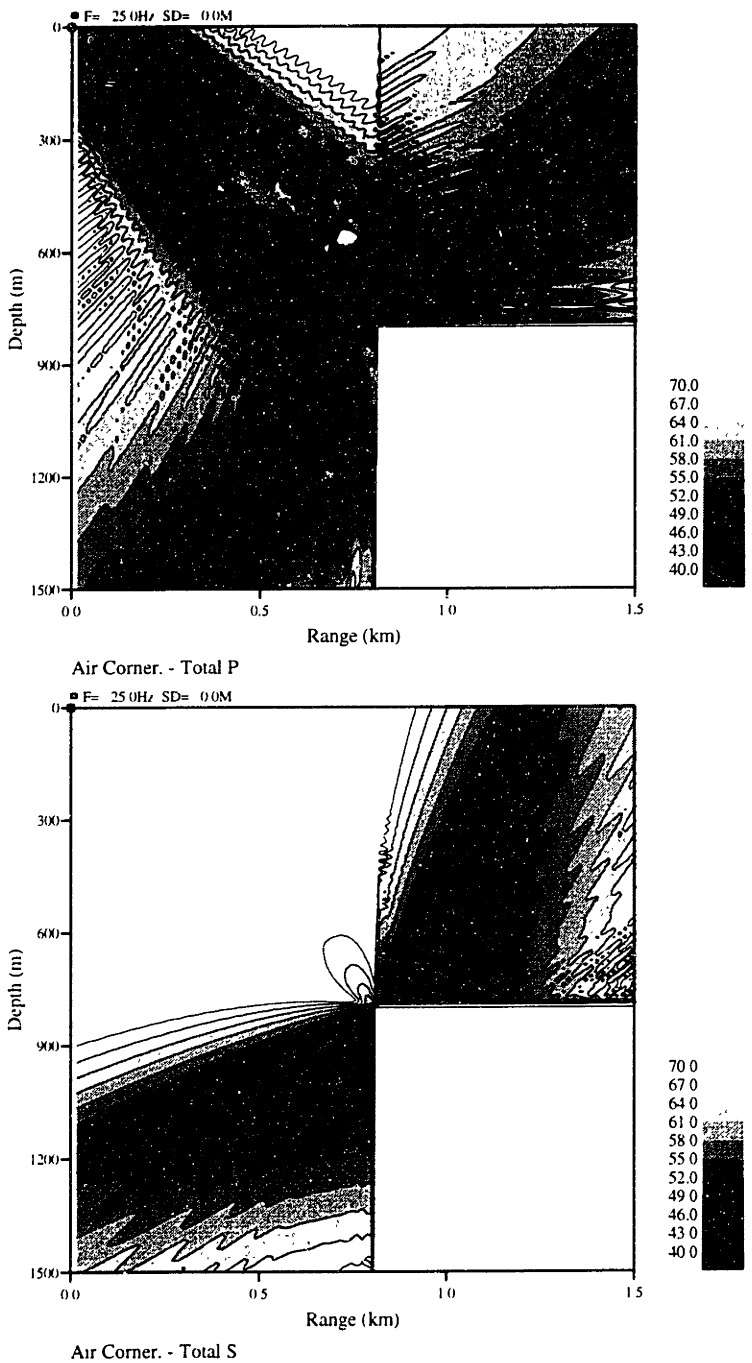

Figure 5-17: Elastic-Air corner (Ex. G) - VISA solution (a) Total dilatation (b) Total shear

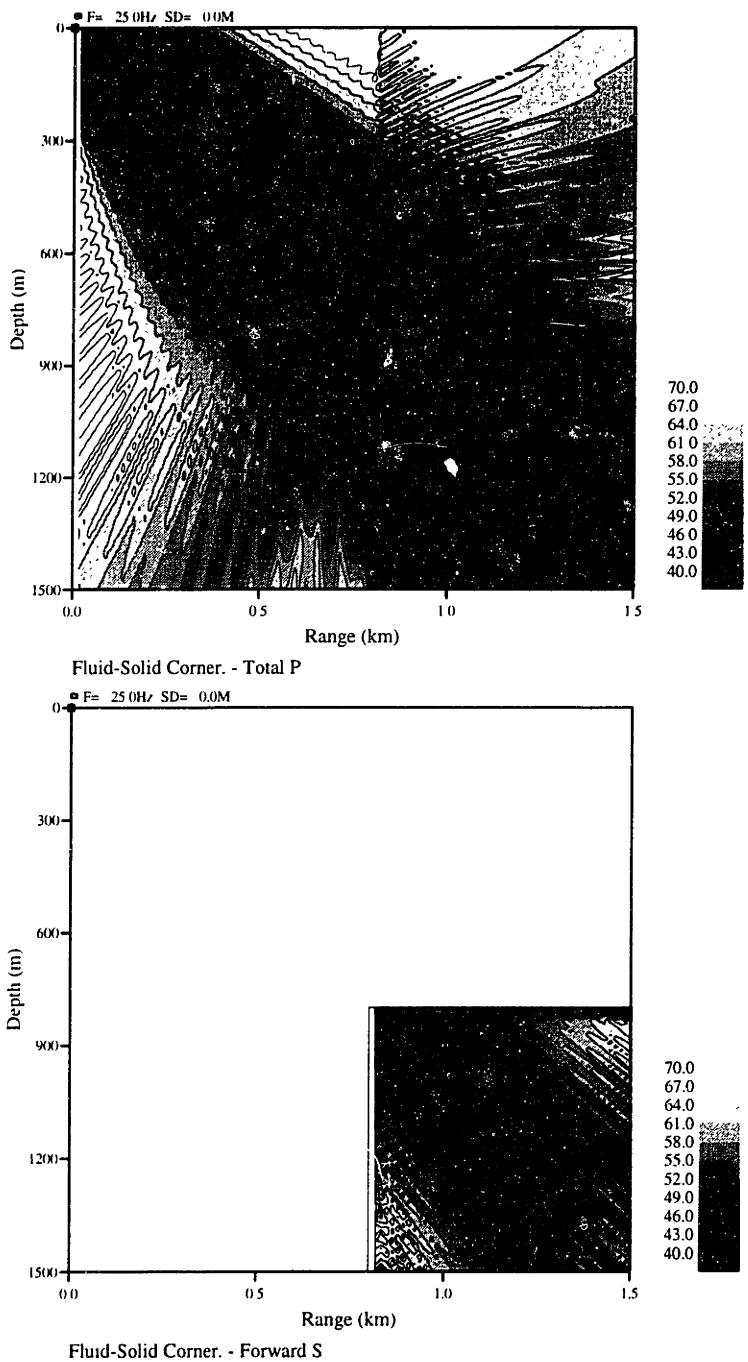

Figure 5-18: Fluid-Elastic corner (Ex. H) - VISA solution (a) Total dilatation (b) Total shear

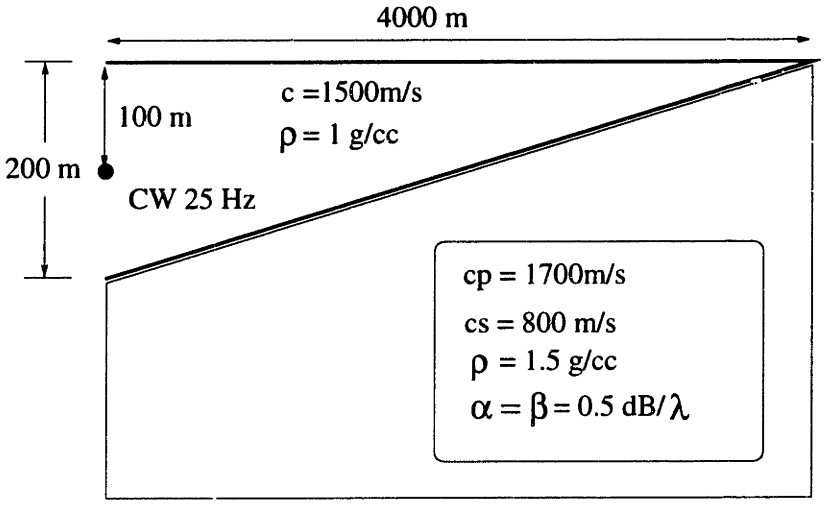

Figure 5-19: Ex. I : Environment for the ASA elastic wedge

5.1.8 I : Elastic ASA Wedge

Example I, shown in Fig. 5-19 is test case 3 from the Parabolic Equation Workshop II [51]. This is an elastic version of the standard ASA wedge benchmark problem. A 25-Hz point source is placed at 100 m depth. The ocean depth decreases linearly with range from 200 m at the source range to zero at $r = 4$ km. The ocean bottom has a compressional sound speed of 1700 m/s and a shear speed of 800 m/s. The density is 1.5 g/cm^3 with the compressional and shear attenuations at 0.5 dB/λ. The environment is discretized into 17 layers, each of about a wavelength in depth, and 56 range sectors. In Fig. 5-20 we present solutions from the parabolic equation model and the super-element method. There is good agreement for the shallow receiver and for the receiver in the bottom, the agreement is still quite good and the differences are primarily due to the particular manner in which the environment is being discretized.

5.1.9 J : Mode conversion - Point Source

Mode conversion from compressional waves to shear and vice versa is an extremely important physical process. It is also the single most important complicating factor in most parabolic equation formulations. Example J considers just this particular problem. A 25-Hz point

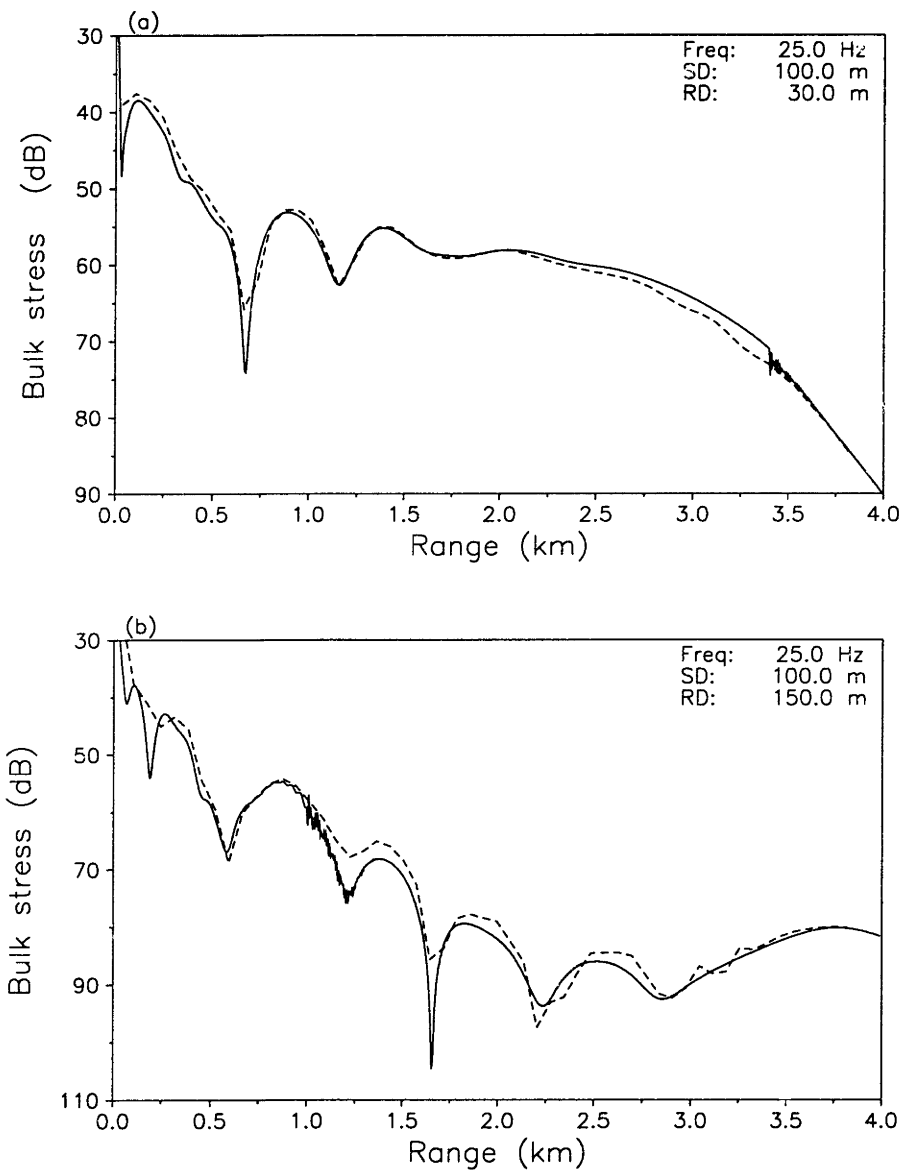

Figure 5-20: ASA elastic wedge (Ex. I) (a) Receiver at 30 m, (b) Receiver at 150 m; Solid - FEPE, Dashed - Spectral super-element

source is placed at 25m depth in a 100-m deep waveguide bounded at the top and bottom by presure-release boundaries. We set up a 2-sector problem with the compressional and shear speed in the left sector being 1700 m/s and 700 m/s respectively. The density is $1.5\,g/cm^3$ and the compressional and shear attenuation is 0.2 dB/λ and 0.5 dB/λ respectively. In the right sector, we have a solid with a compressional speed of 3000 m/s and a shear speed of 1700 m/s. All other parameters remain the same. Here we see that the compressional speed in the left sector is matched to the shear speed on the right, resulting in strong coupling of P-waves from the left to S-waves on the right. Another complicating factor is the extremely large contrast in the sound-speeds. In Fig. 5-21 we show the forward-scattered solutions for the normal stress, vertical and horizontal particle velocity. Fig. 5-22 shows the corresponding back-scattered field.

5.1.10 K : Mode conversion - Vertical Point Force

In Example K, we run the same problem but this time with a vertical point force of 1 N placed in the middle of the waveguide. From the symmetry of the waveguide we can see that now most of the excitation at the vertical discontinuity will be of the shear waves. This example provides a good test of the code to properly model compressional to shear wave conversions. The solutions for this example are shown in Fig. 5-23 and Fig. 5-24.

5.1.11 L : Mode conversion - Horizontal Point Force

Again Example L is identical to Example K except that this time we use a horizontal point force of 1 N placed in the middle of the waveguide. At the vertical interface, most of the excitation will be from the longituidinal waves which couples strongly to the shear waves in the right sector. The solutions for this example are shown in Fig. 5-25 and Fig. 5-26.

5.1.12 M : Step Periodic Roughness Patch

Example M considers a step periodic roughness patch shown in Fig. 5-27. A similar fluid example was first treated by Evans and Gilbert [52]. The patch extends from 5-10 km and the depth variations consists of steps which are 10 m high, 100 m long and 200 m apart. Hence

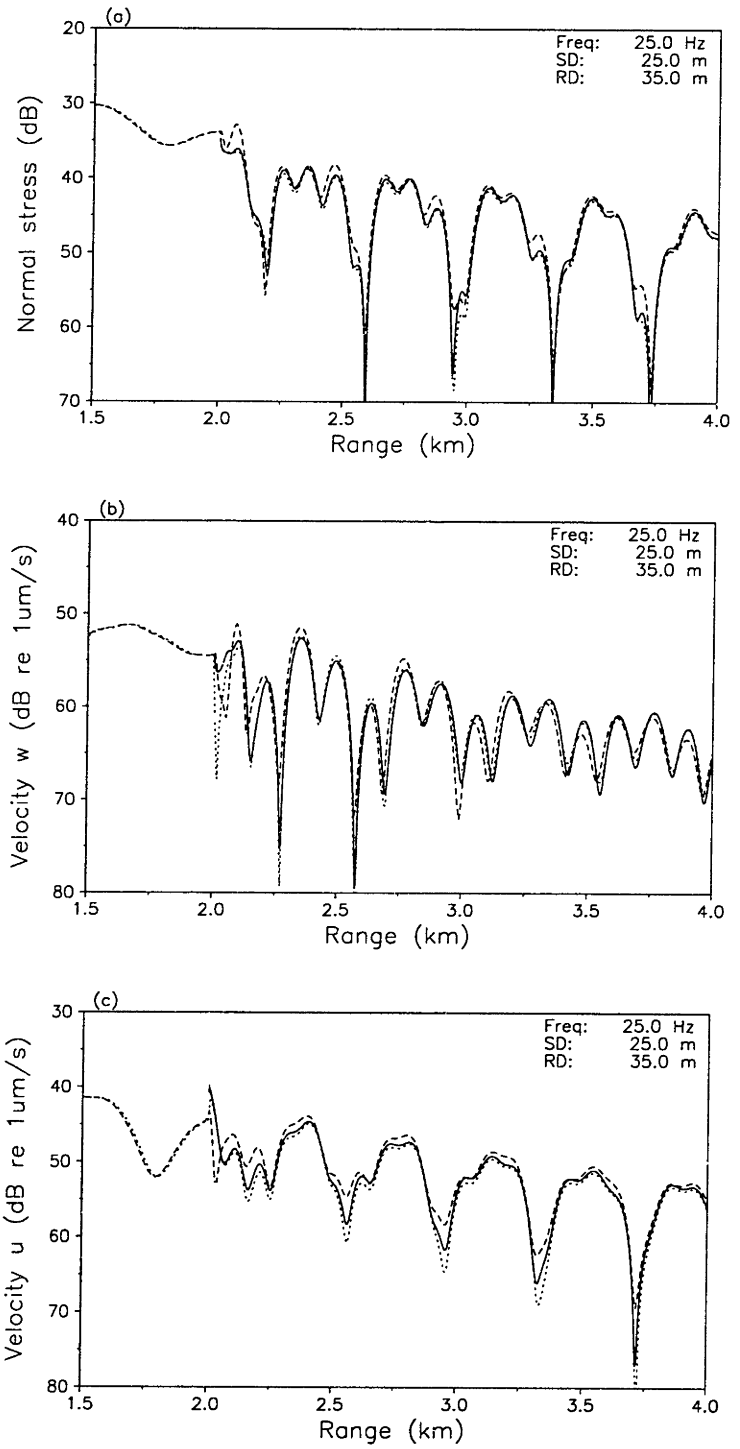

Figure 5-21: Mode conversion with a point source (Ex. J) - Forward scattered field (a) Normal stress, (b) vertical particle velocity, (c) horizontal particle velocity; Solid : BEM, Dashed : VISA, Dotted : Spectral super-element

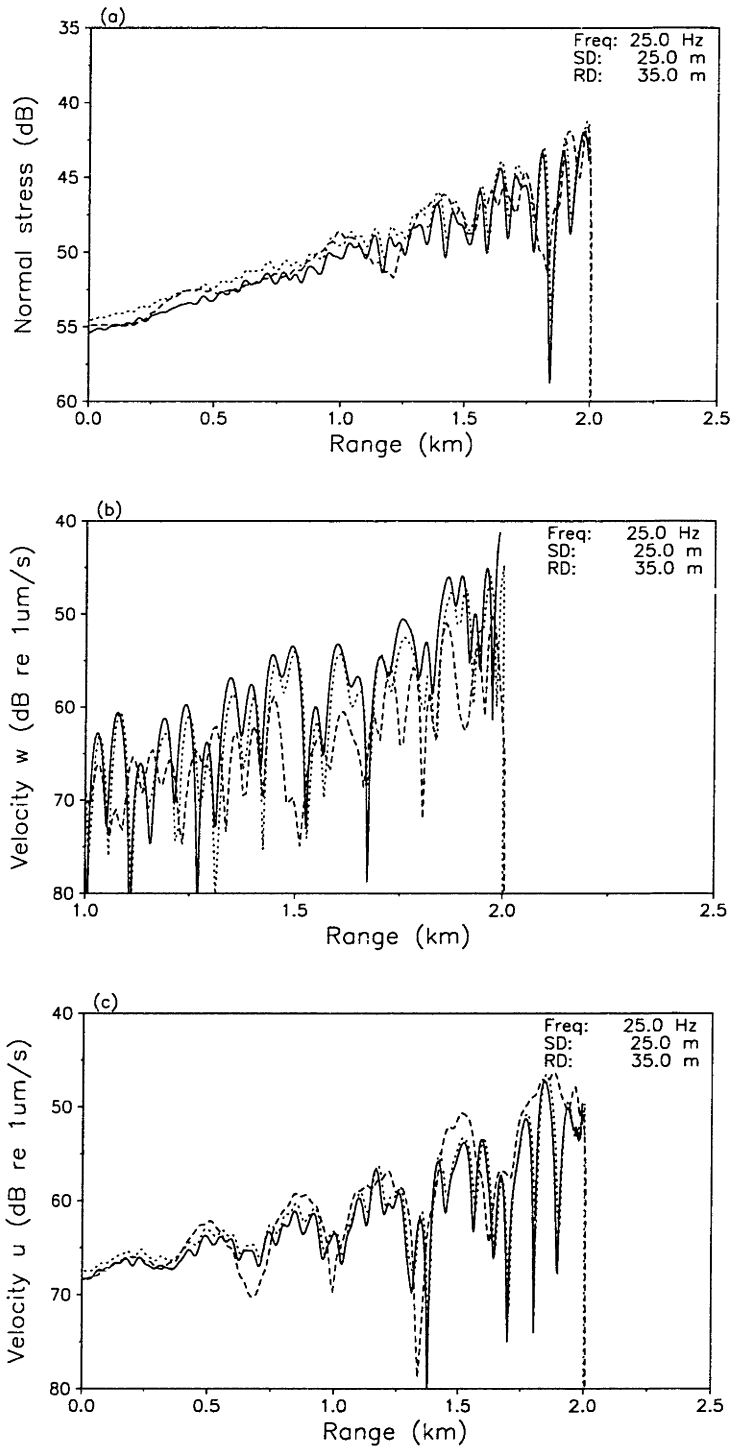

Figure 5-22: Mode conversion with a point source (Ex. J) - Backward scattered field (a) Normal stress, (b) vertical particle velocity, (c) horizontal particle velocity; Solid : BEM, Dashed : VISA, Dotted : Spectral super-element

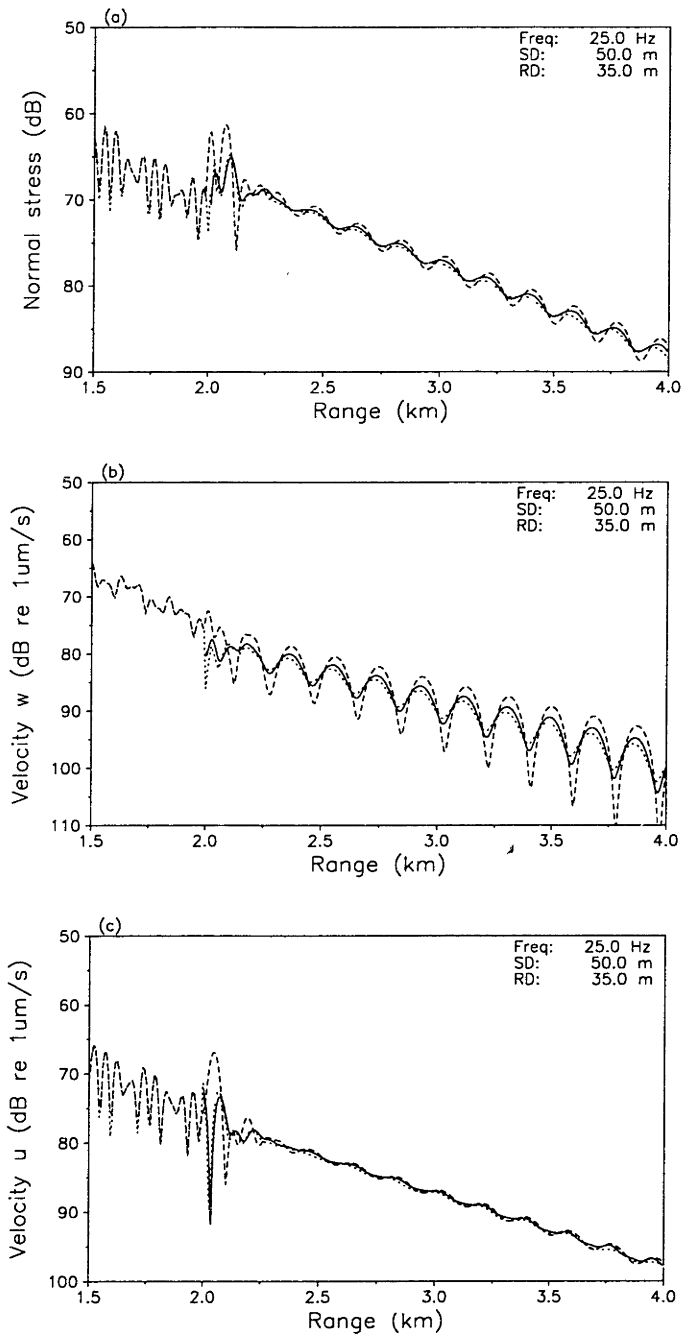

Figure 5-23: Mode conversion with a vertical point force (Ex. K) - Forward scattered field (a) Normal stress, (b) vertical particle velocity, (c) horizontal particle velocity; Solid : BEM, Dashed : VISA, Dotted : Spectral super-element.

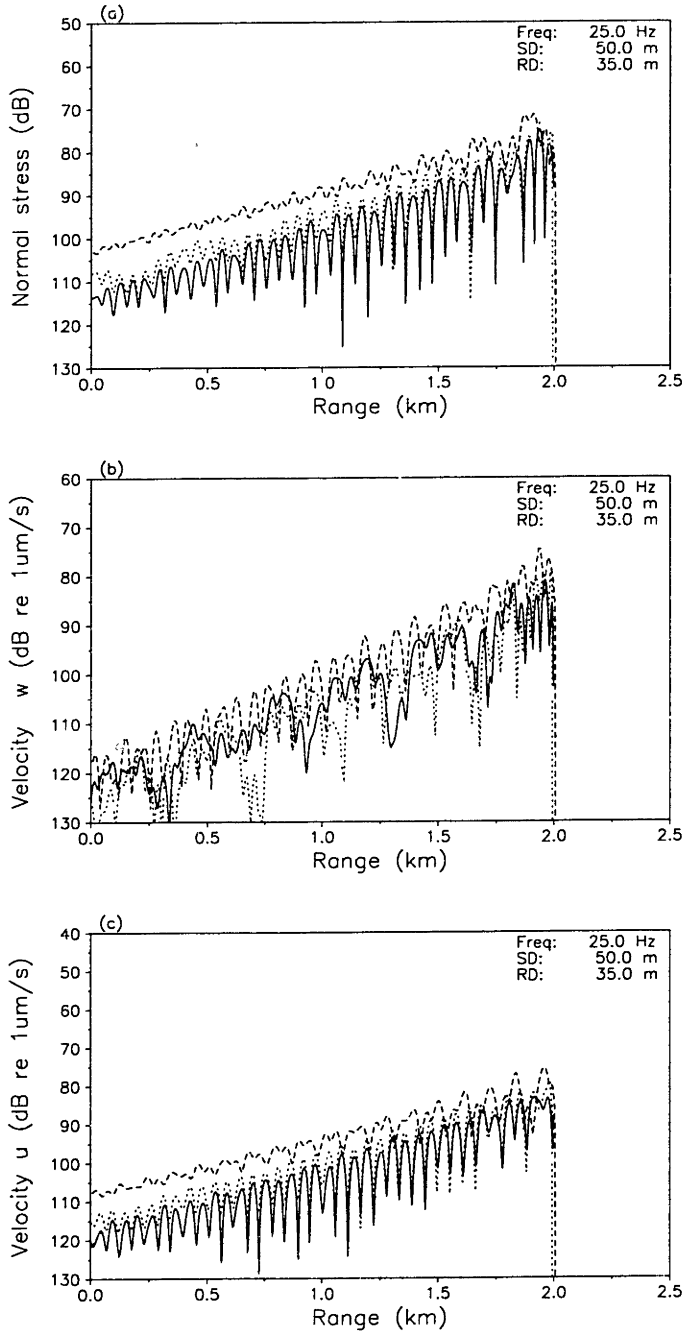

Figure 5-24: Mode conversion with a vertical point force (Ex. K) - Backward scattered field (a) Normal stress, (b) vertical particle velocity, (c) horizontal particle velocity; Solid : BEM, Dashed : VISA, Dotted : Spectral super-element.

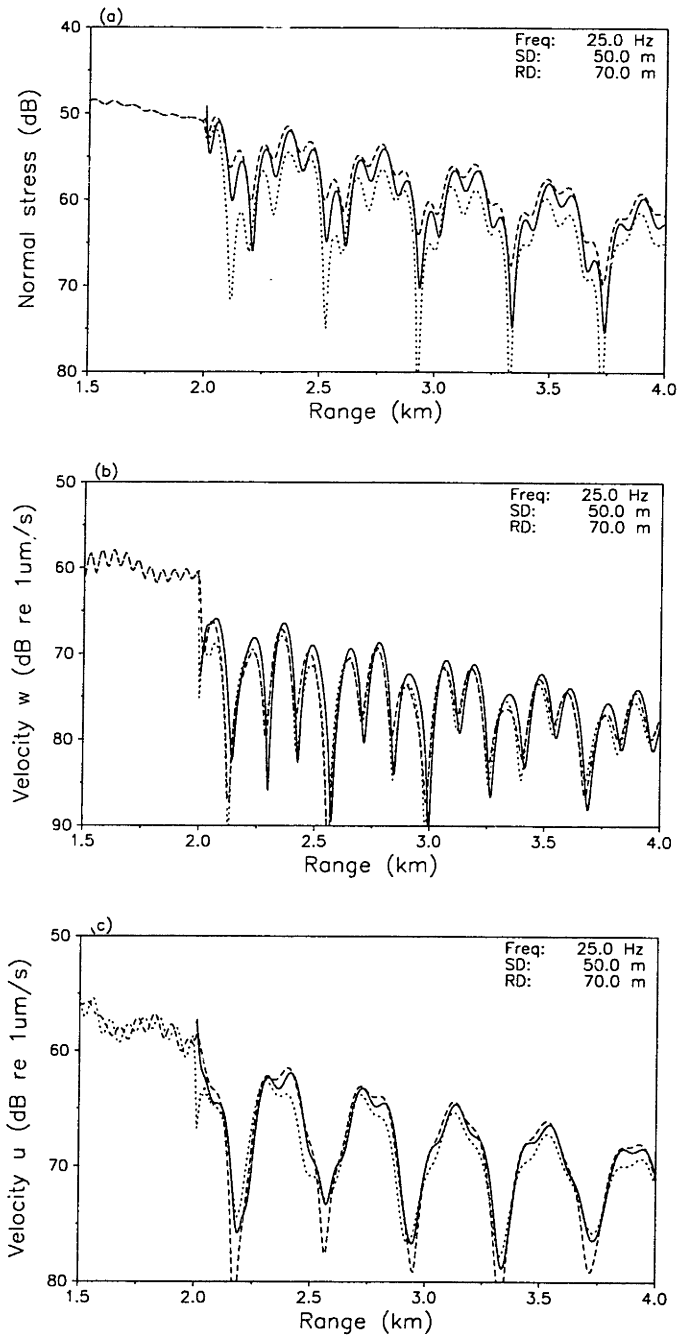

Figure 5-25: Mode conversion with a horizontal point force (Ex. L) - Forward scattered field (a) Normal stress, (b) vertical particle velocity, (c) horizontal particle velocity; Solid : BEM, Dashed : VISA, Dotted : Spectral super-element.

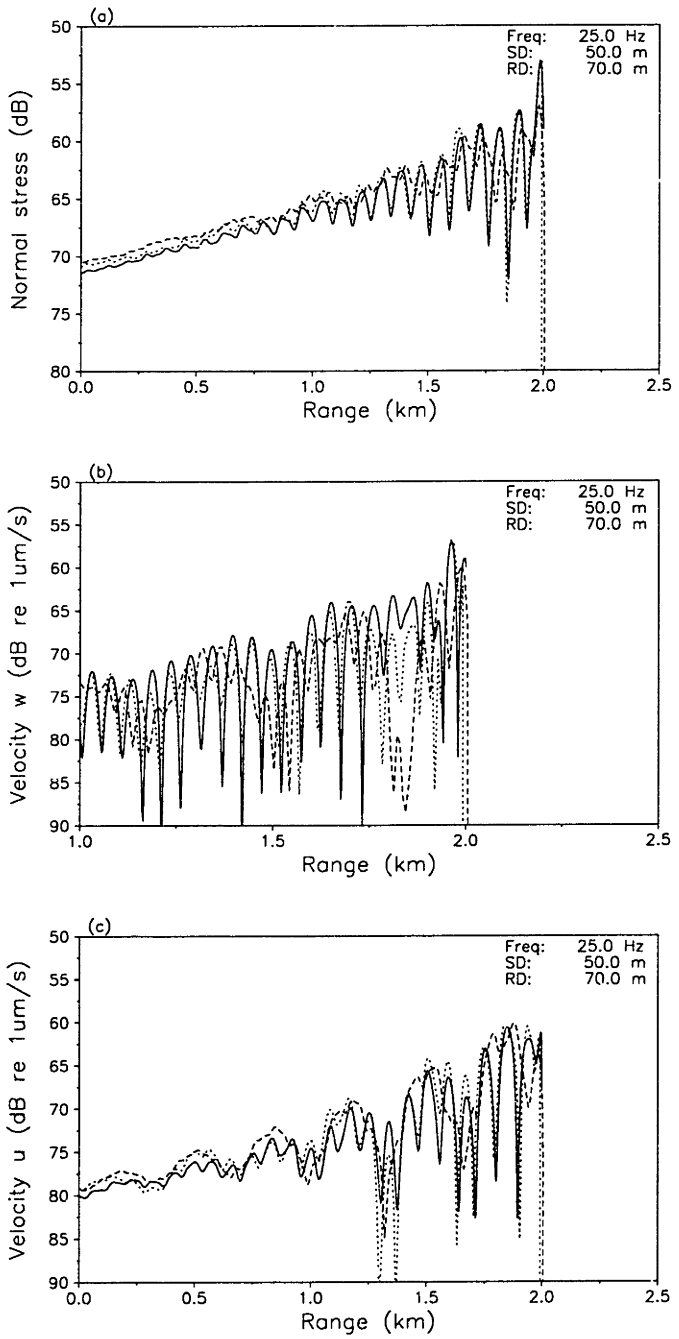

Figure 5-26: Mode conversion with a horizontal force (Ex. L) - Backward scattered field (a) Normal stress, (b) vertical particle velocity, (c) horizontal particle velocity; Solid : BEM, Dashed : VISA, Dotted : Spectral super-element.

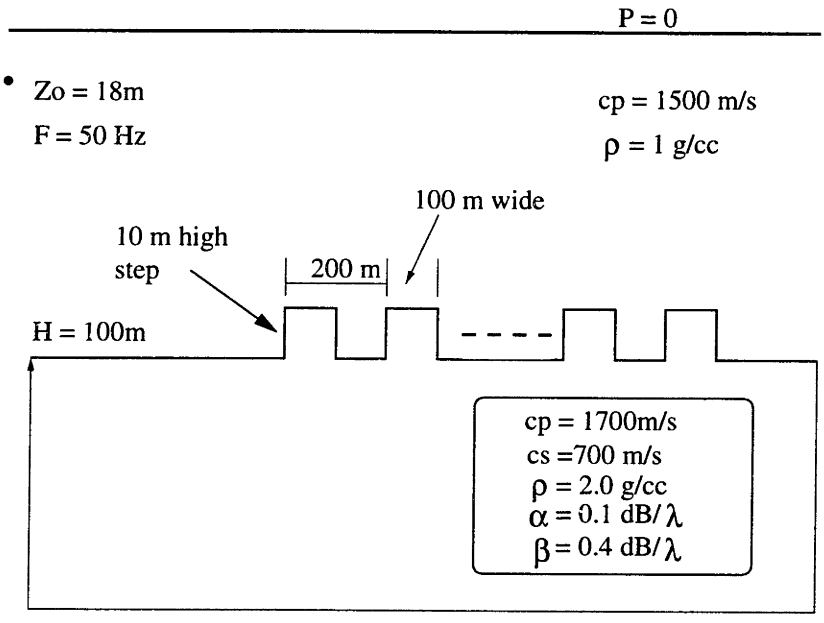

Figure 5-27: Ex. M : Configuration for step periodic roughness patch

there are 5 steps per kilometer. The source, at a frequency of 50 Hz, is at a depth of 18 m, and Fig. 5-28 shows the bulk stress for receiver depths of 50 and 150 m. The spectral element solution is computed using eight orders of expansion. The transmission loss is compared to the reference solution for a flat-bottom waveguide (SAFARI). For the bottom receiver, we see an increase in the field below the roughness patch and this is a result of energy being dumped from the water column into the bottom. This behaviour is most clearly seen in the contour plots of Fig. 5-29. This test problem provides a good example of energy loss due to bottom roughness.

5.1.13 N : Elastic Half-Cylindrical Ridge

Example N, shown in Fig. 5-30a, is modified from an equivalent fluid example in Jensen and Gerstoft [43]. It involves a half-cylindrical ridge in the ocean bottom with a compressional sound speed of 1700 m/s and a shear speed of 700 m/s. The density is $1.5\,\mathrm{g/cm^3}$ and the compressional and shear attenuation is 0.2 dB/λ and 0.5 dB/λ respectively. A 25-Hz line source is placed at depth z = 100m. The ridge is positioned 1.5 km downrange and has a height of 50 m ($\sim$ 1 wavelength) above the sea floor. Fig. 5-30 shows the backscattered

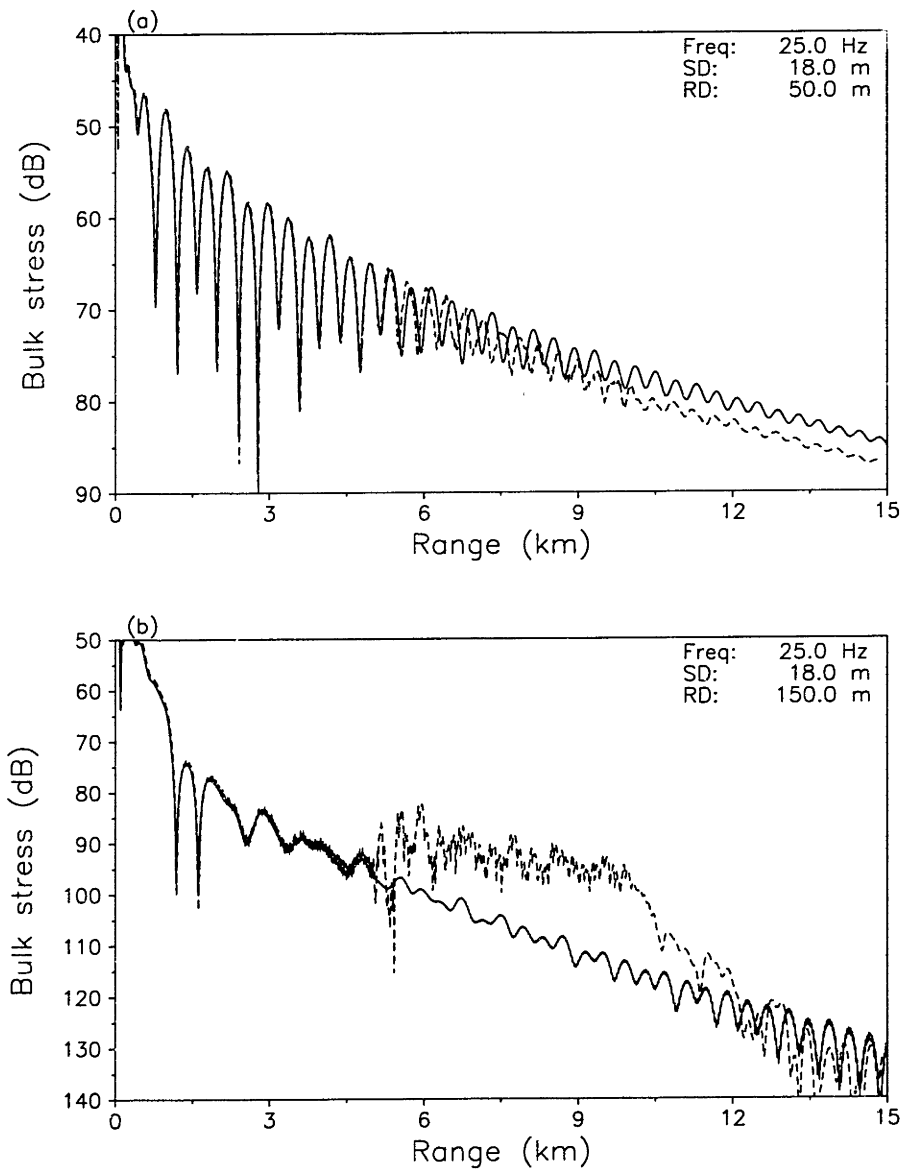

Figure 5-28: Step periodic roughness patch (Ex. M). Forward dilatation : (a) Receiver at 50 m. (b) Receiver at 150 m. Solid - SAFARI; Dashed - Spectral super-element.

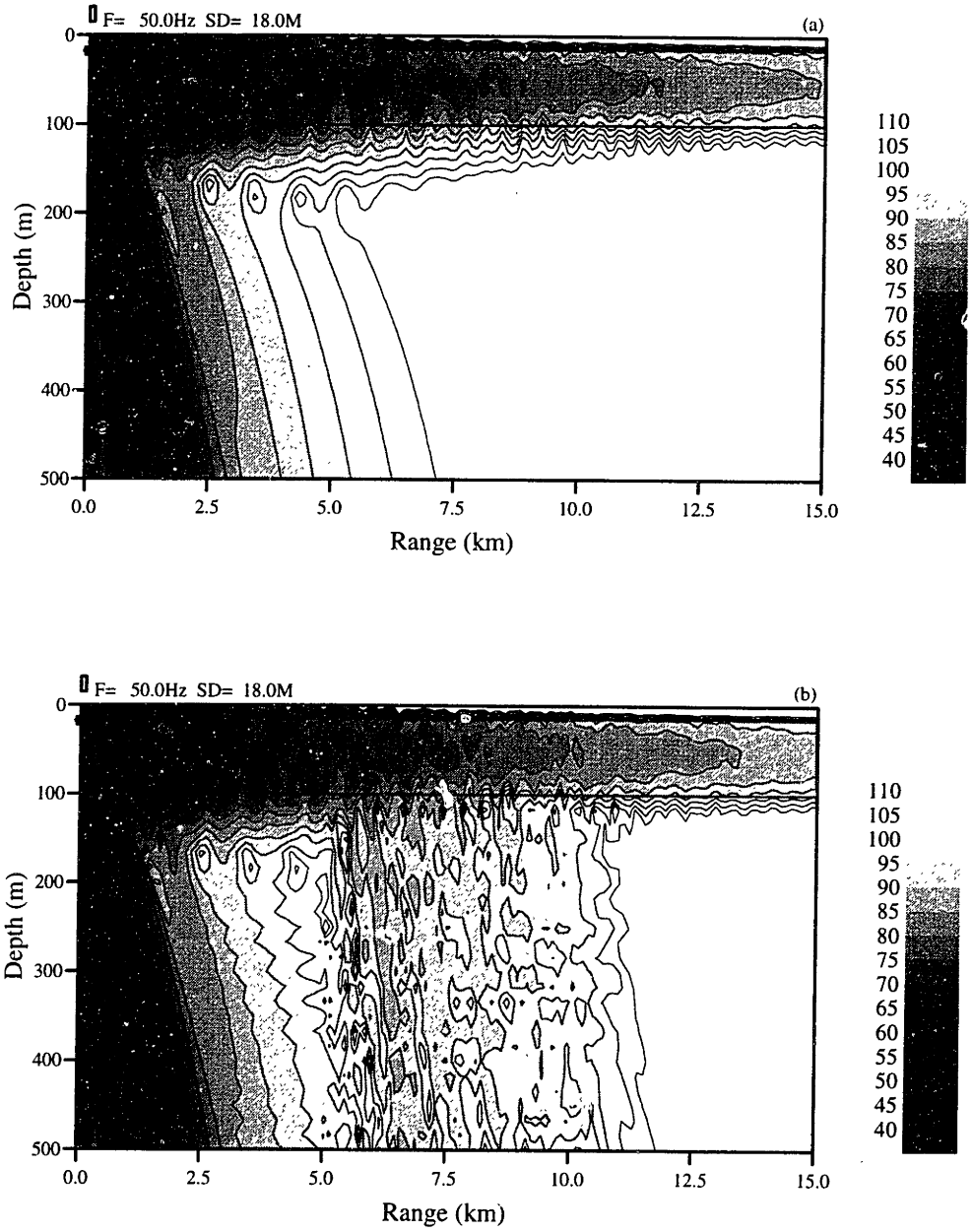

Figure 5-29: Step periodic roughness patch (Ex. M). Forward dilatation : (a) SAFARI solution without the patch (b) Spectral super-element solution with the roughness patch

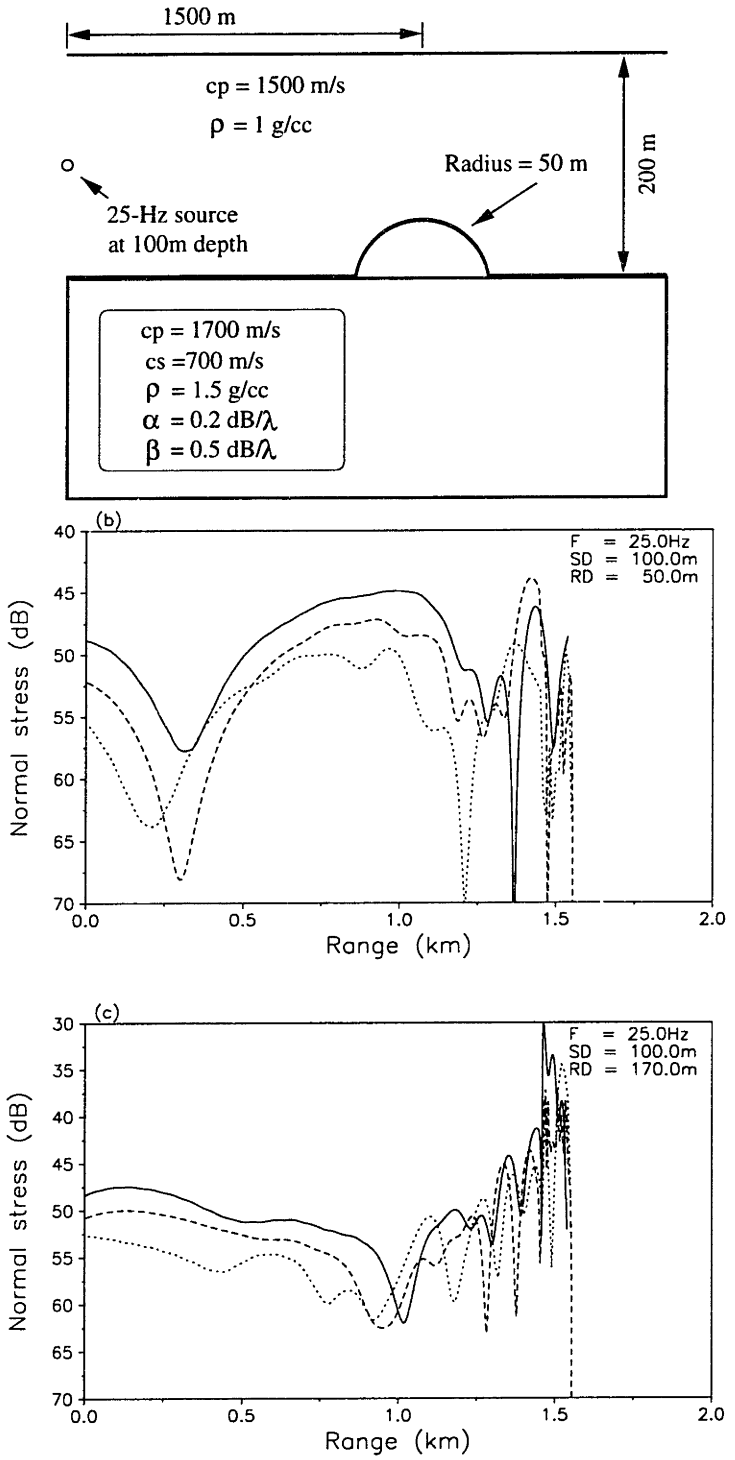

Figure 5-30: Backscattering from an elastic half-cylindrical ridge (Ex. N). (a) Environment (b) Receiver at 50m, (c) Receiver at 170m: Solid - BEM; Dashed - VISA, Dotted - Spectral super-element solution.

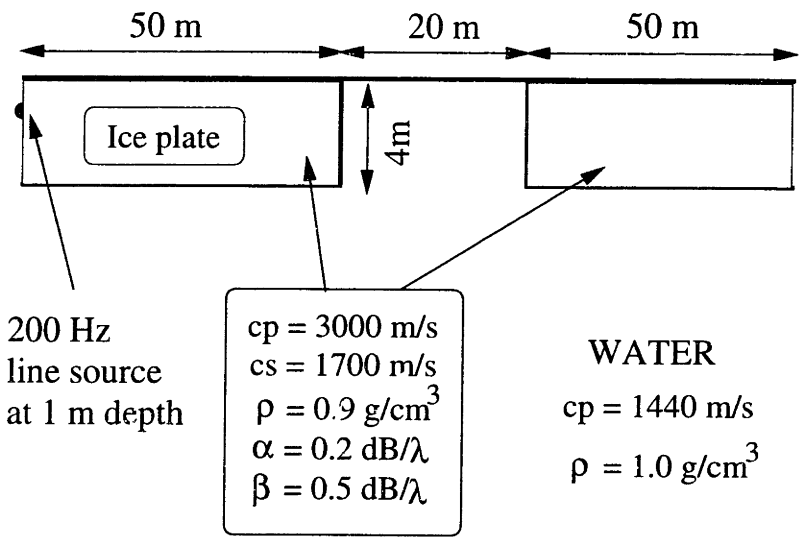

Figure 5-31: Ex. O : Configuration for the ice lead problem

field at two receiver depths for the boundary element method, VISA and the super-element method. In this example, the BEM solution is believed to be the most accurate. There is only qualitative agreement between all the three solutions and we believed this is largely due to errors associated with the single scatter formulation. The ridge is about the size of a wavelength and internal resonances of this nature (multiple scattering within the ridge) cannot be properly handled with the single-scatter formulation.

5.1.14 O : Elastic Ice Lead

Example O, shown in Fig. 5-31, considers a problem in which we have water penetration through a portion of an ice sheet. The ice has a compressional speed of 3000 m/s and shear speed of 1700 m/s. The compressional and shear attenuation is 0.2 dB/λ and 0.5 dB/λ respectively. The ice segments are floating on water with a sound speed of 1440 m/s and a density of 1 g/cm^3. A 200-Hz line source is placed 1 m below the surface of the ice sheet and we present solutions for the bulk stress and vertical particle velocity at receiver depths of 5 and 10 m. The spectral element solutions are obtained using only eight orders of expansions.

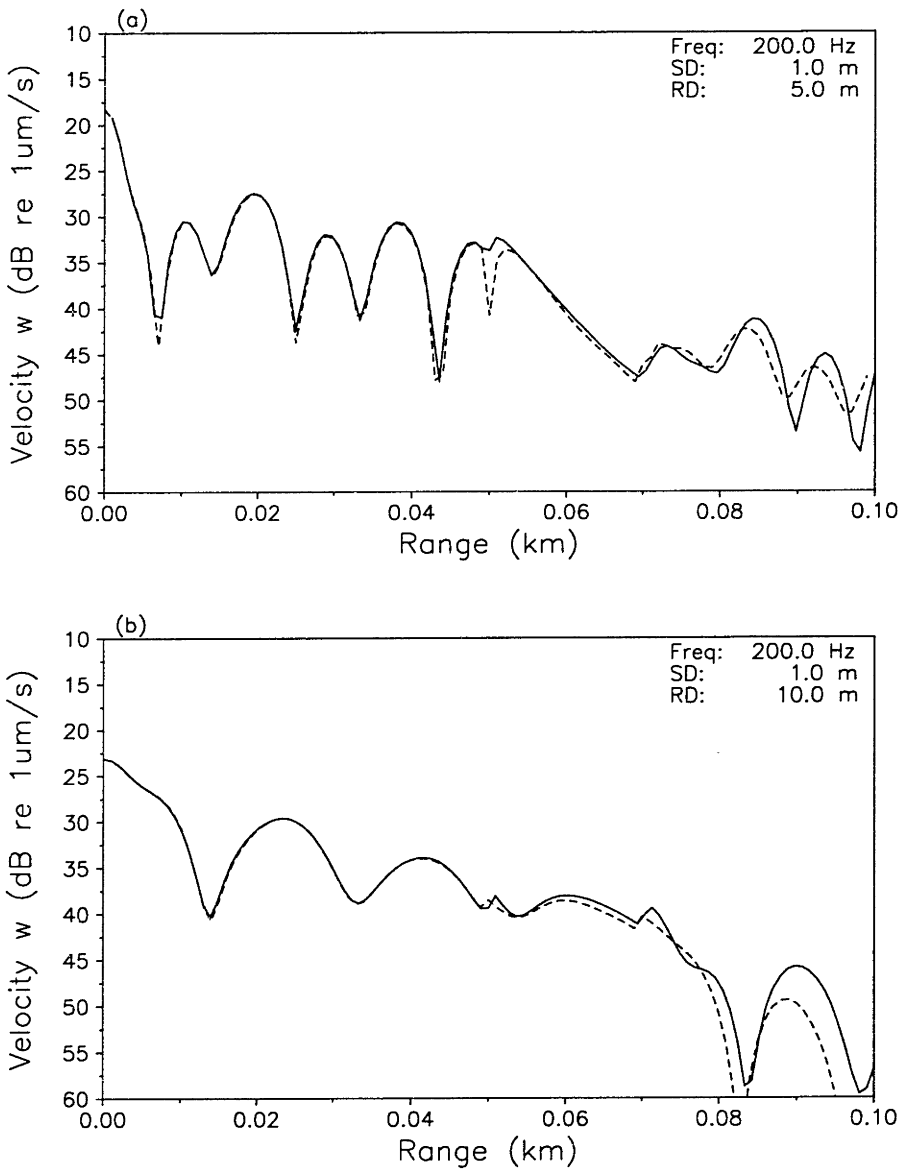

Figure 5-32: Ice lead problem (Ex. O). Forward vertical velocity : (a) Receiver at 5 m (b) Receiver at 10 m. Solid : VISA, Dashed : Spectral super-element

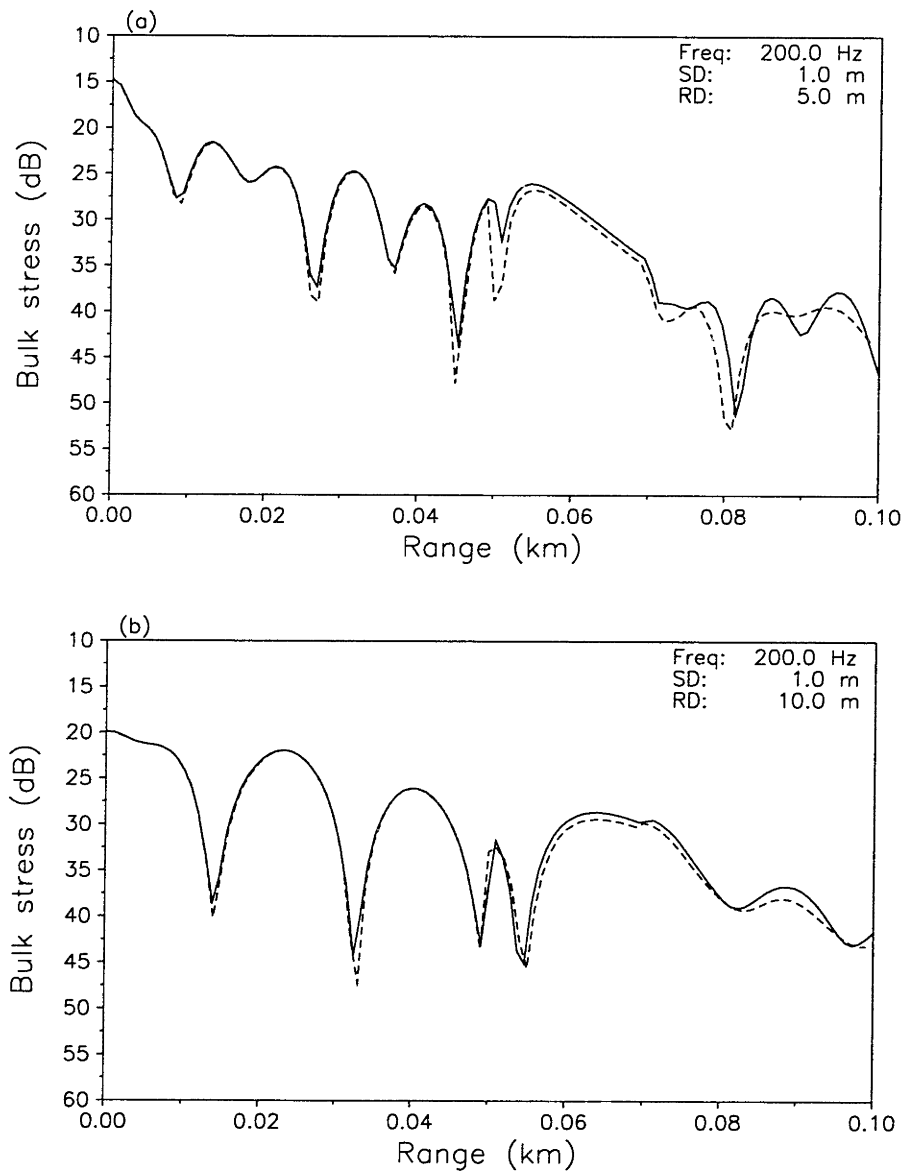

Figure 5-33: Ice lead problem (Ex. O). Forward dilatation : (a) Receiver at 5 m (b) Receiver at 10 m. Solid : VISA, Dashed : Spectral super-element

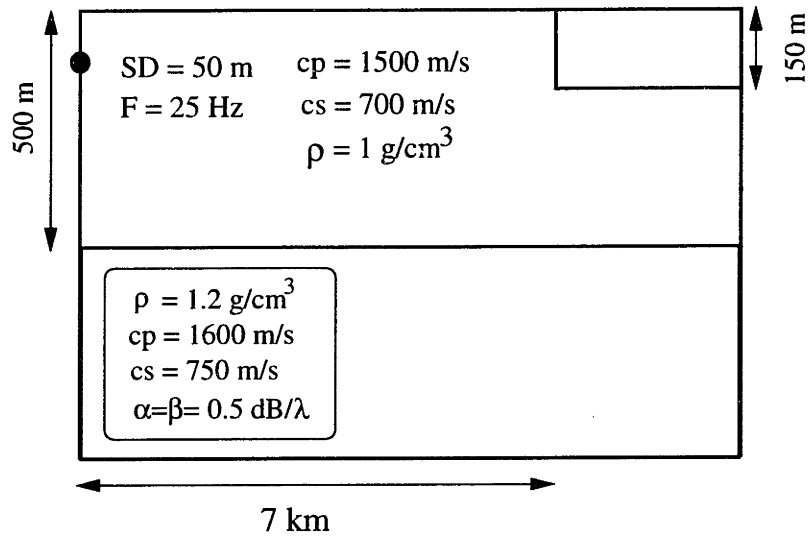

Figure 5-34: Ex. P : Configuration for the entrenched elastic layer problem

5.1.15 P : Entrenched Elastic Layer

Example P, taken from Collins [13] and shown in Fig. 5-34, is similar to the embedded step problem with two modifications: (1) the stair step is removed; and (2) a layer with the same elastic properties as the lower layer is embedded in the upper 150 m of the upper layer for ranges greater than 7 km. In Fig. 5-35 and 5-36 we show the forward and back scattered normal stress for two receiver depths.

5.1.16 Q : Lloyd-mirror beam diffraction

Example Q is similar to the corner diffraction problems discussed earlier. However, instead of generating the beam with a vertical line array, the beam in this problem is part of the Lloyd-mirror beam pattern. The problem is set up such that we have only one beam tilted at an angle of 30° from the sea surface. The position of the corner protrusion is positioned such that the beam is directed at its corner. This test is particularly useful for those codes which does not handle vertical arrays of sources. Fig. 5-37 shows the environment and Fig. 5-38 shows the contour plot for the total normal stress. Transmission loss comparisons with the BEM and VISA solutions are shown in Fig. 5-39 and Fig. 5-40 for both the forward and

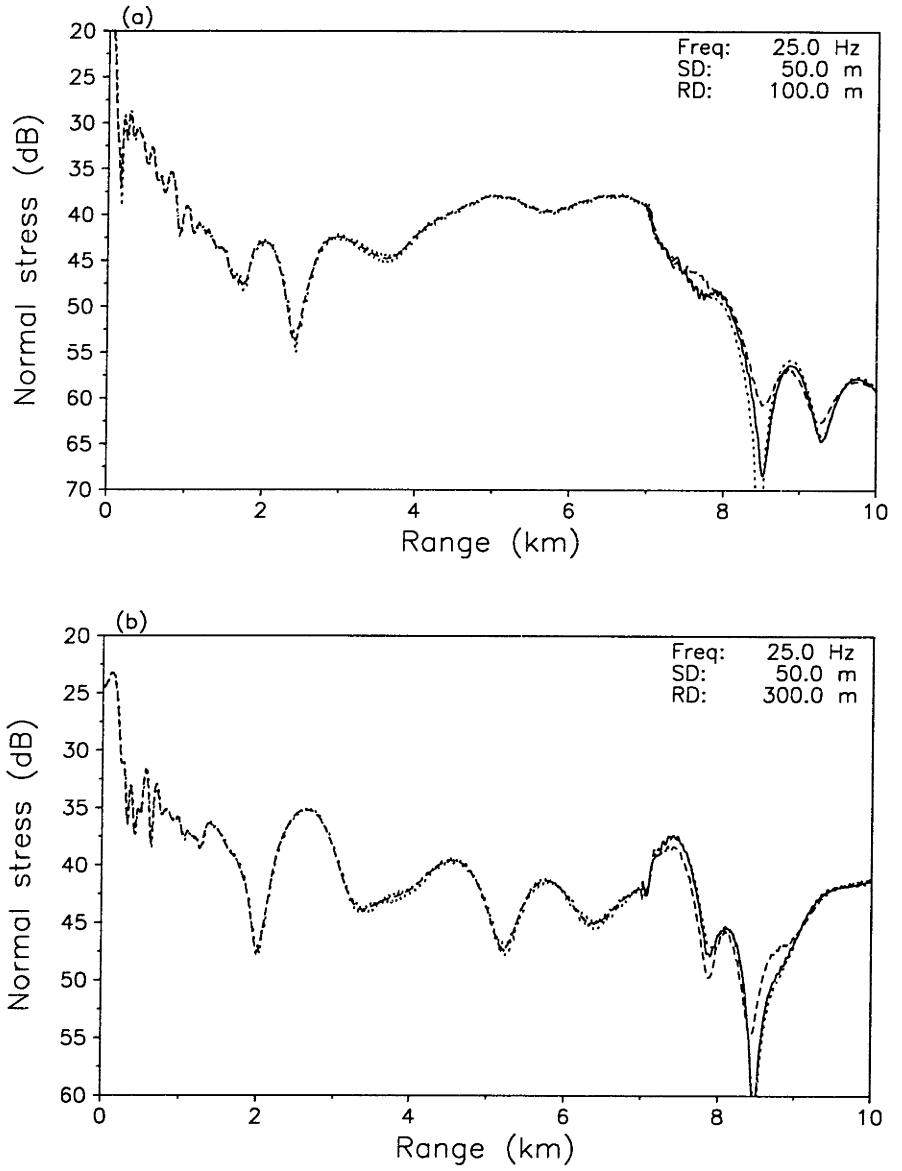

Figure 5-35: Entrenched layer problem (Ex. P). Forward normal stress: (a) Receiver at 100 m (b) Receiver at 300 m. Solid : BEM, Dashed : VISA, Dotted : Spectral super-element

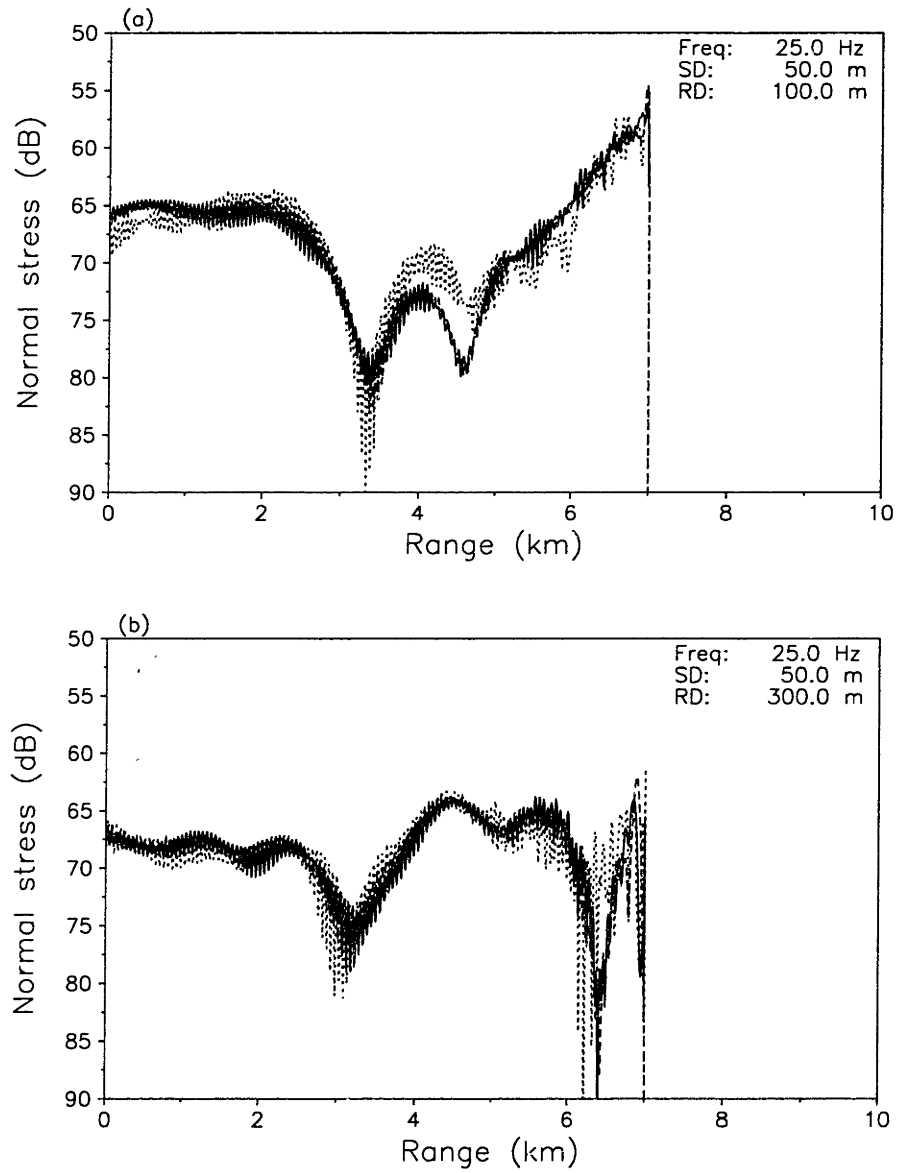

Figure 5-36: Entrenched layer problem (Ex. P). Backward normal stress: (a) Receiver at 100 m (b) Receiver at 300 m. Solid : BEM, Dashed : VISA, Dotted : Spectral super-element

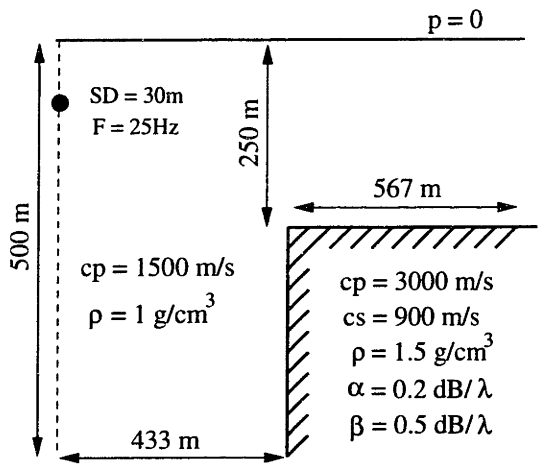

Figure 5-37: Ex. O : Configuration for the Lloyd-mirror beam diffraction problem

backscattered field respectively. Again, one can construct several different benchmarks by changing the host and corner media.

5.2 Summary

In this chapter we have presented a wide variety of benchmarks and their solutions. Even though some of these benchmarks do not represent realistic ocean environments, they nevertheless serve the very important objective of testing the integrity of the code as well as the robustness of the formulation. Many other variations can be derived from the simple examples presented here. Our test cases should also serve as a very useful reference for other modelers as well. The results of our inter-model comparisons demonstrated the accuracy and versatility of the spectral super-element approach in solving a wide variety of seismo-acoustic problems. In the process of our testing we also learned that the choice of field parameters for making comparisons is very important. In particular, the 'equivalent shear stress' which is defined as the contribution from only the shear potential may not be an ideal candidate because it is not a physical variable, unlike displacements, and in some cases may be extremely unstable to compute. These benchmarks also highlight the fact that back-scatter is a particularly difficult process to model, compared to the forward field. This is especially true in cases where there exists a large dynamic range between the forward and back-scattered

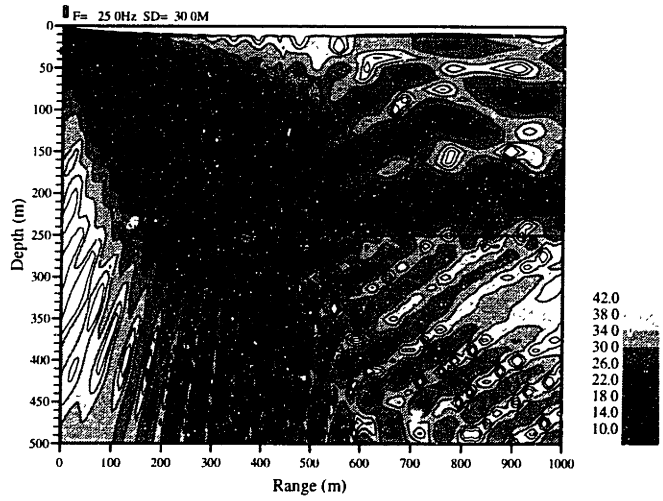

Figure 5-38: Diffraction from a Lloyd-mirror beam (Ex. O). Total normal stress (Spectral super-element solution)

field. In these cases, boundary integral methods that try to simultaneously account for the large dynamic range may fail, and when this happens they are more likely to get the forward field correct but arriving at an incorrect back-scattered field. On the other hand, the VISA formulation which determines the field solely as a reflection-transmission problem at the interface tends to be more robust numerically.

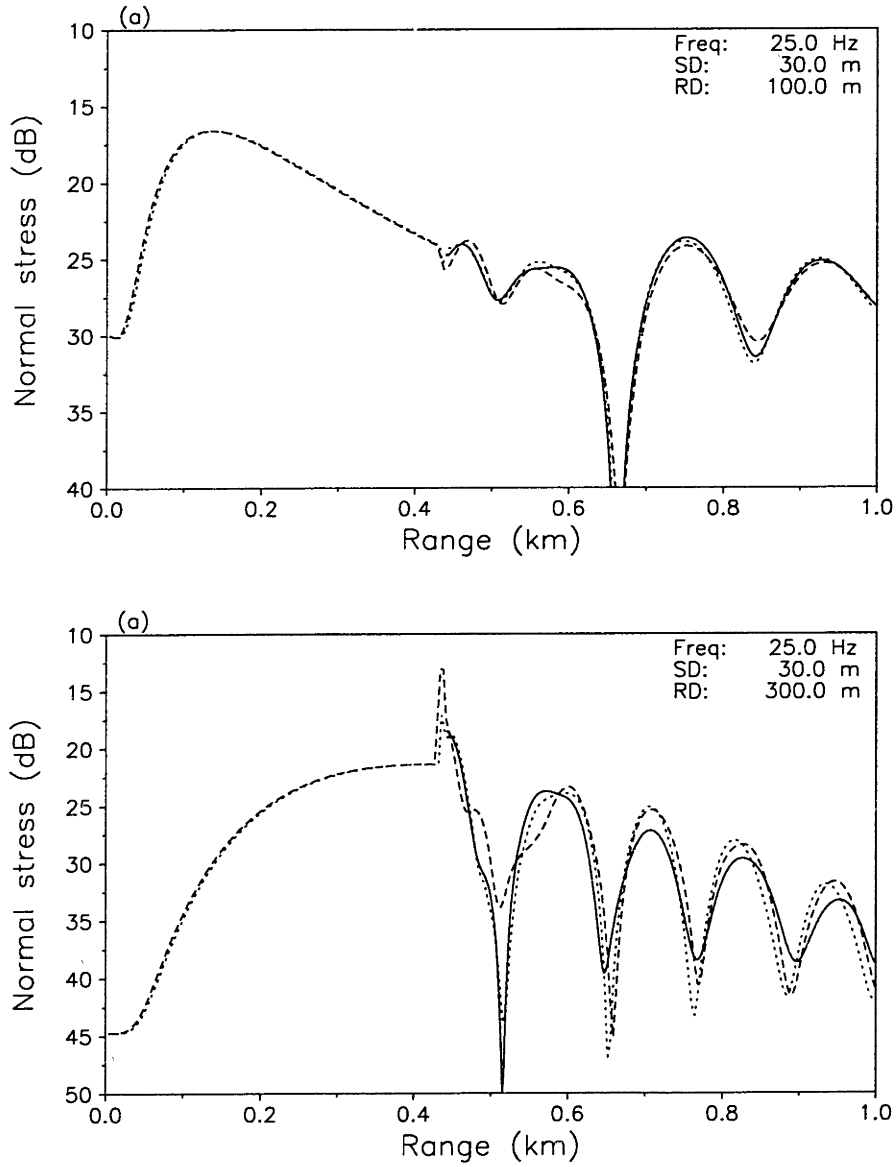

Figure 5-39: Diffraction from a Lloyd-mirror beam (Ex. Q). Forward normal stress (a) Receiver at 100 m (b) Receiver at 300 m. Solid : BEM, Dashed : VISA, Dotted : Spectral super-element

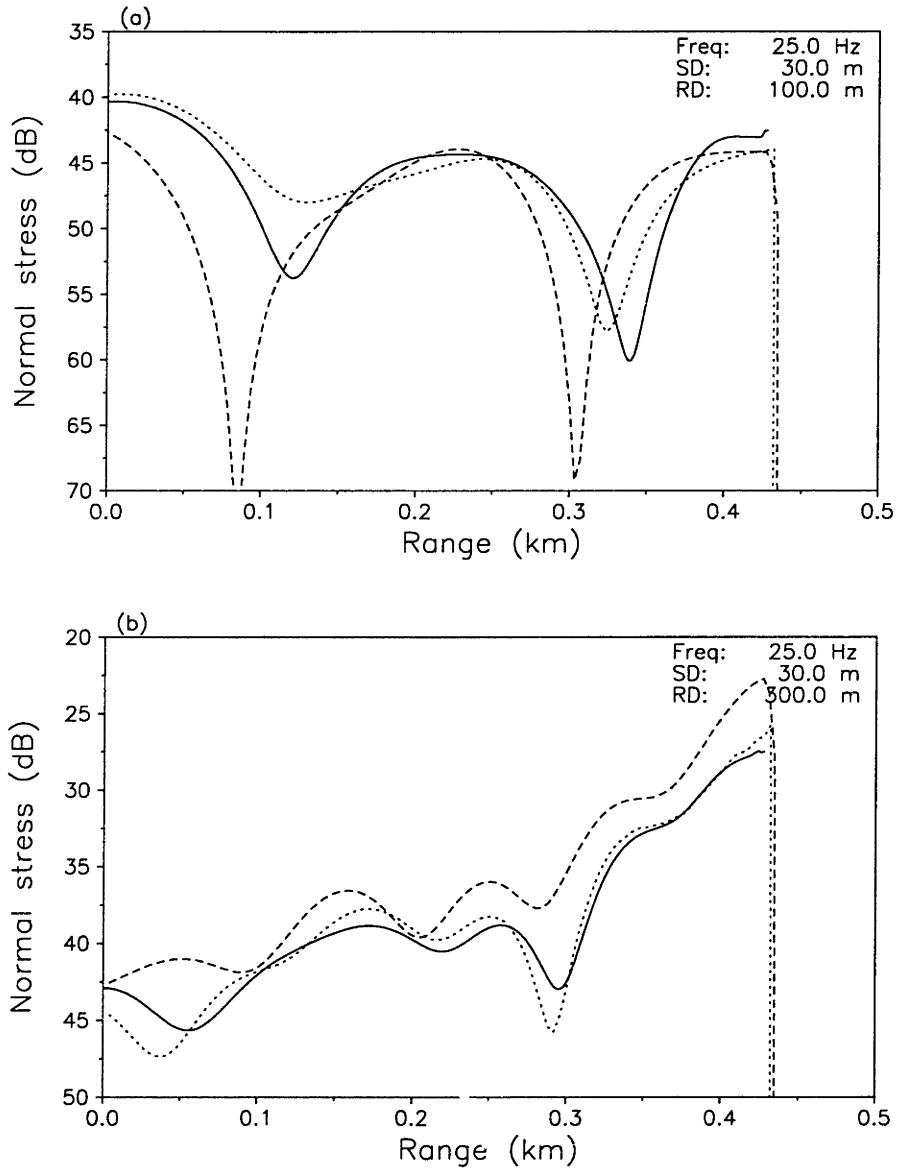

Figure 5-40: Diffraction from a Lloyd-mirror beam (Ex. Q). Backward normal stress (a) Receiver at 100 m (b) Receiver at 300 m. Solid : BEM, Dashed : VISA, Dotted : Spectral super-element

Chapter 6

Epilogue

In this thesis, we examined the application of coupled wavenumber integration techniques to solving the wave equation in *range-dependent elastic* environments. In particular, we are interested in solution techniques that are able to handle both short- and long-range propagation as well as model reverberation from large scale features. These techniques should also be *spectral-based* since they provide for the decomposition of the wavefields into fundamental modal components which helps in the physical interpretation of the numerical results.

In the first part of the thesis, we performed extensive numerical experiments using the adiabatic transform technique developed by Lu and Felsen [17]. The main result of these experiments is that the adiabatic transform approach works well in situations where the wavefield is largely modal in nature. The work contributed towards a better understanding of the mechanics behind the so-called '*spectral mapping*' techniques of Kamel and Felsen [28] and Lu and Felsen [17]. A method proposed by Tang and Guo [29] using the method of multiple scales also falls within this category. An important conclusion arising from this study is that the standard adiabatic mode approach is invalid for *virtual* modes - a point that is not often appreciated. Generally, any solution technique that relies on tracking the horizontal wavenumber as the environment changes must not only do a good job in the discrete spectrum but also track the complex eigenvalues of leaky modes [18]. The design of suitable spectral invariants valid over a wide spectrum of wavenumbers is a difficult task and any approach based on such techniques should be used with great care. Another major gripe with such

techniques is the need to search for complex roots, which is an extremely time consuming and unreliable process, rendering codes based on *spectral mapping* slow and possibly requiring human intervention in the root searching process. Since the spectral mapping process essentially determines the spectral content of the wavefield at any range step, any errors in the search process can erroneously contribute to mode coupling. It is also unclear how the adiabatic transform technique can be extended to elastic environments.

The next part of the work involves the generalisation of the spectral element method developed by Seong [25]. We first introduced several *important* modifications to the original fluid formulation. One of these is the introduction of the single-scatter approximation that decouples the *global* problem into a *local* one, thereby reducing tremendously the computational resources required. We also implemented a two-way marching algorithm that recovers an approximation to the back-scattered field. We also derived mapping matrices that permit us to map the expansion coefficients across sectors with different layer structures. These modifications are important because, with these extensions, the spectral element approach can now handle a much broader class of problems but still requiring only a modest amount of computational resources. We have now laid the groundwork for generalising the method to include the effects of elasticity in a practical code.

The most significant contribution of this thesis is the extension of the spectral method to handle arbitrary *fluid-elastic* stratifications. The formulation is new and non-trivial particularly in its implementation. An indirect contribution is that the derived potentials for the panel sources are also useful as virtual sources in the recently developed VISA code [24]. We have also expanded our toolbox of available source types to include vertical and horizontal point forces. Including these fundamental source types allow us to model more complex seismic processes, such as vertical strike faults [26]. The rigorous testing that we put our code through is also another important contribution. The benchmarks that we have designed have proved useful not only in testing our code but also in identifying weaknesses in other existing codes. These test problems will be an important resource for modelers involved in developing numerical propagation codes. In our benchmarking efforts, we have also learned several important lessons. Firstly, the choice of field parameters for making comparisons is very important. In particular, the 'equivalent shear stress' which is defined as the contribu-

tion from only the shear potential may not be an ideal candidate because it is not a physical variable, unlike displacements, and in some cases may be extremely unstable to compute. These benchmarks also highlight the fact that back-scatter is a particularly difficult process to model, compared to the forward field. This is especially true in cases where there exists a large dynamic range between the forward and back-scattered field. In the design of benchmarks, we found that fundamental source types such as the horizontal or vertical point forces, when placed in a symmetric waveguide, are extremely useful for exciting certain elastic wavefields for testing specific part of a code.

As always, there are further issues that could be addressed:

- Quadrature errors tend to control the accuracy of the final solutions. It would be useful to investigate further techniques, particularly from the mathematics literature, to apply to our integrals. Improving the numerical integration of our rather pathological integrals would go a long way towards further improving the robustness of the code.

- The modeling of the half-space is presently being done with dummy interfaces. This is not only inefficient but also degrades the solution somewhat due to accumulated errors in the quadratures. The present method of using basis function has been shown to fail [25] and a directed effort using new approaches would be needed.

- The current implementation allows for only either an explosive point source or a vertical or horizontal point force as our source types. The next step would be to find an efficient manner to include more than one source without resorting to having an artificial layer at the depth of each source. Ultimately, we would like to have the capability to include line arrays in our simulations.

- Time domain solutions by Fourier synthesis can be included easily.

This page is blank

Appendix A

Axisymmetric Environments

For cylindrical geometries, the Helmholtz reduced wave equation is

$$\frac{1}{r}\frac{\partial}{\partial r}\left(r\frac{\partial \Phi}{\partial r}\right) + \frac{\partial^2 \Phi}{\partial z^2} + h^2\Phi = 0\,. \tag{A.1}$$

We can separate out the cylindrical spreading effect by introducing

$$\phi(r,z) = \sqrt{\frac{\pi r}{2}}\Phi(r,z), \tag{A.2}$$

where the coefficient is selected to give 0 dB loss at $r = 1$ m. Eq. (A.1) then becomes

$$\frac{\partial^2 \phi}{\partial r^2} + \frac{1}{4r^2}\phi + \frac{\partial^2 \phi}{\partial z^2} + h^2\phi = 0\,. \tag{A.3}$$

For large r_j, we may neglect the second term, and we see that cylindrical spreading can be treated with the present 2D derivation simply by including a factor of $\sqrt{\frac{2}{\pi r_j}}$ in the final evaluation of the field.

Appendix B

Point Source Representation for Panel Sources

We derive a discretized equivalent point source spectral representation for the potentials of the distributed panel sources that is valid everywhere inside a layer. This allows the field computation to be carried out by efficient Fast Field Program (FFP) techniques. To simplify notation, we use a generic form,

$$\Phi_\ell(x,z) = \int_{-\infty}^{\infty} \frac{1}{\kappa^2} \left[A\,\Gamma(-i\mathcal{S}\nu) + B\,\Theta(-i\mathcal{S}\nu) \right] \frac{e^{-|z-\frac{t_\ell}{2}|\nu}}{\nu} e^{-ixs}\,ds, \tag{B.1}$$

where

$$\begin{aligned} \nu &= \alpha, \\ A &= -(2\alpha^2+\kappa^2), \\ B &= 2is\mathcal{S}\alpha, \end{aligned} \tag{B.2}$$

for the compressional potential $\Phi_\ell = \phi_\ell$ and

$$\begin{aligned} \nu &= \beta, \\ A &= -2is\mathcal{S}\beta, \\ B &= -(2s^2-\kappa^2), \end{aligned} \tag{B.3}$$

when Φ_ℓ is refering to the shear potential ψ_ℓ. Using the expressions for Γ and Θ in Eq. (4.31), we arrive at

$$\Phi_\ell(x,z) = \int_{-\infty}^{\infty} \frac{1}{\kappa^2} \Big[A \sum_{m=1}^{\infty} i^{m-1} \mathrm{U}_{\ell m}(0) j_{m-1}(\chi) + B \sum_{m=1}^{\infty} i^{m-1} \mathrm{W}_{\ell m}(0) j_{m-1}(\chi) \Big] \times \frac{e^{-|z-\frac{t_\ell}{2}|\nu}}{\nu} e^{-ixs}\, ds, \tag{B.4}$$

where $\chi = -it_\ell \mathcal{S}\nu/2$. We now replace the spherical Bessel function with its integral representation [53],

$$j_q(\chi) = \frac{1}{2}(-i)^q \int_0^\pi e^{i\chi\cos\theta} P_q(\cos\theta) \sin\theta\, d\theta. \tag{B.5}$$

Making the change of variable,

$$\cos\theta = \frac{z_s - t_\ell/2}{t_\ell/2}, \tag{B.6}$$

we obtain

$$\Phi_\ell(x,z) = \int_{-\infty}^{\infty} \frac{1}{\kappa^2} \Big\{ \sum_{m=1}^{\infty} \Big[A\, \mathrm{U}_{\ell m}(0) + B\, \mathrm{W}_{\ell m}(0) \Big] \times \frac{1}{t_\ell} \int_0^{t_\ell} e^{-|z-z_s|\nu} P_{m-1}\Big(\frac{z_s - t_\ell/2}{t_\ell/2} \Big) dz_s \Big\} \frac{e^{-ixs}}{\nu} ds. \tag{B.7}$$

The above equation converges for every field point z and is in the form of a continuous distribution of acoustic point sources. Numerical evaluation of the inner integral is a very expensive operation and instead we will replace it with a summation of point sources. These point sources are located at the Gauss-Legendre quadrature points. We first make the following change of variable,

$$t = \frac{z_s - t_\ell/2}{t_\ell/2}, \tag{B.8}$$

for the inner integral to obtain,

$$\frac{1}{t_\ell} \int_0^{t_\ell} e^{-|z-z_s|\nu} P_{m-1}\Big(\frac{z_s - t_\ell/2}{t_\ell/2} \Big) dz_s = \frac{1}{2} \int_{-1}^{1} P_{m-1}(t)\, e^{-|z-\frac{t_\ell}{2}(t+1)|\nu}\, dt. \tag{B.9}$$

Finally, the equivalent point source representation for the generic form of the potential is

$$\Phi_\ell(x,z) = \sum_{j=1}^{N_e} \frac{1}{2} \int_{-\infty}^{\infty} \frac{e^{-ixs}}{\kappa^2 \nu} ds \sum_{m=1}^{\infty} \Big[A\, \mathrm{U}_{\ell m}(0) + B\, \mathrm{W}_{\ell m}(0) \Big] P_{m-1}(t_j)\, W_j\, e^{-|z-\frac{t_\ell}{2}(t_j+1)|\nu} \tag{B.10}$$

where N_e is the number of discrete sources used to represent the continuous panel sources. A general rule of thumb is that N_e is at least twice the order of Legendre expansion used. The Gauss quadrature points t_j and weights W_j are given by [53]

$$\begin{aligned} t_j &= j\text{th zero of } P_{m-1}(x), \\ W_j &= \frac{2}{1-t_j^2}\left[P'_{m-1}(t_j)\right]^2. \end{aligned} \tag{B.11}$$

Appendix C

Direct Solution for Panel Sources

Horizontal Wavenumber Representation

The potentials in the $s-$domain are

$$\begin{aligned}
\Phi_\ell(x,z) &= \int_{-\infty}^{\infty} \left[-\frac{\vartheta}{s\kappa^2}\,\Gamma(-i\mathcal{S}\alpha) + \frac{2i\mathcal{S}\alpha}{\kappa^2}\,\Theta(-i\mathcal{S}\alpha) \right] e^{-|z-\frac{t_\ell}{2}|\alpha}\,\frac{s}{\alpha}\,e^{-ixs}\,ds, \\
\Psi_\ell(x,z) &= \int_{-\infty}^{\infty} \left[-\frac{2i\mathcal{S}\beta}{\kappa^2}\,\Gamma(-i\mathcal{S}\beta) - \frac{\varpi}{s\kappa^2}\,\Theta(-i\mathcal{S}\beta) \right] e^{-|z-\frac{t_\ell}{2}|\beta}\,\frac{s}{\beta}\,e^{-ixs}\,ds. \qquad \text{(C.1)}
\end{aligned}$$

The field expressions required for the DGM forcing can be compactly written in matrix form,

$$\hat{\mathbf{V}}_\ell(x,z) = \sum_{m=1}^{\infty} \int_{-\infty}^{\infty} [\mathrm{U}_{\ell m}(0)\,\hat{\mathbf{K}}_{\mathbf{u}} + \mathrm{W}_{\ell m}(0)\,\hat{\mathbf{K}}_{\mathbf{w}}]\,\hat{\mathbf{E}}\,\hat{\mathbf{J}}_{\mathbf{m}}\,e^{-ixs}\,ds, \qquad \text{(C.2)}$$

where

$$\begin{aligned}
\hat{\mathbf{V}}_\ell(x,z) &= \begin{bmatrix} u & w & \sigma_{zz}/\mu & \sigma_{xz}/\mu \end{bmatrix}^T, \\
\hat{\mathbf{E}} &= \mathrm{diag}\,[e^{-|z-\frac{t_\ell}{2}|\alpha}, e^{-|z-\frac{t_\ell}{2}|\beta}], \\
\hat{\mathbf{J}}_{\mathbf{m}} &= \begin{bmatrix} i^{m-1}\,j_{m-1}(\,-i\mathcal{S}t_\ell\alpha/2\,) \\ i^{m-1}\,j_{m-1}(\,-i\mathcal{S}t_\ell\beta/2\,) \end{bmatrix}, \\
\hat{\mathbf{K}}_{\mathbf{u}} &= \frac{1}{\kappa^2} \begin{bmatrix} is\vartheta\alpha^{-1} & -2is\beta \\ \mathcal{S}\vartheta & -2\mathcal{S}s^2 \\ -\varpi\vartheta\alpha^{-1} & 4s^2\beta \\ -2i\mathcal{S}s\vartheta & 2i\mathcal{S}s\varpi \end{bmatrix},
\end{aligned}$$

$$\hat{\mathbf{K}}_{\mathbf{w}} = \frac{1}{\kappa^2}\begin{bmatrix} 2\mathcal{S}s^2 & -\mathcal{S}\varpi \\ -2is\alpha & is\varpi\beta^{-1} \\ 2i\mathcal{S}s\varpi & -2i\mathcal{S}s\varpi \\ -4s^2\alpha & \varpi^2\beta^{-1} \end{bmatrix},$$

with

$$\begin{aligned} \mathcal{S} &= \text{sign}(z - t_\ell/2), \\ \alpha &= \sqrt{s^2 - h^2}, \\ \beta &= \sqrt{s^2 - \kappa^2}, \\ \varpi &= 2s^2 - \kappa^2, \\ \vartheta &= 2\alpha^2 + \kappa^2. \end{aligned}$$

Basis Function Expansion

The potentials in the vertical wavenumber domain are given by

$$\begin{aligned} \mathbf{\Phi}_\ell(x,z) &= \int_{-\infty}^{\infty}\left[\frac{\varphi}{\kappa^2\gamma}\,\Gamma(\eta) + \frac{2i\eta}{\kappa^2}\,\Theta(\eta)\right] e^{-x\gamma}e^{-i\eta(z-t_\ell/2)}\,d\eta, \\ \mathbf{\Psi}_\ell(x,z) &= \int_{-\infty}^{\infty}\left[-\frac{2i\eta}{\kappa^2}\,\Gamma(\eta) + \frac{\varphi}{\kappa^2\delta}\,\Theta(\eta)\right] e^{-x\delta}e^{-i\eta(z-t_\ell/2)}\,d\eta. \end{aligned} \tag{C.3}$$

The expansion coefficients can be compactly expressed as

$$\begin{aligned} \hat{\mathbf{V}}_{\ell m}(x) = C_m \sum_{k=1}^{\infty} i^{m+k-2} \int_{-\infty}^{\infty} [\, \mathrm{U}_{\ell k}(0)\,\hat{\mathbf{K}}_{\mathbf{u}} \\ + \mathrm{W}_{\ell k}(0)\,\hat{\mathbf{K}}_{\mathbf{w}}\,]\,\hat{\mathbf{E}}\, j_{m-1}\!\left(\frac{t_\ell\eta}{2}\right) j_{k-1}\!\left(\frac{t_\ell\eta}{2}\right) d\eta, \end{aligned} \tag{C.4}$$

where

$$\hat{\mathbf{V}}_{\ell m}(x) = \begin{bmatrix} \hat{\mathrm{U}}_{\ell m} & \hat{\mathrm{W}}_{\ell m} & \hat{\mathrm{T}}_{\ell m} & \hat{\mathrm{S}}_{\ell m} \end{bmatrix}^T,$$

$$\hat{\mathbf{E}} = \begin{bmatrix} e^{-x\gamma} & e^{-x\delta} \end{bmatrix}^T,$$

$$\hat{\mathbf{K}}_{\mathbf{u}} = \frac{1}{\kappa^2}\begin{bmatrix} -\varphi & 2\eta^2 \\ -i\eta\varphi\gamma^{-1} & 2i\eta\delta \\ \varphi^2\gamma^{-1} & -4\eta^2\delta \\ 2i\eta\varphi & -2i\eta\varphi \end{bmatrix},$$

$$\hat{\mathbf{K}}_{\mathbf{w}} = \frac{1}{\kappa^2}\begin{bmatrix} -2i\eta\gamma & i\eta\varphi\delta^{-1} \\ 2\eta^2 & -\varphi \\ 2i\eta\varphi & -2i\eta\varphi \\ -4\eta^2\gamma & \varphi^2\delta^{-1} \end{bmatrix},$$

with

$$\begin{aligned} \zeta_m &= (-1)^{m-1}, \\ C_m &= \frac{t_\ell}{2\pi}(2m-1)\zeta_m, \\ \gamma &= \sqrt{\eta^2 - h^2}, \\ \delta &= \sqrt{\eta^2 - \kappa^2}, \\ \varphi &= 2\eta^2 - \kappa^2. \end{aligned}$$

Note that the third parameter refers to the stress quantity σ_{xx}/μ instead of σ_{zz}/μ.

Appendix D

Homogeneous Solution for Panel Sources

Horizontal Wavenumber Integral Representation

The horizontal wavenumber integral representation for the homogeneous solution can be obtained by direct extension of the equations presented in Schmidt and Jensen [48]. The complete solution is given by the sum over all finite layers as well as over all orders of expansion.

$$\bar{\mathbf{v}}_\ell(x,z) = \sum_{n=2}^{N-1} \sum_{k=1}^{\infty} \int_{-\infty}^{\infty} \bar{\mathbf{K}}\, \bar{\mathbf{E}}\, [\, \mathrm{U}_{nk}(0)\, \bar{\mathbf{A}} \;+\; \mathrm{W}_{nk}(0)\, \bar{\mathbf{C}}\,]\, e^{-ixs}\, ds, \tag{D.1}$$

where

$$\bar{\mathbf{v}}_\ell(x,z) \;=\; \left[\; u \quad w \quad \sigma_{zz}/\mu \quad \sigma_{xz}/\mu \;\right]^T,$$

$$\bar{\mathbf{K}} \;=\; \begin{bmatrix} -is & -is & i\beta & -i\beta \\ -\alpha & \alpha & s & s \\ \varpi & \varpi & -2s\beta & 2s\beta \\ 2is\alpha & -2is\alpha & -i\varpi & -i\varpi \end{bmatrix},$$

$$\bar{\mathbf{E}} \;=\; \mathrm{diag}\left[e^{-z\alpha}\,,\, e^{(z-t_\ell)\alpha}\,,\, e^{-z\beta}\,,\, e^{(z-t_\ell)\beta} \right],$$

$$\bar{\mathbf{A}} = \left[\begin{array}{cccc} A^-_{\ell,nk} & A^+_{\ell,nk} & B^-_{\ell,nk} & B^+_{\ell,nk} \end{array} \right]^T,$$

$$\bar{\mathbf{C}} = \left[\begin{array}{cccc} C^-_{\ell,nk} & C^+_{\ell,nk} & D^-_{\ell,nk} & D^+_{\ell,nk} \end{array} \right]^T. \tag{D.2}$$

Each combination of indices n and k represents a single SAFARI run. Here $A^{\mp}_{\ell,nk}$ and $B^{\mp}_{\ell,nk}$ are respectively the up/down going compressional and shear waves in layer ℓ due to the kth order *symmetric* source in layer n. The corresponding quantities from the *antisymmetric* source are $C^{\mp}_{\ell,nk}$ and $D^{\mp}_{\ell,nk}$.

Series Representation

Using the orthogonality relation of Legendre polynomials, expansion coefficients can be extracted as

$$\bar{\mathbf{V}}_{\ell m}(x) = (2m-1)i^{m-1} \int_{-\infty}^{\infty} \sum_{n=2}^{N-1} \sum_{k=1}^{\infty} \bar{\mathbf{K}}_\ell \, \bar{\mathbf{E}}_\ell \, \bar{\mathbf{J}}_{\ell m} \times \left[\, \mathrm{U}_{nk}(0) \, \bar{\mathbf{A}}_{\ell,nk} + \mathrm{W}_{nk}(0) \, \bar{\mathbf{C}}_{\ell,nk} \, \right] e^{-ixs} \, ds, \tag{D.3}$$

where

$$\bar{\mathbf{V}}_{\ell m}(x) = \left[\begin{array}{cccc} \bar{\mathrm{U}}_{\ell m} & \bar{\mathrm{W}}_{\ell m} & \bar{\mathrm{T}}_{\ell m} & \bar{\mathrm{S}}_{\ell m} \end{array} \right]^T,$$

$$\bar{\mathbf{K}}_\ell = \left[\begin{array}{cccc} -is & -is & i\beta & -i\beta \\ -\alpha & \alpha & s & s \\ -\vartheta & -\vartheta & 2s\beta & -2s\beta \\ 2is\alpha & -2is\alpha & -i\varpi & -i\varpi \end{array} \right],$$

$$\bar{\mathbf{E}}_\ell = \mathrm{diag}\left[e^{-\frac{t_\ell}{2}\alpha}, e^{-\frac{t_\ell}{2}\alpha}, e^{-\frac{t_\ell}{2}\beta}, e^{-\frac{t_\ell}{2}\beta} \right],$$

$$\bar{\mathbf{A}}_{\ell,nk} = \left[\begin{array}{cccc} A^-_{\ell,nk} & A^+_{\ell,nk} & B^-_{\ell,nk} & B^+_{\ell,nk} \end{array} \right]^T,$$

$$\bar{\mathbf{C}}_{\ell,nk} = \left[\begin{array}{cccc} C^-_{\ell,nk} & C^+_{\ell,nk} & D^-_{\ell,nk} & D^+_{\ell,nk} \end{array} \right]^T,$$

$$\bar{\mathbf{J}}_{\ell m} = \mathrm{diag}\left[j_{m-1}\left(\frac{it_\ell\alpha}{2}\right), \zeta_m j_{m-1}\left(\frac{it_\ell\alpha}{2}\right), j_{m-1}\left(\frac{it_\ell\beta}{2}\right), \zeta_m j_{m-1}\left(\frac{it_\ell\beta}{2}\right) \right].$$

Note that the third parameter refers to the stress quantity σ_{xx}/μ instead of σ_{zz}/μ.

Appendix E

Direct Solution for Physical Sources

In the current implementation, we allow for three types of sources - the explosive point source, vertical point force and horizontal point force. Note here that in the basis function representations, the third field parameter refers to the stress σ_{xx}/μ instead of σ_{zz}/μ.

E.1 Explosive Point Source

The explosive point source has the following integral representations,

$$\begin{aligned} \phi^* &= \int_{-\infty}^{\infty} \frac{e^{-|z-z_s|\alpha}}{\alpha} e^{-i(x-x_s)s}\, ds \\ \chi^* &= 0, \end{aligned} \tag{E.1}$$

where z_s and x_s is the source depth and range respectively.

Horizontal Wavenumber Integral Representation

Field equations for the acoustic point source are given by

$$\overset{*}{\mathbf{v}}_\ell(x,z) = \int_{-\infty}^{\infty} \overset{*}{\mathbf{K}} e^{-|z-z_s|\alpha_n} e^{-i(x-x_s)s} ds, \tag{E.2}$$

with

$$\overset{*}{\mathbf{v}}_\ell(x,z) = \begin{bmatrix} w & u & \sigma_{zz}/\mu & \sigma_{xz}/\mu \end{bmatrix}^T,$$

$$\overset{*}{\mathbf{K}} = \begin{Bmatrix} -\operatorname{sign}(z-z_s) \\ -is/\alpha \\ \varpi/\alpha \\ 2is\operatorname{sign}(z-z_s) \end{Bmatrix}.$$

Basis Function Expansion

Extracting the expansion coefficients via the orthogonality relation of the Legendre polynomials gives us

$$\overset{*}{\mathbf{V}}_m(x) = (2m-1)i^{m-1}\int_{-\infty}^{\infty} \overset{*}{\mathbf{K}} e^{-\frac{t_\ell}{2}\alpha} j_{m-1}\left(\frac{it_\ell\alpha}{2}\right) e^{-i(x-x_s)s}\, ds, \tag{E.3}$$

where

$$\overset{*}{\mathbf{V}}_m(x) = \begin{bmatrix} \overset{*}{\mathrm{U}}_{\ell m} & \overset{*}{\mathrm{W}}_{\ell m} & \overset{*}{\mathrm{T}}_{\ell m} & \overset{*}{\mathrm{S}}_{\ell m} \end{bmatrix}^T,$$

$$\overset{*}{\mathbf{K}} = \begin{Bmatrix} -is/\alpha \\ -\operatorname{sign}(z-z_s) \\ -\vartheta/\alpha \\ 2is\operatorname{sign}(z-z_s) \end{Bmatrix}.$$

E.2 Vertical Point Force

The vertical point force has the following integral representations,

$$\begin{aligned} \phi^* &= \operatorname{sign}(z-z_s)\int_{-\infty}^{\infty} e^{-|z-z_s|\alpha}\, e^{-i(x-x_s)s}\, ds, \\ \psi^* &= i\int_{-\infty}^{\infty} \frac{s}{\beta}\, e^{-|z-z_s|\beta}\, e^{-i(x-x_s)s}\, ds. \end{aligned} \tag{E.4}$$

Horizontal Wavenumber Integral Representation

Field equations for the vertical point force are given by

$$\overset{*}{\mathbf{v}}_\ell(x,z) = \int_{-\infty}^{\infty} \{\, \overset{*}{\mathbf{K}} e^{-|z-z_s|\alpha_n} + \overset{*}{\mathbf{J}} e^{-|z-z_s|\beta_n} \,\}\, e^{-i(x-x_s)s} ds, \tag{E.5}$$

with

$$\overset{*}{\mathbf{v}}_\ell(x,z) = \left[\begin{array}{cccc} w & u & \sigma_{zz}/\mu & \sigma_{xz}/\mu \end{array}\right]^T,$$

$$\overset{*}{\mathbf{K}} = \left\{\begin{array}{c} -\alpha \\ -is\ \mathrm{sign}(z-z_s) \\ \varpi\ \mathrm{sign}(z-z_s) \\ 2is\alpha \end{array}\right\},$$

$$\overset{*}{\mathbf{J}} = \left\{\begin{array}{c} s^2/\beta \\ is\ \mathrm{sign}(z-z_s) \\ -2s^2\ \mathrm{sign}(z-z_s) \\ -is\varpi/\beta \end{array}\right\}.$$

Basis Function Expansion

The expansion coefficients are given by

$$\overset{*}{\mathbf{V}}_m(x) = (2m-1)i^{m-1}\int_{-\infty}^{\infty}\left\{\overset{*}{\mathbf{K}}\, e^{-\frac{t_\ell}{2}\alpha}\, j_{m-1}\left(\frac{it_\ell\alpha}{2}\right) + \overset{*}{\mathbf{J}}\, e^{-\frac{t_\ell}{2}\beta}\, j_{m-1}\left(\frac{it_\ell\beta}{2}\right)\right\} e^{-i(x-x_s)s}\, ds, \quad \text{(E.6)}$$

where

$$\overset{*}{\mathbf{V}}_m(x) = \left[\begin{array}{cccc} \overset{*}{\mathrm{U}}_{\ell m} & \overset{*}{\mathrm{W}}_{\ell m} & \overset{*}{\mathrm{T}}_{\ell m} & \overset{*}{\mathrm{S}}_{\ell m} \end{array}\right]^T,$$

$$\overset{*}{\mathbf{K}} = \left\{\begin{array}{c} -is \\ -\alpha \\ -\vartheta\ \mathrm{sign}(z-z_s) \\ 2is\alpha \end{array}\right\},$$

$$\overset{*}{\mathbf{J}} = \left\{\begin{array}{c} is \\ s^2/\beta \\ 2s^2 \\ -is\varpi/\beta \end{array}\right\}.$$

E.3 Horizontal Point Force

The horizontal point force has the following integral representations,

$$\begin{aligned} \phi^* &= i \int_{-\infty}^{\infty} \frac{s}{\alpha} e^{-|z-z_s|\alpha} e^{-i(x-x_s)s} \, ds, \\ \psi^* &= -\text{sign}(z-z_s) \int_{-\infty}^{\infty} e^{-|z-z_s|\beta} e^{-i(x-x_s)s} \, ds. \end{aligned} \tag{E.7}$$

Horizontal Wavenumber Integral Representation

Field equations for the horizontal point force are given by

$$\overset{*}{\mathbf{v}}_\ell(x,z) = \int_{-\infty}^{\infty} \{ \overset{*}{\mathbf{K}} e^{-|z-z_s|\alpha_n} + \overset{*}{\mathbf{J}} e^{-|z-z_s|\beta_n} \} \, e^{-i(x-x_s)s} ds, \tag{E.8}$$

with

$$\overset{*}{\mathbf{v}}_\ell(x,z) = \begin{bmatrix} w & u & \sigma_{zz}/\mu & \sigma_{xz}/\mu \end{bmatrix}^T,$$

$$\overset{*}{\mathbf{K}} = \begin{Bmatrix} -is \, \text{sign}(z-z_s) \\ s^2/\alpha \\ is\varpi/\alpha \\ -2s^2 \, \text{sign}(z-z_s) \end{Bmatrix},$$

$$\overset{*}{\mathbf{J}} = \begin{Bmatrix} is \, \text{sign}(z-z_s) \\ -\beta \\ -2is\beta \\ \varpi \, \text{sign}(z-z_s) \end{Bmatrix}.$$

Basis Function Expansion

The expansion coefficients are given by

$$\begin{aligned} \overset{*}{\mathbf{V}}_m(x) = (2m-1) i^{m-1} \int_{-\infty}^{\infty} \Big\{ & \overset{*}{\mathbf{K}} \, e^{-\frac{t_\ell}{2}\alpha} \, j_{m-1}\left(\frac{it_\ell\alpha}{2}\right) \\ & + \overset{*}{\mathbf{J}} \, e^{-\frac{t_\ell}{2}\beta} \, j_{m-1}\left(\frac{it_\ell\beta}{2}\right) \Big\} \, e^{-i(x-x_s)s} \, ds, \end{aligned} \tag{E.9}$$

where

$$\overset{*}{\mathbf{V}}_m(x) = \left[\begin{array}{cccc} \overset{*}{\mathrm{U}}_{\ell m} & \overset{*}{\mathrm{W}}_{\ell m} & \overset{*}{\mathrm{T}}_{\ell m} & \overset{*}{\mathrm{S}}_{\ell m} \end{array} \right]^T,$$

$$\overset{*}{\mathbf{K}} = \left\{ \begin{array}{c} s^2/\alpha \\ -is\ \mathrm{sign}(z - z_s) \\ -is\vartheta/\alpha \\ -2s^2\ \mathrm{sign}(z - z_s) \end{array} \right\},$$

$$\overset{*}{\mathbf{J}} = \left\{ \begin{array}{c} -\beta \\ is\ \mathrm{sign}(z - z_s) \\ 2is\beta \\ \varpi\ \mathrm{sign}(z - z_s) \end{array} \right\}.$$

Appendix F

Homogeneous Solution for Physical Sources

Horizontal Wavenumber Integral Representation

The integral representations are given by

$$\tilde{\mathbf{v}}_\ell(x,z) = \int_{-\infty}^{\infty} \tilde{\mathbf{K}}\ \tilde{\mathbf{E}}\ \tilde{\mathbf{A}}\ e^{-i(x-x_s)s}\, ds, \tag{F.1}$$

where

$$\begin{aligned}
\tilde{\mathbf{v}}_\ell(x,z) &= \begin{bmatrix} u & w & \sigma_{zz}/\mu & \sigma_{xz}/\mu \end{bmatrix}^T, \\
\tilde{\mathbf{K}} &= \begin{bmatrix} -is & -is & i\beta & -i\beta \\ -\alpha & \alpha & s & s \\ \varpi & \varpi & -2s\beta & 2s\beta \\ 2is\alpha & -2is\alpha & -i\varpi & -i\varpi \end{bmatrix}, \\
\tilde{\mathbf{E}} &= \operatorname{diag}\left[e^{-z\alpha}, e^{(z-t_\ell)\alpha}, e^{-z\beta}, e^{(z-t_\ell)\beta}\right], \\
\tilde{\mathbf{A}} &= \begin{bmatrix} A_\ell^- & A_\ell^+ & B_\ell^- & B_\ell^+ \end{bmatrix}^T.
\end{aligned}$$

Note how the depth separated part is written such that waves generated at each horizontal interfaces decays as they propagate away, rendering the scheme unconditionally stable.

Basis Function Expansion

Similarly, the basis function expansions are

$$\tilde{\mathbf{V}}_{\ell m}(x) = (2m-1)i^{m-1}\int_{-\infty}^{\infty} \tilde{\mathbf{K}}_\ell\ \tilde{\mathbf{E}}_\ell\ \tilde{\mathbf{J}}_{\ell m}\ \tilde{\mathbf{A}}_\ell\ e^{-i(x-x_s)s}\,ds, \tag{F.2}$$

where $\tilde{\mathbf{K}}$, $\tilde{\mathbf{E}}$ and $\tilde{\mathbf{J}}$ are the same as that of the homogeneous solution for the panel source.

$$\tilde{\mathbf{V}}_{\ell m}(x) = \left[\begin{array}{cccc} \tilde{\mathrm{U}}_{\ell m} & \tilde{\mathrm{W}}_{\ell m} & \tilde{\mathrm{T}}_{\ell m} & \tilde{\mathrm{S}}_{\ell m} \end{array}\right]^T,$$

$$\tilde{\mathbf{K}}_\ell = \left[\begin{array}{cccc} -is & -is & i\beta & -i\beta \\ -\alpha & \alpha & s & s \\ -\vartheta & -\vartheta & 2s\beta & -2s\beta \\ 2is\alpha & -2is\alpha & -i\varpi & -i\varpi \end{array}\right],$$

$$\tilde{\mathbf{E}}_\ell = \mathrm{diag}\left[e^{-\frac{t_\ell}{2}\alpha}, e^{-\frac{t_\ell}{2}\alpha}, e^{-\frac{t_\ell}{2}\beta}, e^{-\frac{t_\ell}{2}\beta}\right],$$

$$\tilde{\mathbf{A}}_\ell = \left[\begin{array}{cccc} A_\ell^- & A_\ell^+ & B_\ell^- & B_\ell^+ \end{array}\right]^T,$$

$$\tilde{\mathbf{J}}_{\ell m} = \mathrm{diag}\left[j_{m-1}\left(\frac{it_\ell\alpha}{2}\right), \zeta_m j_{m-1}\left(\frac{it_\ell\alpha}{2}\right), j_{m-1}\left(\frac{it_\ell\beta}{2}\right), \zeta_m j_{m-1}\left(\frac{it_\ell\beta}{2}\right)\right].$$

Note here that the third parameter refers to the stress σ_{xx}/μ instead of σ_{zz}/μ.

Appendix G

Deriving s-domain Forms for Panel Sources

This Appendix is largely adapted from Woojae's thesis [25] and is included here for completeness. No modifications are needed in the elastic case since it turns out that there is only one branch point in each potential and the same deformation technique can be applied to each potential independently. Below, we describe the technique applied to the potential for the symmetric source.

The panel sources which are originally written in terms of a vertical wavenumber integral,

$$\phi(x,z) = \int_{-\infty}^{\infty} A(\eta)\, e^{-x\sqrt{\eta^2-h^2}}\, e^{-i(z-\frac{l}{2})\eta}\, d\eta \tag{G.1}$$

must be re-written into an integral in terms of a horizontal wavenumber so that we can use the direct global matrix method for layered media (SAFARI) to obtain the corresponding homogeneous solutions. To this end, we employ the mechanics of complex contour integration.

CASE I ($z < l/2$)

Consider a closed contour integration in the complex ξ plane as indicated in Fig. (G-1)

$$I = \oint A(i\sqrt{\xi^2-h^2})\, e^{-ix\xi}\, e^{(z-\frac{l}{2})\sqrt{\xi^2-h^2}}\, \frac{i\xi}{\sqrt{\xi^2-h^2}}\, d\xi \tag{G.2}$$

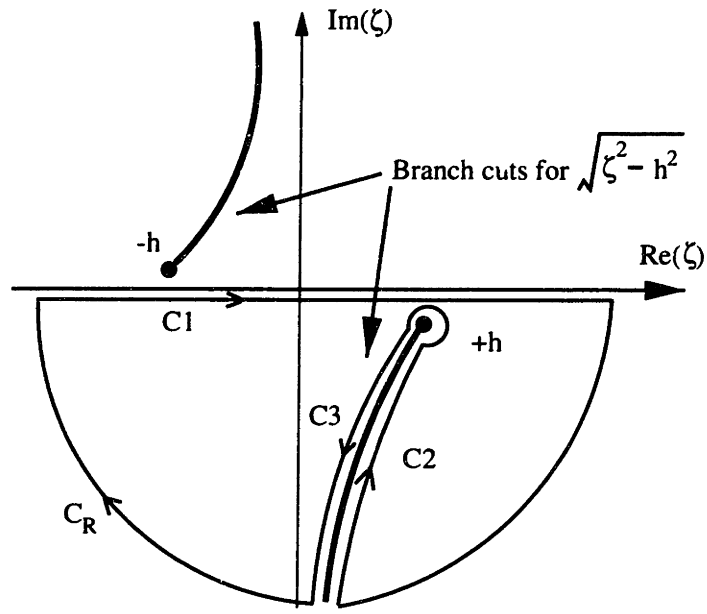

Figure G-1: Contour deformation to derive horizontal wavenumber representation.

where the analytic function A is the same as that of Eq. (G.1) and h is the acoustic medium wavenumber with a small negative imaginary part accounting for the volume attenuation which can be either specified or taken from an empirical formula [16].

The branch cuts originating from the square root singularities $\pm h$ and extending to infinity are chosen such that $\sqrt{\xi^2 - h^2}$ becomes purely imaginary along the branch cut. Denoting each contribution of the closed contour as depicted in Fig. G-1 and realizing that there are no singularities inside the closed contour, Cauchy's theorem gives us

$$I = I_{C_1} + I_{C_2} + I_{C_3} + I_{C_\rho} + I_{C_R} = 0. \tag{G.3}$$

Since C_1 is running along the real axis of the complex ξ plane,

$$I_{C_1} = \int_{-\infty}^{\infty} A(i\sqrt{s^2 - h^2})\, e^{-ixs}\, e^{(z-\frac{l}{2})\sqrt{s^2-h^2}}\, \frac{is}{\sqrt{s^2 - h^2}}\, ds \tag{G.4}$$

and this is the required horizontal wavenumber integral representation. Along C_2 and C_3, the arguments of $\sqrt{\xi^2 - h^2}$ are $-\frac{\pi}{2}$ and $\frac{\pi}{2}$ respectively so that the following change of variables are valid:

$$\sqrt{\xi^2 - h^2} \;=\; -i\eta \quad \text{along } C_2 \tag{G.5}$$

$$\sqrt{\xi^2 - h^2} \;=\; +i\eta \quad \text{along } C_3\,. \tag{G.6}$$

With the above change of variables,

$$\begin{aligned} I_{C_2} + I_{C_3} &= \int_{\infty}^{0} A(\eta)\, e^{-x\sqrt{\eta^2-h^2}}\, e^{-i(z-\frac{l}{2})\eta}\, d\eta \;-\; \int_{0}^{\infty} A(-\eta)\, e^{-x\sqrt{\eta^2-h^2}}\, e^{i(z-\frac{l}{2})\eta}\, d\eta \\ &= -\int_{-\infty}^{\infty} A(\eta)\, e^{-x\sqrt{\eta^2-h^2}}\, e^{-i(z-\frac{l}{2})\eta}\, d\eta \\ &= -\phi(x,z) \end{aligned} \tag{G.7}$$

where the last equality comes directly from Eq. (G.1). Denoting the kernel of Eq. (G.2) as $f(\xi)$, on the circular arc C_ρ, the value of $(\xi - h)f(\xi) \to 0$ uniformly as $\rho \to 0$. Thus from the theorem on limiting contours,

$$I_{C_\rho} = \lim_{\rho \to 0} \int_{C_\rho} f(\xi)\, d\xi = 0\,. \tag{G.8}$$

Using Jordan's lemma, the contribution along the infinite circular arc C_R vanishes if the kernel $f(\xi)$ without the $e^{-ix\xi}$ part, where $x > 0$ for our choice of coordinate system, tends uniformly to zero

$$I_{C_R} = \lim_{R \to \infty} \int_{C_R} f(\xi)\, d\xi = 0 \tag{G.9}$$

Using the principal asymptotic expansion for large arguments of the Bessel function [53] in Eq. (3.20), we obtain

$$\begin{aligned} \frac{f(\xi)}{e^{-ix\xi}} &\sim \frac{1}{\sqrt{\xi^2 - h^2}}\, e^{(z-\frac{l}{2})\sqrt{\xi^2-h^2}}\, j_{m-1}(il\sqrt{\xi^2 - h^2}/2), \\ &\sim \frac{1}{(\xi^2 - h^2)^{\frac{3}{4}}} [e^{(z-l)\sqrt{\xi^2-h^2}} + e^{z\sqrt{\xi^2-h^2}}]. \end{aligned} \tag{G.10}$$

So as long as $z \leq 0$, the kernel tends uniformly to zero along the infinite circular arc and I_{C_R} becomes zero. Collecting Eq. (G.3) through Eq. (G.10), we arrive at the desired equivalent horizontal wavenumber integral representation as

$$\phi(x,z) = \int_{-\infty}^{\infty} A(i\sqrt{s^2 - h^2})\, e^{-ixs}\, e^{(z-\frac{l}{2})\sqrt{s^2-h^2}}\, \frac{is}{\sqrt{s^2 - h^2}}\, ds \tag{G.11}$$

which is valid for $z \leq 0$.

CASE II ($z > l/2$)

Following the same analogy as the previous case, the horizontal wavenumber integral valid for $z \geq l$ becomes

$$\phi(x,z) = \int_{-\infty}^{\infty} A(-i\sqrt{s^2-h^2})\, e^{-ixs}\, e^{-(z-\frac{l}{2})\sqrt{s^2-h^2}}\, \frac{is}{\sqrt{s^2-h^2}}\, ds \ . \tag{G.12}$$

Collecting Eq. (G.11) and Eq. (G.12),

$$\phi(x,z) = i \int_{-\infty}^{\infty} A(-\text{sign}(z-\frac{l}{2})i\sqrt{s^2-h^2})\, e^{-|z-\frac{l}{2}|\sqrt{s^2-h^2}}\, \frac{s}{\sqrt{s^2-h^2}}\, e^{-ixs}\, ds \tag{G.13}$$

which is valid for $z \leq 0$ and $z \geq l$. Although this equation is not valid inside the finite layer where the displacement solution is located, it is still useful to find the accompanying homogeneous solutions for layered medium using the direct global matrix method since the boundary conditions are applied at the interface of the layers where the expression is still valid.

Appendix H

Numerical Evaluation of Influence Integrals

In Chapter 4, we presented the mathematical formulation of our spectral super element method that is capable of handling arbitrary fluid-elastic stratifications. The implementation of the theory into a numerical code requires special attention. In particular extra care must be given to the numerical quadrature of the *infinite* integrals required to obtain the expansion coefficients. These integrations are particularly difficult since the integrands are *slowly convergent* and *highly oscillatory* at infinity with an irregular oscillatory frequency determined by the relative orders of two spherical Bessel functions. In addition, at large wavenumbers, we require proper cancellation of the contributions arising from the symmetric and antisymmetric sources in order to arrive at a finite value for the expansion coefficients. Here we describe the various quadrature schemes adopted to deal with the integrals. Extensive numerical experiments have showed that the adaptive integration approach is the most robust and consistently provided good results.

H.1 Adaptive Integration

We use adaptive integration routines from the QUADPACK [54] library, particularly subroutine QAGS. In addition, we have also included an improved version of the subroutine called

QXGS [55]. QUADPACK is a collection of FORTRAN programs for the numerical evaluation of integrals. The programs are explicitly written for one-dimensional integrals with real integrands. We have implemented wrapper routines that does the same for complex-valued integrands by integrating the real and imaginary parts separately. This is not necessarily the most efficient but nevertheless produces very good results. We transform our infinite integrals into finite ones with the domain of integration between zero and unity. After that, we simply use the QUADPACK routines directly with no further manipulation.

H.2 Integrating in Between Zeros of the Integrand

We have also implemented a brute force method in which partial sums of the integrand are obtained by integrating in between the zeros of the oscillating integrand. An acceleration technique is then used to speed up the convergence of the partial sums.

H.3 Automatic Gauss-Chebyshev Quadrature

In addition to the above two methods, we also employ an automatic Gauss-Chebyshev quadrature technique. The discussion presented here follows closely that of Li [56]. We use a modification of the standard Gauss-Chebyshev quadrature developed by Perez-Jorda *et. al.* [57] and Perez-Jorda and San-Fabian [58]. Their formulation is based on an n-point Gauss-Chebyshev quadrature formula of the second kind. The n-point Gauss-Chebyshev quadrature formula of the second kind can be expressed as [53]

$$\int_{-1}^{1} \frac{f(x)}{\sqrt{1-x^2}}\, dx \sim \sum_{i=1}^{n} w_i^n\, f(x_i^n) = I_n, \tag{H.1}$$

where the abscissas are specified by $x_i^n = \cos(\beta)$ where

$$\beta = \frac{(2i-1)\pi}{2n}, \tag{H.2}$$

and the weights are

$$w_i^n = \pi/n. \tag{H.3}$$

Perez-Jorda *et. al.* [57] made a change of variable,

$$x = 1 + \frac{2}{\pi}\left[z\sqrt{1-z^2}\left\{ 1 + \frac{2}{3}(1-z^2) \right\} - \cos^{-1}(z) \right], \tag{H.4}$$

in a general integral of $f(x)$ on the interval $[-1, 1]$. To extend the integration to the more general interval $[a, b]$ instead, where a and b are real numbers, the integral can be rewritten as

$$\begin{aligned} I &= \int_a^b f(x)\, dx, \\ &= \frac{8(b-a)}{3\pi} \int_{-1}^{1} f\left(\frac{b-a}{2} z + \frac{b+a}{2} \right) (1-z^2)\sqrt{1-z^2}\, dz. \end{aligned} \tag{H.5}$$

Using Eqs. (H.1)-(H.3), the integral above can be expressed as

$$I \sim \sum_{i=1}^{n} w_i^n f\left(\frac{b-a}{2} x_i^n + \frac{b+a}{2} \right) = I_n, \tag{H.6}$$

$$x_i^n = 1 + \frac{2}{\pi}\left[\sin(\alpha)\cos(\alpha)\left\{ 1 + \frac{2}{3}\sin^2(\alpha) \right\} - \frac{2i}{n+1} \right], \tag{H.7}$$

where

$$\alpha = \frac{i\pi}{n+1}, \tag{H.8}$$

$$w_i^n = \frac{8(b-a)}{3(n+1)} \sin^4(\alpha). \tag{H.9}$$

Eqs. (H.6)-(H.9) form the basic formulas for n-point Gauss-Chebyshev quadratures. When more points are required, the $(2n+1)-$point formula can be written as

$$I_{2n+1} = \sum_{i=1}^{2n+1} w_i^{2n+1} f\left(\frac{b-a}{2} x_i^{2n+1} + \frac{b+a}{2} \right). \tag{H.10}$$

The summation can be divided into two separate sums for the even and odd terms,

$$\begin{aligned} I_{2n+1} = &\sum_{i=1}^{n} w_{2i}^{2n+1} f\left(\frac{b-a}{2} x_{2i}^{2n+1} + \frac{b+a}{2} \right) \\ &+ \sum_{i=0}^{n} w_{2i+1}^{2n+1} f\left(\frac{b-a}{2} x_{2i+1}^{2n+1} + \frac{b+a}{2} \right). \end{aligned} \tag{H.11}$$

From Eqs. (H.6) and (H.9), it is easy to show that

$$\begin{aligned} x_{2i}^{2n+1} &= x_i^n, \\ w_{2i}^{2n+1} &= \frac{1}{2} w_i^n, \end{aligned} \tag{H.12}$$

so that I_{2n+1} can be written in terms of I_n as

$$I_{2n+1} = \frac{I_n}{2} + \sum_{i=0}^{n} w_{2i+1}^{2n+1} f\left(\frac{b-a}{2} x_{2i+1}^{2n+1} + \frac{b+a}{2} \right). \tag{H.13}$$

The above recursive relation is very useful for automatic numerical integration since it permits the approximation to be repeatedly refined until it passes a convergence test.

H.4 Contour Integration

Some attempts were made to apply complex integration techniques to reduce the infinite integrals to a more manageable form. Only one approach seems promising and the mathematical details are presented in Appendix I. The resultant integrals obtained from that analysis are numerically integrated using QUADPACK as well as Gauss-Chebyshev quadratures.

Appendix I

Contour Integration for Panel Source Solutions

It is not immediately obvious that the infinite range of integration in the panel source solutions can be reduced to a finite one which is more amenable to numerical computations. Following a similar procedure by Krenk and Schmidt [59], we show that this is indeed possible, via complex plane integration techniques. This technique was also successfully used to study acoustic scattering by a strip [60]. As an example, we tackle the normal stress integral

$$\mathrm{T}_{mk}(x,z) = \frac{Q_{mk}}{\kappa^2} \int_0^\infty \left[\frac{(2\eta^2-\kappa^2)^2}{\gamma}\, e^{-x\gamma} - 4\eta^2\delta\, e^{-x\delta} \right] j_{m-1}\!\left(\frac{t_\ell \eta}{2}\right) j_{k-1}\!\left(\frac{t_\ell \eta}{2}\right) d\eta, \quad \text{(I.1)}$$

where

$$Q_{mk} = \frac{2\mu t_\ell}{2\pi}\,(2m-1)\,\zeta_m\, i^{m+k-2}. \quad \text{(I.2)}$$

Here, we will only treat the case of $x = 0$. When $x \neq 0$, only an additional multiplying exponential factor need to be taken into account. We first observed that the integral above is symmetrical so that

$$\mathrm{T}_{mk}(x,z) = \mathrm{T}_{km}(x,z), \quad \text{(I.3)}$$

implying that we can restrict our analysis to $m \leq k$, without any loss in generality. We define our kernel to be

$$f(\eta) = \gamma^{-1}\,(2\eta^2-\kappa^2)^2 - 4\eta^2\delta, \quad \text{(I.4)}$$

where

$$\gamma = \begin{cases} \sqrt{\eta^2 - h^2} & \eta > h \\ i\sqrt{h^2 - \eta^2} & \eta < h \end{cases}, \tag{I.5}$$

and

$$\delta = \begin{cases} \sqrt{\eta^2 - \kappa^2} & \eta > \kappa \\ i\sqrt{\kappa^2 - \eta^2} & \eta < \kappa \end{cases}. \tag{I.6}$$

Next we look at the limiting forms of f for $\eta \to \infty$ and $\eta \to 0$. It is straightforward to show that

$$\lim_{\eta\to\infty} f(\eta) = 2\eta(h^2 - \kappa^2) + \eta^{-1}\left(\frac{3}{2}h^4 - 2\kappa^2 h^2 + \frac{3}{2}\kappa^4\right) + O(\eta^{-3}), \tag{I.7}$$

$$\lim_{\eta\to 0} f(\eta) = -i\kappa^4 h^{-1}. \tag{I.8}$$

The principle behind the contour integration is to write one of the spherical Bessel functions in the integrand as the sum of spherical Bessel functions of the third kind

$$2j_n(s) = h_n^{(1)}(s) + h_n^{(2)}(s), \tag{I.9}$$

resulting in

$$\mathrm{T}_{mk}(x,z) = \frac{Q_{mk}}{2\kappa^2}\int_0^\infty f(\eta)\left[h_{m-1}^{(1)}\left(\frac{t_\ell\eta}{2}\right) + h_{m-1}^{(2)}\left(\frac{t_\ell\eta}{2}\right)\right] j_{k-1}\left(\frac{t_\ell\eta}{2}\right) d\eta. \tag{I.10}$$

The argument is then extended to the complex half-plane $\Re(z) = s \geq 0$. For large values of z the asymptotic behaviour of the spherical Bessel functions of the third kind is [53]

$$h_n^{(1)}(z) \sim i^{-(n+1)}\, z^{-1}\, e^{iz}, \tag{I.11}$$

$$h_n^{(2)}(z) \sim i^{(n+1)}\, z^{-1}\, e^{-iz}. \tag{I.12}$$

Together with Eq. (I.7), we conclude that the part of the integrand containing $h_n^{(1)}(z)$ behaves asymptotically like $|z|^{-1}$ in the upper half-plane, while that containing $h_n^{(2)}(z)$ behaves asymptotically like $|z|^{-1}$ in the lower half-plane. The integration contours in the complex s-plane is shown in Fig. I-1. The first term in Eq. (I.10) is now integrated along the closed contour in Fig. I-1a, while the second is integrated along the contour in Fig. I-1b. As neither of the integrands contains any poles within the contour, the original integral in Eq. (I.10) can

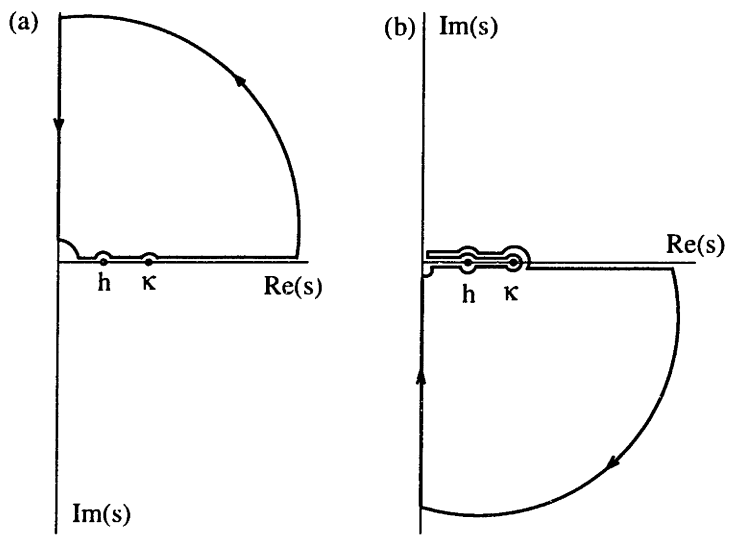

Figure I-1: Integration contours in the complex s-plane: (a) $h_n^{(1)}$-contour; (b) $h_n^{(2)}$-contour; Reprinted from Krenk and Schmidt.

be replaced by integrals over the remainder of the contours, taken in the opposite direction. In these integrals, the large quarter circles do not contribute. The contributions from the imaginary axis cancel as a consequence of the symmetry relation

$$h_m^{(1)}(-z)\, j_k(-z) = h_m^{(2)}(z)\, j_k(z) \qquad m+k = \text{even}. \tag{I.13}$$

Note that this symmetry is valid only when $m+k$ is even, which *excludes the use of this technique for the displacement equations.* The contributions from the small quarter circles depend on the asymptotic behaviour of the integrand as $z \to 0$. From [53], we obtain the asymptotic behaviour of the product of the special functions for small z as

$$h_{m-1}^{(1,2)}(z)\, j_{k-1}(z) \sim \mp i \left[\frac{(2k-3)!!}{(2m-1)!!} \right] z^{k-m-1}, \tag{I.14}$$

where

$$\frac{(2k-3)!!}{(2m-1)!!} = \frac{1 \cdot 3 \ldots (2k-3)}{1 \cdot 3 \ldots (2m-1)}. \tag{I.15}$$

As previously stated, we can impose the condition $m \leq k$ without any loss of generality. Doing that and noting from Eq. (I.8) that the kernel tends to a constant independent of η for small η, we conclude that the contribution to the integral for small η is going to be totally

dominated by the product of the special functions. It is straightforward to see that the worst case decay occurs for the case when $m = k$, when we then have

$$\frac{(2k-3)!!}{(2m-1)!!} = \frac{1}{2k-1}. \tag{I.16}$$

Carrying out the resulting integration around the quarter circle at a small distance ϵ from the origin yields

$$I_o = \int_{i\epsilon}^{\epsilon} -ih\kappa^4 \frac{-i}{2k-1}\frac{dz}{z} - \int_{-i\epsilon}^{\epsilon} -ih\kappa^4 \frac{i}{2k-1}\frac{dz}{z} = 0. \tag{I.17}$$

The small quarter circles therefore do not actually contribute to the integral. Putting the various components of the contour integral together, we arrive at

$$\begin{aligned} \mathrm{T}_{mk}(x,z) = \frac{-iQ_{mk}}{\kappa^2} \lim_{\epsilon\to 0} \Bigg\{ &\int_{\epsilon}^{h} \frac{(2\eta^2-\kappa^2)^2}{\sqrt{h^2-\eta^2}} h_{m-1}^{(2)}\left(\frac{t_\ell \eta}{2}\right) j_{k-1}\left(\frac{t_\ell \eta}{2}\right) d\eta \\ &+ \int_{\epsilon}^{\kappa} 4\eta^2\sqrt{\kappa^2-\eta^2}\, h_{m-1}^{(2)}\left(\frac{t_\ell \eta}{2}\right) j_{k-1}\left(\frac{t_\ell \eta}{2}\right) d\eta \Bigg\} \end{aligned} \tag{I.18}$$

In the limit as $\epsilon \to 0$, each integral is continuous and

$$\begin{aligned} \mathrm{T}_{mk}(x,z) = \frac{-iQ_{mk}}{\kappa^2} \Bigg\{ &\int_{0}^{h} \frac{(2\eta^2-\kappa^2)^2}{\sqrt{h^2-\eta^2}} h_{m-1}^{(2)}\left(\frac{t_\ell \eta}{2}\right) j_{k-1}\left(\frac{t_\ell \eta}{2}\right) d\eta \\ &+ \int_{0}^{\kappa} 4\eta^2\sqrt{\kappa^2-\eta^2}\, h_{m-1}^{(2)}\left(\frac{t_\ell \eta}{2}\right) j_{k-1}\left(\frac{t_\ell \eta}{2}\right) d\eta \Bigg\} \end{aligned} \tag{I.19}$$

The same technique can be employed to deal with the shear stress integral from the anti-symmetric panel source, resulting in

$$\begin{aligned} \mathrm{S}_{mk}(x,z) = \frac{-iQ_{mk}}{\kappa^2} \Bigg\{ &\int_{0}^{h} 4\eta^2\sqrt{h^2-\eta^2}\, h_{m-1}^{(2)}\left(\frac{t_\ell \eta}{2}\right) j_{k-1}\left(\frac{t_\ell \eta}{2}\right) d\eta \\ &+ \int_{0}^{\kappa} \frac{(2\eta^2-\kappa^2)^2}{\sqrt{\kappa^2-\eta^2}} h_{m-1}^{(2)}\left(\frac{t_\ell \eta}{2}\right) j_{k-1}\left(\frac{t_\ell \eta}{2}\right) d\eta \Bigg\} \end{aligned} \tag{I.20}$$

Appendix J

Mapping Expansion Coefficients

The usual method of handling a continuously changing bathymetry is to perform a stair-case discretization. The important interfaces with strong impedance contrasts are the horizontal and vertical interfaces along the stair steps. Unlike most one-way formulations, in the spectral element method the treatment of boundary conditions at both the horizontal and vertical interfaces are accurately implemented. However, in the spectral element method we encounter another kind of difficulty. When propagating the field from one sector to the next, the layer structure at sector j may be different from that at sector $j+1$. As shown in Fig. J-1, we see that layer n in sector j has a height of l_n^j, whereas the corresponding layer in sector $j+1$ has a height of l_n^{j+1}. This implies that the set of expansion coefficients at sector j cannot be used directly at the next range step but instead new sets of coefficients need to be derived. In this Appendix, we derive mapping matrices that allow us to 'march' the expansion coefficients from one range step to the next, even when the layering structure has changed. Even though this is only an approximate solution due to the inherent truncation in the orders of expansion, our numerical experiments have shown that it does improve the solution.

J.1 Case I - Splitting a Layer

To obtain the new coefficients, we simply assume that the field at the previous range step are to be expanded again at the next range step except that it is now over the entire depth

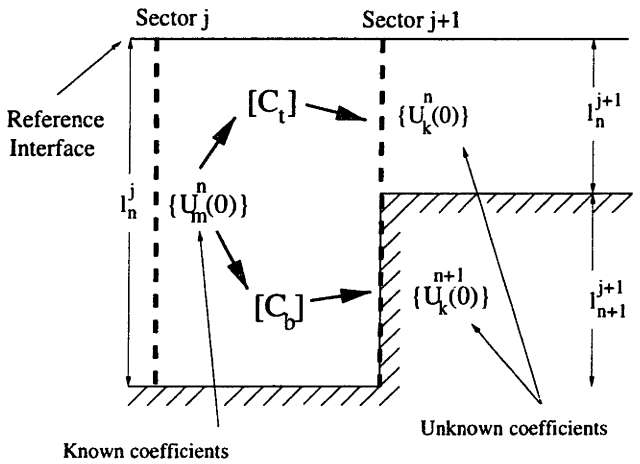

Figure J-1: Splitting of single layer

of $l_n^{j+1} + l_{n+1}^{j+1}$. In this case, the known vector of coefficients is $\{U_m^n(0)\}$ and we denote the new unknown coefficients at sector $j+1$ as $\{U_k^n(0)\}$ and $\{U_k^{n+1}(0)\}$. We then obtain two matrices C_t and C_b which map the old coefficients to the new. These matrices are of size $M \times M$ where M is the order of expansion used in the basis representation of the wavefields. Matrices C_t and C_b can be straightforwardly obtained using the orthogonality properties of the Legendre polynomials. The final expressions for the new coefficients are

$$\begin{aligned}
\{U_k^n(0)\} &= \sum_{m=1}^{M} \{U_m^n(0)\} \frac{2k-1}{l_n^{j+1}} \int_0^{l_n^{j+1}} P_{m-1}(\bar{z})\, P_{k-1}(\bar{a})\, dz, \\
\{U_k^{n+1}(0)\} &= \sum_{m=1}^{M} \{U_m^n(0)\} \frac{2k-1}{l_{n+1}^{j+1}} \int_{l_n^{j+1}}^{l_n^{j+1}+l_{n+1}^{j+1}} P_{m-1}(\bar{z})\, P_{k-1}(\bar{b})\, dz,
\end{aligned} \tag{J.1}$$

where

$$\begin{aligned}
\bar{z} &= 2(z - l_n^j/2)/l_n^j, \\
\bar{a} &= 2(z - l_n^{j+1}/2)/l_n^{j+1}, \\
\bar{b} &= 2(z - l_n^{j+1} - l_{n+1}^{j+1}/2)/l_{n+1}^{j+1}.
\end{aligned}$$

The integrals in Eq. (J.1) are easily obtained using symbolic manipulation packages such as MAPLE [61] or Mathematica [62] and we note that the matrices so obtained are upper-triangular.

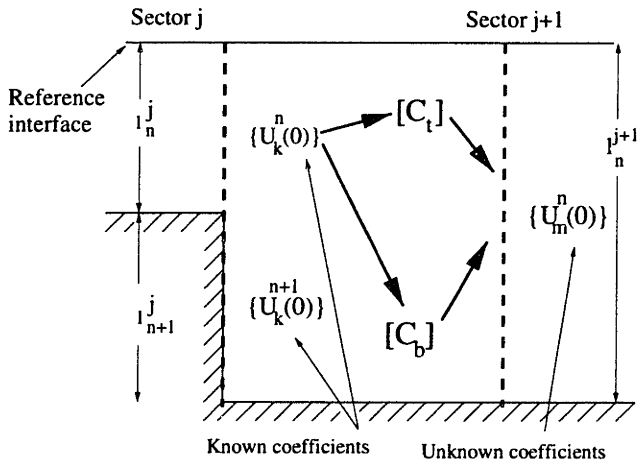

Figure J-2: Combination of 2 layers

J.2 Case II - Combining 2 Layers

A similar analysis can be performed for the case when two layers contribute to the field at the next sector. This situation is presented in Fig. J-2. Instead of having two unknown sets of coefficients, we now have only one which is to be determined as a linear combination of the two known sets at sector j. The expansion coefficients at sector $j+1$ is now given by

$$\{U_m^n(0)\} = \sum_{k=1}^{K} \{U_k^n(0)\} \frac{2m-1}{l_n^{j+1}} \int_0^{l_n^j} P_{k-1}(\bar{a})\, P_{m-1}(\bar{z})\, dz$$
$$+ \sum_{k=1}^{K} \{U_k^{n+1}(0)\} \frac{2m-1}{l_n^{j+1}} \int_{l_n^j}^{l_n^j + l_{n+1}^j} P_{k-1}(\bar{b})\, P_{m-1}(\bar{z})\, dz, \qquad \text{(J.2)}$$

where the normalized depth arguments to the Legendre polynomials are now given by

$$\begin{aligned} \bar{z} &= 2(z - l_n^{j+1}/2)/l_n^{j+1}, \\ \bar{a} &= 2(z - l_n^j/2)/l_n^j, \\ \bar{b} &= 2(z - l_n^j - l_{n+1}^j/2)/l_{n+1}^j. \end{aligned}$$

In addition, the mapping matrices so obtained are lower-triangular.

Appendix K

Elastic Media - Chebyshev Polynomial Formulation

K.1 Field Expansions

We expand the field parameters in a complete sequence of Chebyshev polynomials, in which we also explicitly include the square root singularity for the stresses,

$$\begin{Bmatrix} u(x,z) \\ w(x,z) \\ \sigma_{xx}(x,z)/\mu \\ \sigma_{xz}(x,z)/\mu \end{Bmatrix} = \frac{2\pi}{t_\ell} \sum_{m=1}^{\infty} \begin{Bmatrix} \mathrm{U}_{\ell m}(x) \\ \mathrm{W}_{\ell m}(x) \\ \mathrm{T}_{\ell m}(x)\,[1-(\bar{z}/a)^2]^{-\frac{1}{2}} \\ \mathrm{S}_{\ell m}(x)\,[1-(\bar{z}/a)^2]^{-\frac{1}{2}} \end{Bmatrix} \psi_m(\bar{z}), \tag{K.1}$$

where $a = t_\ell/2$, $\bar{z} = z - a$ and t_ℓ is the thickness of layer ℓ. Note that the depth coordinate z ranges from 0 to t_ℓ. The unknown source strengths $\mathrm{U}_{\ell m}(0)$ through $\mathrm{S}_{\ell m}(0)$ are to be determined by matching boundary conditions along each vertical discontinuity.

K.2 Expansion Eigenfunctions

The eigenfunctions $\psi_m(\bar{z})$ are described by

$$\psi_m(\bar{z}) = \begin{cases} i\sqrt{2}\,\sin[m \arcsin(\bar{z}/a)] & \mathrm{m} = 0,2,4,\ldots \\ \sqrt{2}\,\cos[m \arcsin(\bar{z}/a)] & \mathrm{m} = 1,3,5,\ldots \end{cases} \tag{K.2}$$

or

$$\left.\begin{aligned}\psi_{2m}(\bar{z}) &= i\sqrt{2}\,\sin[m\arcsin(\bar{z}/a)]\\ \psi_{2m+1}(\bar{z}) &= \sqrt{2}\,\cos[m\arcsin(\bar{z}/a)]\end{aligned}\right\}\ m=0,1,2,3,\ldots \tag{K.3}$$

It is easy to show via a change of variable that these eigenfunctions are the usual Chebyshev polynomials, *i.e.*

$$T_m[\sqrt{1-(\bar{z}/a)^2}] = \cos[m\arcsin(\bar{z}/a)]. \tag{K.4}$$

In addition the eigenfunctions have the following property,

$$\int_{-a}^{a} \psi_m(x)\, e^{\pm i\alpha x}\, dx = \begin{cases} \mp\sqrt{2}m\pi\alpha^{-1}\, \mathrm{J}_m(\alpha a) & \text{m=0,2,4,...}\\ \sqrt{2}m\pi\alpha^{-1}\, \mathrm{J}_m(\alpha a) & \text{m=1,3,5,...}\end{cases} \tag{K.5}$$

where $\mathrm{J}_m(z)$ is the Bessel function of integer order m. The orthogonality property of $\psi_m(x)$ is given by

$$\int_{-a}^{a} (a^2-x^2)^{-\frac{1}{2}}\, \psi_k(x)\psi_m^*(x)\, dx = \pi\delta_{km}. \tag{K.6}$$

K.3 Displacement Potentials

We define displacement potentials

$$\begin{aligned}\mathbf{\Phi}_\ell(x,z) &= \int_{-\infty}^{\infty} A_\ell(\eta)\, e^{-x\gamma}\, e^{-i\eta(z-a)}\, d\eta,\\ \mathbf{\Psi}_\ell(x,z) &= \int_{-\infty}^{\infty} B_\ell(\eta)\, e^{-x\delta}\, e^{-i\eta(z-a)}\, d\eta,\end{aligned} \tag{K.7}$$

where $A_\ell(\eta)$ and $B_\ell(\eta)$ are the source spectrums at the discontinuity and

$$\begin{aligned}\gamma &= \sqrt{\eta^2-h^2},\\ \delta &= \sqrt{\eta^2-\kappa^2},\end{aligned} \tag{K.8}$$

where η is the vertical wavenumber and h and κ are the compressional and shear medium wavenumbers respectively. The horizontal wavenumbers are given by $-i\gamma$ and $-i\delta$ respectively.

The Symmetric Problem

The symmetric problem is characterized by two conditions at the discontinuity ($x = 0$),

$$\begin{aligned} \sigma_{xz}(0,z)/\mu &= \frac{\partial u}{\partial z} + \frac{\partial w}{\partial x} = 0, \\ u(0,z) &= \frac{\partial \Phi}{\partial x} - \frac{\partial \Psi}{\partial z} = \frac{2\pi}{t_\ell} \sum_{m=1}^{\infty} \mathrm{U}_{\ell m}(0)\, \psi_m(\bar{z}). \end{aligned} \tag{K.9}$$

Substitution of Eq. (K.7) yields,

$$\begin{aligned} u(0,z) &= \int_{-\infty}^{\infty} \frac{\gamma\kappa^2}{2\eta^2 - \kappa^2} A_\ell^{(1)}(\eta)\, e^{-i\eta(z-a)}\, d\eta, \\ &= \frac{2\pi}{t_\ell} \sum_{m=1}^{\infty} \mathrm{U}_{\ell m}(0)\, \psi_m(\bar{z}). \end{aligned} \tag{K.10}$$

We define the Fourier transform pair as,

$$\begin{aligned} f(z) &= \int_{-\infty}^{\infty} g(\eta) e^{-ikz}\, d\eta, \\ g(\eta) &= \frac{1}{2\pi} \int_{-\infty}^{\infty} f(z) e^{ikz}\, dz. \end{aligned} \tag{K.11}$$

Taking the foward transform of Eq. (K.10), we obtain,

$$\frac{\gamma\kappa^2}{2\eta^2 - \kappa^2} A_\ell^{(1)}(\eta)\, e^{i\eta a} = \frac{1}{t_\ell} \sum_{m=1}^{\infty} \mathrm{U}_{\ell m}(0) \int_0^{t_\ell} \psi_m(\bar{z}) e^{i\eta z}\, dz, \tag{K.12}$$

where we have truncated the limits of integration to the domain where the panel source strengths are non-zero. By making a change of variable $x = \bar{z} = z - a$, we obtain

$$\int_0^{t_\ell} \psi_m(\bar{z})\, e^{\pm i\eta z}\, dz = e^{\pm i\eta a} \int_{-a}^{a} \psi_m(x)\, e^{\pm i\eta x}\, dx, \tag{K.13}$$

whence Eq. (K.5) may be used directly except for an extra multiplying factor of $\exp(\pm i\eta a)$. We then obtain for the symmetric part of the source spectrum $A_\ell(\eta)$,

$$A_\ell^{(1)}(\eta) = \frac{2\eta^2 - \kappa^2}{\kappa^2 \eta\gamma} \sum_{m=1}^{\infty} \mathrm{U}_{\ell m}(0)\, \sqrt{2}\, (-1)^{m+1}\, \frac{m\pi}{t_\ell}\, \mathrm{J}_m(\eta a). \tag{K.14}$$

Similarly,

$$B_\ell^{(1)}(\eta) = -\frac{2i}{\kappa^2} \sum_{m=1}^{\infty} \mathrm{U}_{\ell m}(0)\, \sqrt{2}\, (-1)^{m+1}\, \frac{m\pi}{t_\ell}\, \mathrm{J}_m(\eta a). \tag{K.15}$$

The Antisymmetric Problem

The antisymmetric problem is again characterized by two conditions at the discontinuity,

$$\begin{aligned} \sigma_{xx}(0,z)/\mu &= \left(\frac{\lambda+2\mu}{\mu}\right)\frac{\partial u}{\partial x}+\frac{\lambda}{\mu}\frac{\partial w}{\partial z}=0, \\ w(0,z) &= \frac{\partial \Phi}{\partial z}+\frac{\partial \Psi}{\partial x}=\frac{2\pi}{t_\ell}\sum_{m=1}^{\infty}\mathrm{W}_{\ell m}(0)\,\psi_m(\bar{z}), \end{aligned} \tag{K.16}$$

where λ and μ are the Lamè constants. Proceeding as before, and noting that

$$\begin{aligned} c_p^2 &= (\lambda+2\mu)/\rho, \\ c_s^2 &= \mu/\rho, \\ \gamma^2-\eta^2 &= -h^2, \\ \left(\frac{\lambda+2\mu}{\mu}\right) &= \frac{c_p^2}{c_s^2}=\frac{\kappa^2}{h^2}, \\ \frac{\lambda}{\mu} &= \frac{\kappa^2}{h^2}-2. \end{aligned} \tag{K.17}$$

we obtain

$$A_\ell^{(2)}(\eta)=\frac{2i}{\kappa^2}\sum_{m=1}^{\infty}\mathrm{W}_{\ell m}(0)\,\sqrt{2}\,(-1)^{m+1}\,\frac{m\pi}{t_\ell}\,\mathrm{J}_m(\eta a). \tag{K.18}$$

Similarly,

$$B_\ell^{(2)}(\eta)=\left[\frac{2\eta^2-\kappa^2}{\kappa^2\eta\delta}\right]\sum_{m=1}^{\infty}\mathrm{W}_{\ell m}(0)\,\sqrt{2}\,(-1)^{m+1}\,\frac{m\pi}{t_\ell}\,\mathrm{J}_m(\eta a). \tag{K.19}$$

Horizontal Wavenumber Representations for Potentials

The displacement potentials in the vertical wavenumber domain are

$$\begin{aligned} \Phi_\ell(x,z) &= \int_{-\infty}^{\infty}\left[\frac{2\eta^2-\kappa^2}{\kappa^2\eta\gamma}\,\Gamma(\eta)+\frac{2i}{\kappa^2}\,\Theta(\eta)\right]e^{-x\gamma}e^{-i\eta(z-a)}\,d\eta, \\ \Psi_\ell(x,z) &= \int_{-\infty}^{\infty}\left[-\frac{2i}{\kappa^2}\,\Gamma(\eta)+\frac{2\eta^2-\kappa^2}{\kappa^2\eta\delta}\,\Theta(\eta)\right]e^{-x\delta}e^{-i\eta(z-a)}\,d\eta, \end{aligned} \tag{K.20}$$

where

$$\begin{aligned} \Gamma(\eta) &= \sum_{m=1}^{\infty}\mathrm{U}_{\ell m}(0)\,\sqrt{2}\,(-1)^{m+1}\,\frac{m\pi}{t_\ell}\,\mathrm{J}_m(\eta a), \\ \Theta(\eta) &= \sum_{m=1}^{\infty}\mathrm{W}_{\ell m}(0)\,\sqrt{2}\,(-1)^{m+1}\,\frac{m\pi}{t_\ell}\,\mathrm{J}_m(\eta a). \end{aligned} \tag{K.21}$$

The above integral representations for the potentials can be cast in the form of horizontal wavenumber integrals via contour deformation. The $s-$domain representations are,

$$\begin{aligned}
\Phi_\ell(x,z) &= i\int_{-\infty}^{\infty}\left[A(-i\mathcal{S}\alpha)\right]e^{-|z-a|\alpha}\,\frac{s}{\alpha}\,e^{-ixs}\,ds,\\
\Psi_\ell(x,z) &= i\int_{-\infty}^{\infty}\left[B(-i\mathcal{S}\beta)\right]e^{-|z-a|\beta}\,\frac{s}{\beta}\,e^{-ixs}\,ds,
\end{aligned}\tag{K.22}$$

where $\mathcal{S}=\text{sign}(z-a)$. In the horizontal wavenumber definitions, the vertical wavenumbers are now given by

$$\begin{aligned}
i\alpha &= \sqrt{h^2-s^2},\\
i\beta &= \sqrt{\kappa^2-s^2}.
\end{aligned}\tag{K.23}$$

In addition, we note that $(-i\mathcal{S}\alpha)^2=-\alpha^2$, $(-i\mathcal{S}\beta)^2=-\beta^2$ and $2\beta^2+\kappa^2=2(s^2-\kappa^2)+\kappa^2=2s^2-\kappa^2$. The source spectrums in the $s-$domain are therefore given by

$$\begin{aligned}
A(-i\mathcal{S}\alpha) &= -\frac{2\alpha^2+\kappa^2}{s\mathcal{S}\alpha\kappa^2}\,\Gamma(-i\mathcal{S}\alpha)+\frac{2i}{\kappa^2}\,\Theta(-i\mathcal{S}\alpha),\\
B(-i\mathcal{S}\beta) &= -\frac{2i}{\kappa^2}\,\Gamma(-i\mathcal{S}\beta)-\frac{2s^2-\kappa^2}{s\mathcal{S}\beta\kappa^2}\,\Theta(-i\mathcal{S}\beta).
\end{aligned}\tag{K.24}$$

where we have used is in places where δ and γ occurs. The potentials in the $s-$domain are therefore given by

$$\begin{aligned}
\Phi_\ell(x,z) &= \int_{-\infty}^{\infty}\left[-i\,\frac{2\alpha^2+\kappa^2}{s\mathcal{S}\alpha\kappa^2}\,\Gamma(-i\mathcal{S}\alpha)-\frac{2}{\kappa^2}\,\Theta(-i\mathcal{S}\alpha)\right]e^{-|z-a|\alpha}\,\frac{s}{\alpha}\,e^{-ixs}\,ds,\\
\Psi_\ell(x,z) &= \int_{-\infty}^{\infty}\left[\frac{2}{\kappa^2}\,\Gamma(-i\mathcal{S}\beta)\;-i\,\frac{2s^2-\kappa^2}{s\mathcal{S}\beta\kappa^2}\,\Theta(-i\mathcal{S}\beta)\right]e^{-|z-a|\beta}\,\frac{s}{\beta}\,e^{-ixs}\,ds,
\end{aligned}\tag{K.25}$$

where

$$\begin{aligned}
\Gamma(-i\mathcal{S}\nu) &= \sum_{m=1}^{\infty}\mathrm{U}_{\ell m}(0)\,(-1)^{m+1}\,\frac{m\pi}{t_\ell}\,\mathrm{J}_m(-i\mathcal{S}a\nu),\\
\Theta(-i\mathcal{S}\nu) &= \sum_{m=1}^{\infty}\mathrm{W}_{\ell m}(0)\,(-1)^{m+1}\,\frac{m\pi}{t_\ell}\,\mathrm{J}_m(-i\mathcal{S}a\nu).
\end{aligned}\tag{K.26}$$

It is important to point out here that in the limit of vanishing layer thickness, the lowest order term recovers the potentials for the point source case. This can be seen by noting that

$$\lim_{t_\ell\to 0}\,t_\ell^{-1}\,\mathrm{J}_1(-i\mathcal{S}a\nu)=-\frac{i\mathcal{S}\nu}{4}.\tag{K.27}$$

This explains the normalization factor of t_ℓ^{-1} in the series expansion. The factor of 2π is there for convenience.

K.4 Panel Source Solution

Horizontal Wavenumber Representation

We can now obtain horizontal wavenumber integral expressions for the field parameters simply by definitions and via Hooke's law. For example, the horizontal displacement $u(x,z)$ is given by

$$u(x,z) = \frac{\partial \Phi}{\partial x} - \frac{\partial \Psi}{\partial z} = -is\Phi + \mathcal{S}\beta\Psi, \tag{K.28}$$

where we have used the fact that $\partial\Psi/\partial z = -\mathcal{S}\beta\Psi$ and $\partial\Phi/\partial z = -\mathcal{S}\alpha\Phi$, and $\mathcal{S} = \text{sign}(z-a)$. This result is most easily seen by splitting the absolute operator in the $z-$dependence into two regions, *i.e.* $z < t_\ell/2$ and $z > t_\ell/2$ and performing the differentiations separately. Collecting together the Γ and Θ terms in Eq. (K.28), we have

$$\begin{aligned} u^{(U)} &= \int_{-\infty}^{\infty} \frac{1}{\kappa^2} \left[-s\mathcal{S}\, \frac{2\alpha^2+\kappa^2}{\alpha^2}\, e^{-|z-a|\alpha} + 2s\mathcal{S}\, e^{-|z-a|\beta} \right] \Gamma\, e^{-ixs}\, ds, \\ u^{(S)} &= \int_{-\infty}^{\infty} \frac{1}{\kappa^2} \left[\frac{i}{\alpha}\, 2s^2\, e^{-|z-a|\alpha} - \frac{i}{\beta}(2s^2-\kappa^2)\, e^{-|z-a|\beta} \right] \Theta\, e^{-ixs}\, ds. \end{aligned} \tag{K.29}$$

The components $u^{(U)}$ and $u^{(S)}$ represent the displacements due to the symmetric and asymmetric sources respectively. Note that $u^{(U)}$ and $u^{(S)}$ are out of phase. The complete system of equations in matrix notation is given by

$$\begin{Bmatrix} u(x,z) \\ w(x,z) \\ \sigma_{zz}(x,z)/\mu \\ \sigma_{xz}(x,z)/\mu \end{Bmatrix} = \frac{\sqrt{2}\pi}{t_\ell} \sum_{m=1}^{\infty} \int_{-\infty}^{\infty} \left[\mathrm{U}_m(0)\, \hat{\mathbf{K}}_{\mathbf{u}} + \mathrm{W}_m(0)\, \hat{\mathbf{K}}_{\mathbf{w}} \right] \hat{\mathbf{E}}\, \hat{\mathbf{J}}_{\mathbf{m}}\, e^{-ixs}\, ds, \tag{K.30}$$

where

$$\begin{aligned} \hat{\mathbf{E}} &= \text{diag}\,[e^{-|z-a|\alpha}, e^{-|z-a|\beta}], \\ \hat{\mathbf{J}}_{\mathbf{m}} &= \begin{bmatrix} m\,(-1)^{m+1}\, \mathrm{J}_m(-i\mathcal{S}a\alpha) \\ m\,(-1)^{m+1}\, \mathrm{J}_m(-i\mathcal{S}a\beta) \end{bmatrix}, \\ \hat{\mathbf{K}}_{\mathbf{u}} &= \frac{1}{\kappa^2} \begin{bmatrix} -s\mathcal{S}(2\alpha^2+\kappa^2)\,\alpha^{-2} & 2\mathcal{S}s \\ i(2\alpha^2+\kappa^2)\,\alpha^{-1} & -2is^2\beta^{-1} \\ -i\mathcal{S}(2s^2-\kappa^2)(2\alpha^2+\kappa^2)\,\alpha^{-2} & 4i\mathcal{S}s^2 \\ 2s(2\alpha^2+\kappa^2)\,\alpha^{-1} & -2s(2s^2-\kappa^2)\,\beta^{-1} \end{bmatrix}, \end{aligned}$$

$$\hat{\mathbf{K}_{\mathbf{w}}} = \frac{1}{\kappa^2} \begin{bmatrix} 2is^2\alpha^{-1} & -i(2s^2-\kappa^2)\,\beta^{-1} \\ 2\mathcal{S}s & -\mathcal{S}s\,(2s^2-\kappa^2)\,\beta^{-2} \\ -2s(2s^2-\kappa^2)\,\alpha^{-1} & 2s(2s^2-\kappa^2)\,\beta^{-1} \\ -4i\mathcal{S}s^2 & i\mathcal{S}\,(2s^2-\kappa^2)^2\,\beta^{-2} \end{bmatrix}, \tag{K.31}$$

with

$$\begin{aligned} a &= t_\ell/2, \\ i\alpha &= \sqrt{h^2-s^2}, \\ i\beta &= \sqrt{\kappa^2-s^2}, \\ 2s^2-\kappa^2 &= 2\beta^2+\kappa^2. \end{aligned} \tag{K.32}$$

Chebyshev Expansions Representations

In the Chebyshev expansion form shown in Eq. (K.1), we see that the complete field is determined once the respective expansion coefficients $\mathrm{U}_{\ell m}(x)$ through $\mathrm{S}_{\ell m}(x)$ are determined. These expansion coefficients are functions of the unknown source strengths $\mathrm{U}_{\ell m}(0)$ and $\mathrm{W}_{\ell m}(0)$. In order to solve for these unknown source strengths for each layer ℓ, we first obtain a system of equations from satisfying boundary conditions at the vertical cut. We do this using the expansion forms for the field variables. In this section, we derive the vertical wavenumber representations for the necessary field parameters. Let us consider the coefficient $\mathrm{U}_{\ell j}(x)$,

$$u_\ell(x,z) = \frac{2\pi}{t_\ell} \sum_{j=1}^{\infty} \mathrm{U}_{\ell j}(x)\, \psi_j(\bar{z}). \tag{K.33}$$

We can use the orthogonality properties of the Chebyshev polynomials to reduce the right-hand side of Eq. (K.33) as such,

$$\begin{aligned} & \frac{2\pi}{t_\ell} \sum_{j=1}^{\infty} \mathrm{U}_{\ell j}(x) \int_0^{t_\ell} [1-(\bar{z}/a)^2]^{-\frac{1}{2}}\, \psi_m^*(\bar{z})\, \psi_j(\bar{z})\, dz \\ = & \frac{2\pi}{t_\ell} \sum_{j=1}^{\infty} \mathrm{U}_{\ell j}(x) \int_{-a}^{a} [1-(x/a)^2]^{-\frac{1}{2}}\, \psi_m^*(x)\, \psi_j(x)\, dx \\ = & \; a\,\pi^2\, \mathrm{U}_m(x), \end{aligned} \tag{K.34}$$

where we have made a change of variable of $x = \bar{z} = z - a$. The left-hand side of the integral becomes (upon changing the order of integration),

$$\begin{aligned} I_{lhs} &= \int_0^{t_\ell} u_\ell(x,z)\,[1-(\bar{z}/a)^2]^{-\frac{1}{2}}\,\psi_m(\bar{z})\,dz, \\ &= \int_0^{t_\ell} [-\gamma\Phi + i\eta\Psi]\,[1-(\bar{z}/a)^2]^{-\frac{1}{2}}\,\psi_m(\bar{z})\,dz, \\ &= \int_{-\infty}^{\infty} d\eta\,[-\gamma A(\eta)e^{-x\gamma} + i\eta B(\eta)e^{-x\delta}]\,e^{i\eta a}\int_0^{t_\ell} \frac{\psi_m(\bar{z})}{\sqrt{1-(\bar{z}/a)^2}}\,e^{-i\eta z}\,dz. \end{aligned} \quad \text{(K.35)}$$

Performing the depth integration using the identity

$$\int_0^{t_\ell} [1-(\bar{z}/a)^2]^{-\frac{1}{2}}\,\psi_m(\bar{z})\,e^{-i\eta z}\,dz = ae^{-i\eta a}\,\mathcal{Z}_m(\eta a), \quad \text{(K.36)}$$

where $\mathcal{Z}_m$ is derived in Appendix K.9, we arrive at

$$\mathrm{U}_{\ell m}(x) = \int_{-\infty}^{\infty} [-\gamma\,A(\eta)e^{-x\gamma} + i\eta B(\eta)e^{-x\delta}]\,\frac{1}{\pi^2}\mathcal{Z}_m(\eta a)\,d\eta. \quad \text{(K.37)}$$

Using the source spectrum expressions derived previously, we obtain after some algebra,

$$\begin{aligned} \mathrm{U}_{\ell m}(x) = \frac{\sqrt{2}}{\pi t_\ell}\sum_{j=1}^{\infty}(-1)^{j+1}\,j\int_{-\infty}^{\infty}\Bigg\{\left[-\frac{2\eta^2-\kappa^2}{\kappa^2\eta}e^{-x\gamma} + \frac{2\eta}{\kappa^2}e^{-x\delta}\right]\mathrm{U}_{\ell m}(0) \\ +\left[-\frac{2i\gamma}{\kappa^2}e^{-x\gamma} + \frac{i(2\eta^2-\kappa^2)}{\kappa^2\delta}e^{-x\delta}\right]\mathrm{W}_{\ell m}(0)\Bigg\}\,\mathcal{Z}_m(\eta a)\,\mathrm{J}_j(\eta a)\,d\eta. \end{aligned} \quad \text{(K.38)}$$

Expansion coefficients for the other field parameters can be derived similarly and they are given by

$$\begin{Bmatrix} \mathrm{U}(x,z) \\ \mathrm{W}(x,z) \\ \mathrm{T}(x,z)/\mu \\ \mathrm{S}(x,z)/\mu \end{Bmatrix} = \frac{\sqrt{2}}{\pi t_\ell}\sum_{j=1}^{\infty}(-1)^{j+1}\,j\int_{-\infty}^{\infty}[\mathrm{U}_m(0)\hat{\mathbf{K}}_{\mathbf{u}} + \mathrm{W}_m(0)\hat{\mathbf{K}}_{\mathbf{w}}]\hat{\mathbf{E}}\,\mathcal{Z}_m(\eta a)\mathrm{J}_j(\eta a)\,d\eta \quad \text{(K.39)}$$

where

$$\begin{aligned} \hat{\mathbf{E}} &= [\,e^{-x\gamma} \quad e^{-x\delta}\,]^T, \\ \hat{\mathbf{K}}_{\mathbf{u}} &= \frac{1}{\kappa^2}\begin{bmatrix} -\varphi\,\eta^{-1} & 2\eta \\ -i\varphi\,\gamma^{-1} & 2i\delta \\ \varphi^2\,\gamma^{-1}\,\eta^{-1} & -4\delta\eta \\ 2i\varphi & -2i\varphi \end{bmatrix}, \end{aligned}$$

$$\hat{\mathbf{K}}_{\mathbf{w}} = \frac{1}{\kappa^2}\begin{bmatrix} -2i\gamma & i\varphi\,\delta^{-1} \\ 2\eta & -\varphi\,\eta^{-1} \\ 2i\varphi & -2i\varphi \\ -4\gamma\eta & \varphi^2\,\delta^{-1}\,\eta^{-1} \end{bmatrix}, \tag{K.40}$$

and

$$\begin{aligned} a &= t_\ell/2, \\ \mathcal{S} &= \text{sign}(z-a), \\ \varphi &= 2\eta^2-\kappa^2, \\ \gamma &= \sqrt{\eta^2-h^2}, \\ \delta &= \sqrt{\eta^2-\kappa^2}. \end{aligned} \tag{K.41}$$

Note that the third expansion coefficient corresponds to the stress component σ_{xx}/μ rather than σ_{zz}/μ since the Chebyshev expansion forms are used for satisfying boundary conditions along the vertical cut.

K.5 Homogeneous Solution

The horizontal wavenumber integral representation for the homogeneous solution to the panel sources can be obtained by a direct extension of the equations presented in Schmidt and Jensen [48]. The only change needed is that the solutions need to be summed over all finite layers as well as over all orders of expansion. The basis expansion form of the homogeneous solution can be obtained through a direct application of the orthogonality properties of the Chebyshev polynomials. One need only perform 2 integrals to arrive at the desired solutions, namely

$$\begin{aligned} \int_0^{t_\ell} \psi_m(\bar{z})e^{-z\alpha}\,dz &= \int_0^{t_\ell} \psi_m(\bar{z})e^{-i\eta z}\,dz \\ &= e^{-i\eta a}\int_{-a}^{a} \psi_m(x)e^{-i\eta x}\,dx \\ &= e^{-a\alpha}\,\sqrt{2}m\pi\alpha^{-1}\,\mathrm{J}_m(-ia\alpha), \end{aligned} \tag{K.42}$$

where we made a change of variable $\alpha = i\eta$. In addition, it is straightforward to show that

$$\int_0^{t_\ell} \psi_m(\bar{z})e^{(z-t_\ell)\alpha}\,dz = e^{-a\alpha}\,\sqrt{2}m\pi\alpha^{-1}\,(-1)^{m+1}\,\mathrm{J}_m(-ia\alpha). \tag{K.43}$$

By using the analytic continuation property of the Bessel function, Eq. (9.1.35) in [53], we can reduce the Bessel function computations to only positive arguments,

$$\mathrm{J}_\ell(-z) = (-1)^\ell \, \mathrm{J}_\ell(z) \tag{K.44}$$

Horizontal Wavenumber Representations

The field equations can be written as a superposition of homogeneous solutions for the two type of panel sources located in each finite layer ($n = 2, \ldots, N-1$) over each order ($k = 1, 2, \ldots$) of expansion.

$$\bar{\mathbf{v}}_\ell(x,z) = \sum_{n=2}^{N-1} \sum_{k=1}^{\infty} \int_{-\infty}^{\infty} \bar{\mathbf{K}} \, \bar{\mathbf{E}} \, [\hat{U}_{\ell k}(0)\bar{\mathbf{A}} + \hat{W}_{\ell k}(0)\bar{\mathbf{C}}] \, e^{-ixs} \, ds, \tag{K.45}$$

where the matrices are given by

$$\begin{aligned}
\bar{\mathbf{v}}_\ell(x,z) &= \begin{bmatrix} u & w & \sigma_{zz}/\mu & \sigma_{xz}/\mu \end{bmatrix}^T, \\
\bar{\mathbf{K}} &= \begin{bmatrix} -is & -is & i\beta & -i\beta \\ -\alpha & \alpha & s & s \\ \varpi & \varpi & -2s\beta & 2s\beta \\ 2is\alpha & -2is\alpha & -i\varpi & -i\varpi \end{bmatrix}, \\
\bar{\mathbf{E}} &= \mathrm{diag}\left[e^{-z\alpha}, \, e^{(z-t_\ell)\alpha}, \, e^{-z\beta}, \, e^{(z-t_\ell)\beta}\right], \\
\bar{\mathbf{A}} &= \begin{bmatrix} A^-_{\ell,nk} & A^+_{\ell,nk} & B^-_{\ell,nk} & B^+_{\ell,nk} \end{bmatrix}^T, \\
\bar{\mathbf{C}} &= \begin{bmatrix} C^-_{\ell,nk} & C^+_{\ell,nk} & D^-_{\ell,nk} & D^+_{\ell,nk} \end{bmatrix}^T,
\end{aligned}$$

and $\varpi = 2s^2 - \kappa^2$. The unknown vectors $\bar{\mathbf{A}}$ and $\bar{\mathbf{C}}$ are the down and up-going (superscript $\mp$) compressional (A and C) and shear (B and D) waves due to the horizontal and vertical panel sources. Each combination of indices n and k represents a single SAFARI run.

Chebyshev Basis Representations

Using the orthogonality relation of Chebyshev polynomials, expansion functions can be extracted as

$$\bar{\mathbf{V}}_m(x) = i\sqrt{2}m(-1)^m\pi \sum_{n=2}^{N-1}\sum_{k=1}^{\infty}\int_{-\infty}^{\infty} \bar{\mathbf{K}}\ \bar{\mathbf{E}}\ \bar{\mathbf{J}}\ [\hat{U}_{nk}(0)\bar{\mathbf{A}} + \hat{W}_{nk}(0)\bar{\mathbf{C}}]\, e^{-ixs}\, ds, \qquad \text{(K.46)}$$

where the matrices are given by

$$\begin{aligned}
\bar{\mathbf{V}}_m(x) &= \left[\ \bar{\mathrm{U}}_{\ell m}\ \ \bar{\mathrm{W}}_{\ell m}\ \ \bar{\mathrm{T}}_{\ell m}\ \ \bar{\mathrm{S}}_{\ell m}\ \right]^T,\\
\bar{\mathbf{K}} &= \begin{bmatrix} -is & -is & i\beta & -i\beta \\ -\alpha & \alpha & s & s \\ -\vartheta & -\vartheta & 2s\beta & -2s\beta \\ 2is\alpha & -2is\alpha & -i\varpi & -i\varpi \end{bmatrix},\\
\bar{\mathbf{E}} &= \mathrm{diag}\left[e^{-\frac{t_\ell}{2}\alpha},\, e^{-\frac{t_\ell}{2}\alpha},\, e^{-\frac{t_\ell}{2}\beta},\, e^{-\frac{t_\ell}{2}\beta}\right],\\
\bar{\mathbf{A}} &= \left[\ A^-_{\ell,nk}\ \ A^+_{\ell,nk}\ \ B^-_{\ell,nk}\ \ B^+_{\ell,nk}\ \right]^T,\\
\bar{\mathbf{C}} &= \left[\ C^-_{\ell,nk}\ \ C^+_{\ell,nk}\ \ D^-_{\ell,nk}\ \ D^+_{\ell,nk}\ \right]^T,\\
\bar{\mathbf{J}} &= \mathrm{diag}\left[\alpha^{-1}\,\mathrm{J}_m(ia\alpha),\, \zeta_m\alpha^{-1}\mathrm{J}_m(ia\alpha),\, \beta^{-1}\mathrm{J}_m(ia\beta),\, \zeta_m\beta^{-1}\mathrm{J}_m(ia\beta)\right],
\end{aligned}$$

and

$$\begin{aligned}
a &= t_\ell/2,\\
\zeta_m &= (-1)^{m+1}\\
\varpi &= 2s^2 - \kappa^2,\\
\vartheta &= 2\alpha^2 + \kappa^2.
\end{aligned}$$

K.6 Symmetries of the Influence Function Integrals

Panel Source Contribution

This section examines some of the symmetry properties of these integrals which will be useful not only for reducing the amount of numerical computations required but would also help improve accuracy by removing the need to perform quadratures that would produce vanishing results. Specifically we look for two main kinds of symmetry that may be exploited,

- Simplification of the integrand for the case $x = 0$, *i.e.* right at the discontinuity, and
- the even-odd properties of the integrand.

Before we proceed, we note that for the displacements at $x = 0$, we encounter the following integral,

$$I = \int_{-\infty}^{\infty} \eta^{-1}\, \mathcal{Z}_m(\eta a)\, \mathrm{J}_j(\eta a)\, d\eta. \tag{K.47}$$

The above integral is derived in Appendix K.10 and in the discussion below, we denote the one-sided form of Eq. (K.47) as

$$I_c(m,j) = \int_{0}^{\infty} \eta^{-1}\, \mathcal{Z}_m(\eta a)\, \mathrm{J}_j(\eta a)\, d\eta. \tag{K.48}$$

As an example, we will consider the derivation for the case of the horizontal displacement, u,

$$\mathrm{U}_{mj}^{(U)}(x,z) = C_j \int_{-\infty}^{\infty} \left[-\frac{2\eta^2 - \kappa^2}{\kappa^2\, \eta} e^{-x\gamma} + \frac{2\eta}{\kappa^2} e^{-x\delta} \right] \mathrm{U}_m(0) \mathcal{Z}_m(\eta a)\, \mathrm{J}_j(\eta a)\, d\eta \tag{K.49}$$

where C_j denotes $\sqrt{2}(-1)^{j+1}\, j/\pi t_\ell$. When $x = 0$ the above reduces to

$$\begin{aligned} \mathrm{U}_{mj}^{(U)}(0,z) &= C_j \int_{-\infty}^{\infty} \mathrm{U}_m(0)\, \eta^{-1}\, \mathcal{Z}_m(\eta a)\, \mathrm{J}_j(\eta a)\, d\eta \\ &= \begin{cases} 2C_j\, \mathrm{U}_m(0)\, I_c(m,j) & m,j = \text{odd or even} \\ 0 & \text{otherwise,} \end{cases} \end{aligned} \tag{K.50}$$

For the case when $x \neq 0$, the kernel is given by

$$f(\eta) = \left[-\frac{2\eta^2 - \kappa^2}{\kappa^2\, \eta} e^{-x\gamma} + \frac{2\eta}{\kappa^2} e^{-x\delta} \right] \mathcal{Z}_m(\eta a)\, \mathrm{J}_j(\eta a), \tag{K.51}$$

which exhibits symmetry of the form

$$f(-\eta) = (-1)^{m+j}\, f(\eta) = \begin{cases} f(\eta) & m+j = \text{even} \\ -f(\eta) & m+j = \text{odd}, \end{cases} \tag{K.52}$$

thereby reducing the integral to

$$\mathrm{U}^{(U)}_{mj}(x,z) = \begin{cases} 0 & m+j = \text{odd} \\ 2C_j \int_0^\infty f(\eta)\mathrm{U}_m(0)\, d\eta & m+j = \text{even}\ , \end{cases} \tag{K.53}$$

For the antisymmetric contribution,

$$\mathrm{U}^{(S)}_{mj}(x,z) = C_j \int_{-\infty}^{\infty} \left[-\frac{2i\gamma}{\kappa^2} e^{-x\gamma} + \frac{i}{\kappa^2\delta}(2\eta^2 - \kappa^2) e^{-x\delta} \right] \mathrm{W}_m(0) \mathcal{Z}_m(\eta a)\ \mathrm{J}_j(\eta a)\, d\eta, \tag{K.54}$$

and no simplification is possible for $x = 0$. When $x \neq 0$, the kernel equals

$$f(\eta) = \left[-\frac{2i\gamma}{\kappa^2} e^{-x\gamma} + \frac{i}{\kappa^2\delta}(2\eta^2 - \kappa^2) e^{-x\delta} \right] \mathcal{Z}_m(\eta a)\ \mathrm{J}_j(\eta a), \tag{K.55}$$

which exhibits symmetry of the form

$$f(-\eta) = (-1)^{m+j+1}\, f(\eta) = \begin{cases} f(\eta) & m+j = \text{odd} \\ -f(\eta) & m+j = \text{even}, \end{cases} \tag{K.56}$$

thereby reducing the integral to

$$\mathrm{U}^{(S)}_{mj}(x,z) = 2C_j \int_0^\infty f(\eta)\mathrm{W}_m(0)\, d\eta \qquad m+j = \text{odd} \tag{K.57}$$

Similar manipulations will bring out the symmetry properties in the other field variables.

Homogeneous Contributions

We make use of the fact that for the symmetric source,

$$\begin{aligned} A^{\pm}_{\ell,nk}(-s) &= A^{\pm}_{\ell,nk}(s), \\ B^{\pm}_{\ell,nk}(-s) &= -B^{\pm}_{\ell,nk}(s), \end{aligned} \tag{K.58}$$

and for the anti-symmetric source,

$$\begin{aligned} C^{\pm}_{\ell,nk}(-s) &= -C^{\pm}_{\ell,nk}(s), \\ D^{\pm}_{\ell,nk}(-s) &= D^{\pm}_{\ell,nk}(s), \end{aligned} \tag{K.59}$$

where $A^{\mp}_{\ell,nk}$ and $C^{\mp}_{\ell,nk}$ are the amplitudes of the up/down going compressional waves and $B^{\mp}_{\ell,nk}$ and $D^{\mp}_{\ell,nk}$ are the amplitudes of the up/down going shear waves.

Symmetric Source

For clarity, we treat the expression given by each combination of indices n and k individually as (and dropping the constant factor of $i\sqrt{2}m(-1)^m\pi$),

$$\begin{aligned}
U_{\ell m,nk}(x) &= \int_{-\infty}^{\infty} [\, -is\, A_+\, Q_\alpha \;+\; i\beta\, B_-\, Q_\beta \,]\, e^{-ixs}\, ds, \\
W_{\ell m,nk}(x) &= \int_{-\infty}^{\infty} [\, -\alpha\, A_-\, Q_\alpha \;+\; s\, B_+\, Q_\beta \,]\, e^{-ixs}\, ds, \\
T_{\ell m,nk}(x) &= \int_{-\infty}^{\infty} [\, -\vartheta\, A_+\, Q_\alpha \;+\; 2s\beta\, B_-\, Q_\beta \,]\, e^{-ixs}\, ds, \\
S_{\ell m,nk}(x) &= \int_{-\infty}^{\infty} [\, 2is\alpha\, A_-\, Q_\alpha \;-\; i\varpi\, B_+\, Q_\beta \,]\, e^{-ixs}\, ds,
\end{aligned} \tag{K.60}$$

where

$$\begin{aligned}
\zeta &= (-1)^{m+1}, \\
\varpi &= 2s^2 - \kappa^2, \\
\vartheta &= 2\alpha^2 + \kappa^2, \\
A_+ &= A^-_{\ell,nk} + \zeta_m A^+_{\ell,nk}, \\
A_- &= A^-_{\ell,nk} - \zeta_m A^+_{\ell,nk}, \\
B_+ &= B^-_{\ell,nk} + \zeta_m B^+_{\ell,nk}, \\
B_- &= B^-_{\ell,nk} - \zeta_m B^+_{\ell,nk}, \\
Q_\alpha &= e^{-a\alpha}\, \alpha^{-1}\, \mathrm{J}_m(ia\alpha), \\
Q_\beta &= e^{-a\beta}\, \beta^{-1}\, \mathrm{J}_m(ia\beta).
\end{aligned} \tag{K.61}$$

Since the amplitudes of the up and down-going compressional waves are symmetric with respect to s, therefore at $x = 0$, the above set of equations reduces to,

$$\begin{aligned}
U_{\ell m,nk}(0) &= 0 \\
W_{\ell m,nk}(0) &= 2 \int_0^{\infty} \left\{ -\alpha\, A_-\, Q_\alpha \;+\; s\, B_+\, Q_\beta \right\} ds, \\
T_{\ell m,nk}(0) &= 2 \int_0^{\infty} \left\{ -\vartheta\, A_+\, Q_\alpha \;+\; 2s\beta\, B_-\, Q_\beta \right\} ds, \\
S_{\ell m,nk}(0) &= 0
\end{aligned} \tag{K.62}$$

When $x \neq 0$, we have the exponential term e^{-ixs}, which can be written as $e^{-ixs} = \cos xs - i \sin xs$. Again, using symmetry arguments for the integrands, we arrive at

$$\begin{aligned}
U_{\ell,nk}(x) &= 2 \int_0^\infty -i \sin(xs) \, [\, -is \, A_+ \, Q_\alpha \, + \, i\beta \, B_- \, Q_\beta \,] \, ds, \\
W_{\ell,nk}(x) &= 2 \int_0^\infty \cos(xs) \, [\, -\alpha \, A_- \, Q_\alpha \, + \, s \, B_+ \, Q_\beta \,] \, ds, \\
T_{\ell,nk}(x) &= 2 \int_0^\infty \cos(xs) \, [\, -\vartheta \, A_+ \, Q_\alpha \, + \, 2s\beta \, B_- \, Q_\beta \,] \, ds, \\
S_{\ell,nk}(x) &= 2 \int_0^\infty -i \sin(xs) \, [\, 2is\alpha \, A_- \, Q_\alpha \, - \, i\varpi \, B_+ \, Q_\beta \,] \, ds,
\end{aligned} \tag{K.63}$$

Anti-symmetric Source

Following a similar argument, we obtain for the contributions at the cut $x = 0$,

$$\begin{aligned}
U_{\ell,nk}(0) &= 2 \int_0^\infty [\, -is \, A_+ \, Q_\alpha \, + \, i\beta \, B_- \, Q_\beta \,] \, ds, \\
W_{\ell,nk}(0) &= 0 \\
T_{\ell,nk}(0) &= 0 \\
S_{\ell,nk}(0) &= 2 \int_0^\infty [\, 2is\alpha \, A_- \, Q_\alpha \, - \, i\varpi \, B_+ \, Q_\beta \,] \, ds.
\end{aligned} \tag{K.64}$$

When $x \neq 0$, we have

$$\begin{aligned}
U_{\ell,nk}(x) &= 2 \int_0^\infty \cos(xs) \, [\, -is \, A_+ \, Q_\alpha \, + \, i\beta \, B_- \, Q_\beta \,] \, ds, \\
W_{\ell,nk}(x) &= 2 \int_0^\infty -i \sin(xs) \, [\, -\alpha \, A_- \, Q_\alpha \, + \, s \, B_+ \, Q_\beta \,] \, ds, \\
T_{\ell,nk}(x) &= 2 \int_0^\infty -i \sin(xs) \, [\, -\vartheta \, A_+ \, Q_\alpha \, + \, 2s\beta \, B_- \, Q_\beta \,] \, ds, \\
S_{\ell,nk}(x) &= 2 \int_0^\infty \cos(xs) \, [\, 2is\alpha \, A_- \, Q_\alpha \, - \, i\varpi \, B_+ \, Q_\beta \,] \, ds,
\end{aligned} \tag{K.65}$$

K.7 Physical Source Solution

Horizontal Wavenumber Integral Representation

Field equations for acoustic point source are given by

$$\overset{*}{\mathbf{v}}_\ell(x,z) = \int_{-\infty}^{\infty} \overset{*}{\mathbf{K}} e^{-|z-z_s|\alpha_n} e^{-i(x-x_s)s} ds, \tag{K.66}$$

with

$$\overset{*}{\mathbf{K}} = \begin{Bmatrix} -is/\alpha \\ -1 \\ \varpi/\alpha \\ 2is \end{Bmatrix},$$

where z_s and x_s is the source depth and range respectively.

Basis Function Expansion

Again, extracting expansion coefficient function gives us

$$\overset{*}{\mathbf{V}}_m(x) = \sqrt{2} m (-1)^m \pi \int_{-\infty}^{\infty} \overset{*}{\mathbf{K}} e^{-\frac{\iota_\ell}{2}\alpha} \alpha^{-1} \mathrm{J}_m(ia\alpha)\, e^{-i(x-x_s)s}\, ds, \tag{K.67}$$

where

$$\overset{*}{\mathbf{K}} = \begin{Bmatrix} -is/\alpha \\ -1 \\ -\vartheta/\alpha \\ 2is \end{Bmatrix}.$$

K.8 Homogeneous Solution for Physical Sources

Horizontal Wavenumber Integral Representation

The integral representations are given by

$$\tilde{\mathbf{v}}_\ell(x,z) = \int_{-\infty}^{\infty} \tilde{\mathbf{K}}\ \tilde{\mathbf{E}}\ \tilde{\mathbf{A}}\ e^{-i(x-x_s)s}\, ds, \tag{K.68}$$

where

$$\tilde{\mathbf{K}} = \begin{bmatrix} -is & -is & i\beta & -i\beta \\ -\alpha & \alpha & s & s \\ \varpi & \varpi & -2s\beta & 2s\beta \\ 2is\alpha & -2is\alpha & -i\varpi & -i\varpi \end{bmatrix},$$

$$\tilde{\mathbf{E}} = \operatorname{diag}\left[e^{-z\alpha}, e^{(z-t_\ell)\alpha}, e^{-z\beta}, e^{(z-t_\ell)\beta}\right],$$

$$\tilde{\mathbf{A}} = \begin{bmatrix} A_\ell^- & A_\ell^+ & B_\ell^- & B_\ell^+ \end{bmatrix}^T.$$

Note how the depth separated part is written such that waves generated at each horizontal interfaces decays as they propagate away, rendering the scheme unconditionally stable.

Basis Function Expansion

Similarly, the basis function expansions are

$$\tilde{\mathbf{V}}_m(x) = \sqrt{2}m(-1)^m\pi \int_{-\infty}^{\infty} \tilde{\mathbf{K}}\ \tilde{\mathbf{E}}\ \tilde{\mathbf{J}}\ \tilde{\mathbf{A}}\ e^{-i(x-x_s)s}\, ds, \tag{K.69}$$

where $\tilde{\mathbf{K}}$, $\tilde{\mathbf{E}}$ and $\tilde{\mathbf{J}}$ are the same as that of the homogeneous solution for the panel source.

$$\tilde{\mathbf{K}} = \begin{bmatrix} -is & -is & i\beta & -i\beta \\ -\alpha & \alpha & s & s \\ -\vartheta & -\vartheta & 2s\beta & -2s\beta \\ 2is\alpha & -2is\alpha & -i\varpi & -i\varpi \end{bmatrix},$$

$$\tilde{\mathbf{E}} = \operatorname{diag}\left[e^{-\frac{t_\ell}{2}\alpha}, e^{-\frac{t_\ell}{2}\alpha}, e^{-\frac{t_\ell}{2}\beta}, e^{-\frac{t_\ell}{2}\beta}\right],$$

$$\tilde{\mathbf{A}} = \left[\begin{array}{cccc} A_\ell^- & A_\ell^+ & B_\ell^- & B_\ell^+ \end{array} \right]^T,$$

$$\tilde{\mathbf{J}} = \text{diag}\left[\alpha^{-1}\,\mathrm{J}_m(ia\alpha)\,,\ \zeta_m\alpha^{-1}\mathrm{J}_m(ia\alpha)\,,\ \beta^{-1}\mathrm{J}_m(ia\beta)\,,\ \zeta_m\beta^{-1}\mathrm{J}_m(ia\beta)\right],$$

and $\zeta_m = (-1)^{m+1}$.

K.9 Derivation of $\mathcal{Z}_m(\eta a)$

We have

$$\mathcal{Z}_m(\eta a) = \int_{-a}^{a} \frac{\psi_m(x)}{\sqrt{a^2 - x^2}}\, e^{-i\eta x}\, dx, \tag{K.70}$$

where the eigenfunctions are defined as

$$\psi_m(\bar{z}) = \begin{cases} i\sqrt{2}\, \sin[m \arcsin(\bar{z}/a)] & \text{m = 0,2,4,...} \\ \sqrt{2}\, \cos[m \arcsin(\bar{z}/a)] & \text{m = 1,3,5,...} \end{cases} \tag{K.71}$$

Case of m = odd

In this case,

$$\mathcal{Z}_m(\eta a) = \sqrt{2} \int_{-a}^{a} \frac{\cos[m \arcsin(x/a)]}{\sqrt{a^2 - x^2}}\, e^{-i\eta x}\, dx \tag{K.72}$$

We first make the change of variables,

$$\begin{aligned} y &= x/a, \\ \beta &= \eta a, \end{aligned} \tag{K.73}$$

which transforms the integral to

$$\mathcal{Z}_m(\eta a) = \sqrt{2} \int_{-1}^{+1} \frac{\cos[m \arcsin(y)]}{\sqrt{1 - y^2}}\, e^{-i\beta y}\, dy. \tag{K.74}$$

Next, letting $\sin^{-1}(y) = x$, or $\cos(x) = \sqrt{1 - y^2}$, we arrive at

$$\frac{\cos[m \arcsin(y)]}{\sqrt{1 - y^2}} = \frac{\cos mx}{\cos x}, \tag{K.75}$$

and using Eq. (1.391.4) from [53] for the case of m = odd, we have

$$\frac{\cos mx}{\cos x} = \prod_{k=1}^{\frac{m-1}{2}} \left\{ 1 - \frac{1 - \cos^2 x}{\sin^2 \frac{(2k-1)\pi}{2m}} \right\}. \tag{K.76}$$

We now have

$$\mathcal{Z}_m(\eta a) = \sqrt{2} \int_{-1}^{+1} \prod_{k=1}^{\frac{m-1}{2}} \left\{ 1 - \frac{1 - \cos^2 x}{\sin^2 \frac{(2k-1)\pi}{2m}} \right\} e^{-i\beta y}\, dy, \tag{K.77}$$

and since $\cos^2 x = 1 - y^2$, it is easy to see that in expanding the products of sums above, we require the solution to integrals of the form

$$Q_n = \int_{-1}^{+1} (1-y^2)^n \, e^{-i\beta y} \, dy. \tag{K.78}$$

Using Eq. (3.387.2) from [53] with

$$\begin{aligned} n &= \nu - 1, \\ \mu &= -\beta = -\eta a, \end{aligned} \tag{K.79}$$

we obtain

$$\begin{aligned} Q_n &= \int_{-1}^{+1} (1-y^2)^n \, e^{-i\beta y} \, dy, \\ &= \sqrt{\pi} \, 2^{n+1/2} \, \Gamma(n+1) \, \mu^{-(n+1/2)} \, \mathrm{J}_{n+\frac{1}{2}}(\mu), \\ &= \frac{n! \, 2^{n+1}}{\mu^n} \sqrt{\frac{\pi}{2(-\eta a)}} \, \mathrm{J}_{n+\frac{1}{2}}(-\eta a). \end{aligned} \tag{K.80}$$

Using the following,

$$\begin{aligned} j_n &= \sqrt{\frac{\pi}{2z}} \, \mathrm{J}_{n+\frac{1}{2}}(z), \\ j_n(-z) &= (-1)^n \, j_n(z), \end{aligned} \tag{K.81}$$

we obtain

$$Q_n(\beta) = n! \, 2^{n+1} \, \beta^{-n} \, j_n(\beta), \tag{K.82}$$

where $\beta = \eta a$. Using both Eq. (K.77) and Eq. (K.82), we can now build up closed form expressions for any m, η and a.

Case of m = even

In this case,

$$\mathcal{Z}_m(\eta a) = i\sqrt{2} \int_{-a}^{a} \frac{\sin[m \arcsin(x/a)]}{\sqrt{a^2 - x^2}} \, e^{-i\eta x} \, dx. \tag{K.83}$$

Making the same change of variable as before, we obtain

$$\mathcal{Z}_m(\eta a) = i\sqrt{2} \int_{-1}^{+1} \frac{\sin[m \arcsin(y)]}{\sqrt{1 - y^2}} \, e^{-i\beta y} \, dy. \tag{K.84}$$

Letting $\sin^{-1}(y) = x$, or $\cos(x) = \sqrt{1-y^2}$, we arrive at

$$\frac{\sin[m \arcsin(y)]}{\sqrt{1-y^2}} = \frac{\sin mx}{\cos x}, \tag{K.85}$$

and using Eq. (1.391.1) from [53] for the case of m = even, we have

$$\frac{\sin mx}{\cos x} = m \sin x \prod_{k=1}^{\frac{m-2}{2}} \left\{ 1 - \frac{1-\cos^2 x}{\sin^2 \frac{k\pi}{m}} \right\}. \tag{K.86}$$

Collecting terms, we have

$$\mathcal{Z}_m(\eta a) = i\sqrt{2}\, m \int_{-1}^{+1} \sin x \prod_{k=1}^{\frac{m-2}{2}} \left\{ 1 - \frac{1-\cos^2 x}{\sin^2 \frac{k\pi}{m}} \right\} e^{-i\beta y}\, dy, \tag{K.87}$$

and since $\cos^2 x = 1 - y^2$ and $\sin x = y$, we see that in this case we are concerned with integrals of the form

$$R_n(\beta) = \int_{-1}^{+1} y\, (1-y^2)^n\, e^{-i\beta y}\, dy. \tag{K.88}$$

To obtain closed form expressions for the above, we employ a generalization of the Poisson's integral as presented in Eq. (8) on Pg. 369 of [63],

$$\int_0^{\pi} e^{iz\cos\phi}\, C_m^{\nu}(\cos\phi)\, \sin^{2\nu}\phi\, d\phi = \frac{2^{\nu}\, \Gamma(\nu+\frac{1}{2})\, \Gamma(\frac{1}{2})\, \Gamma(2\nu+m)}{m\, \Gamma(2\nu)}\, i^m\, \frac{\mathrm{J}_{\nu+m}(z)}{z^{\nu}}, \tag{K.89}$$

which is valid for $\Re(\nu) > -1/2$. We start with the change of variable $t = \cos\phi$. For the Gegenbauer polynomial, we let $m = 1$ and note that

$$C_1^{\lambda} = 2\lambda t. \tag{K.90}$$

Now,

$$\begin{aligned} R_g(z) &= \int_0^{\pi} e^{iz\cos\phi}\, C_1^{\nu}(\cos\phi)\, \sin^{2\nu}\phi\, d\phi, \\ &= \int_{-1}^{+1} e^{izt}\, C_1^{\nu}(t)\, [1-t^2]^{\nu-\frac{1}{2}}\, dt. \end{aligned} \tag{K.91}$$

Finally, we let $n = \nu - 1/2$, $z = -\beta$, resulting in

$$R_g(-\beta) = (2n+1) \int_{-1}^{+1} y(1-y^2)^n\, e^{-i\beta y}\, dy = (2n+1)\, R_n(\beta). \tag{K.92}$$

Re-arranging,

$$\begin{aligned} R_n(\beta) &= \frac{1}{2n+1} R_g(-\beta), \\ &= \frac{i}{2n+1} \frac{2^{n+\frac{1}{2}}\,\Gamma(n+1)\,\Gamma(\frac{1}{2})\,\Gamma(2n+2)}{\Gamma(2n+1)} \frac{\mathrm{J}_{n+1+\frac{1}{2}}(-\beta)}{(-\beta)^{n+\frac{1}{2}}}. \end{aligned} \tag{K.93}$$

We further note that $\Gamma(\frac{1}{2}) = \sqrt{\pi}$ and the condition $\Re(\nu) = \Re(n+1/2) > -1/2$ is satisfied. Placing in terms of spherical harmonics, we arrive at

$$R_n(\beta) = -i\, n!\, 2^{n+1}\, \beta^{-n}\, j_{n+1}(\beta), \tag{K.94}$$

where $\beta = \eta a$.

The first 8 terms for $\mathcal{Z}_m(\eta, a)$

In this section we present the first 8 terms for the series, $\mathcal{Z}_m$ obtained using the expressions derived in Appendix K.9. Here, we let the arguments to $\mathcal{Z}_m$ be simply β where $\beta = \eta a$.

$$\begin{aligned} \mathcal{Z}_0 &= 0, \\ \mathcal{Z}_1 &= 2\sqrt{2}\, j_0(\beta), \\ \mathcal{Z}_2 &= 2\sqrt{2}\, j_1(\beta), \\ \mathcal{Z}_3 &= 4\sqrt{2}\, \frac{j_1(\beta)}{\beta}, \\ \mathcal{Z}_4 &= \sqrt{2}\left[32\, \frac{j_2(\beta)}{\beta} - 8\, j_1(\beta) \right], \\ \mathcal{Z}_5 &= \sqrt{2}\left[256\, \frac{j_2(\beta)}{\beta^2} - 80\, \frac{j_1(\beta)}{\beta} + 10\, j_0(\beta) \right], \\ \mathcal{Z}_6 &= \sqrt{2}\left[512\, \frac{j_3(\beta)}{\beta^2} - 128\, \frac{j_2(\beta)}{\beta} + 12\, j_1(\beta) \right], \\ \mathcal{Z}_7 &= \sqrt{2}\left[6144\, \frac{j_3(\beta)}{\beta^3} - 1792\, \frac{j_2(\beta)}{\beta^2} + 224\, \frac{j_1(\beta)}{\beta} - 14\, j_0(\beta) \right], \\ \mathcal{Z}_8 &= \sqrt{2}\left[12288\, \frac{j_4(\beta)}{\beta^3} - 3072\, \frac{j_3(\beta)}{\beta^2} + 320\, \frac{j_2(\beta)}{\beta} - 16\, j_1(\beta) \right]. \end{aligned} \tag{K.95}$$

K.10 Derivation of $I_c(m,j)$

In obtaining the field equations in the vertical wavenumber domain, we encounter for $x = 0$, an integral of the form,

$$I_c^2(m,j) = \int_{-\infty}^{\infty} \frac{1}{\eta}\, \mathrm{J}_j(\eta a)\; \mathcal{Z}_m(\eta a)\; d\eta, \tag{K.96}$$

where the superscript indicates the 2-sided form of $I_c(m,j)$. We note that for m = odd, a typical term in $I_c(m,j)$ is of the form

$$\tilde{\mathcal{Z}}_m = c_m\; (\eta a)^{-k}\; j_k(\eta a), \tag{K.97}$$

and for m = even, a typical term would look like

$$\tilde{\mathcal{Z}}_m = c_m\; j_k(\eta a)\; (\eta a)^{-k+1} \qquad\qquad k > 0 \tag{K.98}$$

where c_m is a real constant. We therefore need to evaluate 2 different forms, namely

$$\begin{aligned} Y_{\text{odd}} &= \int_{-\infty}^{\infty} \frac{1}{\eta}\, \mathrm{J}_j(\eta a)\; \frac{j_k(\eta a)}{(\eta a)^k}\; d\eta, \\ Y_{\text{even}} &= \int_{-\infty}^{\infty} \frac{1}{\eta}\, \mathrm{J}_j(\eta a)\; \frac{j_k(\eta a)}{(\eta a)^{k-1}}\; d\eta. \end{aligned} \tag{K.99}$$

A simple change of variable, $x = \eta a$, transforms the above to

$$\begin{aligned} Y_{\text{odd}} &= \int_{-\infty}^{\infty} x^{-k-1}\; \mathrm{J}_j(x)\; j_k(x)\; dx, \\ Y_{\text{even}} &= \int_{-\infty}^{\infty} x^{-k}\; \mathrm{J}_j(x)\; j_k(x)\; dx. \end{aligned} \tag{K.100}$$

Since the spherical harmonics are Bessel functions of fractional orders, we can rewrite the above (after employing symmetry for negative η) as

$$Y_{\text{odd}} = \begin{cases} 0 & j = \text{even} \\ 2\sqrt{\frac{\pi}{2}}\; \int_0^{\infty} x^{-k-\frac{3}{2}}\; \mathrm{J}_j(x)\; \mathrm{J}_{k+\frac{1}{2}}(x)\; dx & j = \text{odd} \end{cases} \tag{K.101}$$

and

$$Y_{\text{even}} = \begin{cases} 0 & j = \text{odd} \\ 2\sqrt{\frac{\pi}{2}}\; \int_0^{\infty} x^{-k-\frac{1}{2}}\; \mathrm{J}_j(x)\; \mathrm{J}_{k+\frac{1}{2}}(x)\; dx & j = \text{even} \end{cases} \tag{K.102}$$

We next use Eq. (6.574.2) in [53] with appropriate substitutions to obtain,

$$I_c(m,j) = \frac{\sqrt{\pi}}{2^{k+1}} \begin{cases} \frac{\Gamma(k+\frac{3}{2})}{j\,\Gamma(k-\frac{j}{2}+\frac{3}{2})\,\Gamma(k+\frac{j}{2}+\frac{3}{2})} & m,j = \text{odd} \\ \frac{\Gamma(k+\frac{1}{2})}{\Gamma(k-\frac{j}{2}+1)\,\Gamma(k+\frac{j}{2}+1)} & m,j = \text{even} \end{cases} \tag{K.103}$$

Bibliography

[1] F.B. Jensen, W.A. Kuperman, M.B. Porter, and H. Schmidt. *Computational Ocean Acoustics.* American Institute of Physics, Woodbury, NY, 1993.

[2] P.C. Etter. *Underwater Acoustic Modeling.* Elsevier, Amsterdam, The Netherlands, 1991.

[3] C. Canuto, M.Y. Hussaini, A. Quarteroni, and T.A. Zang. *Spectral Methods in Fluid Dynamics.* Springer Verlag, NY, 1988.

[4] E. Priolo, J.M. Carcione, and G. Seriani. Numerical simulation of interface waves by high-order spectral modeling techniques. *J. Acoust. Soc. Am.*, 95:681–693, 1994.

[5] Ding Lee and A.D. Pierce. Parabolic equation development in recent decade. *Journal Computational Acoustics*, 3(2):95–173, 1995.

[6] M.D. Collins and R.B. Evans. A two-way parabolic equation for acoustic backscattering in the ocean. *J. Acoust. Soc. Am.*, 91 (3):1357–1368, 1992.

[7] J.A. Hudson. A parabolic approximation for elastic waves. *Wave Motion*, 2:207–214, 1980.

[8] Corones J.P., DeFacio B, and R.J. Krueger. Parabolic approximations to the time-independent elastic wave equation. *Journal Math. Phys.*, 23(4):577–586, 1982.

[9] Wales S.C. and McCoy J.J. A comparison of parabolic wave theories for linearly elastic solids. *Wave Motion*, 5:99–113, 1983.

[10] Greene R.R. A high-angle one-way wave equation for seismic wave propagation along rough and sloping interfaces. *J. Acoust. Soc. Am.*, 77:1991–1998, 1985.

[11] B.T.R. Wetton and G.H. Brooke. One-way wave equations for seismoacoustic propagation in elastic waveguides. *J. Acoust. Soc. Am.*, 87(2):624–632, 1990.

[12] M.D. Collins. A two-way parabolic equation method for elastic media. *J. Acoust. Soc. Am.*, 91:1815–1825, 1992.

[13] M.D. Collins. An energy conserving parabolic equation for elastic media. *J. Acoust. Soc. Am.*, 94 (3):975–982, 1993.

[14] F.B. Jensen and H. Schmidt. Spectral decomposition of PE fields in a wedge-shaped ocean. In H.M. Merklinger, editor, *Progress in Underwater Acoustics.* Plenum Press, New York, 1987.

[15] R.B. Evans. A coupled mode solution for acoustic propagation in a waveguide with stepwise depth variations of a penetrable bottom. *J. Acoust. Soc. Am.*, 74:188–195, 1983.

[16] H. Schmidt. SAFARI: Seismo-acoustic fast field algorithm for range independent environments. User's guide. SR 113, SACLANT ASW Research Centre, La Spezia, Italy, 1987.

[17] I.T. Lu and L.B. Felsen. Adiabatic transforms for spectral analysis and synthesis of weakly range-dependent shallow ocean Green's functions. *J. Acoust. Soc. Am.*, 81:897–911, 1987.

[18] J.T. Goh and H. Schmidt. Validity of spectral theories for weakly range-dependent ocean environments - Numerical results. *J. Acoust. Soc. Am.*, 95 (2):727–732, 1994.

[19] K.E. Gilbert and R.B. Evans. A Green's function method for one-way wave propagation in a range dependent ocean environment. In T. Akal and J.M. Berkson, editors, *Ocean Seismo-Acoustics.* Plenum Press, New York, 1986.

[20] G.T. Schuster and L.C. Smith. Modeling scatterers embedded in a plane-layered media by a hybrid Haskell-Thomson and boundary integral equation method. *J. Acoust. Soc. Am.*, 78:1387–1394, 1985.

[21] T.W. Dawson and J.A. Fawcett. A boundary integral equation method for acoustic scattering in a waveguide with nonplanar surfaces. *J. Acoust. Soc. Am.*, 87:1110–1125, 1990.

[22] P. Gerstoft and H. Schmidt. A boundary element approach to seismo-acoustic facet reverberation. *J. Acoust. Soc. Am.*, 89:1629–1642, 1991.

[23] M.W. Haartsen, M. Bouchon, and M.N. Toksöz. A study of seismic acoustic wave propagation through a laterally varying multilayered medium using the boundary-integral-equation-discrete-wave-number method. *J. Acoust. Soc. Am.*, 96:3010–3021, 1994.

[24] H. Schmidt. Marching wavenumber-integration approach to range-dependent, two-way seismoacoustic propagation modeling. *J. Acoust. Soc. Am.*, 97(5):3316 (A), 1995.

[25] W. Seong. *Hybrid Galerkin boundary element - wavenumber integration method for acoustic propagation in laterally inhomogeneous media.* PhD thesis, Massachusetts Institute of Technology, January 1991.

[26] D. G. Harkrider. Surface waves in multilayered elastic media i. rayleigh and love waves from buried sources in a multilayered elastic half-space. *Bull. Seism. Soc. Am.*, 54(2):627–679, 1964.

[27] H. Kawase. Time-domain response of a semi-circular canyon for incident SV, P and Rayleigh waves calculated by the discrete wavenumber boundary element method. *Bull. Seismol. Soc. Am.*, 78:1415–1437, 1988.

[28] A. Kamel and L.B. Felsen. Spectral theory of sound propagation in an ocean channel with weakly sloping bottom. *J. Acoust. Soc. Am.*, 73:1120–1130, 1983.

[29] D.J. Tang and Y.P. Guo. Spectral formalism of wave propagation in a range-dependent shallow water waveguide. *J. Acoust. Soc. Am.*, 93:2284 (A), 1993.

[30] F.B. Jensen and C.M. Ferla. Numerical solutions of range-dependent benchmark problems in ocean acoustics. *J. Acoust. Soc. Am.*, 87:1499–1510, 1990.

[31] F.B. Jensen and W.A. Kuperman. Sound propagation in a wedge-shaped ocean with a penetrable bottom. *J. Acoust. Soc. Am.*, 67:1564–1566, 1980.

[32] F.B. Jensen and M.C. Ferla. SNAP : The SACLANTCEN Normal-Mode Acoustic Propagation Model. SM 121, SACLANT ASW Research Centre, La Spezia, Italy, 1979.

[33] Michael D. Collins. Benchmark calculations for higher-order parabolic equations. *J. Acoust. Soc. Am.*, 87:1535–1538, 1990.

[34] E. Bahar. Radio wave propagation in stratified media with nonuniform boundaries and varying electromagnetic parameters: Full Wave Analysis. *Can. J. Phys*, 50:3132–3142, 1972.

[35] E. Bahar. Electromagnetic wave propagation in inhomogeneous multilayered structures of arbitrarily varying thickness - Generalized field transforms. *Journal Math. Phys.*, 14(8):1024–1029, 1973.

[36] E. Bahar. Electromagnetic wave propagation in inhomogeneous multilayered structures of arbitrary thickness - Full wave solutions. *Journal Math. Phys.*, 14(8):1030–1036, 1973.

[37] E. Bahar. Field transforms for multilayered cylindrical and spherical structures of finite conductivity. *Can. J. Phys*, 53(8):1078–1087, 1975.

[38] J. M. Carcione and F. Cavallini. On the acoustic-electromagnetic analogy. *Wave Motion*, 21:149–162, 1995.

[39] H. Schmidt and G. Tango. Efficient global matrix approach to the computation of synthetic seismograms. *Geophys. J. R. Astr. Soc.*, 84:331–359, 1986.

[40] P.A. Heelan. Radiation from a cylindrical source of finite length. *Geophysics*, 18:685–696, 1953.

[41] I.S. Gradshteyn and I.M. Ryzhik. *Table of integrals, series and products.* Academic Press, 1980.

[42] E.K. Westwood. Ray model solutions to the benchmark wedge problems. *J. Acoust. Soc. Am.*, 87:1539–1545, 1990.

[43] F.B. Jensen and Peter Gerstoft. Benchmark solutions for backscattering in simple waveguide geometries. In L. Bjorno, editor, *Proceedings of the second European Conference on Underwater Acoustics, Vol. I.* European Commission, Luxembourg, 1994.

[44] D.B. King, S.A. Chin-Bing, R.B. Evans, and J.A. Davis. *Benchmark Solutions in Reverberation and Scattering - Proceedings of the Reverberation and Scattering Workshop.* Naval Research Laboratory, 1994.

[45] K.F. Graff. *Wave motion in elastic solids.* Dover, New York, 1991.

[46] A. D. Achenbach. *Wave propagation in elastic solids.* North Holland Publishing Company, Amsterdam, 1975.

[47] Henrik Schmidt, Woojae Seong, and J.T. Goh. Spectral super-element approach to range-dependent ocean acoustic modeling. *J. Acoust. Soc. Am.*, 98(1):465–472, 1995.

[48] H. Schmidt and F.B. Jensen. A full wave solution for propagation in multilayered viscoelastic media with application to Gaussian beam reflection at fluid-solid interfaces. *J. Acoust. Soc. Am.*, 77(3):813–825, 1985.

[49] J.T. Goh and H. Schmidt. A hybrid coupled wavenumber integration approach to range-dependent seismo-acoustic modeling. *J. Acoust. Soc. Am.*, Submitted for publication, 1996.

[50] J.A. Davis, D. White, and R.C. Cavanaugh. *NORDA Parabolic Equation Workshop.* NORDA Tech Note 143, 1982.

[51] S.A. Chin-Bing, D.B. King, J.A. Davis, and R.B. Evans. *PE Workshop II - Proceedings of the Second Parabolic Equation Workshop.* Naval Research Laboratory, 1993.

[52] R.B. Evans and K.E. Gilbert. The periodic extension of stepwise coupled modes. *J. Acoust. Soc. Am.*, 77(3):983–988, 1985.

[53] M. Abramowitz and I.A. Stegun. *Handbook of Mathematical Functions.* Dover Publications, 1972.

[54] R. Piessens and *et.al. QUADPACK - A Subroutine Package for Automatic Integration.* Springer Verlag, Berlin, 1983.

[55] P. Favati, G. Lotti, and F. Romani. ALGORITHM 691 - Improving QUADPACK Automatic Integration Routines. *ACM Trans. Math. Softw.*, 17:218–232, 1991.

[56] Y. L. Li. Efficient computation of sound field above ground in horizontally stratified media using a Wentzel-Kramers-Brillouin-type approximation with Airy functions. *J. Acoust. Soc. Am.*, 98 (6):3405–3411, 1995.

[57] J.M. Perez-Jorda, E. San-Fabian, and F. Moscardo. A simple, reliable and efficient scheme for automatic numerical integration. *Computer Physics Communications*, 70:271–284, 1992.

[58] J.M. Perez-Jorda and E. San-Fabian. A simple, efficient and more reliable scheme for automatic numerical integration. *Computer Physics Communications*, 77:46–56, 1993.

[59] S. Krenk and H. Schmidt. Elastic wave scattering by a circular crack. *Phil. Trans. R. Soc. Lond.*, 308:167–198, 1982.

[60] Peter M. van den Berg. Transition matrix in acoustic scattering by a strip. *J. Acoust. Soc. Am.*, 70(2):615–619, 1981.

[61] Bruce W. Char and *et.al. Maple V Library Reference Manual.* Springer Verlag, 1991.

[62] Stephen Wolfram. *Mathematica - A System for Doing Mathematics by Computer.* Addison Wesley, 1991.

[63] G. N. Watson. *A Treatise on the theory of Bessel functions.* Cambridge University Press, 1941.

THESIS PROCESSING SLIP

FIXED FIELD: ill _____ name _____

index _____ biblio _____

▶ COPIES: (Archives) Aero Dewey (Eng) Hum

Lindgren Music Rotch Science

TITLE VARIES: ▶☐ _____

NAME VARIES: ▶☐ _____

IMPRINT (COPYRIGHT) _____

▶ COLLATION: 181 p.

▶ ADD. DEGREE: _____ ▶ DEPT.: _____

SUPERVISORS: _____

NOTES:

cat'r. date:

page. T143

▶ DEPT: O.E.

▶ YEAR: 1996 ▶ DEGREE: Ph.D

▶ NAME GOH, Joo Thiam